



UNIVERSITY OF LJUBLJANA
FACULTY OF MATHEMATICS AND PHYSICS

Ilija Bizjak

**Measurement of $|V_{ub}|$ Using Inclusive Semileptonic Decays on a Sample of
Reconstructed B mesons with the Belle Detector**

Doctoral Thesis

Supervisor: Prof. Dr. Peter Križan

Ljubljana, 2005



UNIVERZA V LJUBLJANI
FAKULTETA ZA MATEMATIKO IN FIZIKO

Ilija Bizjak

**Meritev parametra $|V_{ub}|$ z inkluzivnimi semileptonskimi razpadi v vzorcu
rekonstruiranih mezonov B detektorja Belle**

Doktorska disertacija

Mentor: prof. dr. Peter Križan

Ljubljana, 2005

*I was gratified to be able to answer promptly
and I did. I said I didn't know.*

Mark Twain

Zahvaljujem se mentorju prof. Petru Križanu, ker se je neutrudno prebijal čez moje izdelke in me je vedno uspel usmeriti na pravi način, pri tem pa mi je pokazal, da je rana ura zlata ura in da vsega res ni treba oddati zadnjo minuto, marsikaj pa lahko . . .

Zahvaljujem se Boštjanu Golobu, ker me je vzel na grbo ob samih začetkih mojega raziskovalnega dela in uspešno pripomogel, da ni samo pri začetkih tudi ostalo.

Rad bi se zahvalil prof. Svjetlani Fajfer, ker je bila vedno na voljo za pogovor, ker je verjela vame, tudi ko sam nisem, in ker me je naučila, naj ne pišem o stvareh, o katerih ne vem dovolj.

Zahvaljujem se Tomažu Podobniku, ki mi je pomagal vzljubiti statistiko, Marku Bračku, ki me je z dobro mero ironije uspel potiskati v pravo smer, ter Samu Korparju, ki mi je z enim zamahom natisnil večji del doktorata.

The work in an international collaboration offers an opportunity to learn from many excellent scientists. I am grateful for all the support and advice I got, without it, this work would be poorer. Thank you all for letting me explore physics, culture and myself in your company.

I would like to express my gratitude to prof. Tadao Nozaki and prof. Toru Iijima, for their time, help, countless discussions, patience and understanding. Because of them my experience in Japan was invaluable.

I would like to thank prof. Kay Kinoshita, prof. Tom Browder and prof. Yoshihide Sakai, who have shown me that it can be done, and that it can be done well.

Special thanks to Christoph Schwanda, who had a practical solution to any practical problem, and for pleasant discussions and delightful food in Kaneki. Special thanks also to Antonio Limosani, who was selflessly leading the way and made mine easier and more interesting.

I appreciate the time and the effort from Takahiro Matsumoto and Isamu Nakamura, to prepare and maintain the fully reconstructed sample.

Zahvaljujem se Jerneju, Kristi, Jerici in Nini, ker so mi pokazali, da je institut lahko moj drugi dom, da se da iti direktno s kave na kosilo, in da ni vse tako hudo, kot se zdi.

Dragi starši, brez vaše vzpodbude in zaupanja vsega tega ne bi bilo, hvala za vse. Draga Doroteja, tebi pa posvečam to delo: čeprav mi veliko pomeni, si ga zares osmislila šele ti, s svojo ljubeznijo in nasmehom.

Abstract

A precise measurement of the magnitude of the Cabibbo-Kobayashi-Maskawa matrix element V_{ub} is of fundamental importance for over-constraining the Unitarity Triangle and thus testing the predictions of the Standard Model.

We present a measurement of $|V_{ub}|$, based on 253 fb^{-1} of data collected by the Belle detector at the KEKB e^+e^- asymmetric collider. Events are tagged by fully reconstructing the decay chain of one of the B mesons, which are produced in pairs in the decays of the $\Upsilon(4S)$ resonance. An inclusive search for charmless semileptonic decays was performed in the decay products of the other B meson.

The signal for $b \rightarrow u$ semileptonic decay is distinguished from the $b \rightarrow c$ background semileptonic decay using three inclusive kinematic variables: the hadronic invariant mass M_X , the leptonic invariant mass squared q^2 and the variable $P_+ \equiv E_X - |\vec{p}_X|$. The charmless semileptonic partial rates $\Delta\Gamma_{u\ell\nu}(\Delta\Phi)$ into a kinematical signal region $\Delta\Phi$ are obtained for events with the prompt-lepton momentum $p^* \geq 1 \text{ GeV}/c$ in three kinematic regions: (1) $M_X < 1.7 \text{ GeV}/c^2$, (2) $M_X < 1.7 \text{ GeV}/c^2$ combined with $q^2 > 8 \text{ GeV}^2/c^2$, and by (3) $P_+ < 0.66 \text{ GeV}/c$, allowing for a comparison of the three methods.

The matrix element $|V_{ub}|$ is found to be $(4.09 \pm 0.19 \pm 0.20^{+0.14}_{-0.15} \pm 0.18) \times 10^{-3}$, where the errors are statistical, systematic including MC modeling, theoretical and from shape function parameter determination, respectively.

Keywords: *Standard Model, CKM matrix, Unitarity Triangle, semileptonic decays of B mesons, full reconstruction tag.*

PACS:

- 12.15.Hh Determination of Kobayashi-Maskawa matrix elements,
- 13.25.Hw Decays of bottom mesons,
- 11.30.Er Charge conjugation, parity, time reversal, and other discrete symmetries.

Izveček

Natančna določitev velikosti matričnega elementa V_{ub} matrike Cabibbo-Kobayashi-Maskawa je izjemno pomembna pri preverjanju napovedi Standardnega Modela.

V delu je predstavljena meritev $|V_{ub}|$ na vzorcu podatkov, ki ustrezajo integrirani luminoznosti 253 fb^{-1} , izmerjeni pa so bili z detektorjem Belle na asimetričnem trkalniku elektronov in pozitronov KEKB. Dogodke izbiramo s pomočjo polne rekonstrukcije razpadne verige enega od obeh mezonov B , ki nastaneta v paru pri razpadu resonance $\Upsilon(4S)$. V razpadih drugega od obeh mezonov iščemo semileptonske razpade, pri katerih je kvark b prešel v kvark u .

Iskane semileptonske razpade $b \rightarrow u$ ločimo od semileptonskih razpadov $b \rightarrow c$ s pomočjo treh kinematičnih količin: hadronske invariantne mase M_X , kvadrata leptonske invariantne mase q^2 in spremenljivke $P_+ \equiv E_X - |\vec{p}_X|$. Nato za dogodke z zaznanim leptonom gibalne količine $p^* \geq 1 \text{ GeV}/c$ izračunamo $\Delta\Gamma_{u\ell\nu}(\Delta\Phi)$, delno semileptonsko razpadno širino za razpadne produkte s kvarkom u v treh kinematičnih območjih $\Delta\Phi$: (1) $M_X < 1.7 \text{ GeV}/c^2$, (2) $M_X < 1.7 \text{ GeV}/c^2$ skupaj s $q^2 > 8 \text{ GeV}^2/c^2$, in (3) $P_+ < 0.66 \text{ GeV}/c$.

Rezultat meritve je velikost matričnega elementa $|V_{ub}| = (4.09 \pm 0.19 \pm 0.20^{+0.14}_{-0.15} \pm 0.18) \times 10^{-3}$, podane napake so povrsti statistična, sistematska, vključno z napako zaradi modeliranja MC, teoretična napaka ter napaka zaradi določitve parametrov strukturne funkcije.

Ključne besede: *Standardni Model, matrika CKM, unitarnostni trikotnik, semileptonski razpadi mezonov B, določanje s polno rekonstrukcijo.*

PACS: 12.15.Hh, 11.30.Er, 13.25.Hw.

Contents

Introduction	1
1 Introduction	7
2 Motivation for a V_{ub} Measurement	9
2.1 Standard Model	9
2.2 Weak decays	10
2.2.1 Theory of the CKM matrix	10
2.2.2 The origin of the CKM Matrix	10
2.2.3 Parametrization of the CKM Matrix	12
2.2.4 Unitarity conditions of the CKM Matrix	13
2.2.4.1 Constraining the Unitarity Triangle	14
2.2.4.2 Measurement of $ V_{ub} $ and $ V_{cb} $	14
2.3 Summary	16
3 Theoretical Background of the Inclusive Semileptonic B Decays	17
3.1 Inclusive decay width calculation	17
3.1.1 Beyond the simple spectator model	18
3.1.1.1 Operator Product Expansion	19
3.1.2 Inclusive kinematical variables	20
3.1.2.1 QCD factorization	22
3.1.3 Shape functions	23
3.1.3.1 Shape function parametrization	23
3.2 Extraction of $ V_{ub} $	25
3.2.1 Sources of theoretical uncertainties	25
3.2.1.1 The choice of shape-function functional forms	26
3.2.1.2 Perturbative uncertainties	26

3.2.1.3	Weak-annihilation effects	26
3.3	Modeling $b \rightarrow ul\nu$ decays	26
3.3.0.4	Non-resonant decay mode	27
4	The Belle experiment	29
4.1	The KEKB accelerator and storage ring	29
4.2	The Belle detector	31
4.2.0.5	Coordinate systems	32
4.2.1	Beam Pipe	32
4.2.2	Silicon Vertex Detector (SVD)	32
4.2.3	Central Drift Chamber (CDC)	35
4.2.4	Aerogel Čerenkov Counter (ACC)	36
4.2.5	Time of Flight counter (TOF)	39
4.2.6	Electromagnetic Calorimeter (ECL)	40
4.2.7	K_L/μ Detector (KLM)	43
4.2.8	Solenoid Magnet	45
4.2.9	Extreme Forward Calorimeter (EFC)	45
4.3	Trigger and Data Acquisition System	46
4.3.0.1	Data Acquisition System	48
4.4	Monte Carlo Simulation	49
4.4.1	Event generators	49
4.4.2	Simulation of detector response	50
4.5	Particle reconstruction	50
4.5.1	Reconstruction of Charged Particle Tracks	50
4.5.2	Reconstruction of Photon Clusters	50
4.5.3	Charged Particle Identification	51
4.5.3.1	Muon Identification	51
4.5.3.2	Electron Identification	52
4.5.3.3	Identification of Charged Hadrons: K/π Separation	54
5	Full Reconstruction of B Meson Decays	55
5.1	Meson reconstruction	55

5.1.1	Reconstruction of light mesons	55
5.1.1.1	Reconstruction of K_S mesons	56
5.1.2	Reconstruction of D mesons	57
5.1.3	Reconstruction of B mesons	58
5.1.3.1	Energy conservation	59
5.1.3.2	Fit to the M_{bc} variable	60
5.1.3.3	Best candidate selection	62
5.2	Analysis on a fully reconstructed sample	65
5.2.1	Effect of constraints on the signal side	65
5.2.2	Optimization of the $\Delta E/M_{bc}$ region	66
6	Selection of charmless semileptonic decays	69
6.1	Particle selection	70
6.1.1	Duplicated track rejection	70
6.1.2	Selection of charged particles	72
6.1.3	Selection of neutral particles	73
6.1.4	Final lepton selection	73
6.1.5	Summary of particle selection	76
6.1.5.1	Duplicated tracks	76
6.1.5.2	Charged tracks	76
6.1.5.3	Neutral particles	76
6.1.5.4	Selection of photons	77
6.1.5.5	High momentum lepton candidates	77
6.2	Event selection	78
6.2.1	Selection of semileptonic decays	79
6.2.2	Net charge of the event	79
6.2.3	Number of detected kaons	80
6.2.4	K_L contribution	82
6.2.5	Partial reconstruction of a D^* meson	83
6.2.6	Missing mass (neutrino reconstruction)	84
6.2.7	Efficiency of selection criteria	87

	6.2.7.1	Cumulative efficiency	87	
	6.2.7.2	Single efficiency	88	
6.3		Separation using inclusive kinematical variables	90	
	6.3.1	Inclusive kinematical variables	90	
		6.3.1.1 M_X distribution	90	
		6.3.1.2 Momentum transfer distribution	90	
		6.3.1.3 P_+ distribution	92	
	6.3.2	Signal region optimization	93	
	6.3.3	Resolution of reconstructed variables	96	
	6.3.4	Reconstructed kinematical variables	96	
	6.3.5	Monte Carlo simulation of $b \rightarrow c$ decays	99	
		6.3.5.1 Fine-tuning of $b \rightarrow c$ MC simulation	99	
		6.3.5.2 Kaon background composition	100	
		6.3.5.3 Test on the $b \rightarrow u$ depleted sample	101	
7		Measurement of V_{ub}	103	
	7.1	Partial charmless semileptonic rate $\Delta\Gamma_{ul\nu}(\Delta\Phi)$	103	
		7.1.1 Signal yield	104	
			7.1.1.1 M_X/q^2	106
			7.1.1.2 M_X	107
			7.1.1.3 P_+	108
		7.1.2 Efficiency and unfolding	109	
		7.1.3 Signal efficiency	109	
		7.1.4 Normalization to the number of the semileptonic decays	110	
			7.1.4.1 Number of semileptonic decays	110
			7.1.4.2 Determination of efficiency ratios	111
		7.1.5 Extraction of $\Delta\Gamma_{ul\nu}(\Delta\Phi)$	112	
			7.1.5.1 Average semileptonic branching fraction and the inclusive B meson lifetime	112
	7.2	Error estimation	114	
		7.2.1 Data	114	
		7.2.2 Background $b \rightarrow c$ MC	114	

7.2.2.1	Systematics: Monte Carlo statistics	114
7.2.2.2	Systematics: detector simulation and K_L contamination	115
7.2.2.3	Systematics: Monte Carlo modeling	115
7.2.3	Signal $b \rightarrow u$ MC	116
7.2.3.1	Systematics: Monte Carlo statistics	116
7.2.3.2	Systematics: detector simulation	116
7.2.3.3	Systematics: Monte Carlo modeling	116
7.2.4	Summary of the error estimation	118
7.3	Tests on sub-samples	118
7.4	Extraction of $ V_{ub} $	120
7.4.1	Determination of shape function parameters	120
7.4.1.1	Procedure	120
7.4.1.2	Monte Carlo simulated photon energy spectrum	121
7.4.1.3	Fitting the spectrum	121
7.4.1.4	The best fit and $\Delta\chi^2$ contour	121
7.4.1.5	Results	121
7.4.1.6	Summary	122
7.4.1.7	Improved determination of shape function parameters	124
7.4.2	$ V_{ub} $ result	125
8	Interpretation of the results	127
8.1	Comparison of the results	127
8.1.1	Are the results consistent with each other?	128
8.1.2	The M_X distribution	130
8.1.3	Comparison of the three methods	131
8.1.4	Final $ V_{ub} $ result	131
8.1.4.1	Comparison with other inclusive measurements	132
8.2	Constraints on the $\rho - \eta$ plane	134
8.3	Future improvements	134
9	Povzetek	137
9.1	Uvod	137

9.2	Matrika CKM	138
9.3	Teoretično ozadje	139
9.4	Določanje s popolno rekonstrukcijo	140
9.5	Analiza dogodkov	143
9.6	Meritev matričnega elementa $ V_{ub} $	146
9.7	Interpretacija rezultatov	150

Introduction

Elementary particle physics is trying to understand fundamental particles and their interactions, the answers to some of the most fundamental questions about Nature, namely, what it is made of and what holds it together. In a bit more than a century since the discovery of the electron by J. J. Thomson, the elementary particle physics has come a long way and evolved into a mature scientific field in which many experiments have to be done in collaborations of hundreds of physicists and in which theoretical calculations can take years to improve the accuracy of predictions by a few percent.

Our current knowledge on elementary particle physics is gathered in the Standard Model, a result of an immense experimental and theoretical effort spanning more than fifty years. It is extremely successful in describing basically all gathered experimental data, yet there are strong indications that it is not the final answer to all the questions on the nature of elementary particles and their interactions.

The role of the experimental particle physics is to test our present knowledge: to estimate the validity of our predictions and to point at the problems and inconsistencies that can inspire the advance of our understanding. Many experiments have been set up around the world to put to the test the predictions of different segments of the Standard Model. One of the segments that received special attention in the last few years is the so-called flavor physics, which describes quark flavor-changing transitions and is within the Standard Model described by a mechanism proposed by Kobayashi and Maskawa in 1973.

The formalism of all quark flavor-changing transitions within the Standard Model is governed by the Cabibbo-Kobayashi-Maskawa (CKM) matrix, a unitary matrix with four independent free parameters, which have to be determined by experiment. In 2001 two independent measurements observed a large CP violation in decays of B mesons, confirming that the CKM matrix is complex. The unitarity conditions of the CKM matrix can therefore be graphically represented as triangles in a complex plane. One of the triangles, which can be determined by measurements of B meson decays alone, is known as the *Unitarity Triangle*, and became the “test bed” of Standard Model predictions.

The Unitarity Triangle can be over-determined by a variety of redundant measurements that determine different angles and sides of the Triangle. If the predictions of the Standard Model are not describing different B meson phenomena consistently, the construction of the triangle will be unsuccessful and would be a clear indication of physics beyond the Standard Model. To spot inconsistencies between predictions for different processes, however, the measurements have to achieve high accuracy and well understood errors.

The measurement of angle ϕ_1 in 2001, which was determined by observed CP violation in decays of B mesons, opened a new theoretically clean way of testing Standard Model predictions. The side of the Unitarity Triangle that lies opposite to the angle ϕ_1 is determined by the measurement of the matrix element $|V_{ub}|$, one of the smallest CKM matrix elements. While the measurement of ϕ_1 includes loops in its Feynman diagrams that are sensitive to possible new contributions of physics beyond the Standard Model, the measurement of $|V_{ub}|$ can be determined from tree-type diagrams that are insensitive to new physics. Comparison of the measurements of ϕ_1 and $|V_{ub}|$ is therefore an excellent opportunity to test the consistency of Standard Model predictions.

Two e^+e^- colliders with asymmetric energies of beams (so-called B factories), KEKB and PEP-II, have been set up at KEK and SLAC respectively, to perform precision quantitative studies of B mesons decays. They host the experiments Belle and BaBar, the main goal of which is a precise measurement of CP asymmetries in B meson decays. The B mesons are produced in pairs from the decays of the $\Upsilon(4S)$ resonance, and the two experiments have so far managed to collect several hundred million decays of B meson pairs. Such a large data sample enables the physicists to perform

a large set of different measurements. The analysis described in the thesis was done on a sample collected by the Belle detector at the KEK institute in Japan.

There are several ways to measure $|V_{ub}|$ at B factories, since the matrix element determines the strength of interaction in purely leptonic, semileptonic and hadronic decays. The method that currently offers the smallest overall uncertainty of the $|V_{ub}|$ measurement is an inclusive measurement on charmless semileptonic B meson decays. Such an analysis is a compromise between adequate theoretical understanding, experimental capabilities and satisfactory statistics.

The largest experimental challenge in measuring inclusive charmless semileptonic decays is to distinguish them from a much more copious semileptonic decays to final states with a charmed quark. Several kinematical variables of semileptonic decays were proposed to be exploited in the separation of the two types of the decays, namely the hadronic invariant mass M_X , the momentum transfer squared q^2 and the hadronic light cone variable P_+ [1, 2]. In the analysis described in the thesis, three different kinematical selections were used based on the three proposed kinematical variables, and the obtained results are directly compared with each other to determine the advantages of each choice.

The reconstruction of the inclusive kinematical variables is only possible if we are able to isolate the final state particles from one of the B mesons. The isolation is obtained by fully reconstructing the decay of one of the two B mesons, and performing the analysis on the final state particles of the remaining B meson. To cancel out several systematic effects, the experimental results are obtained by normalizing the number of extracted charmless semileptonic decays to the number of all reconstructed semileptonic decays.

The theoretical considerations of charmless semileptonic decays have to deal with large non-perturbative contributions to the calculations that transform the measured result into the value of $|V_{ub}|$. An approach to parameterize the non-perturbative contributions and determine them from fits to the kinematical distributions of inclusive $B \rightarrow X_s \gamma$ and $B \rightarrow X_c \ell \nu$ decays has been proposed [3], and the accuracy of the $|V_{ub}|$ extraction has been improved by using the experimental determination of non-perturbative contributions.

The analysis presented in the thesis obtains the value of $|V_{ub}|$ with an accuracy that shows that the measurement of $|V_{ub}|$ is becoming a precision measurement, which plays an important role in placing constraints on the Unitarity Triangle and testing the Standard Model predictions.

The thesis is organized as follows: in Chapters 2 and 3 we first discuss the motivation for the present measurement and review the theoretical framework of the $|V_{ub}|$ measurement in the inclusive semileptonic decays. In the next chapter we present the experimental environment and the general event reconstruction techniques used at the Belle detector. It is followed by a description of meson reconstruction in the light of the full reconstruction of B mesons. In Chapter 6 we review the particle and event selection needed to reconstruct the kinematical variables and review the optimization of kinematical regions used for the extraction of charmless semileptonic decays. The partial rates with the experimental errors are obtained in Chapter 7, which are with the help of theoretical calculations transformed into the $|V_{ub}|$ values. In the last chapter we critically review the results and propose future improvements.

Motivation for a $|V_{ub}|$ Measurement

In this chapter we review why the $|V_{ub}|$ measurement, a measurement of one of the smallest CKM matrix elements, is important for our understanding of the validity of Standard Model predictions. The CKM matrix is introduced and we explain how its unitarity leads to the Unitarity Triangle, one of the testing grounds for the predictions of the Standard Model. Finally, the semileptonic decays of B mesons, which play an important role in the determination of the Unitarity Triangle, are presented in the context of the $|V_{ub}|$ measurement.

2.1 Standard Model

The Standard Model (SM) is a set of gauge theories that explain how elementary particles interact with each other through basic interactions. The elementary particles are, according to their quantum-mechanical properties, separated into three groups: fermions, gauge bosons, and the predicted Higgs particle. There are twelve elementary fermions (with their twelve antiparticles): six leptons and six quarks, which are grouped into three generations,

$$\begin{pmatrix} \nu_e \\ e \end{pmatrix} \quad \begin{pmatrix} \nu_\mu \\ \mu \end{pmatrix} \quad \begin{pmatrix} \nu_\tau \\ \tau \end{pmatrix}, \\ \begin{pmatrix} u \\ d \end{pmatrix} \quad \begin{pmatrix} c \\ s \end{pmatrix} \quad \begin{pmatrix} t \\ b \end{pmatrix}.$$

Elementary particles in the SM interact through three interactions¹: weak, strong and electro-magnetic, by exchanging appropriate gauge bosons pertaining to the interaction. The gauge group describing the interactions is $SU(3)_C \times SU(2)_L \times U(1)_Y$. The group $SU(3)$ denotes Quantum Chromodynamics (QCD), which governs the strong interaction among quarks, while unified electroweak interactions are characterized by the gauge group $SU(2)_L \times U(1)_Y$.

The Standard Model is a result of a joint effort of theoretical and experimental physicists over last 50 years. Its predictions are continuously confronted by new data and experimental methods. Until recently, all the measured results could be described, within theoretical and experimental errors, by SM predictions. Nevertheless, physicists expect that the SM is not the final theory and that eventually physical processes will be observed that will need theories beyond the Standard Model. Recently, the neutrino oscillations have been experimentally confirmed, and show that neutrinos are not massless particles: to include this, Standard Model needs to be extended. Other conceptual problems, for example the so-called gauge hierarchy problem, a large number of free parameters of SM and some cosmological observations all hint at the possibility of physical processes that cannot be satisfactorily explained and described by the Standard Model.

There is a wide range of proposed elementary particle processes in which the contributions beyond Standard model can arise, and are important tests of Standard Model predictions. A set of tests is currently performed in the weak decays of heavy mesons, of which the measurement of $|V_{ub}|$ plays an important part.

¹A unified theory including gravitational interaction has not been achieved yet. Since the gravitational interaction is much weaker than the other three at elementary particle level, its omission does not affect the applicability of SM predictions to phenomena at the energies obtainable at accelerators today.

2.2 Weak decays

One way how to test the Standard Model predictions is to look at weak interactions. Weak interaction is described within SM with an exchange of W^\pm and Z^0 bosons. Both quarks and leptons are affected by the weak interaction, and it is the only interaction of the neutrino. Weak decays are also the only one to depend on quark flavor. Weak decays violate discrete symmetries, like parity (P), charge conjugation (C) as well as the combined CP symmetry. These unique properties of the weak interaction constitute the phenomenological framework of this thesis, and are explained within the Standard Model by the mechanism introduced by Cabibbo, Kobayashi and Maskawa.

2.2.1 Theory of the CKM matrix

The transformation property under the electroweak gauge group $SU(2)_L \times U(1)_Y$ is different for left and right-handed fermions. The right-handed components of the leptons and quarks are singlets under the weak symmetry $SU(2)_L$, while the left-handed components transform as weak $SU(2)_L$ doublets:

$$\begin{pmatrix} u \\ d' \end{pmatrix}_L \quad \begin{pmatrix} c \\ s' \end{pmatrix}_L \quad \begin{pmatrix} t \\ b' \end{pmatrix}_L . \quad (2.1)$$

The quark mass states are not eigen-states of the weak interaction, so the states coupled in the doublets need to be rotated into the weak eigen-state frame, where the rotated states are denoted with a prime (see Eq. 2.1). This rotation was first proposed by Cabibbo in 1963 [4] for the case of three quarks that were known at that time, and was later generalized for three quark generations with six quark flavors by Kobayashi and Maskawa (1973) [5], by the introduction of the Cabibbo-Kobayashi-Maskawa (CKM) mixing matrix.

The model was proposed when only three quarks were known and was able to successfully predict the existence of six quarks. Between successful predictions of the model is also a large CP violation in the system of neutral B mesons [6].

2.2.2 The origin of the CKM Matrix

The elementary particles in the Standard Model are by themselves massless, since mass terms in the Lagrangian break the local gauge invariance. But it was shown that by introducing scalar Higgs fields the particles can, after spontaneous symmetry breaking (SSB), acquire mass by coupling with the Higgs fields. The derivation follows the steps described in Ref. [7].

The masses of the fermions are obtained from the Yukawa coupling between fermionic fields (e, ν, u, d) and the Higgs field (ϕ):

$$\mathcal{L}_Y = -C_{ij}^e (\bar{\ell}_{iL} \phi) e'_{jR} - C_{ij}^u (\bar{q}_{iL} \phi^c) u'_{jR} - C_{ij}^d (\bar{q}_{iL} \phi) d'_{jR} + h.c. \quad , \quad (2.2)$$

where u' and d' represent vectors of all up-type and down-type quarks, e is one of the charged leptons, and ℓ and q represent one of the leptons and one of the quarks, respectively. The indices i and j denote the generation of the quark or the lepton, and subscripts L and R denote the left-handed and right-handed particle fields, respectively. The coefficients C_{ij}^f are three 3×3 matrices that determine the strength of the Yukawa couplings between fermions and Higgs fields (f represents either charged leptons, up-type quarks or down-type quarks) and can be arbitrary complex matrices.

After SSB with weak isospin doublet Higgs fields, the Higgs doublet can be written as follows:

$$\phi^{(c)} \rightarrow \frac{1}{\sqrt{2}}(v + H)\chi^{(c)} \quad , \quad \chi = \begin{pmatrix} 0 \\ 1 \end{pmatrix} \quad , \quad (2.3)$$

where the Higgs field is split into its vacuum expectation value v and the remaining Higgs field H , which in the process of SSB obtained its mass. Inserting Eq. 2.3 in Eq. 2.2 we obtain the following form of the Yukawa part of the Lagrangian:

$$\mathcal{L}_Y = - \left(1 + \frac{H}{v} \right) (\bar{\mathbf{e}}'_L \mathcal{M}'_e \mathbf{e}'_R + \bar{\mathbf{u}}'_L \mathcal{M}'_u \mathbf{u}'_R + \bar{\mathbf{d}}'_L \mathcal{M}'_d \mathbf{d}'_R + h.c.) \quad . \quad (2.4)$$

The non-diagonal mass matrices are directly connected to the Yukawa coupling coefficients in Eq. 2.2:

$$\mathcal{M}'_f = \frac{v}{\sqrt{2}} C_{ij}^f \quad . \quad (2.5)$$

Since the matrices representing the Yukawa coupling constants C_{ij}^f can be arbitrary, the mass matrices are by default neither diagonal nor symmetric. The absence of right-handed neutrinos results in a diagonalized mass matrix for leptons (\mathcal{M}'_e), which means that the lepton fields in the electroweak Lagrangian have also definite mass. This is not the case for quark fields: the quark field states \mathbf{u}' and \mathbf{d}' in the Yukawa Lagrangian in Eq. 2.2 do not have a definite mass. To obtain the physical states with definite mass, we perform a unitary transformation using unitary matrices S and T to diagonalize the quark mass matrices \mathcal{M}'_q :

$$\mathcal{M}'_q = S_q^\dagger \mathcal{M}_q S_q T_q \quad . \quad (2.6)$$

The matrices S_q transform the gauge (interaction) quark eigen-states ψ'_q into the mass eigen-states ψ_f :

$$\psi_{qL} \equiv S_q \psi'_{qL} \quad (2.7)$$

$$\psi_{qR} \equiv S_q T_q \psi'_{qR} \quad . \quad (2.8)$$

The fact that the interaction quark eigen-states are not the same as the mass eigen-states has important consequences on the electroweak interactions, which can be derived from the Lagrangian term:

$$\mathcal{L} = \bar{\Psi}_L i \gamma^\mu D_\mu^L \Psi_L + \bar{\Psi}_R i \gamma^\mu D_\mu^R \Psi_R \quad . \quad (2.9)$$

After explicitly writing the covariant derivatives D_μ^L and D_μ^R , we obtain three types of electroweak interactions, weak charged, weak neutral and electromagnetic interaction. The weak neutral and electromagnetic interactions are not flavor-changing, so they have the same form in both physical and interaction bases.

The weak charged interaction, which plays the most important role in semileptonic decays, on the other hand has a different form in the two bases. The corresponding term in the Lagrangian of the weak charged interaction is of the form:

$$\mathcal{L}^{w.c.} = - \frac{g}{\sqrt{2}} (J^{\mu\dagger} W_\mu + J^\mu W_\mu^\dagger) \quad , \quad (2.10)$$

where the weak charged current J^μ is coupled to a charged massive boson field W_μ and the strength of the interaction is determined by the coupling constant g .

The quark contribution to this charged current $J_{w.c.}^\mu$ is:

$$J_{w.c.}^\dagger = \bar{\mathbf{u}}'_L \gamma_\mu \mathbf{d}'_L = \bar{\mathbf{u}}_L \gamma_\mu S_u S_d^\dagger \mathbf{d}_L = \bar{\mathbf{u}}_L \gamma_\mu V_{CKM} \mathbf{d}_L \quad . \quad (2.11)$$

We define the Cabibbo-Kobayashi-Maskawa matrix $V_{CKM} \equiv S_u S_d^\dagger$, a unitary matrix that was introduced by Kobayashi and Maskawa in 1973 [5] and rotates the down-type quark states, while leaving the up-type quarks unchanged:

$\mathbf{d}' = V_{CKM} \mathbf{d}$.

$$\begin{pmatrix} d' \\ s' \\ b' \end{pmatrix} = \begin{pmatrix} V_{ud} & V_{us} & V_{ub} \\ V_{cd} & V_{cs} & V_{cb} \\ V_{td} & V_{ts} & V_{tb} \end{pmatrix} \begin{pmatrix} d \\ s \\ b \end{pmatrix}, \quad (2.12)$$

such that the charged current can be written as:

$$J_{c.c.}^\dagger = \left(\bar{u} \ \bar{c} \ \bar{t} \right)_L \gamma_\mu \begin{pmatrix} V_{ud} & V_{us} & V_{ub} \\ V_{cd} & V_{cs} & V_{cb} \\ V_{td} & V_{ts} & V_{tb} \end{pmatrix} \begin{pmatrix} d \\ s \\ b \end{pmatrix}_L. \quad (2.13)$$

The weak charged interaction involves a change of quark flavor between the up-type and down-type quarks, and the V_{CKM} matrix elements determine the strength of the coupling of up-type quarks to down-type quarks. The probability for a flavor transition of the i -th generation up-type quark to a j -th generation down-type quark is proportional to the CKM matrix element squared, $|V_{ij}|^2$.

2.2.3 Parametrization of the CKM Matrix

CKM matrix is in general a complex $n \times n$ matrix, where n is the number of generations of elementary particles. In the case of three generations there are 18 real parameters, but due to unitarity conditions only nine of them are independent, and further five phases can be removed by appropriate rotations of the quark fields, reducing the number of the independent parameters to four. The CKM matrix can thus be parametrized with four parameters (three real angles and one complex phase). These four parameters are free parameters of the Standard Model

The standard parameterization [8] of the matrix is given by:

$$V_{CKM} = \begin{pmatrix} c_{12}c_{13} & s_{12}c_{13} & s_{13}e^{-i\delta} \\ -s_{12}c_{23} - c_{12}s_{23}s_{13}e^{i\delta} & c_{12}c_{23} - s_{12}s_{23}s_{13}e^{i\delta} & s_{23}c_{13} \\ s_{12}s_{23} - c_{12}c_{23}s_{13}e^{i\delta} & -s_{23}c_{12} - s_{12}c_{23}s_{13}e^{i\delta} & c_{23}c_{13} \end{pmatrix}, \quad (2.14)$$

where $c_{ij} = \cos \theta_{ij}$, $s_{ij} = \sin \theta_{ij}$ where $i, j = 1, 2, 3$ label the quark generation and δ is the phase. The c_{ij} and s_{ij} can all be chosen to be positive and δ may vary in the range $0 \leq \delta \leq 2\pi$.

One of the more common and illustrative parameterizations is the Wolfenstein parameterization [9], which takes into account the hierarchical structure of the sizes of CKM matrix elements:

$$V_{CKM} = \begin{pmatrix} 1 - \frac{\lambda^2}{2} & \lambda & A\lambda^3(\rho - i\eta) \\ -\lambda & 1 - \frac{\lambda^2}{2} & A\lambda^2 \\ A\lambda^3(1 - \rho - i\eta) & -A\lambda^2 & 1 \end{pmatrix} + O(\lambda^4). \quad (2.15)$$

It is an expansion in powers of $\lambda \equiv |V_{us}| = 0.2200 \pm 0.0026$ [10]. Parameters $A = 0.85 \pm 0.09$ and λ are known to high precision, while ρ , and η (Eq. 2.17) are not well determined yet. If we define

$$s_{12} = \lambda; \quad s_{23} = A\lambda^2; \quad s_{13}e^{-i\delta} = A\lambda^3(\rho - i\eta), \quad (2.16)$$

it follows that

$$\rho = \frac{s_{13}}{s_{12}s_{23}} \cos \delta, \quad \eta = \frac{s_{13}}{s_{12}s_{23}} \sin \delta. \quad (2.17)$$

We can write the CKM matrix parameterization that is correct to $\mathcal{O}(\lambda^7)$ [11]:

$$\hat{V}_{\text{CKM}} = \begin{pmatrix} 1 - \frac{1}{2}\lambda^2 - \frac{1}{8}\lambda^4 & \lambda + \mathcal{O}(\lambda^7) & A\lambda^3(\varrho - i\eta) \\ -\lambda + \frac{1}{2}A^2\lambda^5[1 - 2(\varrho + i\eta)] & 1 - \frac{1}{2}\lambda^2 - \frac{1}{8}\lambda^4(1 + 4A^2) & A\lambda^2 + \mathcal{O}(\lambda^8) \\ A\lambda^3(1 - \bar{\varrho} - i\bar{\eta}) & -A\lambda^2 + \frac{1}{2}A\lambda^4[1 - 2(\varrho + i\eta)] & 1 - \frac{1}{2}A^2\lambda^4 \end{pmatrix}, \quad (2.18)$$

where we have, by including the corrections of the order of λ^2 , defined two parameters:

$$\bar{\varrho} = \varrho \left(1 - \frac{\lambda^2}{2}\right), \quad \bar{\eta} = \eta \left(1 - \frac{\lambda^2}{2}\right). \quad (2.19)$$

2.2.4 Unitarity conditions of the CKM Matrix

The CKM matrix V_{CKM} is unitary by construction, $V_{\text{CKM}}V_{\text{CKM}}^\dagger = I$, which leads to the following relations amongst its elements:

$$\sum_i V_{ij}V_{ik}^* = \delta_{jk}. \quad (2.20)$$

Since the matrix elements of V_{CKM} are in general complex, the unitarity conditions for different rows ($j \neq k$) can be illustrated as triangles in the complex plane. The triangle formed from the unitarity relation imposed on the first and third columns has sides of roughly the same length ($\mathcal{O}(\lambda^3)$), enabling the measurement of the angles of the triangle, if the complex phase is different from zero. The relation is given by

$$V_{ud}V_{ub}^* + V_{cd}V_{cb}^* + V_{td}V_{tb}^* = 0, \quad (2.21)$$

and determines the so called *Unitarity Triangle*. For convenience, we normalize one of the sides by dividing the

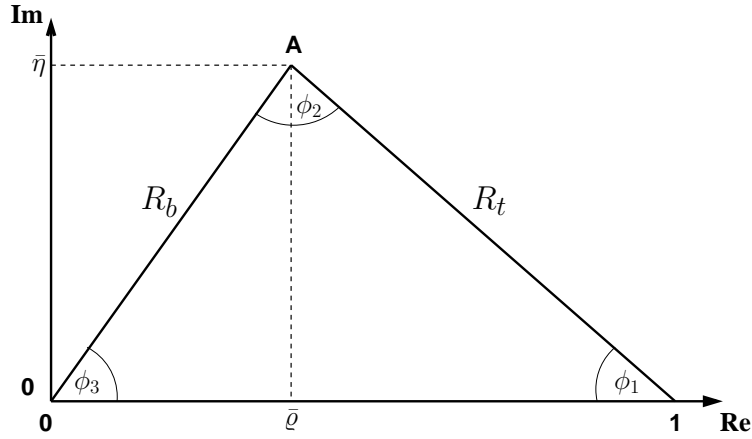


Figure 2-1. The rescaled Unitarity Triangle

relation in Eq. 2.21 with $|V_{cd}V_{cb}^*|$ and choose a phase convention such that $(V_{cd}V_{cb}^*)$ is real. The vertices along the normalized side are fixed at $(0,0)$ and $(0,1)$, while the remaining vertex has the coordinates $(\bar{\varrho}, \bar{\eta})$, and needs to be determined by experiment (see Fig. 2-1).

The angles and side-lengths of the Unitarity Triangle are given by:

$$\phi_1 \equiv \left[-\frac{V_{cd}V_{cb}^*}{V_{td}V_{tb}^*} \right]; \quad \phi_2 \equiv \left[-\frac{V_{ud}V_{ub}^*}{V_{td}V_{tb}^*} \right]; \quad \phi_3 \equiv \left[-\frac{V_{cd}V_{cb}^*}{V_{ud}V_{ub}^*} \right] \equiv \pi - \phi_1 - \phi_2; \quad (2.22)$$

$$R_b \equiv \frac{|V_{ud}V_{ub}^*|}{|V_{cd}V_{cb}^*|} = \sqrt{\bar{\varrho}^2 + \bar{\eta}^2} = \left(1 - \frac{\lambda^2}{2}\right) \frac{1}{\lambda} \left| \frac{V_{ub}}{V_{cb}} \right|; \quad (2.23)$$

$$R_t \equiv \frac{|V_{td}V_{tb}^*|}{|V_{cd}V_{cb}^*|} = \sqrt{(1 - \bar{\varrho})^2 + \bar{\eta}^2} = \frac{1}{\lambda} \left| \frac{V_{td}}{V_{cb}} \right|. \quad (2.24)$$

2.2.4.1 Constraining the Unitarity Triangle

There are several processes that can determine different sides or angles of the Unitarity Triangle. Since both V_{cb} and V_{ub} are present in Eq. 2.21, decays of B mesons play an important role in these determinations. While the angle ϕ_1 can be measured from the time-dependent CP violation in decays like $B^0 \rightarrow J/\psi K_S$, the side R_b is determined by the ratio of $|V_{ub}|/|V_{cb}|$, which can be measured in semileptonic B decays.

There is one important difference in the two measurements: the loops in box and penguin diagrams in the ϕ_1 determination make it sensitive to contributions from possible new particles that would appear in the loop, whereas the measurements of matrix elements $|V_{ub}|$ and $|V_{cb}|$ are determined from tree-amplitude diagrams, which are practically insensitive to such contributions. Comparison of such measurements can, when the theoretical and experimental precision allows, show the possible departure from unitarity, hinting at the existence of physics that is not predicted by the Standard Model (see Fig. 2-2).

In 2001 the prediction of a large CP violation in the decays of B mesons was confirmed by independent measurements [12, 13], which now set the allowed range of the angle ϕ_1 of the Triangle (see Fig. 2-2). The measurement of the angle ϕ_1 is done by observing the time-dependent asymmetries between the decays of B and \bar{B} mesons to a common final state. The asymmetries arise due to the interference between the amplitudes for the direct decay and for a decay to the same final state combined with the mixing of the B meson. The decay in which the theoretical prediction of the asymmetry is most accurate, is $B^0 \rightarrow J/\psi K_S$, a decay with a relatively large branching fraction in which only a single CKM phase appears in the leading decay amplitudes [12]. The average of all measurements for $\sin 2\phi_1$ is $\sin 2\phi_1 = 0.687 \pm 0.032$ [14], with a total error of less than 5%. It is therefore important to determine the side opposite to ϕ_1 by an accurate measurement of the ratio $|V_{ub}|/|V_{cb}|$.

2.2.4.2 Measurement of $|V_{ub}|$ and $|V_{cb}|$

Semileptonic decays of B mesons are decays of a B meson into a pair of leptons (a charged lepton and its neutrino), and a set of hadrons, $B \rightarrow X\ell\nu$, where X stands for the hadronic part. These decays are one of the best candidates for the determination of $|V_{ub}|$ and $|V_{cb}|$ matrix elements: they are relatively common and since the leptons are not affected by the strong interaction, the QCD corrections are smaller than in the hadronic decays. As already mentioned, they are also determined by tree Feynman diagrams (see Fig. 3-1), making them insensitive to possible contributions of physics beyond the Standard Model.

Both exclusive and inclusive measurements of these matrix elements can be performed: the exclusive measurements focus on a specific decay mode, for example $B \rightarrow D\ell\nu$ or $B \rightarrow \pi\ell\nu$, while the inclusive ones measure all decays with the same quark-level transition, for example $b \rightarrow c\ell\nu$ or $b \rightarrow u\ell\nu$, regardless of a specific decay mode. In general, exclusive measurements can exploit kinematical properties of the specific decay in question, while inclusive measurements benefit from a larger sample due to more modes, and a more reliable theoretical determination.

The exclusive measurement of the matrix element $|V_{cb}|$ is performed by studying $B \rightarrow D\ell\nu$ and $B \rightarrow D^*\ell\nu$ decays, where the relation between the rates and the matrix element are determined using form factors from the Heavy Quark Effective Theory (HQET) [16, 17]. The obtained world average value is $|V_{cb}| = (42.0 \pm 1.1 \pm 1.9) \times 10^{-3}$ [10], where the errors are experimental and theoretical, respectively.

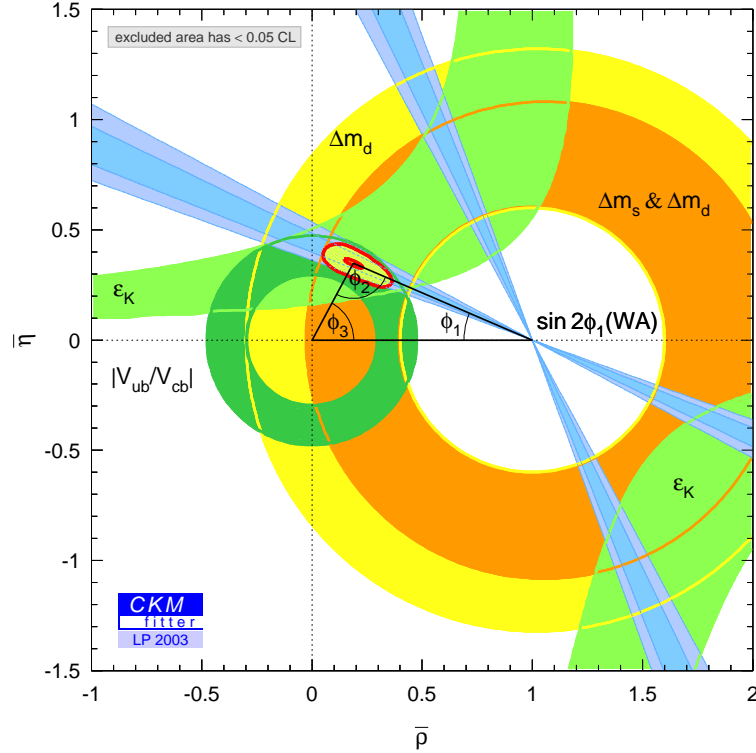


Figure 2-2. Schematic view of the Unitarity Triangle and the determination of its upper vertex, by intersecting areas defined by measurements of different quantities. The constraints are obtained in measurements of the following processes: ϵ_K in CP violation of K mesons, Δm_d and Δm_s from $B\bar{B}$ and $B_s\bar{B}_s$ oscillations, respectively, $\sin(2\phi_1)$ in CP -violating B decays like $B \rightarrow J/\psi K_S$, and $|V_{ub}|/|V_{cb}|$ in the B meson semileptonic decays. Different measurements agree within current accuracy and their intervals intersect in a common area (shaded red). From Ref. [15].

The inclusive measurement of $|V_{cb}|$ is obtained from the measured inclusive branching fraction for $b \rightarrow c$ semileptonic decays, and the lifetime of B mesons. The calculation used is similar to the one presented in Sec. 3.1.1.1. The obtained world average result is $|V_{cb}| = (41.0 \pm 0.5 \pm 0.5 \pm 0.8) \times 10^{-3}$ [10], where the errors are experimental, from Heavy Quark Expansion parameters, and theoretical, respectively.

The $|V_{cb}|$ matrix element is determined with an accuracy of a few percent, while the uncertainty of the matrix element $|V_{ub}|$ is much larger, around 10%. The uncertainty on the ratio $|V_{ub}|/|V_{cb}|$ is therefore dominated by the uncertainty of $|V_{ub}|$, and in order to determine the upper vertex the effort should be focused on an accurate determination of $|V_{ub}|$.

The exclusive measurement of the matrix element $|V_{ub}|$ is mostly done using the $B \rightarrow \pi \ell \nu$ and $B \rightarrow \rho \ell \nu$ decays (for a review of measurements see Ref. [10]), where the neutrino has to be reconstructed or the particles have to be separated between the two B mesons in order to reconstruct such an event. The form factors for this heavy to light quark transition are determined by lattice calculations [18, 19] or light cone sum rules [20], and the $|V_{ub}|$ results vary significantly between calculations [14].

From the theoretical point of view inclusive rates are much more reliably estimated than in the exclusive case, so currently the most reliable extraction of $|V_{ub}|$ comes from the measurements in the inclusive semileptonic decays. Inclusive $b \rightarrow u$ semileptonic decays are unfortunately not easily separated from the $b \rightarrow c$ semileptonic transitions, which are about 80 times more common. The $b \rightarrow u$ transitions have to be extracted using inclusive kinematical variables like the charged lepton momentum p_ℓ , the invariant mass of the hadronic part of the decay M_X , or the leptonic four-momentum squared q^2 .

The extraction of semileptonic $b \rightarrow u$ decays near the endpoint of charged lepton momentum [21, 22, 23] can be performed without the separation of particles according to which B meson they are coming from. Unfortunately the backgrounds of leptons coming from continuum $e^+e^- \rightarrow q\bar{q}$ transitions where $q \neq b$, and the remaining $b \rightarrow c$ decays, are several times higher than the number of expected $b \rightarrow u$ decays. The total uncertainty of this measurement is therefore highly dependent on the systematical error of background subtraction.

One of the ways how to improve the uncertainty of the $|V_{ub}|$ beyond the systematical error of background subtraction, is to greatly reduce the number of background decays compared to the $b \rightarrow u$ decays by fully reconstructing the decay of one of the B mesons. The inclusive variables like the hadronic mass M_X and q^2 can be constructed on such a sample. Using these variables the ratio of signal to background decays can be increased up to one or more, which improves the uncertainty of the measurement significantly. On the other hand, such samples have a very low efficiency of reconstruction, and the total uncertainty is dominated by the statistical error.

The task of this thesis is thus to separate as much as possible the $b \rightarrow c$ and $b \rightarrow u$ transitions, which would enable us to reliably determine the value of the matrix element $|V_{ub}|$ and more accurately constrain the upper vertex of the Unitarity Triangle.

2.3 Summary

The Standard Model is a very successful theory, the predictions of which are continuously tested by experimental measurements. The tests are stimulated by the intriguing possibility of finding processes that would need theoretical treatment beyond Standard Model. The experimental determinations in the area of physics of B mesons are becoming more accurate and will be able to test if different Standard Model predictions using different experimental information are consistent with each other.

One of the testing grounds is the rescaled Unitarity Triangle, where measured quantities determine its angles and sides. For Standard Model predictions to hold, different measurements should constrain the upper vertex of the Unitarity Triangle to a common area. Such an over-constraining of the upper vertex is shown in Fig. 2-2, where different measurements are represented by bands in the $\bar{\varrho} - \bar{\eta}$ space in which they constrain the upper vertex.

For now the predictions from different measurements overlap, but the uncertainties in many of the measurements and calculated theoretical predictions are still rather large. To spot possible deviations, it is therefore important to over-constrain the predictions of the Standard Model with as many as accurate measurements as possible. The analysis described in the thesis is an attempt to contribute to the test of these predictions by improving the accuracy of the $|V_{ub}|$ measurement.

Theoretical Background of the Inclusive Semileptonic B Decays

The following chapter is an attempt to introduce the important concepts and briefly sketch the theoretical treatments used in calculations of inclusive semileptonic B meson decays. This description is useful for the understanding of the complex issues arising in the calculations, which inevitably influence the experimental determination of the matrix element $|V_{ub}|$.

Any calculations of the bound state of the b quark in the B meson are affected by the fact that the strong coupling constant α_s is not small enough at energies of a few hundred MeV, which are exchanged in the meson, to be the expansion parameter. The scale of energies at which the QCD becomes non-perturbative is called Λ_{QCD} ($\Lambda_{\text{QCD}} \approx 200$ MeV), and the calculations have to deal with large non-perturbative contributions. To derive useful predictions, theories have to systematically exploit small expansion parameters, which arise from some kinematical property of the decay. In the B meson decays momenta are small compared to the mass of the b quark, and $1/m_b$ can be used as an expansion parameter.

Such theories are called effective field theories, and are based on the assumption that only certain degrees of freedom are important for the description of some processes, while others can be integrated out to produce an effective description. In the theoretical framework of this analysis the Heavy Quark Effective Theory (HQET) and Soft Collinear Effective Theory (SCET) have been used for the treatment of non-perturbative phenomena.

The use of the Operator Product Expansion (OPE) is also briefly sketched, which is used to separate the perturbative and the non-perturbative part of the calculation. The idea of estimating the non-perturbative contribution to the calculations from experimental data has been exploited, by parameterizing the so-called shape function, and fitting it to kinematical distributions of another process. The concept of the shape function is outlined.

In the end the description of the Monte Carlo simulation used to simulate the semileptonic $b \rightarrow u$ decays in this thesis is presented.

3.1 Inclusive decay width calculation

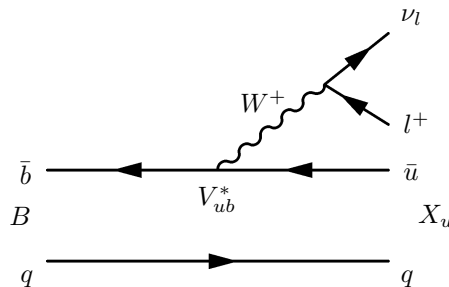


Figure 3-1. Feynman diagram of a charmless semileptonic B meson decay.

The properties of semileptonic decays are nicely illustrated by the Feynman diagram (see Fig. 3-1): the b quark changes its flavor through weak charged current by emitting a W boson, which in turn emits a lepton-neutrino pair. The strength of b -flavor transition is determined by the appropriate V_{CKM} element, either $|V_{cb}|$ or $|V_{ub}|$ for a transition to a c or a u quark, respectively. The other quark in the B meson does not directly affect the transition and is therefore called the spectator quark. The spectator quark only contributes to the diagram by the so-called hadronic corrections, by emitting and absorbing gluons.

The extraction of the matrix element $|V_{ub}|$ depends on the theoretical calculation of the charmless semileptonic rate. The simplest calculation of the inclusive semileptonic rate is therefore the case where the spectator quark is non-interacting, and the rate can be deduced from the calculation of the muon decay [7]:

$$\Gamma(B \rightarrow X_u \ell \nu) = \frac{G_F^2 m_b^5}{192\pi^3} \times f\left(\frac{m_u}{m_b}\right) \quad (3.1)$$

where, m_u and m_b are the quark masses, G_F is the Fermi coupling constant: $G_F = 1.166 \times 10^{-5} \text{ GeV}^{-2}$, and the function f is defined as $f(x) = 1 - 8x^2 + 8x^6 - x^8 - 24x^4 \ln x$. Since for the $b \rightarrow u$ transition $x = m_u/m_b \ll 1$, the value of the function f is $f(m_u/m_b) \approx 1$.

For extraction of $|V_{ub}|$ with a theoretical uncertainty below 10%, the simple non-interacting spectator model is not satisfactory, and different perturbative and non-perturbative corrections, which take into account the hadronic interaction between quarks in the decay, have to be introduced.

3.1.1 Beyond the simple spectator model

The necessary steps to calculate the semileptonic rate beyond the simple non-interacting spectator model are presented, following the derivation in Refs. [24, 25, 26].

The exchanged momenta in the semileptonic decay are much smaller than the mass of the W boson, so the semileptonic decay is described well by the low energy effective Hamiltonian, where the momentum of the W boson is much smaller than its mass and can be neglected [7, 24]:

$$H_W = \frac{4G_F}{\sqrt{2}} V_{ub} \bar{u} \gamma^\mu \frac{1}{2} (1 - \gamma_5) b \bar{\ell} \gamma_\mu \nu_\ell. \quad (3.2)$$

The triple differential decay rate written in terms of the virtual W boson mass squared, q^2 , the invariant mass squared of the hadronic part, $M_{X_u}^2$ and the energy of the charged lepton E_ℓ is then given by [24]:

$$\frac{d^3\Gamma(B \rightarrow X_u \ell \nu)}{dq^2 dM_{X_u}^2 dE_\ell} = \frac{1}{4} \sum_{X_u} \sum_{\text{spins}} \frac{|\langle X_u \ell \nu | H_W | \bar{B} \rangle|^2}{2m_B} (2\pi)^3 \delta^4(p_B - q - p_{X_u}) \quad (3.3)$$

Since the leptonic part of the decay is not affected by strong interaction, the leptonic and hadronic contributions can be separated into leptonic and hadronic tensors, $L_{\alpha\beta}$ and $H_{\alpha\beta}$, respectively [24]:

$$\frac{d^3\Gamma(B \rightarrow X_u \ell \nu)}{dq^2 dM_{X_u}^2 dE_\ell} = 2G_F^2 |V_{ub}|^2 H_{\alpha\beta} L^{\alpha\beta}, \quad (3.4)$$

The leptonic tensor is evaluated using properties of γ -matrices and the Dirac equation, while the hadronic tensor [24]

$$H^{\alpha\beta} = \sum_{X_u} \frac{(2\pi)^3}{m_B} \langle \bar{B}(p_B) | J^{\dagger\alpha} | X_u(p_{X_u}) \rangle \langle X_u(p_{X_u}) | J^\beta | \bar{B}(p_B) \rangle \delta^4(p_B - q - p_{X_u}) \quad (3.5)$$

where the hadronic current is $J^\alpha = \bar{u}\gamma^\alpha\frac{1}{2}(1 - \gamma_5)b$, cannot be estimated without simplification and needs to be approximated. We use the Optical Theorem [25] to write the tensor with the time ordered product of currents:

$$H_{\alpha\beta} = -\frac{1}{\pi} \text{Im} \int d^4x e^{-iq \cdot x} \frac{\langle \bar{B} | T [J_\alpha^\dagger(x) J_\beta(0)] | \bar{B} \rangle}{2m_B}. \quad (3.6)$$

3.1.1.1 Operator Product Expansion

The hadronic tensor now involves a time-ordered product of local operators $J_\alpha^\dagger(x)J_\beta(0)$ of the hadronic weak charged currents. In quantum field theory a product of two local operators $A(x)$ and $B(y)$ is singular for $x \rightarrow y$ [26]. The way to treat such singular products was developed by Wilson in 1969 and it is called the Operator Product Expansion (OPE) [27]. It states that a product of two local operators $A(x)B(y)$, when $x \rightarrow y$, can be expanded in the following series [26]:

$$A(x)B(y) \xrightarrow{x \rightarrow y} \sum_n C_{AB}^n(x-y) \cdot O_n(x), \quad (3.7)$$

where O_n are local operators of dimension n with the same Lorentz and gauge properties as the initial product, and the C_{AB}^n are the so-called Wilson coefficients, which are complex functions and absorb the singularity of the product. Wilson has shown that the coefficients C_{AB}^n can be calculated perturbatively, and the Operator Product Expansion actually separates the perturbative and the non-perturbative contributions to the QCD corrections.

The OPE can be used for the semileptonic rate, since the momenta flowing in any internal lines are large due to large b -quark mass and the distance between emission and reabsorption of particles happens nearly at the same place (satisfying $x \rightarrow y$) [7].

The expanded semileptonic rate, after inserting the Operator Product Expansion of the hadronic tensor (Eq. 3.6), becomes [7]:

$$\Gamma(B \rightarrow X_u \ell \nu) = \frac{G_F^2}{192\pi^3} m_b^5 \times \left[\sum_n c_n^{SL} \times \frac{\langle B | O_n | B \rangle}{2m_B} \right]. \quad (3.8)$$

The Wilson coefficients depend only on the mode on which the b quark decays to; in the case of semileptonic decays they obtain the label SL . They are calculated using a perturbative expansion in α_s and include the CKM matrix element squared $|V_{ub}|^2$ [25].

For the evaluation of the non-perturbative effect gathered in local operators O_n , we define the normalized forward matrix elements of local operators [25]:

$$\langle O_n \rangle_B = \frac{\langle B | O_n | B \rangle}{2m_B}. \quad (3.9)$$

The operators O_n of smallest dimension that contribute to Eq. 3.8, are of dimension three, $\langle \bar{b}b \rangle_B$, and dimension five, $\langle \bar{b} g_s \sigma_{\mu\nu} G^{\mu\nu} b \rangle_B$ (see Fig. 3-2). The OPE expansion of a semileptonic decay width can be written in the form:

$$\Gamma(B \rightarrow X_u \ell \nu) = \frac{G_F^2}{192\pi^3} m_b^5 \times \left[c_3^{SL} \langle \bar{b}b \rangle_B + c_5^{SL} \frac{\langle \bar{b} g_s \sigma_{\mu\nu} G^{\mu\nu} b \rangle_B}{m_b^2} \dots \right]. \quad (3.10)$$

The two matrix elements are calculated using the Heavy Quark Effective theory, by expanding them in powers of $1/m_b$ [25]:

$$\langle \bar{b}b \rangle_B = 1 + \frac{\lambda_1 + 3\lambda_2}{2m_b^2} + \mathcal{O}(1/m_b^3) \quad (3.11)$$

$$\frac{\langle \bar{b} g_s \sigma_{\mu\nu} G^{\mu\nu} b \rangle_B}{m_b^2} = \frac{6\lambda_2}{m_b^2} + \mathcal{O}(1/m_b^3). \quad (3.12)$$

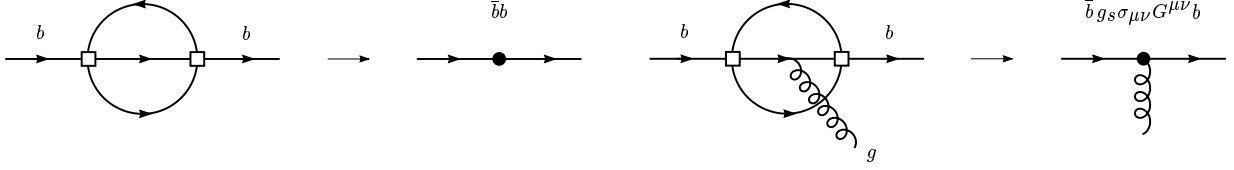


Figure 3-2. The two lowest perturbative contributions to the hadronic tensor $H_{\alpha\beta}$ and their local operators in the HQET $1/m_b$ expansion. From Ref. [25]

The HQET parameters λ_1 and λ_2 arise from non-perturbative physics and need to be determined from a measurement or calculated using non-perturbative methods [25]. The parameter λ_2 is determined from the hyper-fine $B - B^*$ splitting, while λ_1 is proportional to the average kinetic energy of the b quark within the B meson [25]:

$$\lambda_1 = -2m_b E_b^{kin} \quad (3.13)$$

$$\lambda_2 = \frac{m_{B^*}^2 - m_B^2}{4} \simeq 0.12 \text{ GeV}^2 \quad (3.14)$$

In summary, the calculation of the charmless semileptonic decay width up to the order of $1/m_b^2$ gives [25]:

$$\Gamma(B \rightarrow X_u \ell \nu) = \frac{G_F^2 |V_{ub}|^2}{192\pi^3} m_b^5 \times \left[1 - \frac{9\lambda_2 - \lambda_1}{2m_b^2} + \dots - \mathcal{O}(\alpha_s) \right] \quad (3.15)$$

The corrections up to $\mathcal{O}(\alpha_s^2)$ have been calculated [28]. The dependence of the result on the quark mass is significant due to the factor m_b^5 , and brings large uncertainty to the calculated result. The quark masses act as couplings within the SM, so they have to be determined from the processes that depend on them. The b -quark mass is a scheme-dependent, renormalized quantity [11], and a few different definitions of masses are regularly used in different calculations (see Section 3.1.3).

3.1.2 Inclusive kinematical variables

The semileptonic rate is successfully calculated using OPE when no kinematical restrictions are imposed on the decay products [11]. This is experimentally not always feasible, since we need to separate $b \rightarrow u$ from $b \rightarrow c$ transitions by exploiting kinematical differences between the two transitions. Calculation of the rate when cutting out a selected kinematical region (also called in this thesis a kinematical phase space) needs much more complicated approaches, for example the so-called twist expansion [29]. Unfortunately the non-perturbative contributions become enhanced when calculating rates for limited kinematical phase space, increasing the overall uncertainty of the calculation.

The natural choice of kinematical variables of a semileptonic decay are for example the invariant mass and the energy of the hadronic part of the decay (M_X and E_X , respectively), or the so-called four-momentum transfer q^2 , equal to the four-momentum of the leptonic pair. The theoretical situation for evaluating the calculations is different in different parts of the kinematical region of the charmless semileptonic decay (see Fig. 3-3). The phase space can be divided into three regions [30]:

region	kinematical region		inclusive calculation
generic	$M_X \gg \Lambda_{\text{QCD}}$	$M_X^2/E_X \gg \Lambda_{\text{QCD}}$	OPE
shape function	$M_X \gg \Lambda_{\text{QCD}}$	$M_X^2/E_X \sim \Lambda_{\text{QCD}}$	twist [29]
resonance	$M_X \sim \Lambda_{\text{QCD}}$		/

Where the invariant mass of the hadronic system is large compared to Λ_{QCD} and the energy of the hadronic system, the expansion can be done successfully using OPE [30]. This region is called generic, since it covers everything but the two calculation-problematic parts. In the region where the mass of the hadronic system is still larger than Λ_{QCD} , but the energy of the hadronic system is much larger than the invariant mass, the OPE calculation breaks down. The non-perturbative corrections have to be parametrized using non-perturbative shape functions (see Section 3.1.3), that describe the internal structure of the B meson. This region is called the shape function region (see Fig. 3-3). Finally, if the invariant mass is low enough to be comparable to Λ_{QCD} , the region is dominated by resonances and inclusive descriptions are not possible [30].

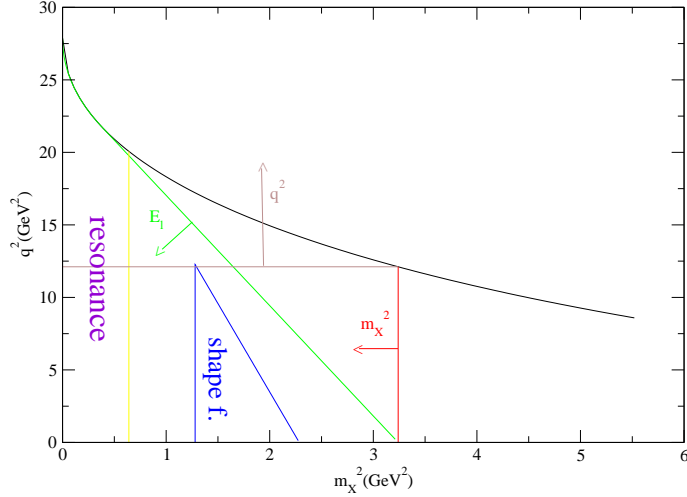


Figure 3-3. Phase space for the $B \rightarrow X_u \ell \nu$ decay, with regions of different theoretical treatment and possible phase space selections to remove $B \rightarrow X_c \ell \nu$ decays. From Ref. [30].

The $b \rightarrow u$ transitions are extracted in the regions that are kinematically inaccessible to $b \rightarrow c$ transitions. Such selection of kinematical variables includes:

inclusive variable	phase space selection	fraction of $b \rightarrow u$ phase space
hadronic invariant mass	$M_X < m_D$	80%
lepton pair four momentum squared	$q^2/c^2 < (m_B - m_D)^2$	20%
variable $P_+ \equiv E_X/c - \vec{p}_X $	$P_+/c < m_D^2/m_B$	75%

Judging from the fraction of $b \rightarrow u$ phase space that is left after the selection, the selection using M_X shows to be the most appropriate. But since the detector resolution smears the distributions over larger areas than they are kinematically allowed, the selections need to be tightened much more than it can be estimated naively only from the theoretical distributions. Lowering the upper limit of the M_X region to successfully remove $b \rightarrow c$ transition increases the fraction of events that are in the shape function region (see Fig. 3-3) described by non-perturbative shape functions, greatly reducing the precision of the theoretical estimates.

The selection using lepton pair invariant mass q^2 severely reduces the phase space of the $b \rightarrow u$ transition (down to 20%) to remove $b \rightarrow c$ transition, which is further worsened when taking into account the detector resolution. But theoretical estimation using q^2 is less affected by the shape function region (see Fig. 3-3), so a combined selection of M_X and q^2 was proposed [1] to reduce the uncertainty due to non-perturbative contributions in theoretical estimation.

The hadronic light cone variable $P_+ \equiv E_X/c - |\vec{p}_X|$ was proposed recently [2], since it is a variable that is useful in the calculation of inclusive semileptonic decays. Experimentally it is similar to M_X ($M_X^2 = P_+P_-/c^2$), but there is a buffer zone between the region of phase space filled with $b \rightarrow u$ and that of $b \rightarrow c$ region, promising for a better possible control of $b \rightarrow c$ background. Theoretical treatment is also less affected by perturbative uncertainties in the case of P_+ , making it a compelling candidate for $|V_{ub}|$ extraction.

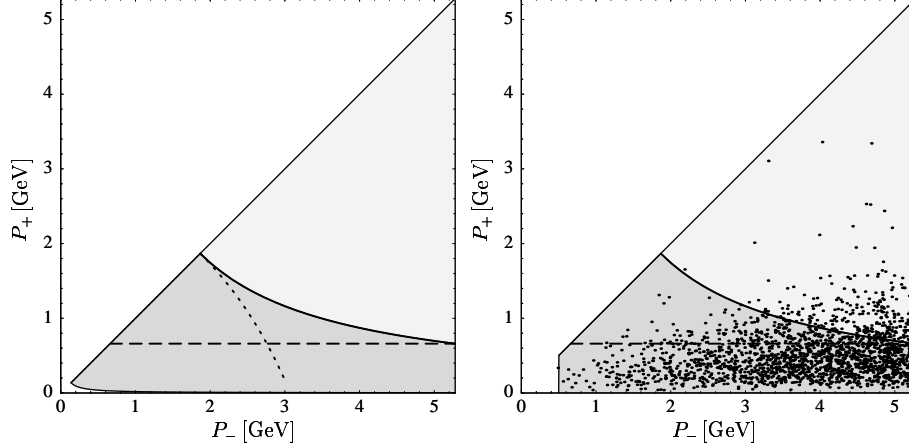


Figure 3-4. Left: Distribution of the variables $P_- \equiv E_X/c + |\vec{p}_X|$ and P_+ , with possible phase space selections to remove $B \rightarrow X_c \ell \nu$ decays: region where $M_X^2 < M_D^2$ (dark gray), the dashed line corresponds to $P_+/c = M_D^2/M_B$ and the dotted line to $q^2/c^2 = (M_B - M_D)^2$. Right: The scatter points indicate the distribution of events $b \rightarrow u$ events as predicted by the model of [31].

3.1.2.1 QCD factorization

Recently, a theoretical approach was presented for inclusive semileptonic charmless decays that incorporates all known contributions to the decay rate and can interpolate smoothly between theoretical estimates in the shape function and generic regions [3].

The procedure [32] separates physical processes occurring at different momenta by introducing three mass scales: "hard" at M_B , "hard-collinear" at $\sqrt{M_B \Lambda_{\text{QCD}}}$ and "soft" at Λ_{QCD} . The three scales represent the mass of the initial state, the invariant mass of the hadronic state M_X and the scale at which the inclusive calculation breaks down, respectively [3].

The obtained differential inclusive decay rate is factorized into contributions at different scales, where the contribution at each scale is described by an effective field theory [3]:

$$d\Gamma \sim H \cdot J \otimes S, \quad (3.16)$$

where H is the part containing hard corrections, J is the *jet function* that contains the "hard-collinear" effects on the final-state hadronic jet, and is convoluted (\otimes) with the shape function S [3], which describes non-perturbative physics at scales of Λ_{QCD} .

3.1.3 Shape functions

The shape functions include the non-perturbative contributions to the calculation of the semileptonic decay rates. Our knowledge of shape functions is thus crucial for an accurate determination of $|V_{ub}|$: therefore an improved shape-function determination was one of the objectives of the analysis presented in the thesis.

The shape function is a hadronic structure function, describing the inner structure of the B meson, such as the motion of the b quark within the B meson. In the leading order of Λ_{QCD}/m_b , the shape function (also called the leading order shape function) depends only on the properties of the B meson, regardless of the decay mode, and therefore the same shape function describes non-perturbative corrections to all transitions of a b to a light quark [11]. Thus, the $B \rightarrow X_u \ell \nu$ and $B \rightarrow X_s \gamma$ decays, transitions to light u and s quarks, respectively, share the same leading order shape function.

If the leading order shape function is determined in one of the transitions, it can be subsequently used in the calculations of other transitions. This fact is exploited by first parameterizing the shape function, then determining the shape function parameters from $B \rightarrow X_s \gamma$ decays, and finally using the result in the calculation of $\Gamma(B \rightarrow X_u \ell \nu)$. It is important to note that the next order corrections and the so-called sub-leading shape functions are found to be different for the two types of decays [3]. In the theory treatment used, the sub-leading shape function contributions are calculated [33] and the uncertainty due to sub-leading shape functions is estimated [3].

There are several possibilities for measuring shape function parameters by fitting the inclusive distributions of kinematical variables. In $B \rightarrow X_s \gamma$ decays one can fit the shape and the moments of the photon energy distribution, while in $B \rightarrow X_c \ell \nu$ decays the fitted quantities are usually the moments of the charged-lepton energy distribution or the moments of the hadronic invariant mass distribution. The present analysis used the fits to the photon energy distribution obtained by Belle [34], in accordance to the proposal of the authors of the theoretical treatment, obtaining improved accuracy of the shape function parameters. Recently, a simultaneous fit to several photon energy, charged-lepton energy and hadronic mass distributions obtained from different experiments was performed, significantly improving the accuracy of the parameters. The final $|V_{ub}|$ results are calculated using parameters of this determination, while the method and results of the shape function determination from photon-energy spectrum fit is also presented (see Sec. 7.4.1).

3.1.3.1 Shape function parametrization

As previously mentioned, the mass of the b quark plays a role of a parameter in the transitions, and is scheme dependent. The "shape function" scheme was proposed by the authors of the theoretical treatment [32], in which the mass of the b quark, $m_b(SF)$, incorporates the bulk properties of the shape function. The role of the heavy quark expansion parameter λ_1 is taken by $\mu_\pi^2(SF)$, the parameter describing the average kinetic energy of the b quark in the shape-function scheme. The relations to two-loop order of $m_b(SF)$ and $\mu_\pi^2(SF)$ parameters to other common definitions of heavy-quark parameters were also calculated [35], to enable the transition between different schemes.

The fully inclusive OPE calculation result is highly dependent on the value of m_b due to the m_b^5 factor (see section 3.1.1.1), and the power is effectively increased to powers of approximately m_b^{10} [3] when the calculation is restricted to a selected kinematical region. By incorporating shape function properties to m_b , the contribution to the uncertainty due to the value of m_b is appended to the shape function determination and the overall accuracy is controlled by the accuracy of shape function parameter measurement. The largest theoretical error is thus transformed into an experimental error, which can be improved by better experimental determination.

The calculation of the non-perturbative contribution to the rates depends not only on the shape function parameters, but also on the specific choice of the functional form used in the parametrization. To estimate how much the functional form of the shape function affects the result, the measurement is repeated with different forms of parametrization. Three shape function forms suggested in the literature are employed in the present analysis; exponential, gaussian and

hyperbolic [3, 32]. Their functional forms are described in Table 3-1: they are a function of the so-called light-cone momentum¹ variable $\hat{\omega}$ [36] and are parameterized by two parameters: Λ and b . The comparison of the three shape function forms is shown in Fig.3-5.

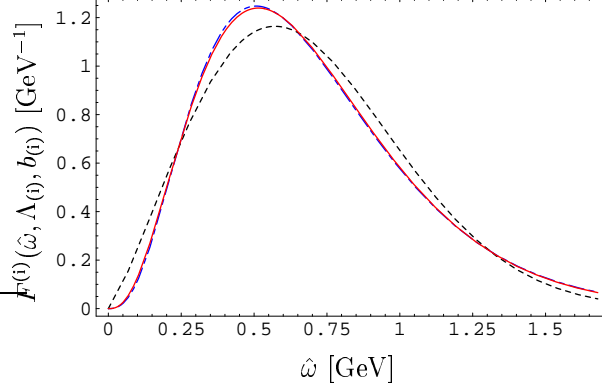


Figure 3-5. Three different functional forms used for shape functions: $F^{(\text{exp})}$ (solid), $F^{(\text{gauss})}$ (dashed), and $F^{(\text{hyp})}$ (dash-dotted), for parameters that correspond to $m_b(SF) = 4.63 \text{ GeV}/c^2$ and $\mu_\pi^2(SF) = 0.2 \text{ GeV}^2/c^2$. From Ref. [3].

Shape Function	Form
exponential	$F^{(\text{exp})}(\hat{\omega}; \Lambda, b) = \frac{N^{(\text{exp})}}{\Lambda} \left(\frac{\hat{\omega}}{\Lambda}\right)^{b-1} \exp(-d_{\text{exp}} \frac{\hat{\omega}}{\Lambda})$
gaussian	$F^{(\text{gauss})}(\hat{\omega}; \Lambda, b) = \frac{N^{(\text{gauss})}}{\Lambda} \left(\frac{\hat{\omega}}{\Lambda}\right)^{b-1} \exp\left(-d_{\text{gauss}} \frac{\hat{\omega}^2}{\Lambda^2}\right)$
hyperbolic	$F^{(\text{hyp})}(\hat{\omega}; \Lambda, b) = \frac{N^{(\text{hyp})}}{\Lambda} \left(\frac{\hat{\omega}}{\Lambda}\right)^{b-1} \cosh^{-1}\left(d_{\text{hyp}} \frac{\hat{\omega}}{\Lambda}\right)$

where the constants are:

$$\begin{aligned}
 N^{(\text{exp})} &= \frac{d_{\text{exp}}^b}{\Gamma(b)}, & d_{\text{exp}} &= b, \\
 N^{(\text{gauss})} &= \frac{2 d_{\text{gauss}}^{b/2}}{\Gamma(b/2)}, & d_{\text{gauss}} &= \left(\frac{\Gamma(\frac{1+b}{2})}{\Gamma(\frac{b}{2})}\right)^2, \\
 N^{(\text{hyp})} &= \frac{[4 d_{\text{hyp}}]^b}{2 \Gamma(b) [\zeta(b, \frac{1}{4}) - \zeta(b, \frac{3}{4})]}, & d_{\text{hyp}} &= \frac{b}{4} \frac{\zeta(1+b, \frac{1}{4}) - \zeta(1+b, \frac{3}{4})}{\zeta(b, \frac{1}{4}) - \zeta(b, \frac{3}{4})}, \\
 \zeta(b, a) &= \sum_{k=0}^{\infty} (k+a)^{-b} \text{ is the generalized Riemann zeta function}
 \end{aligned}$$

Table 3-1. The three functional forms used for shape function parametrization. From Ref. [3].

The parameters Λ and b are related to the HQET parameters $\bar{\Lambda}$ and μ_π^2 by analytical expressions Eq. 46 and Eq. 47 in Ref. [3] for exponential and gaussian models, respectively, while for the hyperbolic model the corresponding HQET parameters have to be calculated numerically. The shape function parameters $m_b(SF)$ and $\mu_\pi^2(SF)$ are obtained from the HQET parameters $\bar{\Lambda}$ and μ_π^2 using the relations in Eq. 41 of Ref. [3], where the reference scale of 1.5 GeV is used.

¹In the description of light particles with high momenta the mass can be neglected to simplify the formalism and the momenta are confined to the light cone.

3.2 Extraction of $|V_{ub}|$

Extraction of the matrix element $|V_{ub}|$ is the main task of the thesis. From the experimental determination we obtain the inclusive charmless semileptonic partial rate of B mesons

$$\Delta\Gamma_{ul\nu}(\Delta\Phi) . \quad (3.17)$$

The $\Delta\Phi$ stands for a particular kinematical region that is used for the extraction of $b \rightarrow u$ decays. The theoretical model from Ref. [3] is used to convert the measured result directly into $|V_{ub}|$. The theoretical treatment was implemented in an inclusive generator that calculates $R(\Delta\Phi)$, the theoretical prediction of $\Delta\Gamma_{ul\nu}(\Delta\Phi)$, the partial rate within the selected part of the kinematical phase space, divided by $|V_{ub}|^2$ ($R(\Delta\Phi)$ is given in units of ps^{-1}). $|V_{ub}|$ is then obtained by the formula:

$$|V_{ub}| = \sqrt{\frac{\Delta\Gamma_{ul\nu}(\Delta\Phi)}{R(\Delta\Phi)}} . \quad (3.18)$$

The calculated result is strongly dependent on the shape function parameters (see Fig. 3-6).

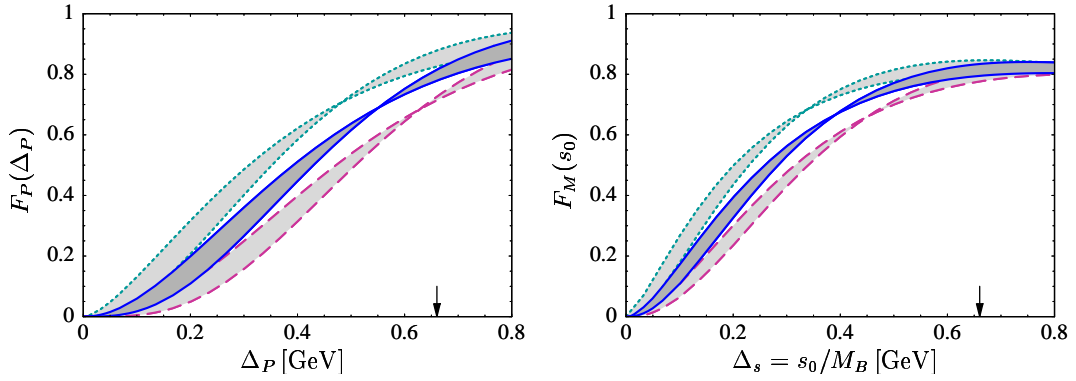


Figure 3-6. Fraction of $\bar{B} \rightarrow X_u l^- \bar{\nu}$ events with $P_+ \leq \Delta_P$ (left), and fraction of events with hadronic invariant mass $M_X^2 \leq s_0$ (right). The two fractions correspond to $F_P = R(\Delta P_+)/R(0)$ and $F_M = R(\Delta M_X^2)/R(0)$. In each plot, the darker band corresponds to the central value of m_b (see Sec. 7.4.1.7) and the two lighter to m_b values 70 MeV/c^2 above and below the central value. The width of the band reflects the sensitivity to the value of μ_π^2 , also varied by 70 MeV . The arrow indicates the point above which the charm background starts. From Ref. [3].

3.2.1 Sources of theoretical uncertainties

The possible contributions to the theoretical uncertainty were studied with the inclusive generator which implement the theoretical treatment from Ref. [3]. Three classes of contributions to the uncertainty were considered:

- The choice of functional forms of the leading and sub-leading shape functions
- perturbative uncertainties
- weak-annihilation effects

The non-perturbative contributions that are parametrized by the shape function are considered to be experimental in nature, since the shape function parameters are obtained by measurements to data, and their precision can be improved when more data are gathered. They are estimated from the measurement and given separately (see Sec. 7.4.2).

3.2.1.1 The choice of shape-function functional forms

The need to parametrize the leading shape function in order to obtain shape function parameters experimentally, introduces the uncertainty due to the choice of the functional form of the shape function. The effect is estimated by obtaining the result with the exponential and gaussian forms (given in Table 3-1) and observing the amount of discrepancy. This gives a measure of the scale of the effect, but does not guarantee that a different functional form that also with suitable properties could have a larger discrepancy [3].

The functional form of the sub-leading shape functions is also a source of theoretical uncertainty. Six explicit functional forms were proposed [3] for sub-leading shape functions and the spread of results obtained by different functional forms is taken as the related uncertainty, while an average of the results was used for the central value.

3.2.1.2 Perturbative uncertainties

The results should in principle be independent of the choice of the scales, at which the effective theories are matched [3] (see Sec. 3.1.2.1), but since the perturbation is truncated, the choice of the matching scales $\mu_h \sim m_b$, $\mu_i \sim \sqrt{m_b \Lambda_{\text{QCD}}}$ and $\bar{\mu} \sim \mu_i$, used in the calculation, is a source of perturbative uncertainties.

The hard scale was chosen to be $\mu_h = m_b/2 \approx 2.3 \text{ GeV}$, and the variation between $\mu_h/\sqrt{2}$ and $\mu_h\sqrt{2}$ was used as the measure of the uncertainty [3].

The intermediate scale $\mu_i = 1.5 \text{ GeV}$ brings a fixed relative error of

$$\pm \left(\frac{\alpha_s(\mu_i)}{\pi} \right)^2, \quad \alpha_s(\mu_i) = 0.286 \quad (3.19)$$

to the value of R [3].

The additional scale $\bar{\mu} = \mu_i$, with its variation between $\mu_i/\sqrt{2}$ and $\mu_i\sqrt{2}$ representing the error [3], was used in the calculation.

The overall perturbative uncertainty was obtained by summing the squares of individual contributions. Since the contributions are asymmetric, it is worth noting that for $|V_{ub}|$ we interchange the upper and lower bounds of the relative errors on $R(\Delta\Phi)$.

3.2.1.3 Weak-annihilation effects

The contribution to the semileptonic rate of the weak annihilation process, where the $b \rightarrow u$ transition happens between the b and u quarks within the B^0 meson, is not included in the calculation of $R(\Delta\Phi)$. The possible uncertainty due to this process was roughly estimated to be $\pm 1.8\%$ of the total rate, that is calculated to be $R_{tot} = 70 \text{ ps}^{-1}$. Thus, a fixed absolute error of $\Delta R_{WA} = \pm 1.3 \text{ ps}^{-1}$ is assigned to the calculation of $R(\Delta\Phi)$.

3.3 Modeling $b \rightarrow u\ell\nu$ decays

The Monte Carlo (MC) simulation of the $b \rightarrow u\ell\nu$ decays was used to estimate the selection efficiency and to model the distributions of kinematical variables when optimizing the selection. A mixture of exclusive (resonant) and inclusive contributions was used. The decays to $X_u\tau\nu_\tau$ are not modeled.

The resonant B^0/\bar{B}^0 decays to $\pi^\pm\ell\nu$ and $\rho^\pm\ell\nu$ are modeled with form-factors calculated by QCD Light Cone Sum Rules (LCSR) [37], while $a_{0,1,2}\ell\nu$ and $b_1\ell\nu$ have form-factors from ISGW2 [38]. The resonant B^+/B^- decays to

$\pi^0\ell\nu$, $\rho^0\ell\nu$ and $\omega\ell\nu$ are modeled with form-factors calculated by LCSR, all other resonant decays have form-factors from ISGW2. The summary of resonant modes used in the MC simulation is given in Table 3-2.

B^+ modes	$\mathcal{B}(\times 10^{-3})$	FF model	B^0 modes	$\mathcal{B}(\times 10^{-3})$	FF model
$\pi^0\ell\nu$	0.072	LCSR	$\pi^+\ell\nu$	0.133	LCSR
$\rho^0\ell\nu$	0.152	LCSR	$\rho^+\ell\nu$	0.280	LCSR
$\eta\ell\nu$	0.084	ISGW2			
$\eta'\ell\nu$	0.055	ISGW2			
$\omega\ell\nu$	0.152	LCSR			
$a_0^0\ell\nu$	0.004	ISGW2	$a_0^+\ell\nu$	0.009	ISGW2
$a_1^0\ell\nu$	0.085	ISGW2	$a_1^+\ell\nu$	0.151	ISGW2
$a_2^0\ell\nu$	0.032	ISGW2	$a_2^+\ell\nu$	0.057	ISGW2
$b_1^0\ell\nu$	0.107	ISGW2	$b_1^+\ell\nu$	0.189	ISGW2
$f_0\ell\nu$	0.006	ISGW2			
$f_1\ell\nu$	0.081	ISGW2			
$f_2\ell\nu$	0.036	ISGW2			
$h_1\ell\nu$	0.113	ISGW2			
exclusive	0.979		exclusive	0.819	
inclusive	1.101		inclusive	1.101	
total	2.080		total	1.920	

Table 3-2. Summary of $b \rightarrow u$ decay modes used in the Monte Carlo simulation.

3.3.0.4 Non-resonant decay mode

The simulation of inclusive charmless semileptonic decays, where the invariant mass of the hadronic state is larger than $2m_\pi$, is simulated by a model proposed by De Fazio and Neubert [31], with parameters $m_b^{\text{pole}} = 4.80 \text{ GeV}/c^2$, parameter of Fermi motion $a = 1.29$ (see eq. 3.21), $\alpha_S = 0.22$ and $\lambda_1^{SF} = -0.30 \text{ GeV}^2/c^2$.

This model is the predecessor of the model described in sec. 3.1.2 and calculates the triple differential decay rate $d^3\Gamma/dq^2 dM_X^2 dE_\ell$, with corrections up to $\mathcal{O}(\alpha_S)$. The non-perturbative effects of the Fermi motion are included by convolving the parton-level decay rate with a shape function:

$$d\Gamma = \int d\omega S(\omega) d\Gamma_{\text{parton}}(m_b + \omega). \quad (3.20)$$

The shape function implemented in the model is the function of the residual momentum of the b quark $k_+ = k^\mu - k_\perp$. It has two independent free parameters $\bar{\Lambda}^{SF}$ and λ_1^{SF} , where $\bar{\Lambda}^{SF} \equiv m_B - m_b^{\text{pole}}$ is the difference between the masses of the B meson and the b quark, and $-\lambda_1^{SF}$ is the average momentum squared of the b quark in the meson. The shape function parametrization used in the model is:

$$F(k_+) = N(1-x)^a e^{(1+a)x}; \quad x = \frac{k_+}{\bar{\Lambda}^{SF}}; \quad a = -3\frac{(\bar{\Lambda}^{SF})^2}{\lambda_1^{SF}} - 1 \quad (3.21)$$

To estimate the model dependence of results, a set of five $b \rightarrow u$ MC samples with different shape function parameters is used:

sample 1:	$m_b^{\text{pole}} = 4.80 \text{ GeV}/c^2$	$\lambda_1^{SF} = -0.15 \text{ GeV}^2/c^2$
sample 2:	$m_b^{\text{pole}} = 4.80 \text{ GeV}/c^2$	$\lambda_1^{SF} = -0.30 \text{ GeV}^2/c^2$
sample 3:	$m_b^{\text{pole}} = 4.80 \text{ GeV}/c^2$	$\lambda_1^{SF} = -0.45 \text{ GeV}^2/c^2$
sample 4:	$m_b^{\text{pole}} = 4.65 \text{ GeV}/c^2$	$\lambda_1^{SF} = -0.52 \text{ GeV}^2/c^2$
sample 5:	$m_b^{\text{pole}} = 4.95 \text{ GeV}/c^2$	$\lambda_1^{SF} = -0.14 \text{ GeV}^2/c^2$

The last two samples are generated with shape function parameters that represent the largest effect on the kinematical distributions².

The only resonant model added is $\pi\ell\nu$ (modeled with ISGW2 model), the M_X contribution of which is below $2m_\pi$, where the inclusive contribution starts. The samples are not fully reconstructed, because low efficiency of full reconstruction would demand huge starting samples; instead we rely on the presupposition that the modeling effects are not correlated with the effects of full reconstruction. The modeling effects are assessed by the comparison of results with different models (see section 7.2.3.3).

²The effect of the two shape function parameters on the partial branching fraction is expected to be largest around the edges on the major axis of the $\chi^2 = 1$ contour ellipse, obtained from the fit to the $B \rightarrow X_s \gamma$ spectrum [39].

The Belle experiment

The Belle experiment is designed to perform precision quantitative studies of B mesons. It is conducted at the High Energy Accelerator Research Organization, known as KEKB, which is located in Tsukuba, Japan, as a joint effort of more than 350 physicists from 54 institutes and 10 countries.

Its main goal is a precise measurement of CP asymmetries in B meson decays. Studies of CP violation and rare B meson decays require a data sample of many millions of B mesons. They are produced in collisions of electrons and positrons at KEKB, a B factory with asymmetric energies of beams set at the center-of-mass energy best corresponding to the mass of the $\Upsilon(4S)$ resonance.

The $\Upsilon(4S)$ resonance is a vector meson $b\bar{b}$ state, which decays with strong interaction to a $B\bar{B}$ meson pair. Since the energies of the beams are asymmetric, the particles are boosted in the direction of the more energetic beam. This boost enables the study of time-dependent CP asymmetries by increasing the distances between decay vertices of the two B mesons. The Belle detector is situated at the interaction region of the e^+e^- beams, covering a large portion of the solid angle. Several detector sub-parts enable reconstruction of tracks and identification of particles that were produced in the collision.

The KEKB accelerator commissioning began in December 1998, and six months after the Belle detector started its data-taking. Since then it managed to accumulate a data-sample of over 400 million decays of B meson pairs. This chapter briefly describes the experimental apparatus of KEKB and Belle.

4.1 The KEKB accelerator and storage ring

KEKB is a ring accelerator, measuring 3 kilometers in circumference and colliding electrons and positrons at a center-of-mass energy of 10.58 GeV. Electrons with energy of 8.0 GeV and positrons with energy of 3.5 GeV are accelerated in bunches in the High Energy Ring (HER) and Low Energy Ring (LER), respectively. The two rings continuously collide bunches of particles at the Interaction Point (IP). To reduce background synchrotron radiation, the beams collide at a finite crossing angle of 22 mrad. The IP is located in Tsukuba Hall - site of the Belle detector, see figure 4-1.

At the IP, electrons and positrons interact in processes like Bhabha scattering, tau and muon pair production, quark pair production and two-photon events. Even though the center-of-mass energy is tailored for production of the $\Upsilon(4S)$ resonance (see figure 4-2), only one in every seventy e^+e^- interactions produces an $\Upsilon(4S)$. The rate of production, R , is defined as the interaction cross section, σ , multiplied by the luminosity, \mathcal{L} , measured in units of cm^2 and $\text{cm}^{-2}\text{s}^{-1}$, respectively:

$$R = \sigma\mathcal{L}. \quad (4.1)$$

The interaction cross section for $\Upsilon(4S)$ production at the center-of-mass energy of 10.58 GeV is

$$\sigma(e^+e^- \rightarrow b\bar{b}) = 1.1 \text{ nb}, \quad (4.2)$$

where the unit is barn, $\text{b} \equiv 10^{-24}\text{cm}^2$. The luminosity is a measure of the beam-colliding performance, and is given by

$$\mathcal{L} = f \cdot n \cdot \frac{N_1 N_2}{A}, \quad (4.3)$$

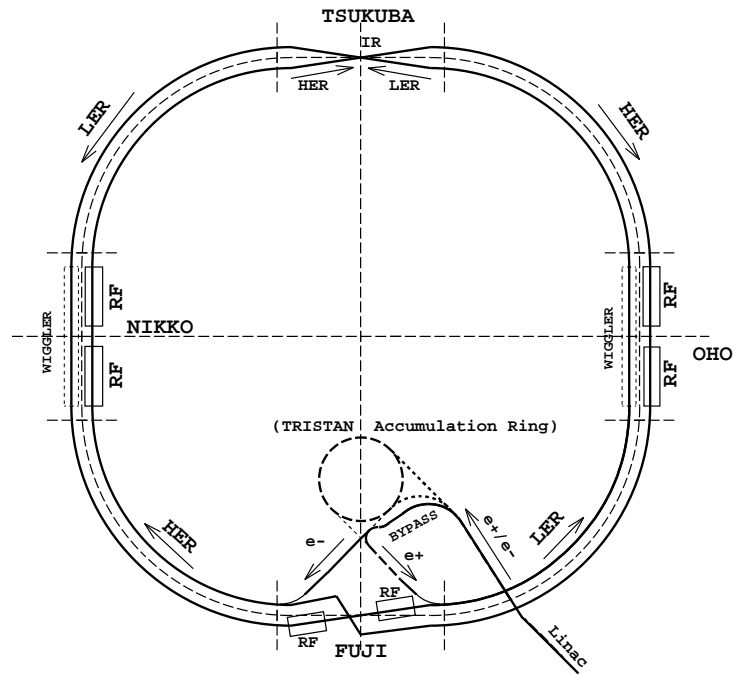


Figure 4-1. The KEKB storage rings, LER and HER, with the IP located in Tsukuba Hall.

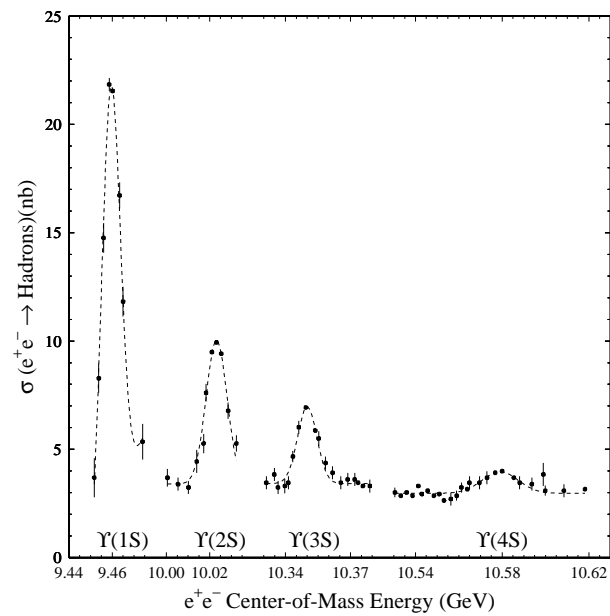


Figure 4-2. Cross section of Υ production in e^+e^- collisions.

where n bunches of N_1 and N_2 particles in opposing beams meet f times per second, where the overlapping area of the beams is A .

The estimated maximum luminosity to be achieved in the proposal was $10^{34} \text{ cm}^{-2}\text{s}^{-1}$, and has already been surpassed. A maximum luminosity of $1.581 \times 10^{34} \text{ cm}^{-2}\text{s}^{-1}$ was achieved on May 18, 2005, and is currently the highest luminosity ever achieved by a collider. The measure of collected data is the integrated luminosity:

$$\mathcal{L}_{int} = \int \mathcal{L} dt . \quad (4.4)$$

Taking the detector dead-time into account, Belle has accumulated the integrated luminosity of $\mathcal{L}_{int} = 468.9 \text{ fb}^{-1}$.

4.2 The Belle detector

The Belle detector is a particle spectrometer, configured within a 1.5 T superconducting solenoid and iron structure. It is located at the interaction region of the KEKB beams and reflects the beam energy asymmetry. It covers 97% of the solid angle and consists of seven sub-detectors, the; silicon vertex detector (SVD); central wire drift chamber (CDC); aerogel Čerenkov counters (ACC); time of flight counters (TOF); electro-magnetic calorimeter (ECL); extreme forward calorimeter (EFC); and a K_L and μ detector (KLM). The Belle detector scheme with detector sub-parts is depicted in figure 4-3.

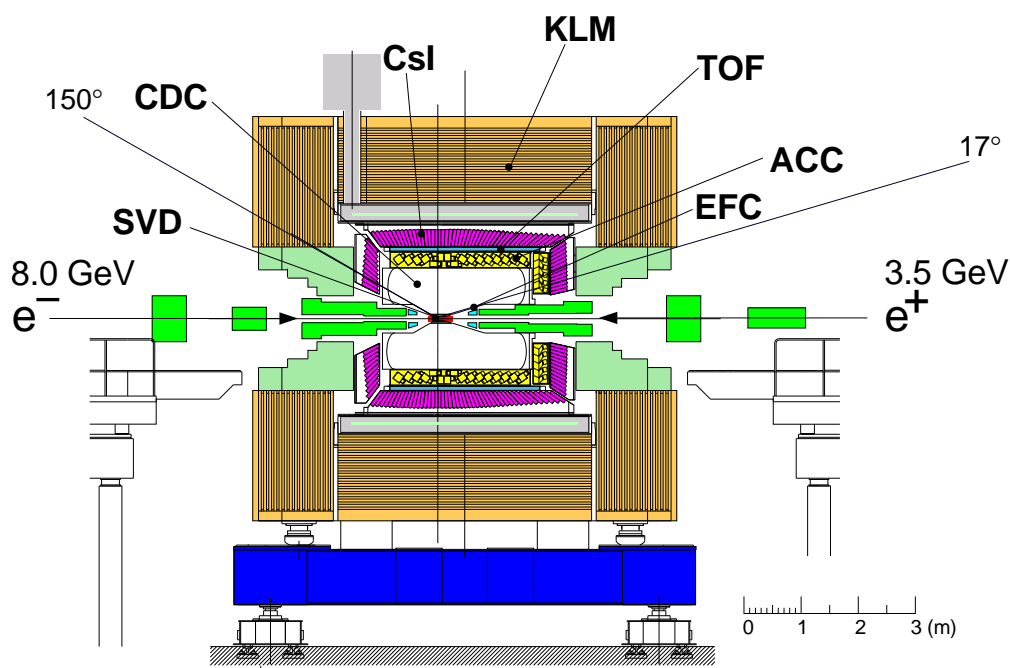


Figure 4-3. Side view of the Belle detector.

The SVD measures B meson decay vertices and aids the CDC in providing charged particle tracking. Specific ionization energy loss measurements made with the CDC are combined with light yield readings from the ACC and time of flight information from the TOF to provide charged kaon and pion identification. Electromagnetic shower measurements and calorimetry, crucial for electron identification and photon detection, are performed by the ECL and EFC. The KLM is used to identify muons and detect K_L mesons. The solenoid magnet provides a magnetic field

needed for the measurement of momenta. The following subsections describe the Belle sub-detectors. A detailed description of the Belle detector is given in Ref. [40].

4.2.0.5 Coordinate systems

The origin of the coordinate system is defined as the position of the nominal IP. The common z axis is defined as the direction of the magnetic field within the solenoid, which coincides with the direction opposite to the positron beam. The x and y axes are horizontal and vertical, respectively, and correspond to a right-handed coordinate system. The polar angle θ is measured relative to the positive z axis. The azimuthal angle ϕ , laying in the $x - y$ plane, is measured relative to the positive x axis. The radius in the cylindrical coordinate system is defined as $r = \sqrt{x^2 + y^2}$.

4.2.1 Beam Pipe

The beam pipe encloses the interaction point and maintains the accelerator vacuum. To precisely determine the decay vertices, Silicon Vertex Detector (SVD) should be as close to the IP as possible, but two effects force the SVD to be displaced from the IP: the beam-induced heating of the beam pipe and large beam backgrounds due to the multiple Coulomb scattering in the beam pipe. These considerations are balanced by providing a central double-wall beryllium beam pipe extending from $z = -4.6$ cm to $z = 10.1$ cm with an inner radius of $r = 20$ mm. Helium gas is cycled in the gap between the inner and outer walls to provide cooling and its low Z minimizes Coulomb interactions. The beam pipe is shown in figure 4-4. In 2003, when a new SVD detector was installed, the existing beam pipe was replaced

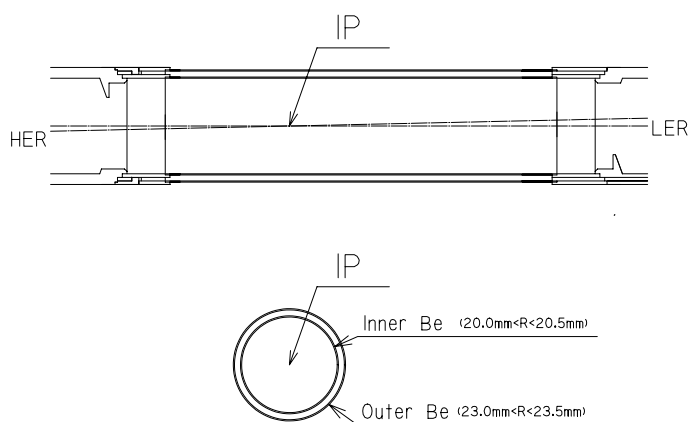


Figure 4-4. The cross section of the beryllium beam pipe at the interaction point.

with a one with smaller dimensions, where the inner radius was reduced to $r = 15$ mm.

4.2.2 Silicon Vertex Detector (SVD)

The measurement of the separation of the two B meson decay vertices, which can be translated into a life-time difference between neutral B meson decays, is necessary for the measurement of time dependent CP violation in

mixing. The $\Upsilon(4S)$ Lorentz boost in the laboratory frame allows measurement of the B meson decay vertices. The average flight distance of B mesons at Belle is $200\ \mu\text{m}$, while SVD is able to resolve vertices to within a precision of $100\ \mu\text{m}$.

The SVD detects particles passing through a Double Sided Silicon Detector (DSSD), by observing the charge collected by the sense-strips on both sides of the DSSD. At Belle this occurrence is known as a SVD hit. The SVD uses S6936 type DSSDs, fabricated by Hamamatsu Photonics. The read-out is based on the VA1 chip, fabricated by Austrian Micro Systems.

The DSSD is essentially a pn junction, operated under reverse bias to reach full depletion. A charged particle passing through the junction liberates electrons from the valence band into the conduction band, creating electron-hole (e^-h^+) pairs. The free e^-h^+ pairs instigate current in p^+ and n^+ strips situated along the surface of the bulk on opposing sides of the DSSD. The DSSD operation is depicted in figure 4-5. The p^+ strips are aligned along the beam axis to

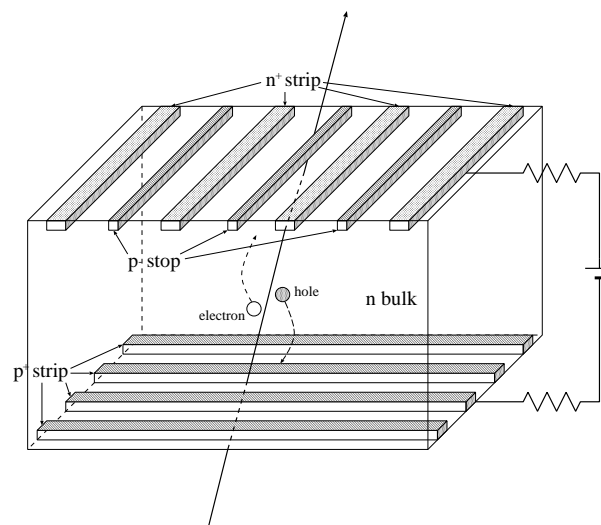


Figure 4-5. Schematic view of a Double Sided Silicon Detector.

measure the azimuthal angle, ϕ , while the n^+ strips, are aligned perpendicular to the beam axis to measure z . The pitch for different configurations can be read off Table 4-1.

The DSSD size is $57.5 \times 33.5 \times 0.3\ \text{mm}^3$ and consists of 1280 sense strips and 640 readout pads on each side. Only every second sense strip is read out and the current is read using a hybrid card. Either one or two DSSDs connected to a hybrid form a short or long half ladder (HL), respectively. A full ladder consists of two half-ladders, connected together with the hybrids at the ends. Full ladders are arranged in cylindrical layers.

Two SVD configurations were used in the period of the data taking, SVD1 (1998-2003) and SVD2 (2003-to date). Since the SVD detector has to be very close to the beam-pipe, it has to endure a large particle irradiation. SVD2 has a greatly increased radiation tolerance, and by adding another layer of ladders the spatial resolution was improved as well as the solid angle coverage of the detector. The characteristics of the two configurations are summarized in table 4-1. Further detail on the SVD can be found in [41].

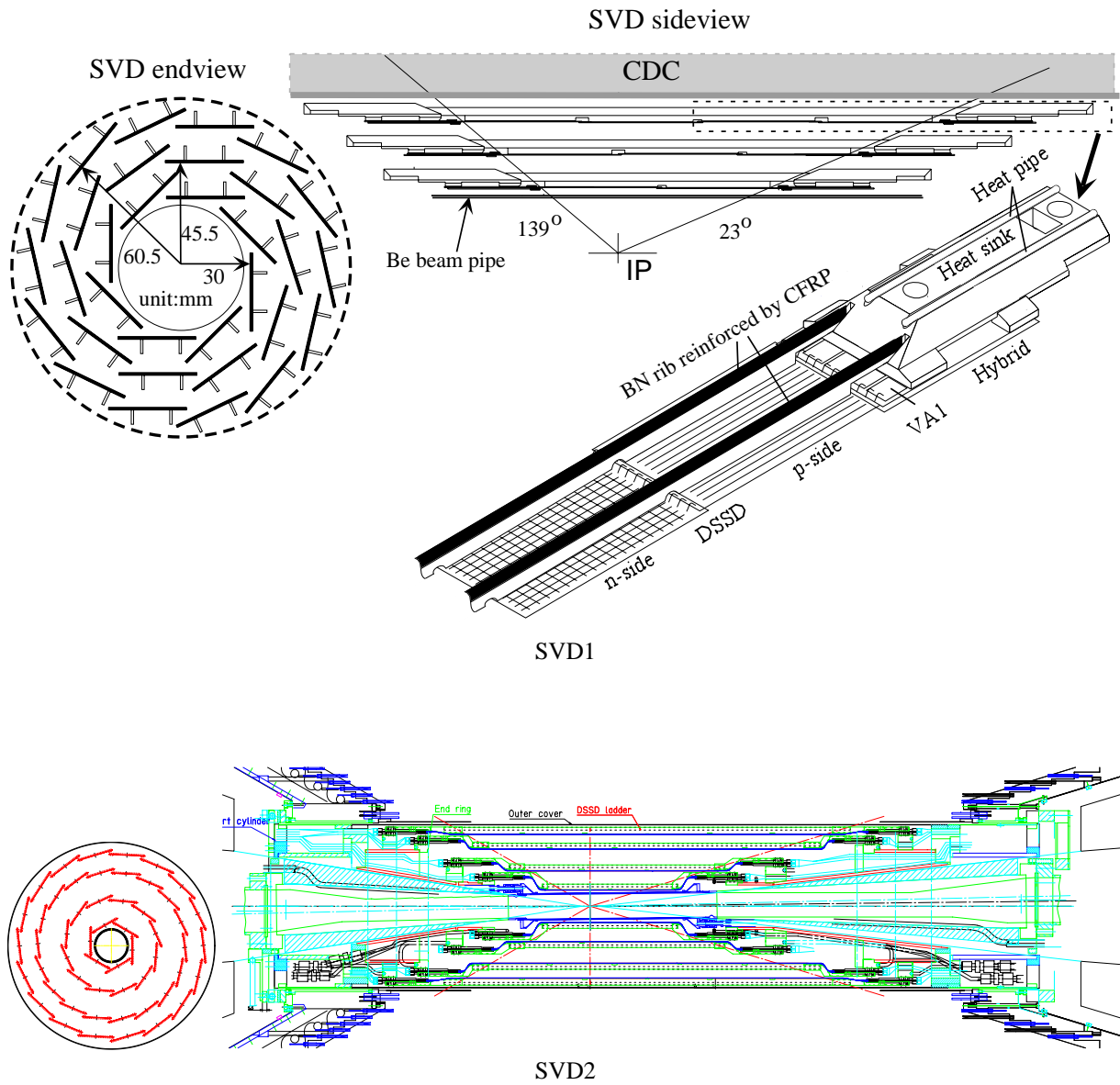


Figure 4-6. The Silicon Vertex Detector detector configuration for SVD1 and SVD2.

	SVD1	SVD2
Beam-pipe radius (mm)	20	15
No. of layers	3	4
No. of DSSD ladders in layers 1/2/3/4	8/10/14/Na	6/12/18/18
No. of DSSDs in a ladder in layers 1/2/3/4	2/3/4/Na	2/3/5/6
Radii of layers 1/2/3/4 (mm)	30.0/45.5/60.5/Na	30.0/45/5/60.5/Na
Angular coverage	$23^\circ < \theta < 140^\circ$	$23^\circ < \theta < 140^\circ$
Angular acceptance	0.86	0.86
Total number of channels	81920	110592
Strip pitch (μm) for z	84	75 (73 for layer 4)
Strip pitch (μm) for $r\phi$	25 (50 for readout)	50 (65 for layer 4)
DSSD thickness (μm)	300	300
Total material at $\theta = 90^\circ$ (Z_0)	1.85%	2.6%
Readout chip	VA1	VA1TA
Radiation tolerance (MRad)	~ 1	> 20
Intrinsic DAQ dead-time/trigger (μs)	128	25.6

Table 4-1. Characteristics of SVD1 and SVD2 (from [30]).

4.2.3 Central Drift Chamber (CDC)

The Central Drift Chamber (CDC) is designed to reconstruct trajectories of charged particles by detecting the ionization of the gas from the passing particle. Particle specific ionization energy loss, dE/dx , is also measured for particle identification purposes. Information on the hits in the CDC is used in the triggering.

The CDC encloses the SVD, extending radially from 77 mm to 880 mm. It consists of 32 axial layers, 18 small angle stereo layers, and 3 cathode strip layers. Axial layers measure the $r - \phi$ position, while stereo layers in conjunction with axial layers, inclined at a small angle to the beam pipe, measure the z position. The CDC covers a polar angle region of $17^\circ \leq \theta \leq 150^\circ$. The spatial resolution in $r - \phi$ is $130 \mu\text{m}$, and is better than 2 mm in the z direction. The CDC contains a total of 8400 drift cells. A drift cell is the functional unit of the CDC, consisting of a positively biased sense wire, surrounded by six negatively biased field wires, strung along the beam direction. When the SVD2 was installed the inner layers of the CDC were removed to accommodate for a larger SVD.

The cells are immersed in a helium-ethane gas mixture of ratio 1:1. The helium-ethane gas mixture has a relatively long radiation length of 640 m to minimize the effect of multiple Coulomb scatterings on the momentum resolution. The ethane component increases the electron density, which improves the resolution of the ionization-energy-loss measurement.

A charged particle, traversing the cell, ionizes the gas along its path. The ionized electrons and positive ions are attracted to the anode and cathode sense wires, respectively. Their drift in high electromagnetic fields near the wire instigates further ionization, resulting in avalanches of electrons and positive ions. When the avalanches reach the sense wire, current is induced, and if the signal is higher than the threshold, a CDC hit is detected. The distance between the ionizing track and the sense wire is estimated from the time taken for the ionization column to form.

Track parameters are determined using a track segment finder, which sorts hits into tracks. A helix, which describes the path of a charged particle in a constant magnetic field, is fitted to the track. The obtained helix parameters are combined with the magnetic field strength to determine the charged particle momentum. The transverse momentum

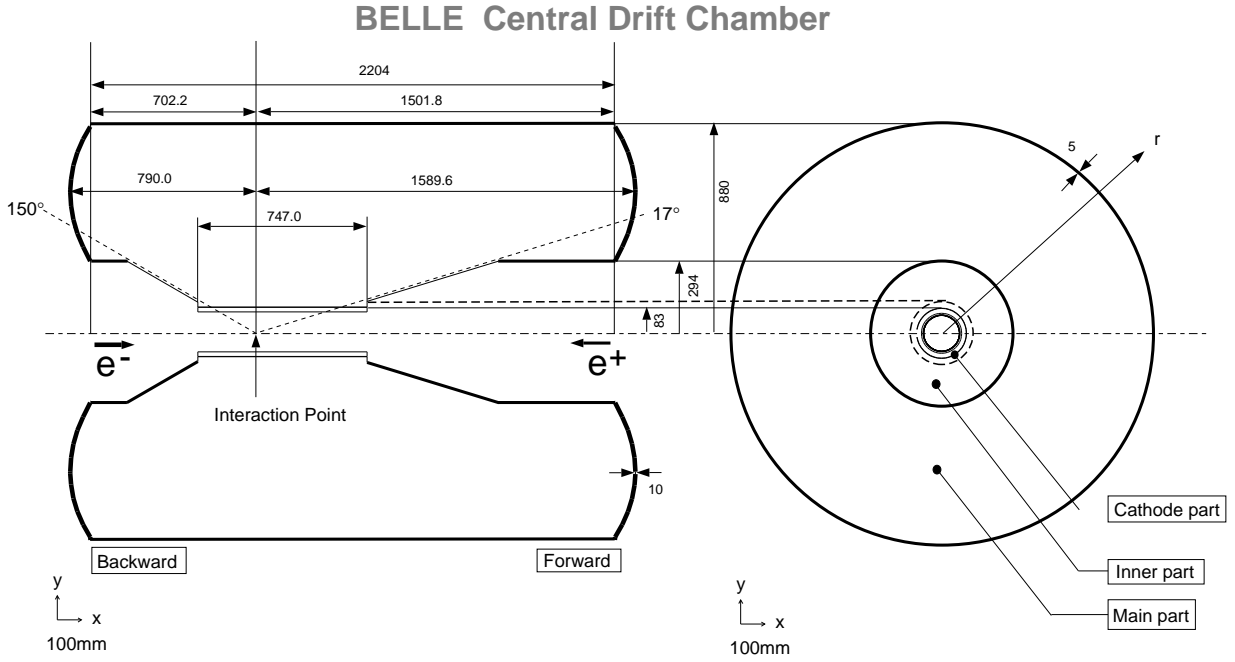


Figure 4-7. The Central Drift Chamber.

resolution, measured from cosmic ray data, is

$$\frac{\sigma_{p_T}}{p_T} = \sqrt{(0.20p_T)^2 + (0.29/\beta)^2} \% \quad (4.5)$$

where p_T is in units of GeV/c and β is the particle velocity divided by the speed of light.

Particle energy loss in the drift cell due to ionization, dE/dx , is determined from the hit amplitude recorded on the sense wire. Since the energy loss depends on the particle velocity at a given momentum, dE/dx distributions differs for different particle masses, as shown in figure 4-8. The ionization energy loss is measured for each CDC hit and measurements along the trajectory are combined to calculate the truncated mean, $\langle dE/dx \rangle$, of the track.

The $\langle dE/dx \rangle$ resolution, measured on a sample of pions from K_S decays, is 7.8%. The CDC can be used to distinguish pions from kaons of momenta up to $0.8 \text{ GeV}/c$ with a 3σ separation. A detailed description of CDC is presented in Ref. [42].

4.2.4 Aerogel Čerenkov Counter (ACC)

The silica Aerogel Čerenkov Counter (ACC) plays a crucial role in discriminating charged pions from kaons. When a particle travels faster than the speed of light in that medium, it will emit Čerenkov light. The light emitted appears in the form of a coherent wavefront at a fixed angle with respect to the trajectory.

To emit Čerenkov light, the particle velocity has to be greater than the threshold value:

$$\beta > \beta_{\text{threshold}} = \frac{1}{n} \quad (4.6)$$

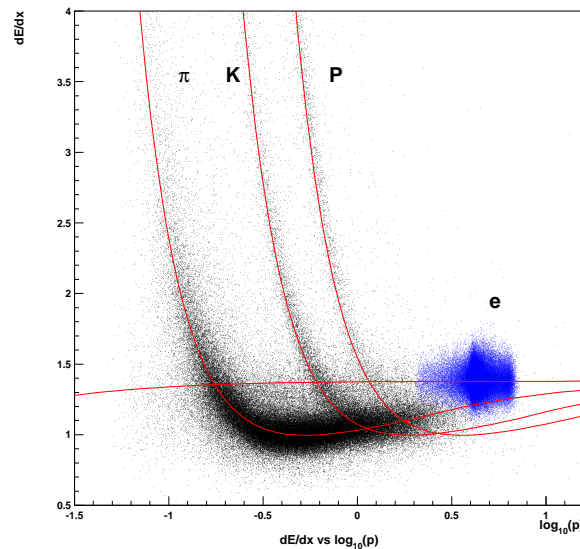


Figure 4-8. Truncated mean of dE/dx versus momentum. The points are measurements taken during accelerator operations, and the lines are the expected distributions for each particle type. p is measured in GeV/c .

where n is the refractive index of the medium. Threshold Čerenkov counters exploit the fact that only particles with velocity above $\beta_{\text{threshold}}$ emit Čerenkov photons. Since the momentum is measured by other sub-detectors, the particles can be identified by observing whether Čerenkov photons have or have not been detected.

K/π discrimination can be achieved by selecting media with appropriate refractive indices to cover typical momenta. The ACC augments the other detector subsystems by performing excellent K/π separation for momenta between 2.5 and 3.5 GeV/c , and is also able to provide useful information for momenta as low as 1.5 GeV/c and as high as 4.0 GeV/c .

The ACC is divided into barrel and forward endcap regions and is shown in figure 4-9. It spans a polar angle region of $17^\circ \leq \theta \leq 127^\circ$. The barrel contains 960 counter modules, segmented into 60 cells in the ϕ direction. The forward endcap contains 228 counter modules, arranged into 5 concentric layers. Depending on the polar angle, the refractive index of the aerogel tiles ranges from $n = 1.01$ to 1.03. One of concerns when using aerogel is that its transparency is greatly reduced with age due to its hydrophilic properties. A special aerogel production procedure has been developed that is able to produce hydrophobic aerogel.

Čerenkov photons are detected by either one or two fine mesh-type photo-multiplier tubes (FM-PMT), which are affixed to each counter. The ACC detector is positioned within a strong magnetic field, which drastically reduces the gain and the collection efficiency of the photoelectrons. By using a fine mesh-type photo-multiplier tube with 19 dynodes, a high gain of 10^8 is maintained even in the strong magnetic field. Three different sizes of FM-PMT are used, with radii of 1, 1.25, and 1.5 inches. The choice is dependent on the refractive index to keep the constant photon yield, since a lower refractive index results in a lower yield. Barrel and endcap modules are depicted in figure 4-10.

The pulse heights for each FM-PMT have been calibrated using μ -pair events. The average number of detected photoelectrons, $\langle N_{pe} \rangle$, ranges from 10 to 20 for the barrel ACC and from 25 to 30 for the endcap ACC.

Since pions are the most ubiquitous particles in hadronic events, the ACC performance is measured by its ability to identify kaons amongst pions - for which the ACC can provide good K/π separation with a kaon efficiency above

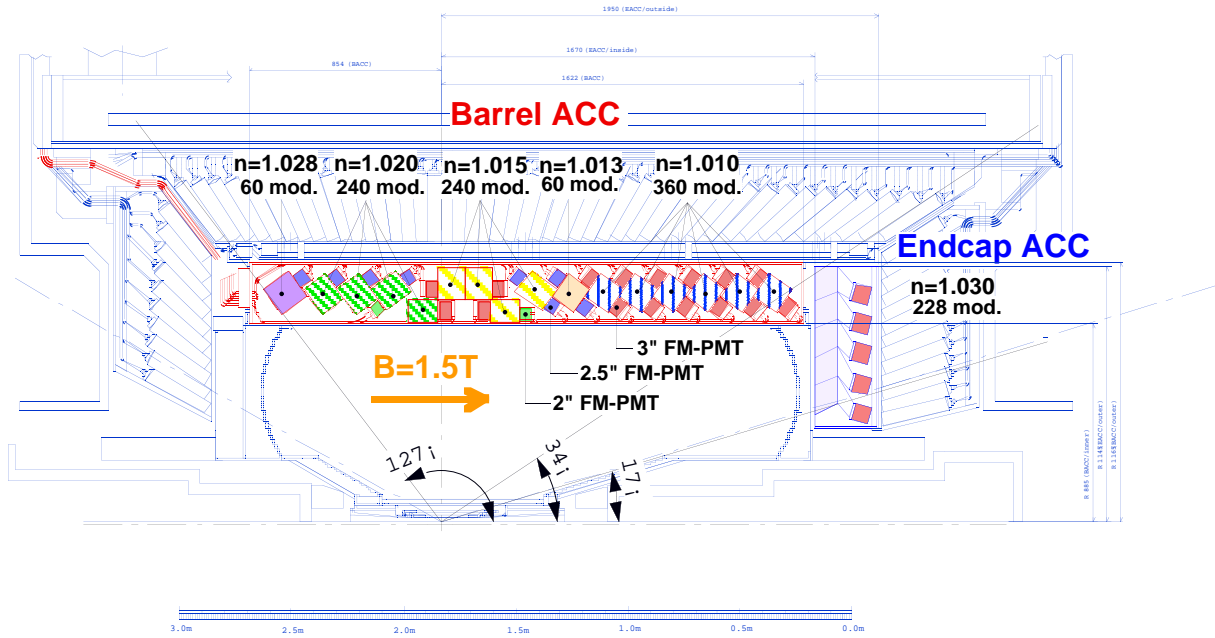
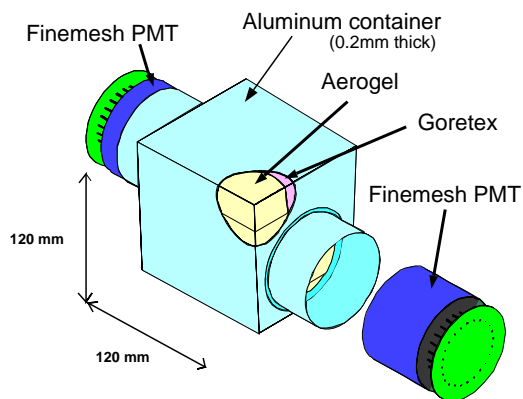


Figure 4-9. The configuration of the Aerogel Čerenkov Counter.

a) Barrel ACC Module



b) Endcap ACC Module

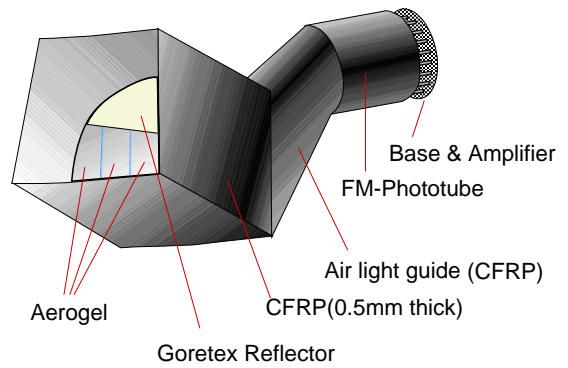


Figure 4-10. Schematic drawing of a typical ACC counter module: (a) barrel and (b) endcap ACC.

80% and a pion-to-kaon fake rate below 10%, as demonstrated in figure 4-11. A more detailed description of ACC is presented in Refs. [43, 44].

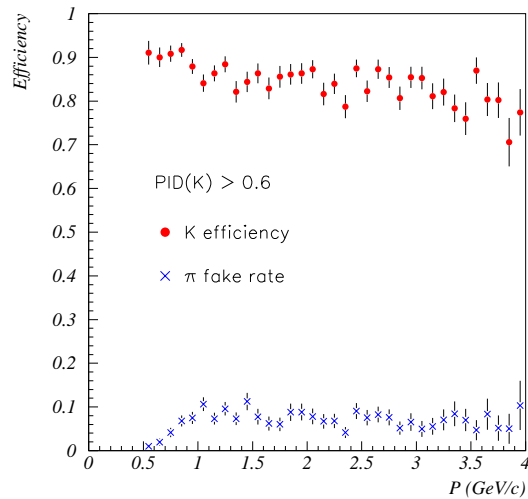


Figure 4-11. Kaon efficiency and pion fake rate, measured with $D^{*+} \rightarrow D^0(\rightarrow K\pi) + \pi^+$ decays, for the barrel region of the ACC.

4.2.5 Time of Flight counter (TOF)

The Time of Flight counter (TOF) is used for identification of charged particles in an intermediate momentum range of $0.8 \text{ GeV}/c$ to $1.2 \text{ GeV}/c$. It measures the velocity of particles from the time of flight over the distance, which in turn is determined by the track helix parameters, measured in the CDC. Particle identity is determined by combining its momentum (measured by CDC) and velocity, obtained by TOF.

The TOF is comprised of long plastic scintillators, chemical compounds that emit short light pulses after excitation by the passage of charged particles or by photons of high energy. The TOF measures the time of flight between a particle originating at the IP and passing through the scintillator, by detecting the emitted light pulses.

The TOF system consists of 64 modules, concentrically arranged around the z -axis at a radius of 1.2 m. A module is made up of two trapezoidally shaped time-of-flight counters and one Trigger Scintillation Counter (TSC), separated by a radial gap of 1.5 cm, as shown in figure 4-12. The thin TSC modules help reject photon conversion backgrounds by taking a coincidence between TOF and TSC counters for triggering purposes. Scintillation light from a counter is collected by a fine-mesh-dynode photo-multiplier tube (FM-PMT). The fine-mesh type PMT was chosen due to excellent gain in the magnetic field. Two FM-PMTs are used for a TOF counter while only one is used for a TSC counter. The FM-PMTs are mounted directly on the scintillator to eliminate the need for light guides.

Time intervals are measured to within a precision of 100 ps. The kaon-pion separation is plotted as a function of momentum in figure 4-13(a), it shows that for momenta below $1.0 \text{ GeV}/c$ a separation of more than 3σ is achieved. The mass distribution, shown in figure 4-13(b), measured from hadronic events, shows a comparison of real data with

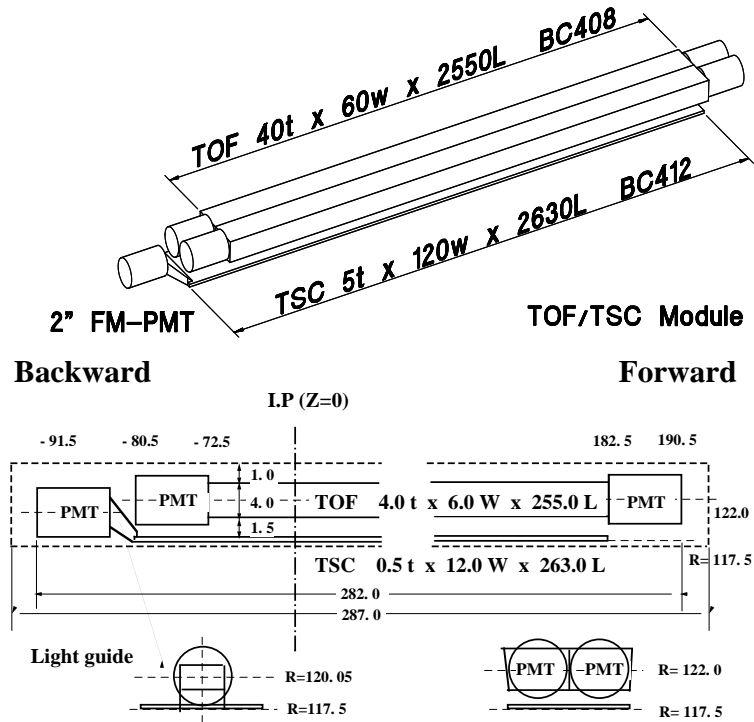


Figure 4-12. Dimensions of a TOF/TSC module.

Monte Carlo simulation for a timing resolution of 100 ps. Clear peaks are evident for pions, kaons and protons. The detailed description of TOF detector can be found in Ref. [45].

4.2.6 Electromagnetic Calorimeter (ECL)

The Electromagnetic Calorimeter (ECL) is designed to measure the energy and direction of photons and electrons produced in Belle and it is crucial for electron identification. Fine-grained fragmentation of the detector is needed for $\pi^0 \rightarrow \gamma\gamma$ reconstruction, since two nearby photons with their opening angle have to be detected.

High energy electrons and photons that enter the calorimeter material produce an electromagnetic shower by interaction with matter, mainly bremsstrahlung and electron-positron pair production. A lateral shower shape ensues from Coulomb scattering of the shower particles. Eventually, all of the incident energy appears as ionization or excitation (light) in the absorbing material.

The ECL consists of a highly segmented array of 8,736 cesium iodide crystals, doped with thallium (CsI(Tl)). The thallium shifts the excitation light into the visible spectrum. The light is detected by a pair of PIN photodiodes placed at the rear of each crystal.

The crystals are arranged into three sections: the backward endcap; the barrel; and the forward endcap. The barrel, positioned at an inner radius of 1.25 m, is 3.0 m long, and spans the polar angle region of $32.2^\circ \leq \theta \leq 128.7^\circ$. The annular-shaped forward endcap is situated at $z = +2.0$ m, and spans a polar angle region of $12.0^\circ \leq \theta \leq 31.4^\circ$. The likewise annular shaped endcap is situated at $z = -1.0$ m, and spans a polar angle region of $130.7^\circ \leq \theta \leq 155.7^\circ$. The ECL configuration is shown in figure 4-14.

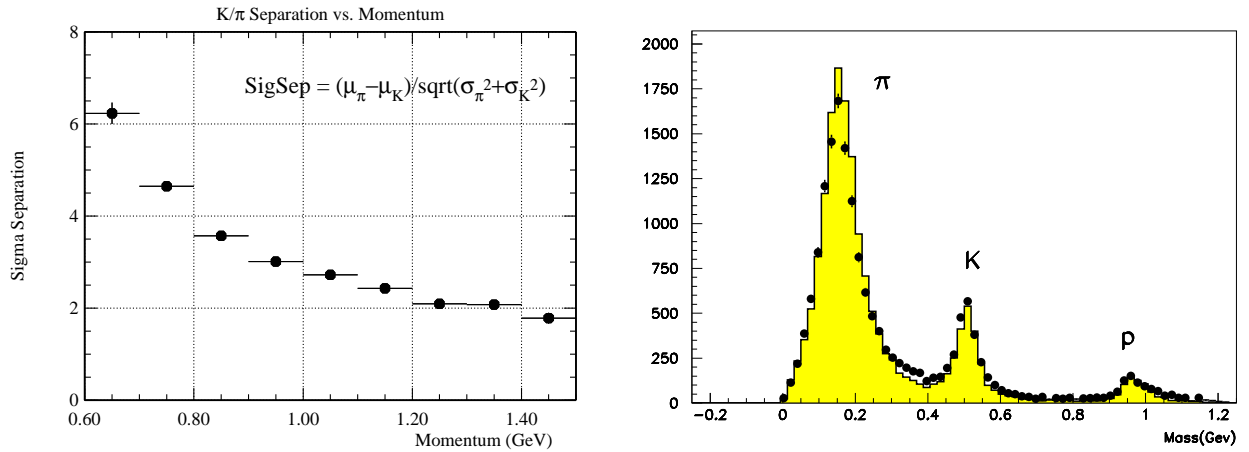


Figure 4-13. Time of Flight counter particle identification performance.

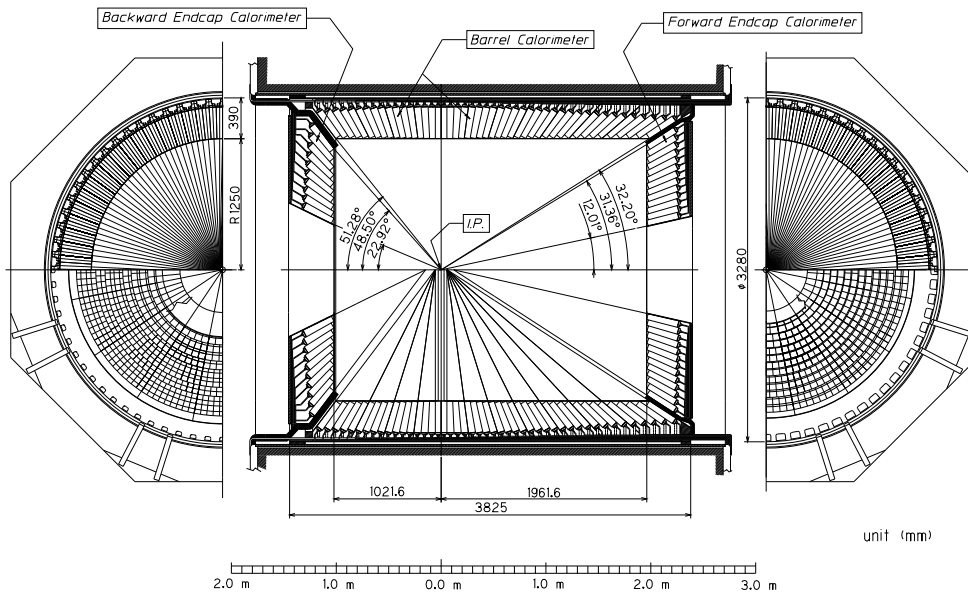


Figure 4-14. The configuration of Electromagnetic Calorimeter, with annular-shaped forward and backward endcaps.

A crystal is typically 30 cm long, equivalent to 16.2 radiation lengths (X_0) for electrons and photons, and is chosen to minimize energy resolution deterioration at high energies due to the fluctuation of shower leakage at the back of the crystal. The crystals are designed such that a photon entering a particular crystal at its center will deposit at least 80% of its energy in that crystal.

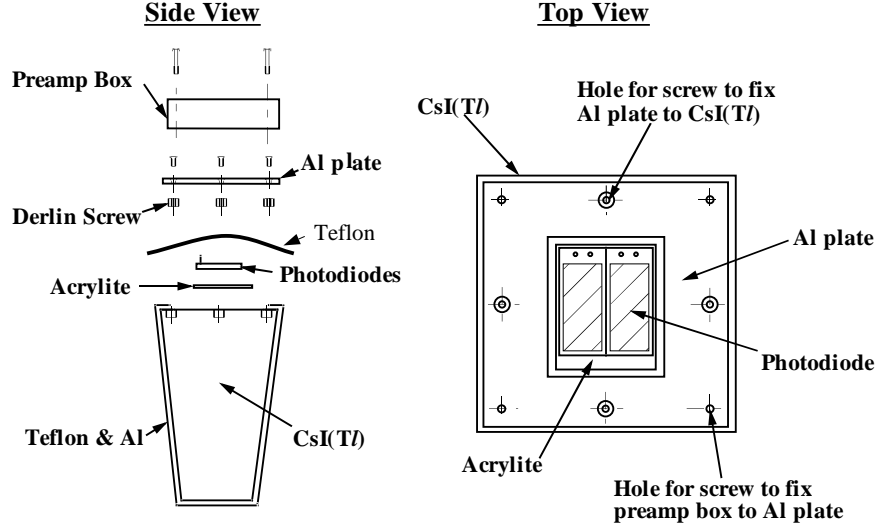


Figure 4-15. Mechanical assembly of the ECL detector.

A typical crystal in the barrel has a forward and backward face measuring $55 \text{ mm} \times 55 \text{ mm}$ and $65 \text{ mm} \times 65 \text{ mm}$ respectively. In the forward and backward endcaps the profiles vary from 44.5 mm to 70.8 mm and from 54 mm to 82 mm respectively. Each crystal possesses a tower like structure. In the barrel they are tilted at an angle of approximately 1.3° in the θ and ϕ directions to prevent particles escaping through gaps between crystals.

The crystals are wrapped in a diffuse reflector, a $200 \mu\text{m}$ thick sheet of Goretex teflon, to enable light-collection by two photodiodes at the rear side (see Fig. 4-15).

The ECL is able to measure energies in the range of $0.02 < E_\gamma < 5.40 \text{ GeV}$. It provides a measured energy resolution of

$$\left(\frac{\sigma_E}{E}\right) = \sqrt{1.34^2 + \left(\frac{0.066}{E}\right)^2 + \left(\frac{0.81}{E^{1/4}}\right)^2} \% , \quad (4.7)$$

and position resolution of

$$\sigma_{\text{pos}} = \frac{0.5 \text{ cm}}{\sqrt{E}} , \quad (4.8)$$

where E is measured in GeV.

Since pions deposit much less of their energy in the crystal, the difference of the energy deposit in the ECL can be used to distinguish charged pions from electrons, as illustrated in Figure 4-16. The plot also shows the difference between the response of negatively and positively charged pions that is a direct result of their different nuclear cross sections. The peak on the left is from minimum ionizing particles, which did interact strongly with the material of ECL. Less than 1% of pions are mis-identified as electrons for momenta above $2 \text{ GeV}/c$.

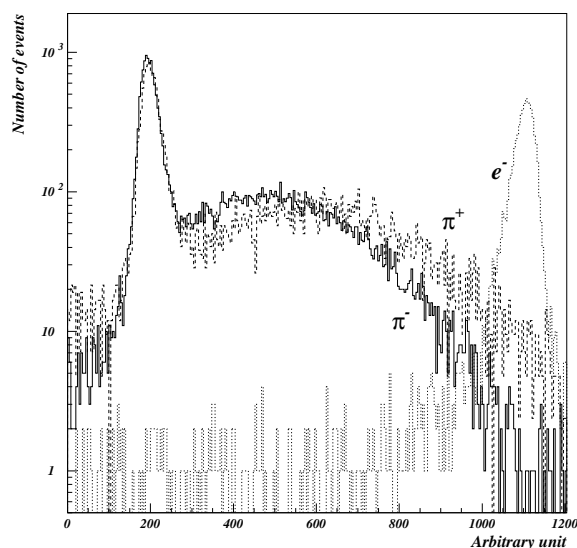


Figure 4-16. Distribution of the energy deposit by electrons (dotted line), by positive pions (dashed line) and by negative pions (solid line) at 1 GeV/c.

4.2.7 K_L/μ Detector (KLM)

The K_L and μ detector (KLM) is the outermost sub-detector system and was designed to identify K_L mesons and muons with high efficiency for momenta greater than 600 MeV/c. A K_L from the IP will typically traverse one interaction length (mean free path before an inelastic interaction) before reaching the KLM, most of which (0.8) is due to the ECL. Another 3.9 interaction lengths are provided by iron plates in the KLM, to produce a shower of ionizing particles when a K_L interacts with matter. The shower location is then measured to provide K_L flight direction, but the fluctuations in the shower size prevent any useful measurement of K_L energy.

Muons of sufficient energy (> 500 MeV) will penetrate the KLM easily, since they do not feel the strong interaction and the Bremsstrahlung radiation loss is much smaller than for the electron. A track, penetrating several layers of the KLM, is most likely a muon. Since the muons suffer smaller deflections in material, they can be distinguished from charged pions and kaons. The separation further improves for higher momenta.

The KLM consists of alternating layers of charged-particle detectors and 4.7 cm thick iron plates. The barrel region is octagonally shaped and is made of 15 detector layers and 14 iron layers. The forward and backward endcaps contain 14 detector layers each.

A detector layer is a super-layer of two glass-electrode Resistive Plate Counters (RPC), sandwiched between two orthogonal pickup strips. The RPC modules consist of two high-voltage plates, insulated by high-bulk-resistivity glass plates from a gas-filled gap, as shown in figure 4-17. An ionizing particle, traversing the gas-filled gap of the RPC, initiates a streamer in the gas that results in a local discharge of the plates. The discharge induces a signal on the external orthogonal pickup strips.

The pickup strips, typically 5 cm wide, provide $\phi - z$ and $\theta - \phi$ information in the barrel and endcap regions, respectively. The size of the strips matches the uncertainty due to the multiple scattering of particles as they travel through iron, and limits the spatial resolution to a few centimeters. The barrel and endcaps contain 240 and 122 RPC

modules. The polar angular coverage is $20^\circ < \theta < 155^\circ$. Figures 4-18(a) and 4-18(b) show barrel and endcap RPCs respectively. The KL angular resolution measured from the IP is better than 10 m rad. For momenta above 1.5 GeV/ c the muon identification efficiency is greater than 90% with a mis-identification rate of less than 5%. A more detailed description of KLM detector can be found in Ref. [46].

4.2.8 Solenoid Magnet

A super-conducting solenoid provides a magnetic field of 1.5 T in a cylindrical volume of 3.4 m in diameter and 4.4 m in length. The solenoid encases all the sub-detectors except the KLM. The external iron structure of the Belle detector serves as the return path of magnetic flux and as absorber material for the KLM. The solenoid details are shown in table 4-2. The magnetic field mapping, measured with accelerator final-focus quadrupole magnets located within the solenoid, QCS-R and QCS-L, is shown in Fig 4-19.

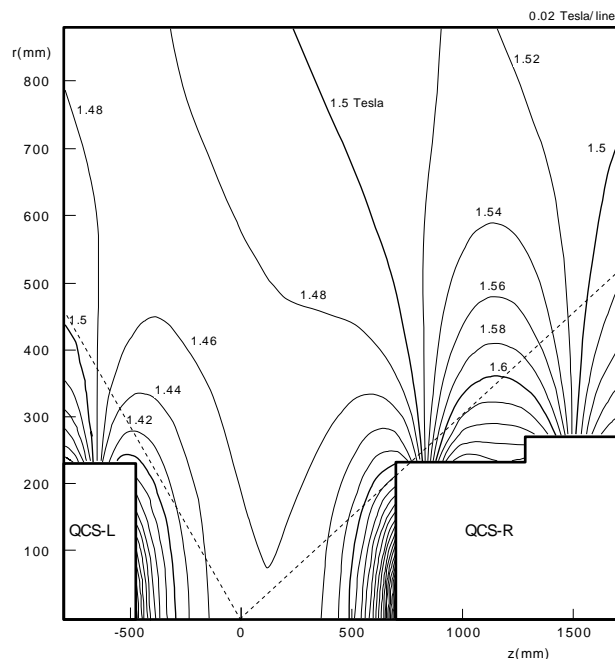


Figure 4-19. Contour plot of the measured magnetic field in the Belle detector.

4.2.9 Extreme Forward Calorimeter (EFC)

The Extreme Forward Calorimeter (EFC) offers electron and photon calorimetry at the extreme forward and backward regions, defined as $6.4^\circ < \theta < 11.5^\circ$ and $163.3^\circ < \theta < 171.2^\circ$, respectively. The EFC is placed on the cryostat front faces of the KEKB accelerator compensation solenoid magnet, which is surrounding the beam pipe.

The EFC is constructed from crystals of Bismuth Germanate (BGO), which was chosen for its ability to withstand radiation doses at the megaread level, while still providing good energy resolution. The detector is segmented into 32 azimuthal and 5 polar sections for both backward and forward cones. Each crystal is tower shaped and is aligned to point towards the IP. The arrangement is illustrated in Fig. 4-20.

	Central field	1.5 T
	Length	4.41 m
General	Weight	23 t
	Cool-down time	≤ 6 days
	Quench-recovery time	≤ 1 day
Cryostat	Inner/outer Radius	1.70/2.00 m
	Effective radius	1.8 m
	Length	3.92 m
	Superconductor	NbTi/Cu
Coil	Nominal current	4400 A
	Inductance	3.6 H
	Stored energy	35 MJ
	Typical charging time	0.5 h

Table 4-2. Main parameters of the solenoid magnet.

Since the BGO crystals are resistive to radiation, the EFC shields the CDC from beam related backgrounds and synchrotron radiation. The EFC is also used as a beam monitor and luminosity meter for KEKB accelerator control.

4.3 Trigger and Data Acquisition System

In the environment of a beam-crossing rate of 509 MHz, much more processes occur than we are able to store in our data acquisition system. Many of the processes are due to the interactions of beams with the residual gas or beam pipe material and not of interest for the B physics measurements, so a complex triggering system has to be adopted to focus on the events of interest. Physics of interest includes hadron production, Bhabha scattering, μ -pair and τ -pair production and two-photon events. Two-photon and Bhabha scattering events are needed for detector calibration and luminosity measurements, but they need to be reduced about hundred times due to the copious amounts in which they are produced.

At an instantaneous luminosity of $10^{34} \text{cm}^{-2}/\text{s}^{-1}$, the rate for physics events of interest is around 100 Hz, and the typical trigger operating output rate is 350 Hz. The Belle data acquisition system can handle rates as high as 500 Hz. Since the beam-related backgrounds depend on accelerator operating conditions, their level cannot be determined accurately and the trigger has to be robust enough to handle large variations in background rates.

Triggering is done using information from each of the sub-detectors, which is processed in parallel and fed to Global Decision Logic (GDL). The trigger is arranged into four levels, denoted as level 0, 1, 3 and 4 respectively.

The level 0 trigger (L0) is a prompt timing signal from the TOF which forces the SVD into the HOLD state.

The level 1 trigger (L1) is implemented in hardware. It is made up of sub-detector triggers which feed the GDL. The GDL sources information from all sub-detectors bar the SVD. All triggers, processed in parallel, are used by the GDL to characterize the event type. The CDC provides $r - \phi$ and $r - z$ track trigger signals. The TOF trigger system provides an event timing signal and delivers information on the hit multiplicity and topology. The ECL provides two triggers based on total energy deposition and cluster multiplicity, each sensitive to different types of hadronic events. The KLM provides a high efficiency trigger for muon tracks. When available, the trigger timing is provided by the TOF, otherwise the ECL is used. The Level 1 trigger configuration is depicted in

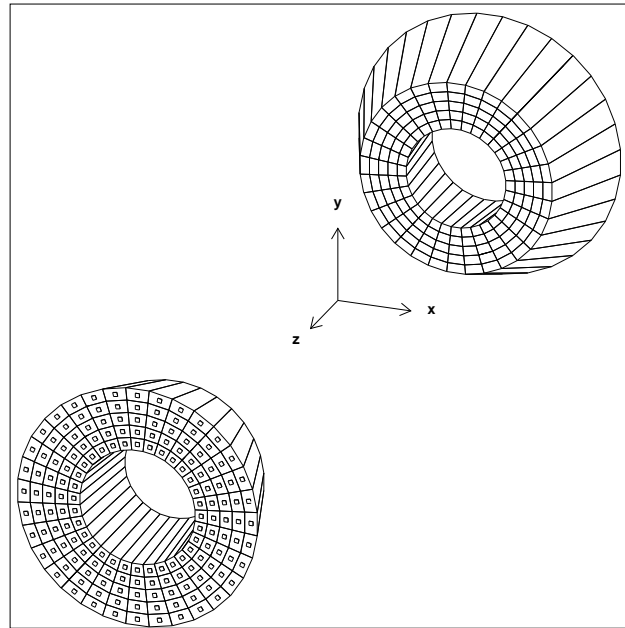


Figure 4-20. An isometric view of the BGO crystals of the forward and backward EFC detectors.

Fig. 4-21. To keep hadronic events, the GDL typically relies on three main trigger classes; multi-tracks from CDC, total energy deposition and isolated cluster counts. Each provides more than 96% efficiency for hadronic events individually, combined the total efficiency is 99.5%.

The level 3 trigger (L3) is implemented in software in an online computer farm. Using an ultra-fast track finder it requires at least one track with an impact parameter in z less than 5.0 cm and the total energy deposit in the ECL to be greater than 3.0 GeV. The trigger reduces the event rate by 50 ~ 60% while retaining 99% of events of interest.

The level 4 trigger (L4) is implemented in software and performed offline on a computer farm before full event reconstruction. Its purpose is to reduce the amount of data that goes in the full event reconstruction, and its algorithms are optimized for speed. The conditions that activate the trigger, are:

- Events, tagged by the hardware L1 trigger preselection to be events used for luminosity measurement, detector calibration or beam-background studies, are accepted.
- A total ECL energy deposit of less than $4 \text{ GeV}/c^2$ by fast cluster-finder routine. To reduce background from cosmic rays, this is vetoed by events with coincident KLM and ECL hits as encoded in L1 trigger information.
- At least one track with r and $|z|$ distances to IP of less than 1.0 cm and 4.0 cm, respectively, and $p_T > 300 \text{ MeV}/c$.
- For monitoring purposes, 1% of non-triggered events are kept.

The criteria retain hadronic events with an efficiency of 99.8% while reducing the total event trigger rate by around 73%.

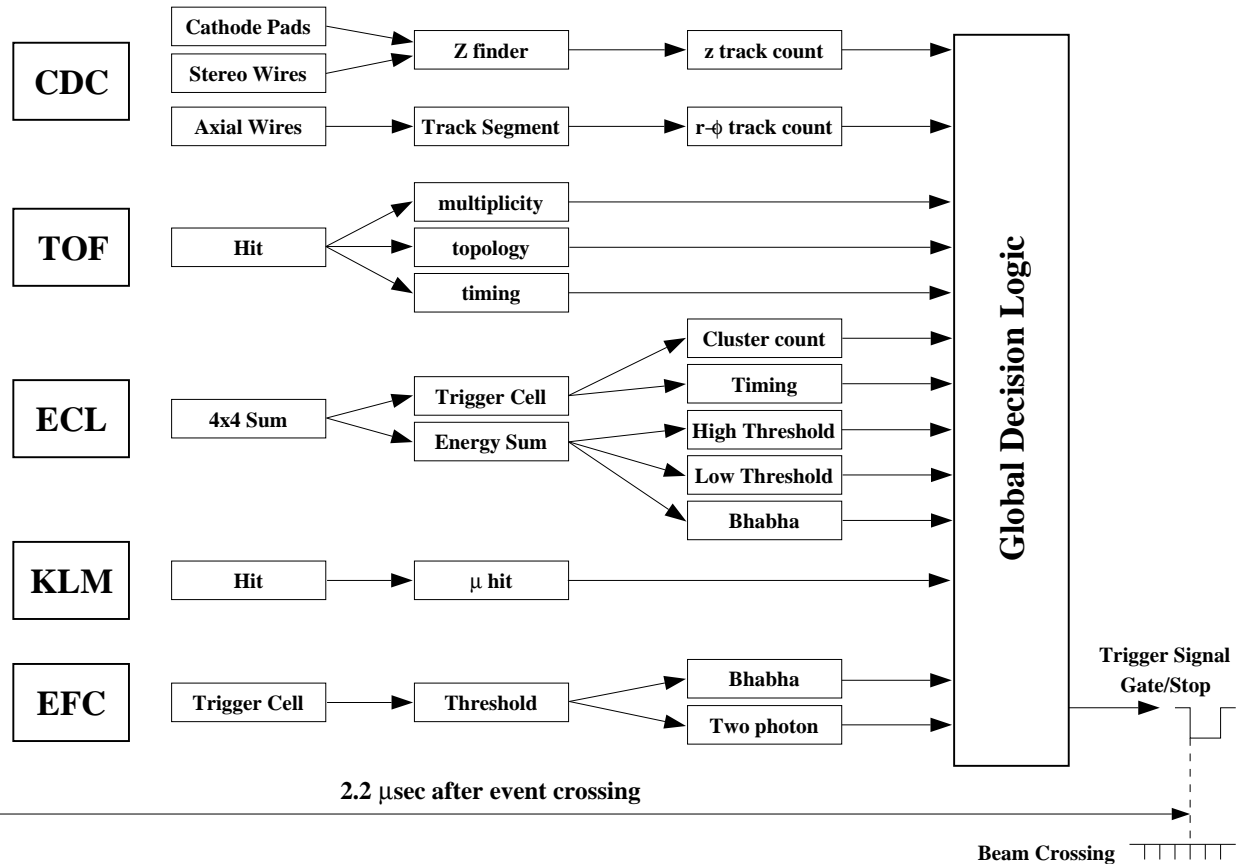


Figure 4-21. The Level-1 trigger system.

4.3.0.1 Data Acquisition System

The Data Acquisition (DAQ) system manages and stores the data collected at the Belle detector. It is able to process data at the trigger rate of 500 Hz, while having a dead-time of less than 10%. The system is shown in figure 4-22. The data from each sub-detector processed in seven parallel sub-systems, and transformed into full event records by the Event Builder. Full event records are sent to the online farm, where the data is filtered through the L3 software trigger and transformed into the offline event format, suitable for offline analysis. A single event occupies approximately 30 kBytes of disk space, which translates into a data flow of 15MBytes/s. The data is sent to the tape library at the computer center 2 km away, where it is written to a tape by a high-speed tape drive. Data monitoring system analyzes a rate of approximately 20 Hz of events and can be plugged into the data stream without affecting it.

The offline computer farm filters the data, written to the tapes, through the L4 trigger, where a fast event reconstruction is performed to reject uninteresting data. Afterwards, a full reconstruction of the event is performed and the data is translated into a Data Summary Tape (DST) format. A DST is made up of higher level data structures with physical quantities of the decay, for example four-vectors of particle momenta.

Further analysis filters events into hadronic, Bhabha, τ -pair, μ -pair and two-photon event skims. The skims are saved into mini data summary tape (MDST) files. The MDST is a subset of the DST, containing the data needed for physics analyses.

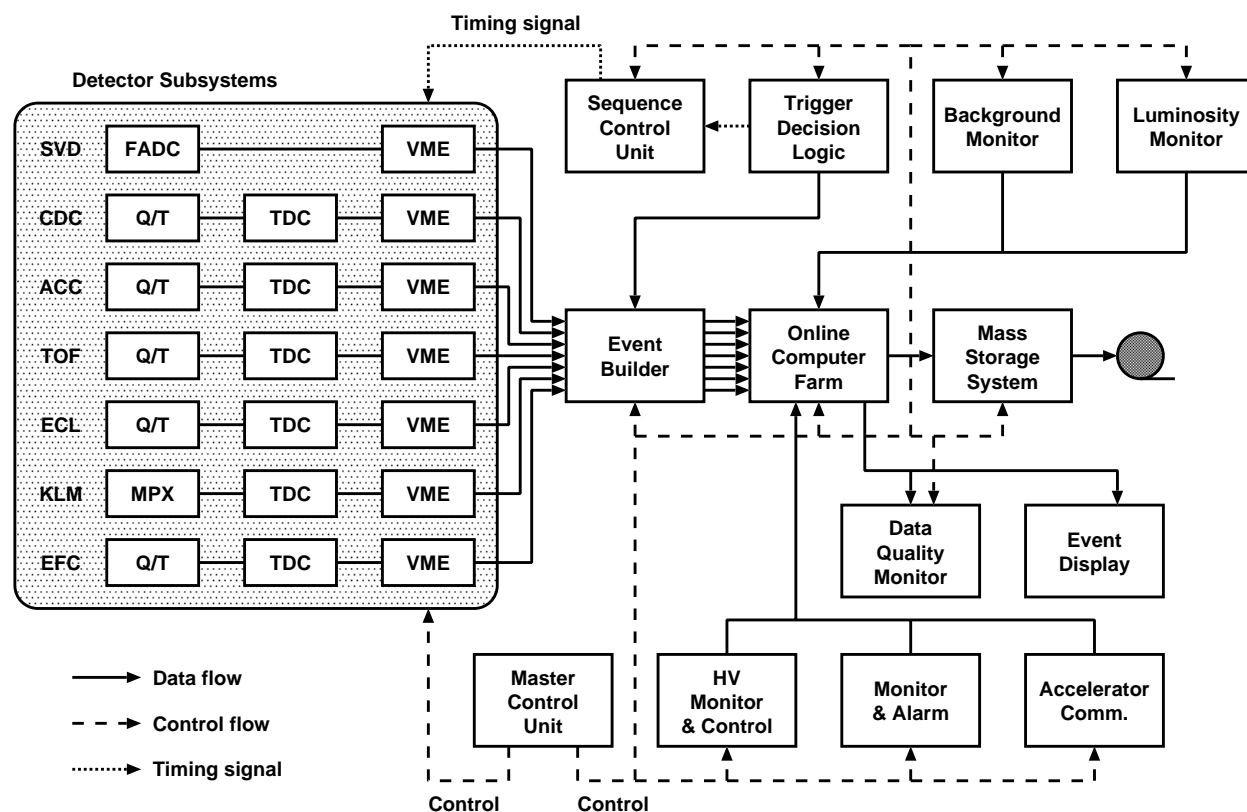


Figure 4-22. The Belle DAQ system.

4.4 Monte Carlo Simulation

Analysis of data requires a detailed understanding of detector effects, possible background components of the analysis and the interpretation of results. A large sample of Monte Carlo (MC) simulation is used, usually corresponding to several times the amount of data collected, in which the theoretical understanding of physical processes in observed decays and our knowledge of detector effects is incorporated. Two levels of simulation are present, one focused on the physics of decays and the other on simulation of the interaction of particles with the detector.

4.4.1 Event generators

Event generators focus on the description of physical processes occurring at the decay of particles produced in the e^+e^- decays. The description includes decay chains of all the particles and the kinematical properties of their decays, such as position four-vectors of all decay vertices and momentum four-vectors of all decaying particles.

Two event generators have been used in the simulation of the current analysis, QQ98 [47] and EVTGEN [48]. Both generators are dedicated for modeling the B meson decays. Hadronic continuum events, namely $e^+e^- \rightarrow q\bar{q}$ interactions where $q = (u, d, s, c)$ is the quark flavor, are generated using JETSET [49, 50] which is based on the LUND string fragmentation model [51].

QQ98 uses a decay table in which decay modes, their decay models, branching fractions, lifetimes, and decay parameters are given by the user. The decay table information is usually composed from world averages. The `EVTGEN` event generator is also used in Belle analyses, and has the advantage in that it uses decay amplitudes instead of probabilities, and can simulate the entire decay tree from the amplitudes of each branch. Both are phenomenological in nature and rely on a detailed description of decays of interest.

4.4.2 Simulation of detector response

After the decay chains are generated, they are passed to modules that propagate each particle through the detector. The detector geometry is described using `GEANT` [52] which simulates the passage of elementary particles through the matter. A set of detector simulation modules based on `GEANT` is grouped in `GSIM`. Detector parameters are continually updated with current experimental conditions and information from real data studies.

4.5 Particle reconstruction

4.5.1 Reconstruction of Charged Particle Tracks

Charged particles crossing the detector leave tracks in the tracking detectors, CDC and SVD (for the description see 4.2.3 and 4.2.2). The event timing by TOF and Level4 Trigger is used to discriminate between hits produced by tracks from beam background and tracks of interest. The tracks are first searched for using hit information obtained from CDC, where axial wire hits provide $r - \phi$ coordinates, while stereo wire hits measure the z coordinate. Since the degree of non-uniformity of the magnetic field is small, the hits of these reconstructed tracks are fitted with a helix with the following parameters: κ , the reciprocal to the transverse momentum), the slope of the track, and three pivot point coordinates (the point of closest approach to the detector origin). The helix model also neglects energy loss due to ionization and multiple scattering.

Then, the hits in SVD are matched to the fitted tracks and the final tracks are fitted through a non-homogeneous magnetic field using Kalman filter algorithm, where energy loss due to ionization and multiple scattering is accounted for. Finally, to enable muon identification, tracks are extrapolated all the way to the KLM by solving equations of motion with a Runge-Kutta method. Corrections are applied to the momentum obtained from helix parameters to compensate for the stronger non-uniform magnetic field effects in the extreme forward and background regions. The corrections are calculated from observed shifts of invariant mass peak positions of known particles [53].

The tracking provides both track parameters and their error matrices that are needed for reliable fitting of kinematical constraints.

4.5.2 Reconstruction of Photon Clusters

The ECL is constructed in such a way that a large part of the energy of an electro-magnetic shower produced by a photon is deposited in the ECL. The crystal with the largest energy deposit is taken as a seed of a cluster of hits and the energies of 3×3 and 5×5 counters around the seed are summed up to form the cluster energy. The position of the cluster is obtained by calculating the "center of gravity" of energy, and the momentum vector of each photon is calculated from the position and the energy of the cluster. If clusters from different photons overlap, the overlapping region is unfolded by comparing the ratio of non-overlapping energy depositions of the two clusters. The ECL is calibrated to obtain the global correction factors and the correction factors of each crystal.

4.5.3 Charged Particle Identification

Present analysis depends strongly on an efficient particle identification. Prompt charged leptons, electrons and muons, are used to recognize semileptonic decays, while a presence of a kaon in the decay signals the background $b \rightarrow c$ transition. For the former the leptons have to be successfully separated from hadrons, while for the latter kaon/pion separation is crucial. The particle identification is done based on the information from several detector sub-parts: CDC, ACC, TOF, EFC and KLM.

4.5.3.1 Muon Identification

Muons are heavy charged leptons that lose their energy mainly by multiple scattering in the detector material. Already with momenta greater than 500 MeV/c they can easily penetrate to the outermost part of the detector, the KLM. To identify a track produced by a muon, the reconstructed track is extrapolated to KLM and associated hits are searched for within 25 cm of the extrapolated track. Two quantities are used to test the hypothesis that a track is a muon: the difference between the measured and expected range of the track (ΔR), and the normalized transverse deviations of all hits associated with the track (χ_r^2). The probability for a hypothesis is constructed by multiplying the separate probabilities (assuming a weak correlation between the two quantities): $p(\Delta R, \chi_r^2) = p_1(\Delta R) \cdot p_2(\chi_r^2)$. Muon candidates are selected based on the value of the normalized ratio

$$\text{Prob}(\mu) = \frac{p_\mu}{p_\mu + p_\pi + p_K}.$$

The efficiency for muon selection and the pion fake rate for two different $\text{Prob}(\mu)$ selections are shown in Fig. 4-23.

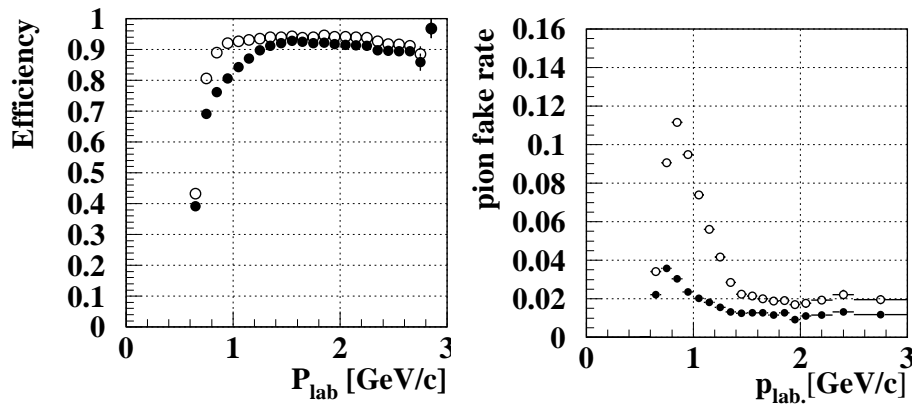


Figure 4-23. The efficiency for muon selection (left) and the pion fake rate (right) in the barrel as a function of the lab momentum, measured in $e^+e^- \rightarrow e^+e^-, \mu^+\mu^-$. Open circles for $\text{Prob}(\mu) > 0.1$, closed circles for $\text{Prob}(\mu) > 0.9$. From Ref. [54].

4.5.3.2 Electron Identification

Electrons produce a narrow shower in ECL in which they lose nearly all their energy. The energy deposition and the difference in the velocity at a given measured momentum, obtained from CDC and ACC, are used in the electron identification. Information from TOF is not included, since the timing resolution does not permit separation of electrons from pions.

Five discriminating variables are used in electron identification:

Track to Cluster Matching: the electron tracks are required to match the position of an ECL cluster. The matching is assessed by a χ^2 -like variable based on the separation of the extrapolated track and the center of the ECL cluster.

E/p: the ratio of deposited energy in ECL to the momentum measured by the CDC. Since electrons leave a large part of their energy in the calorimeter, and their mass is negligible compared to the energy, $E \approx p$ and $E/p \approx 1$ (see Fig. 4-24(a)). Hadrons leave only a fraction of their energies in ECL and have the ratio below 1 – as well as a small part of electrons that have lost some energy in the material before reaching the ECL.

E9/E25: since the shape of the electron energy deposit is narrow, the transverse shower shape is compared by observing the ratio of deposited energy in 3×3 (E_9) and 5×5 (E_{25}) crystals. The ratio is close to one (≈ 0.95) for electrons, while it differs from one for hadrons, since their passage instigates more than one shower (see Fig. 4-24(b)).

dE/dx: the energy loss due to ionization along a charged track's trajectory is measured by CDC. The energy loss is dependent on particle's velocity β , which provides excellent separation between electrons and pions for momenta greater than $0.5 \text{ GeV}/c$, as shown in Fig. 4-24(c).

ACC light yield $\langle N_{pe} \rangle$: the presence or absence of photoelectrons from Čerenkov effect in ACC can reveal the identity of the passing particle, since the threshold for emitting photons is different for different particles, and is a few MeV for electrons and in the momentum range of $0.5 - 1 \text{ GeV}/c$ for pions. The separation of electrons and pions is thus possible only in the range below $1 \text{ GeV}/c$.

The likelihood for electron and pion hypothesis is constructed by combining the probability density functions from the five variables. The overall likelihood used for identification of an electron is defined as the sum of products of likelihoods from a single variable:

$$\text{Prob}(e) = \frac{\prod_{i=1}^5 \mathcal{L}_i^e}{\prod_{i=1}^5 \mathcal{L}_i^e + \prod_{i=1}^5 \mathcal{L}_i^\pi}. \quad (4.9)$$

The distribution of the overall normalized likelihood can be seen on Fig. 4-24(d). The efficiency for electron selection and the pion fake rate as a function of the lab momentum, measured in radiative Bhabha events, is shown in Fig. 4-25.

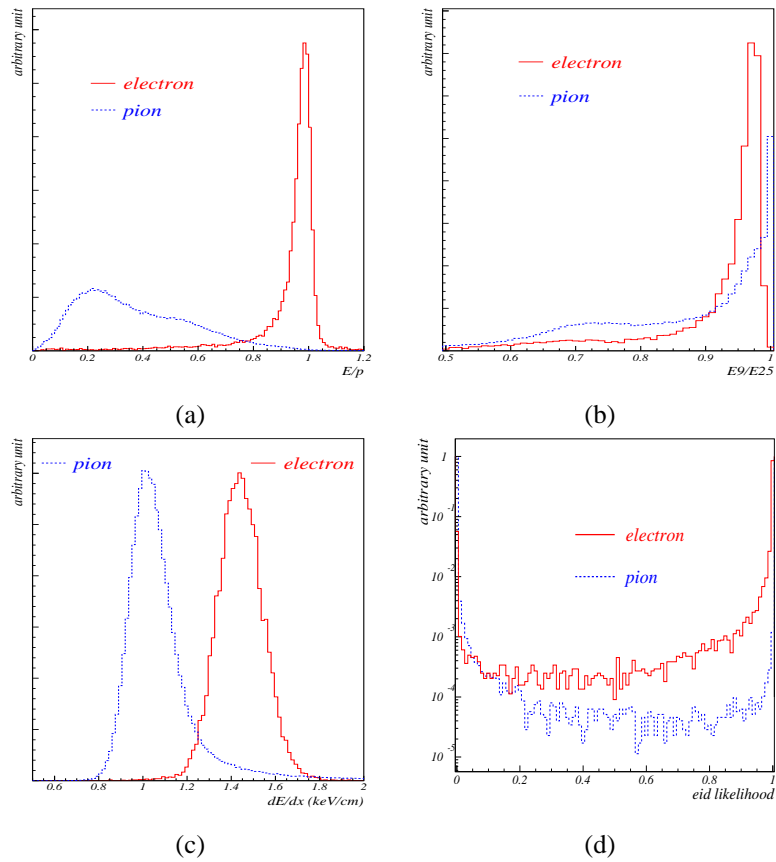


Figure 4-24. (a) Ratio of energy deposition to track momentum, E/p , (b) Transverse energy shape, E_9/E_{25} , and (c) Rate of ionization energy loss, $\frac{dE}{dx}$, for electrons (solid line) and pions (broken line). (d) The electron likelihood, $\text{Prob}(e)$, for electrons (solid line) and pions (broken line). From Ref. [55].

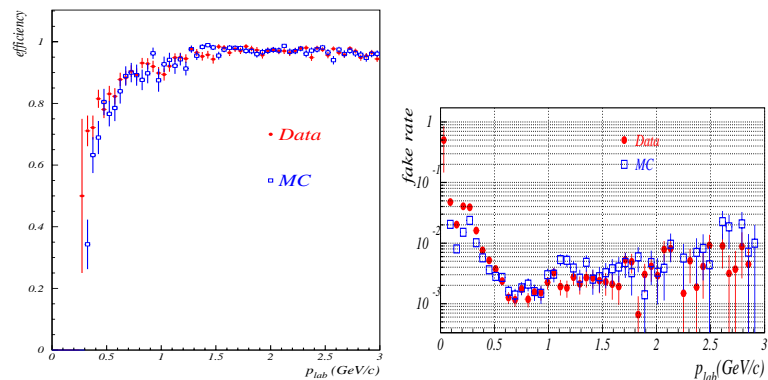


Figure 4-25. The efficiency for electron selection (left) and the pion fake rate (right) as a function of the lab momentum, measured in radiative Bhabha events. From Ref. [55].

4.5.3.3 Identification of Charged Hadrons: K/π Separation

The identification of charged hadrons, mainly kaons and pions, is performed using the combined information on specific ionization dE/dx (CDC), the time-of-flight measurement (TOF) and the measurement of the number of photoelectrons in ACC, to cover the typical momenta of hadrons (see Fig. 4-26). The refractive indices of aerogel Čerenkov

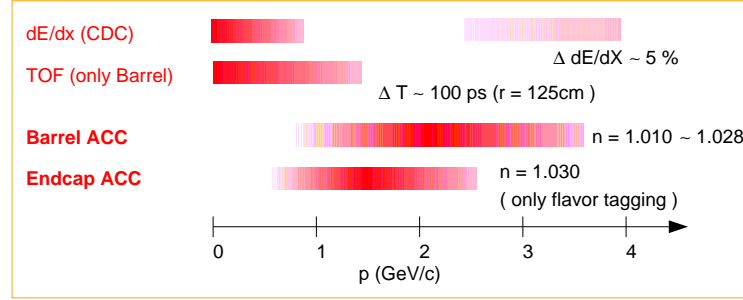


Figure 4-26. Momentum coverage of kaon/pion separation at Belle

radiators in ACC are optimized for successful separation for high momentum hadrons ($1.2 < p < 3.5 \text{ GeV}/c$), and the likelihood for different particle hypotheses is calculated from the obtained light yield.

The TOF is used to measure particle velocities from the time used for a particle to fly over a certain distance, and is useful for separation of kaons and pions with low momentum, below $1.2 \text{ GeV}/c$. The likelihood is calculated from the difference between the expected time of flight for a hypothesis and the measured time:

$$\mathcal{L}_{TOF} = \frac{e^{-\frac{1}{2}\chi_{TOF}^2}}{\sqrt{2\pi}\sigma_{TOF}}, \quad \chi_{TOF}^2 = \left[\frac{t_{meas} - t_{hyp}}{\sigma_{TOF}} \right]^2. \quad (4.10)$$

Similarly, the likelihood obtained from the measurement of ionization loss is obtained as:

$$\mathcal{L}_{dE/dx} = \frac{e^{-\frac{1}{2}\chi_{dE/dx}^2}}{\sqrt{2\pi}\sigma_{dE/dx}}, \quad \chi_{dE/dx}^2 = \left[\frac{(dE/dx)_{meas} - (dE/dx)_{hyp}}{\sigma_{dE/dx}} \right]^2. \quad (4.11)$$

The total likelihood of a hypothesis is obtained as the product of single likelihoods:

$$\mathcal{L}(hyp) = \mathcal{L}_{ACC}(hyp) \times \mathcal{L}_{TOF}(hyp) \times \mathcal{L}_{dE/dx}(hyp). \quad (4.12)$$

The separation of charged hadrons is achieved by calculating the probability $\text{Prob}(\text{signal}/\text{background})$ of the signal particle hypothesis, when separating it from the background particle. The probability is calculated from the likelihoods of signal and background hypotheses:

$$\text{Prob}(\text{signal}/\text{background}) = \frac{\mathcal{L}(\text{signal})}{\mathcal{L}(\text{signal}) + \mathcal{L}(\text{background})}. \quad (4.13)$$

The signal and the background particle can be any of the following: e , p , K , π . The kaon selection efficiency and the pion fake rate for $\text{Prob}(K/\pi) > 0.6$ is shown in Fig. 4-11.

Full Reconstruction of B Meson Decays

The construction of inclusive kinematical variables from semileptonic B meson decays is possible only if we are able to separate out the decay products of one of the two B mesons. The semileptonic decay includes an undetected neutrino and therefore cannot be easily reconstructed, since the neutrino momentum is missing and can be mimicked by other undetected particles. The B mesons are produced in pairs at the $\Upsilon(4S)$, so one can reconstruct the decay chain of the associated B meson when it is decaying into hadronic final states, remove its decay products and search for a semileptonic decay in the rest of the event. This is only possible since in the case of decays of $\Upsilon(4S)$ to B mesons only a B meson pair is produced with no additional particles. Since the full reconstruction of its decay is tagging the other B meson, the reconstructed B meson is called B_{tag} . We expect to obtain the signal $b \rightarrow u$ semileptonic decays from the remaining B meson, hence we denote it by B_{sig} .

This analysis is performed on a sample where a set of approximately 180 hadronic decay channels was searched for in the collisions of e^+e^- . Due to small branching fractions of single hadronic decay channels, lost and mis-reconstructed particles, and detector resolution, the efficiency for reconstructing a decay is small, 0.30% for charged and 0.19% for neutral B mesons. Although a sample with very good separation of particles is obtained, the small efficiency of reconstruction limits the accuracy of the $|V_{ub}|$ measurement due to the fact that the $b \rightarrow u$ semileptonic transitions are relatively rare.

5.1 Meson reconstruction

Unstable mesons are reconstructed by combining the momenta of their decay products. Since there are about 10 detected particles per event, many combinations are possible, and the combinations of particles that do not correspond to the same mother particle constitute the so-called combinatorial background of the reconstruction. The plausibility that a certain combination of particles is coming from the same mother particle is estimated using variables that depend on the quality of reconstruction, the most common being the invariant mass of the combination: $M \equiv \sqrt{(\sum_i P_i)^2/c^2}$, which should correspond to the mass of the mother particle. Other variables are also used for some decays, making use of specific properties of the decay in question.

Particles that are used in the reconstruction or being reconstructed are: π^+ , π^0 , K^+ , K_S , ρ^+ , ρ^0 , a_1^+ , D^- , D^0 , D_S^- , D^{*-} , D_S^{*-} , D^{*0} , B^0 and B^+ (throughout the text the charge conjugated modes and particles are implied, unless otherwise specified).

5.1.1 Reconstruction of light mesons

From primary charged particles and photons we reconstruct three types of light neutral particles, π^0 , K_S^0 , ρ^0 , and two types of light charged particles, ρ^\pm and a_1^\pm . A π^0 candidate is combined from pairs of photons where the invariant mass of the pair lies between $117 - 150 \text{ MeV}/c^2$ and photon energy absorbed in ECL of each photon is larger than 50 MeV to reduce background from photons coming from other processes.

The ρ^0 meson is reconstructed from a pair of oppositely charged pions with the invariant mass within ± 225 MeV from the nominal mass of the ρ^0 ($775.8 \text{ MeV}/c^2$), and ρ^\pm from a charged pion and an additional π^0 , with the same invariant mass constraint imposed as in the case of a ρ^0 .

Combining a ρ^0 with another charged pion yields an a_1^\pm meson candidate, if the invariant mass of the $\rho^0 - \pi$ pair is within $0.7 < M_{\rho^0-\pi} < 1.6 \text{ GeV}/c^2$.

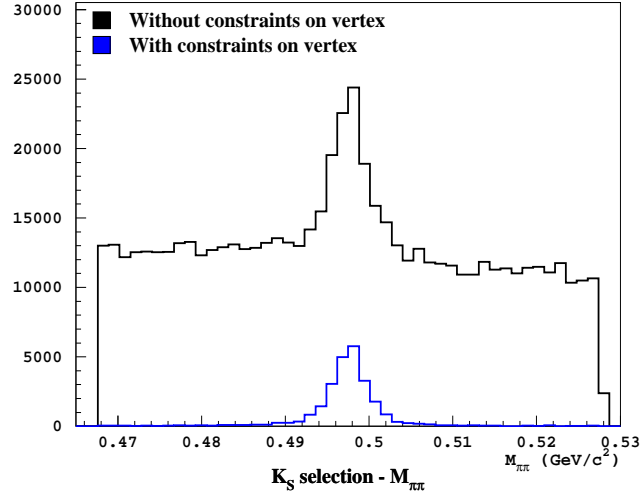


Figure 5-1. The invariant mass of the pion pair in the K_S selection, with and without the selection criteria described in Table 5-1.

5.1.1.1 Reconstruction of K_S mesons

The K_S meson is reconstructed from two oppositely charged pions with the invariant mass of the pair within $\pm 30 \text{ MeV}/c^2$ from the nominal mass of K_S ($497.65 \text{ MeV}/c^2$). Since the average lifetime of $\tau_{K_S} \approx 0.9 \times 10^{-10} \text{ s}$ is enough for the particle to fly a detectable distance from the IP, additional selection criteria were developed to improve the purity of reconstructed K_S mesons [56]. The selection makes use of the following quantities:

Δr : The smallest distance of approach in the $x - y$ plane to the IP by any of the two charged pions.

$\Delta\phi$: The angle between the K_S momentum and its decay-vertex vector.

d_z : The distance in the z direction between the two pions at the point of closest approach.

l_{flight} : The flight length of the candidate K_S in the $x - y$ plane.

$p_{K_S} (\text{GeV}/c)$	$\Delta r (\text{cm})$	$\Delta\phi (\text{rad})$	$d_z (\text{cm})$	$l_{\text{flight}} (\text{cm})$
< 0.5	> 0.05	< 0.3	< 0.8	—
$0.5 - 1.5$	> 0.03	< 0.1	< 1.8	> 0.08
> 1.5	> 0.02	< 0.03	< 2.4	> 0.22

Table 5-1. K_S selection criteria based on the decay vertex information of the candidate K_S .

The selection criteria make sure that the K_S candidate has flown a significant distance from the IP before decaying, that the decay-particle momenta are consistent with the direction of flight of the candidate K_S and that they intersect closely enough. The criteria are summarized in Table 5-1.

The improvement of the purity of the K_S candidate selection is significant, as seen in Fig. 5-1.

5.1.2 Reconstruction of D mesons

The decay modes used for reconstruction of D mesons are summarized in Table 5-2 [57]. The exclusive reconstruction of D decays has to cope with a very large set of hadronic decays with small branching fractions. The selection criteria were optimized separately for events with only charged particles and for those with some neutral particles, resulting in a different tolerance for deviations of reconstructed mass from the expected parent mass. For example in the case of a $\overline{D}^0 \rightarrow K_S \pi^0$, where two pions are reconstructed in a candidate K_S and two photons in a candidate π^0 , the selection window need to be $60 \text{ MeV}/c^2$, which is twice as wide as in for example very clean $\overline{D}^0 \rightarrow K^+ \pi^-$ decays.

channel	Branching fraction(%)	parent mass	selection window
$\overline{D}^0 \rightarrow K^+ \pi^-$	3.80 ± 0.09	$1864.5 \text{ MeV}/c^2$	$\pm 30 \text{ MeV}/c^2$
$\overline{D}^0 \rightarrow K^+ \pi^- \pi^-$	7.46 ± 0.31	$1864.5 \text{ MeV}/c^2$	$\pm 30 \text{ MeV}/c^2$
$\overline{D}^0 \rightarrow K_S \pi^+ \pi^-$	2.05 ± 0.12	$1864.5 \text{ MeV}/c^2$	$\pm 30 \text{ MeV}/c^2$
$\overline{D}^0 \rightarrow K^+ K^-$	$0.39^{+0.12}_{-0.15}$	$1864.5 \text{ MeV}/c^2$	$\pm 30 \text{ MeV}/c^2$
$\overline{D}^0 \rightarrow K^+ \pi^- \pi^0$	13.0 ± 0.8	$1864.5 \text{ MeV}/c^2$	$\pm 45 \text{ MeV}/c^2$
$\overline{D}^0 \rightarrow K_S \pi^+ \pi^- \pi^0$	3.75 ± 0.44	$1864.5 \text{ MeV}/c^2$	$\pm 45 \text{ MeV}/c^2$
$\overline{D}^0 \rightarrow K_S \pi^0$	0.792 ± 0.075	$1864.5 \text{ MeV}/c^2$	$\pm 60 \text{ MeV}/c^2$
$D^0 \rightarrow \text{recon.}$	31.2 ± 1.0		
$D^- \rightarrow K^+ \pi^+ \pi^-$	9.2 ± 0.6	$1869.4 \text{ MeV}/c^2$	$\pm 30 \text{ MeV}/c^2$
$D^- \rightarrow K_S \pi^-$	0.972 ± 0.065	$1869.4 \text{ MeV}/c^2$	$\pm 30 \text{ MeV}/c^2$
$D^- \rightarrow K_S \pi^- \pi^+ \pi^-$	2.44 ± 0.34	$1869.4 \text{ MeV}/c^2$	$\pm 30 \text{ MeV}/c^2$
$D^- \rightarrow K^+ K^- \pi^-$	0.89 ± 0.08	$1869.4 \text{ MeV}/c^2$	$\pm 30 \text{ MeV}/c^2$
$D^- \rightarrow K^+ \pi^- \pi^- \pi^0$	6.5 ± 1.1	$1869.4 \text{ MeV}/c^2$	$\pm 45 \text{ MeV}/c^2$
$D^- \rightarrow K_S \pi^+ \pi^0$	3.3 ± 1.0	$1869.4 \text{ MeV}/c^2$	$\pm 45 \text{ MeV}/c^2$
$D^- \rightarrow \text{recon.}$	23.3 ± 1.6		
$D_s^- \rightarrow K^- K^+ \pi^-$	4.3 ± 1.2	$1969.0 \text{ MeV}/c^2$	$\pm 30 \text{ MeV}/c^2$
$D_s^- \rightarrow K^- K_S$	1.24 ± 0.37	$1969.0 \text{ MeV}/c^2$	$\pm 30 \text{ MeV}/c^2$
$D_s^- \rightarrow \text{recon.}$	5.5 ± 1.3		

Table 5-2. Summary of decay modes used in reconstruction of D and D_s mesons, with their branching fractions [10] and reconstructed parent mass tolerance in the selection.

The D_s decay mode with two kaons $D_s^- \rightarrow K^- K^+ \pi^-$ proceeds in about half of the cases over the ϕ resonance $D_s^- \rightarrow \phi (\rightarrow K^- K^+) \pi^-$ ($\mathcal{B}(D_s^- \rightarrow K^- K^+ \pi^-) = (4.3 \pm 1.2)\%$, $\mathcal{B}(D_s^- \rightarrow \phi (\rightarrow K^- K^+) \pi^-) = (1.8 \pm 0.4)\%$). To improve the purity of reconstructed D_s mesons, in some modes we reject candidates for which the mass of kaon pair is more than $20 \text{ MeV}/c^2$ away from the nominal mass of ϕ ($1019.5 \text{ MeV}/c^2$). This is in case the other candidate charmed meson in the $B \rightarrow DD_s$ decay (see Table 5-4) is not reconstructed in $\overline{D}^0 \rightarrow K^+ \pi^-$, $D^- \rightarrow K^+ \pi^+ \pi^-$ or $D_s^- \rightarrow K^- K_S$, since the combinatorial background would be otherwise too high.

D^* mesons are combined from a reconstructed D or D_s meson and a low momentum pion or a photon. The variable estimating the quality of reconstruction is the mass difference between the D^* and D or D_s^* and D_s mesons: $\Delta m = m_{D\pi/\gamma} - m_D$. The reconstructed modes with selection criteria are summarized in Table 5-3.

channel	Branching fraction(%)	$\Delta m \equiv m_{D_{(s)}^*} - m_{D_{(s)}}$	selection window
$\overline{D}^{*0} \rightarrow \overline{D}^0 \pi^0$	61.9 ± 2.9	$142.12 \text{ MeV}/c^2$	$\pm 5 \text{ MeV}/c^2$
$\overline{D}^{*0} \rightarrow \overline{D}^0 \gamma$	38.1 ± 2.9	$142.12 \text{ MeV}/c^2$	$\pm 20 \text{ MeV}/c^2$
$D^{*-} \rightarrow \overline{D}^0 \pi^-$	67.7 ± 0.5	$140.64 \text{ MeV}/c^2$	$\pm 5 \text{ MeV}/c^2$
$D^{*-} \rightarrow \overline{D}^- \pi^0$	30.7 ± 0.5	$140.64 \text{ MeV}/c^2$	$\pm 5 \text{ MeV}/c^2$
$D_s^{*-} \rightarrow D_s^- \gamma$	94.2 ± 2.5	$143.9 \text{ MeV}/c^2$	$\pm 20 \text{ MeV}/c^2$

Table 5-3. Summary of decay modes used in reconstruction of D^* and D_s^* mesons, with their branching fractions [10] and the tolerance in the selection for the deviations in the difference between masses of D^* (D_s^*) and D (D_s) mesons.

5.1.3 Reconstruction of B mesons

Finally, a B meson candidate is reconstructed from the $D^{(*)}$ meson and another charged particle in one of the following two-body decay modes [57]:

$$\begin{aligned}
 & - B^0 \rightarrow D^{(*)-} \left(\pi^+ / \rho^+ / a_1^+ / D_s^{(*)+} \right) \\
 & - B^+ \rightarrow \overline{D}^{(*)0} \left(\pi^+ / \rho^+ / a_1^+ / D_s^{(*)+} \right)
 \end{aligned}$$

To increase the purity of the sample, the possible combinations were reduced in the case of a_1 , which by itself is constituted of three pions (and by the ϕ mass constraint for D_s as described in Sec. 5.1.2):

- For $B^+ \rightarrow \overline{D}^{(*)0} a_1^+$, only the mode $\overline{D}^0 \rightarrow K^+ \pi^-$ is used.
- For $B^+ \rightarrow \overline{D}^{*0} (\rightarrow \overline{D}^0 \pi^0) a_1^+$, the mode $\overline{D}^0 \rightarrow K_S \pi^- \pi^+ \pi^0$ is **not** used.
- For $B^0 \rightarrow D^- a_1^+$, only modes $D^- \rightarrow K^+ \pi^- \pi^-$ and $K_S \pi^-$ are used.

It is important to mention that the sum of branching fractions of decay modes for charged B mesons is higher than that for the neutral B mesons, and the difference is increased further since the sum of reconstructed charmed meson modes is higher for neutral charmed mesons than for charged ones.

The combinatorial background from jet-like $e^+e^- \rightarrow q\bar{q}$ processes is suppressed by an event topology requirement based on the normalized second Fox-Wolfram moment $R_2 < 0.5$ [58], and for some modes also by $|\cos \theta_{\text{thrust}}^*| < 0.8$, where θ_{thrust}^* is the angle between the thrust axis of the reconstructed B meson candidate and that of the rest of the event.

B^+ decay modes	Branching fraction (%)	B^0 decay modes	Branching fraction (%)
$B^+ \rightarrow \bar{D}^0 \pi^+$	0.498 ± 0.029	$B^0 \rightarrow D^- \pi^+$	0.276 ± 0.025
$B^+ \rightarrow \bar{D}^0 \rho^+$	1.34 ± 0.18	$B^0 \rightarrow D^- \rho^+$	0.77 ± 0.13
$B^+ \rightarrow \bar{D}^0 a_1^+$	0.25 ± 0.20	$B^0 \rightarrow D^- a_1^+$	0.30 ± 0.17
$B^+ \rightarrow \bar{D}^0 D_S^+$	1.3 ± 0.4	$B^0 \rightarrow D^- D_S^+$	0.8 ± 0.3
$B^+ \rightarrow \bar{D}^0 D_S^{*+}$	0.9 ± 0.4	$B^0 \rightarrow D^- D_S^{*+}$	1.0 ± 0.5
$B^+ \rightarrow \bar{D}^{*0} \pi^+$	0.46 ± 0.04	$B^0 \rightarrow D^{*-} \pi^+$	0.276 ± 0.021
$B^+ \rightarrow \bar{D}^{*0} \rho^+$	0.98 ± 0.17	$B^0 \rightarrow D^{*-} \rho^+$	0.68 ± 0.09
$B^+ \rightarrow \bar{D}^{*0} a_1^+$	0.95 ± 0.25	$B^0 \rightarrow D^{*-} a_1^+$	0.65 ± 0.14
$B^+ \rightarrow \bar{D}^{*0} D_S^+$	1.2 ± 0.5	$B^0 \rightarrow D^{*-} D_S^+$	1.07 ± 0.29
$B^+ \rightarrow \bar{D}^{*0} D_S^{*+}$	2.7 ± 1.0	$B^0 \rightarrow D^{*-} D_S^{*+}$	1.9 ± 0.5
$B^+ \rightarrow \text{recon.}$	10.5 ± 1.3	$B^0 \rightarrow \text{recon.}$	7.7 ± 0.9

Table 5-4. B -meson decay modes used in fully reconstructed sample.

5.1.3.1 Energy conservation

The energy conservation of the decay of $\Upsilon(4S)$ to a B meson pair connects the beam energy of the e^+e^- beams with the energy of B mesons. The decay of $\Upsilon(4S)$ to a B meson pair is a two-body decay, and in the center-of-mass system (cms) of $\Upsilon(4S)$ the energies and momenta of the two B mesons are equal to half the total cms energy, \sqrt{s} . Energy difference ΔE can then be constructed as:

$$\Delta E = E_B^* - E_{\text{beam}}^* \quad , \quad (5.1)$$

where $E_{\text{beam}}^* = \sqrt{s}/2$ is the cms energy of the beam, and E_B^* is the cms energy of the reconstructed B meson. The distribution of ΔE is shown in Fig. 5-2, with the overlaid estimated contribution of $e^+e^- \rightarrow q\bar{q}$ decays. This variable

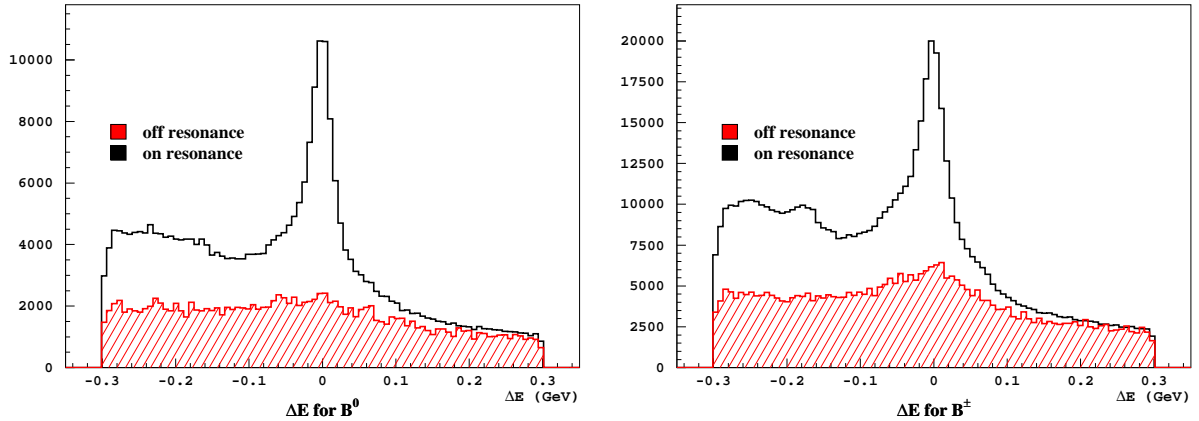


Figure 5-2. The ΔE distribution for data with the expected contribution from continuum processes, obtained from off-resonance data.

is sensitive to lost and misidentified particles, since a particle with an incorrect mass assumption has incorrect energy (while the measured momentum can still be correct). The resolution of this variable is approximately 25 MeV and depends on the number of charged particles and neutral pions in the event.

Another variable can be constructed that is basically independent of correct identification of particles, the so-called beam-constrained mass, M_{bc} :

$$M_{bc} = \sqrt{(E_{\text{beam}}^*)^2/c^4 - p_B^{*2}/c^2} \quad (5.2)$$

This is the invariant mass of the reconstructed B meson, where the reconstructed energy of the B meson that depends on correct reconstruction and identification of particles, is replaced by the beam energy in cms. Since B mesons are nearly at rest in the decay ($p_B^* \ll E_{\text{beam}}^*/c$), this variable has a clear peak near the value of E_{beam}^*/c^2 .

5.1.3.2 Fit to the M_{bc} variable

The variables ΔE and M_{bc} replace the invariant mass of B meson candidate in the estimation of the quality of reconstruction. Since their dependence on reconstruction effects is different, both are used in the analysis to secure effective reconstruction. The contributions of well reconstructed events and combinatorial background to the beam-constrained mass M_{bc} are estimated from a fit to M_{bc} . The contribution from $e^+e^- \rightarrow q\bar{q}$ decays is determined from off-resonance data, and subtracted before the fit.

The contribution of the combinatorial background is estimated using an empirical parameterization [59], the so-called ARGUS function:

$$\frac{dN}{d(M_{bc})} = N \cdot M_{\text{max}} \cdot x \cdot \sqrt{1-x^2} \cdot e^{-\beta \cdot (1-x^2)} \quad (5.3)$$

where β determines the shape of the background and is obtained from the fit, and the variable $x \equiv M_{bc}/M_{\text{max}}$ is the normalized beam constrained mass with the endpoint cut-off at M_{max} . Since from definition M_{bc} has a maximum value of M_{bc} at E_{beam}^* , we fix $M_{\text{max}} = E_{\text{beam}}^*/c^2 = 5.2885 \text{ MeV}/c^2$.

The contribution of well-reconstructed B mesons is parameterized by the so-called Crystal Ball function [60] as a Gaussian with a tail starting $\alpha \cdot \sigma$ below the position of the Gaussian peak:

$$M_{bc} > m_0 - \alpha \cdot \sigma:$$

$$\frac{dN}{d(M_{bc})} = A \cdot e^{-\frac{(M_{bc}-m_0)^2}{2\sigma^2}} \quad (5.4)$$

$$M_{bc} < m_0 - \alpha \cdot \sigma:$$

$$\frac{dN}{d(M_{bc})} = A \cdot \frac{e^{-\frac{\alpha^2}{2}}}{\left(1 - \frac{\alpha \cdot (M_{bc}-m_0)}{n \cdot \sigma} - \frac{\alpha^2}{n}\right)^n} \quad (5.5)$$

There are five parameters of the Crystal Ball function: m_0 , σ and A are the position of the peak, the width of the Gaussian and its normalization, respectively, α determines how many σ below the Gaussian peak position starts the tail and n is the parameter determining the shape of the tail. This "radiative" tail is needed to describe M_{bc} from B candidates with missed or mis-reconstructed π^0 (see Fig. 5-5). Together with N and β they are the seven free parameters obtained from the fit to M_{bc} .

We observe that the ARGUS function accurately describes all the main full reconstruction backgrounds of the analysis: continuum processes and events where the charge of the meson was not correctly reconstructed (see Fig. 5-3).

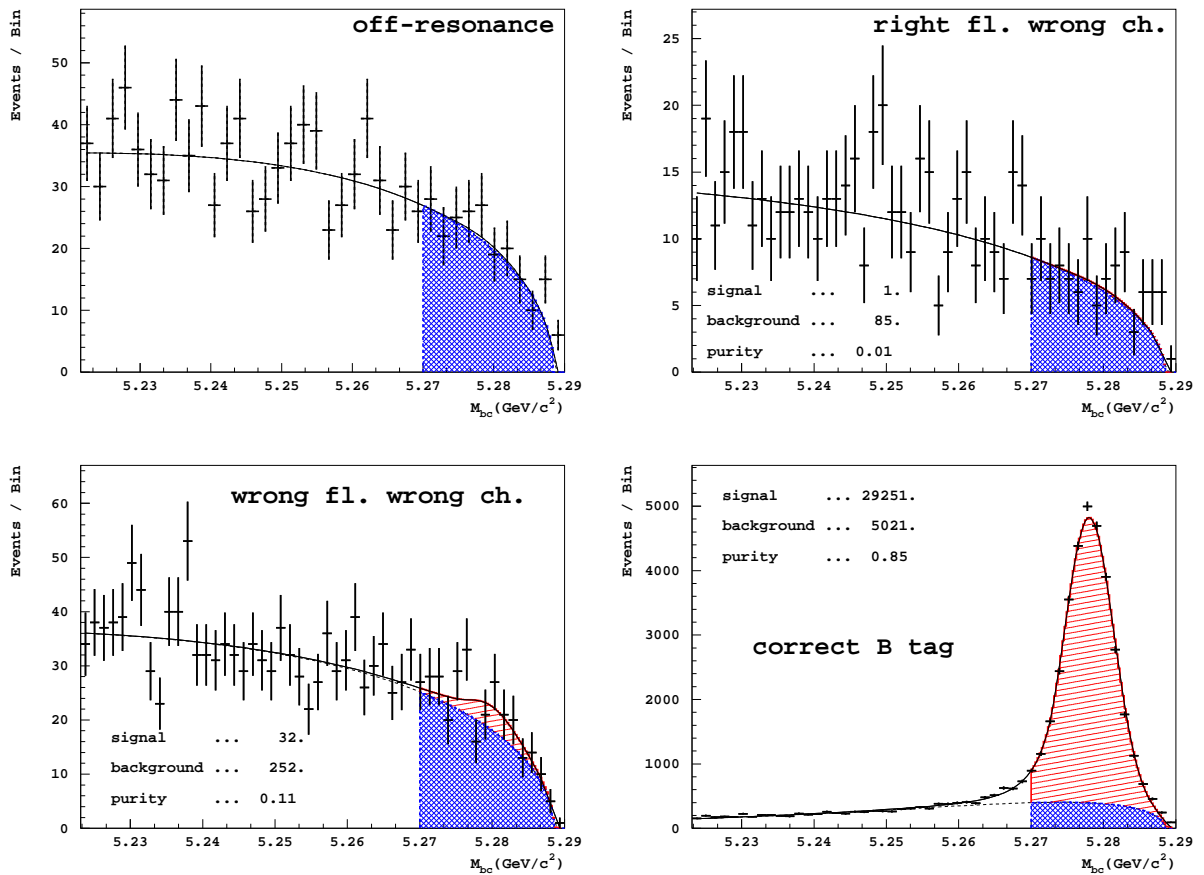


Figure 5-3. Comparison of M_{bc} distributions for different possible backgrounds to the analysis: continuum processes, obtained from off-resonance data (top left), events where the right flavor of the B_{tag} was reconstructed, but wrong charge (top right) and events where both charge and flavor were wrong (bottom left). For comparison we show the distribution where the type of B_{tag} meson was correctly identified (bottom right).

5.1.3.3 Best candidate selection

In case there are multiple B meson candidates, the candidate for $D^{(*)}\pi$ decay mode is chosen if present (due to its purity; see Fig. 6-15); if not, candidate with the smallest χ^2 is chosen, defined as

$$\chi^2 = \left(\frac{\Delta E}{\sigma_{\Delta E}} \right)^2 + \left(\frac{\delta M_D}{\sigma_{\delta M_D}} \right)^2 + \left(\frac{\delta \Delta m}{\sigma_{\delta \Delta m}} \right)^2$$

ΔE is the energy difference defined in Eq. 5.1, $\sigma_{\Delta E}$ is determined from the fit to the ΔE distribution and depends on the particular reconstructed B meson decay, δM_D is the difference between the reconstructed and the nominal mass of the reconstructed D meson; $\Delta m = m_{D^*} - m_D$ is used if applicable [57].

The M_{bc} fit to the total sample of B candidates with $-0.2 \text{ GeV} < \Delta E < 0.05 \text{ GeV}$ gives:

	N(sign.)	N(backg.)	purity	reconstr. eff.
B^+	435685	236102	0.65	0.30%
B^0	267769	158726	0.63	0.19%

where purity is defined as $N(\text{sign.})/(N(\text{sign.}) + N(\text{backg.}))$. The M_{bc} distribution with the fitted signal and background contributions is shown in Fig. 5-4.

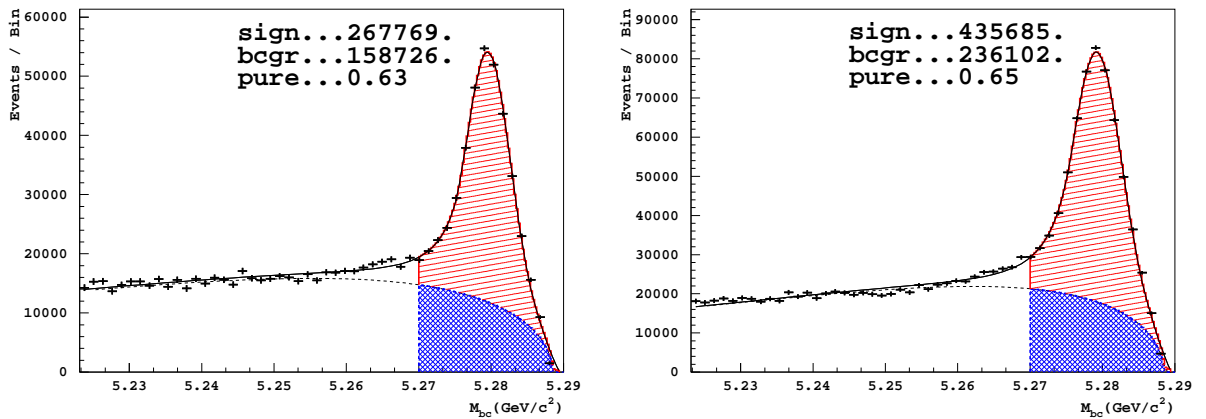


Figure 5-4. M_{bc} for data with subtracted off-resonance contribution and satisfying $-0.2 \text{ GeV} < \Delta E < 0.05 \text{ GeV}$. Fit with a Crystal Ball function (red full line) and ARGUS function (dashed black line) to obtain yield and purity was performed. Left for neutral B , right for charged B .

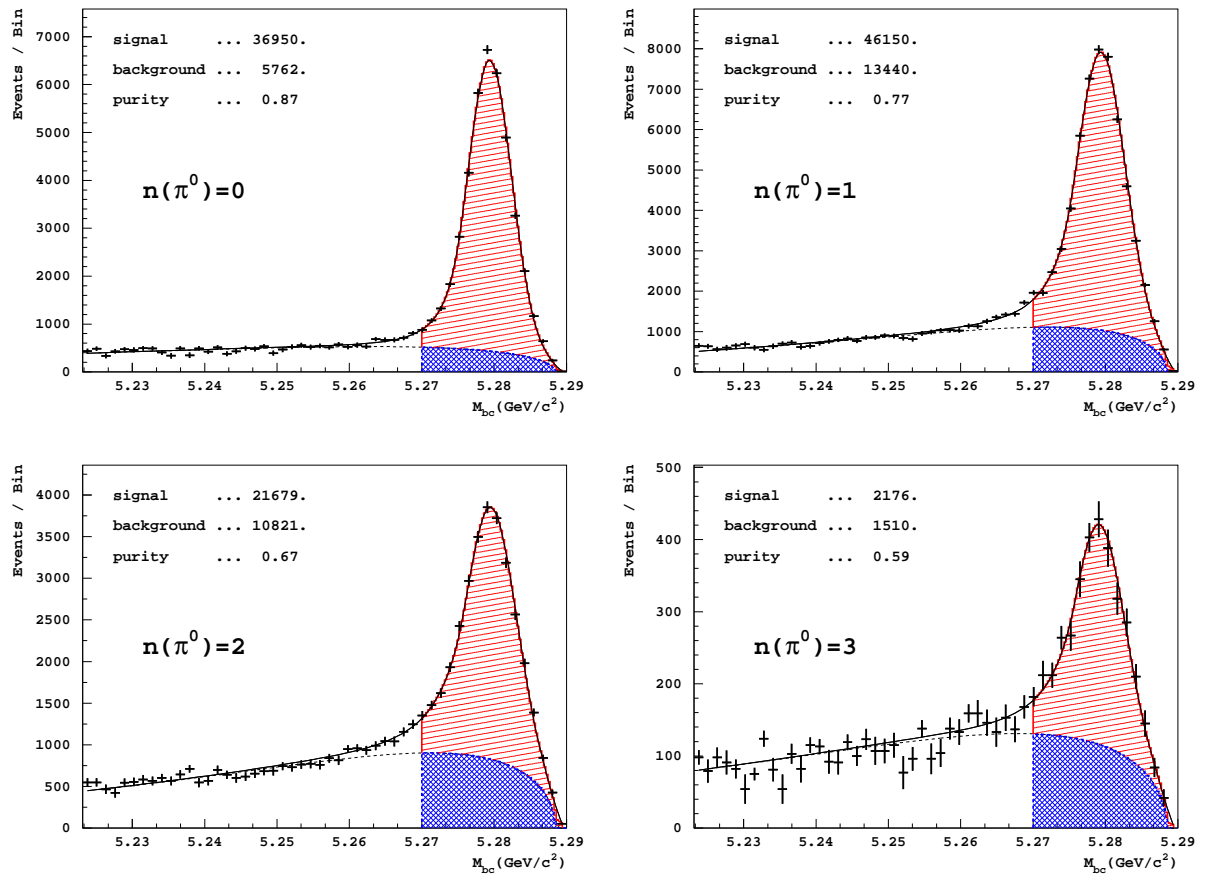


Figure 5-5. The distribution of M_{bc} for events with different number of π^0 mesons in the reconstructed decay mode.

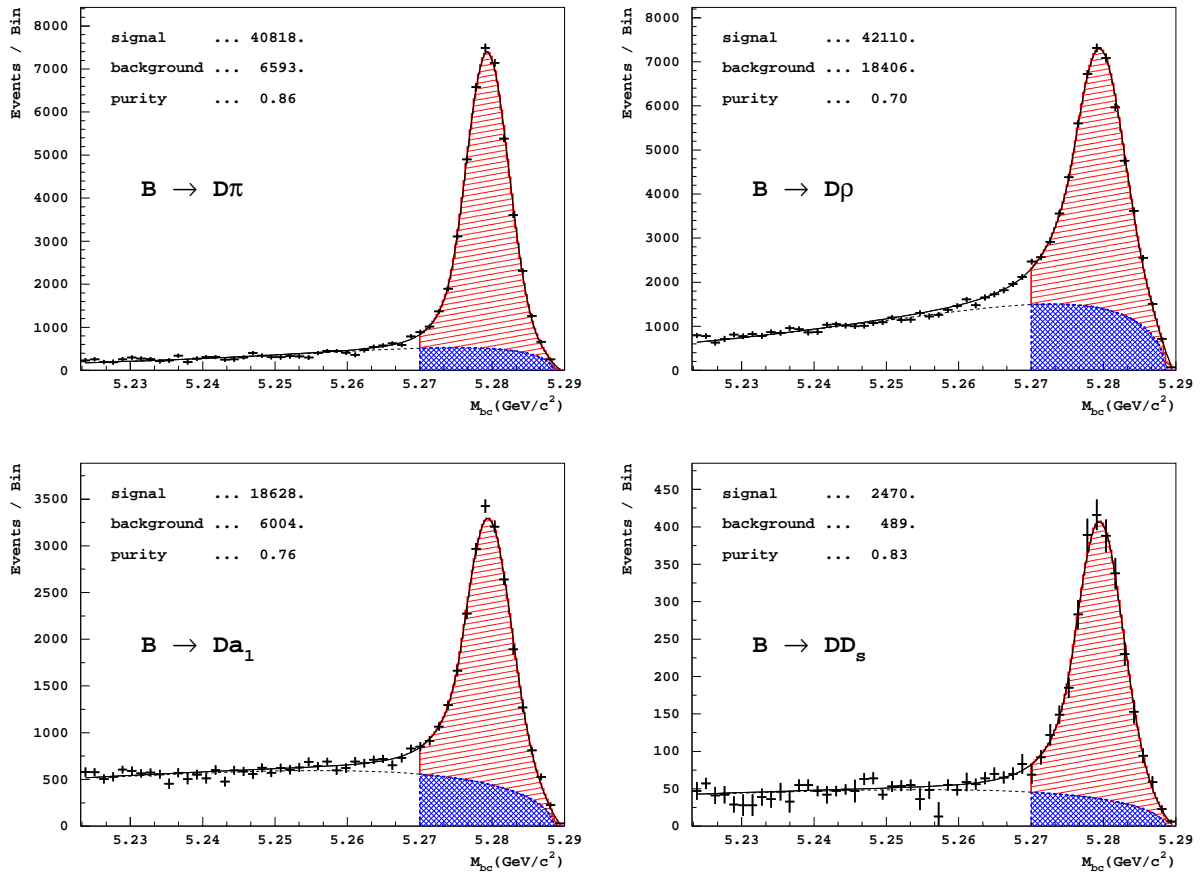


Figure 5-6. The distribution of M_{bc} for events where the B meson was reconstructed from a $D^{(*)}$ and one of the following mesons: a charged pion (top left), a charged ρ (top right), the a_1 meson (bottom left) or a D_s meson (bottom right).

5.2 Analysis on a fully reconstructed sample

It is important to stress at this point that the focus of this analysis is an accurate measurement on the part of the event that remains after removing decay products of the reconstructed B_{tag} meson. Accurate reconstruction is thus needed only to secure good separation of particles between the two B mesons. Since $b \rightarrow u$ decays are relatively rare, the number of reconstructed B mesons limits the statistical accuracy of the measurement, and one could gain by relaxing the corresponding selection criteria. We note that inaccurate reconstruction, where some or many particles are assigned to the decay chain of the wrong B meson worsens the resolution of reconstructed kinematical variables (see Fig. 5-10) and a trade-off between the purity and the size of the sample is needed to fully exploit the potential of the fully reconstructed sample.

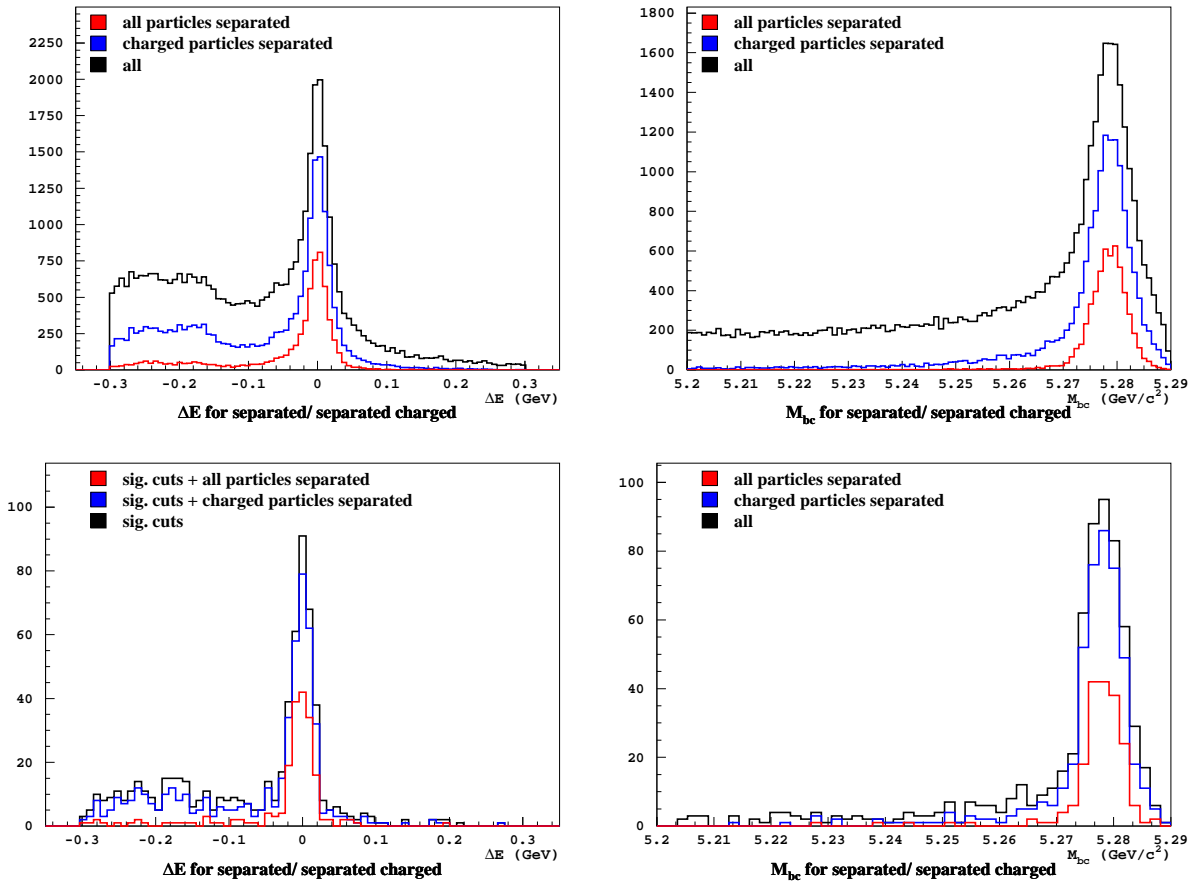


Figure 5-7. M_{bc} and ΔE distributions on $b \rightarrow c$ MC with contributions from events where all(charged) particles were successfully separated according to the B meson of origin, shown in red(blue). Bottom: same after event selection cuts were applied. Plots for $b \rightarrow c$ MC.

5.2.1 Effect of constraints on the signal side

The selection of a charmless semileptonic decay on the part of the event that remains after reconstructing the B_{tag} meson is directly or indirectly connected with the quality of reconstruction of the B_{tag} itself:

- The number of particles in the B_{sig} decay affects both the quality and the efficiency of B_{tag} reconstruction,
- total charge and missing momentum directly probe the degree of reconstruction of the whole event,
- some inclusive variables are obtained using the momentum and direction of the reconstructed B_{tag} .

The effect of stringent selection of charmless semileptonic decays on the quality of reconstruction can be seen in Fig. 5-7: after applying the selection nearly all events have at least all the charged particles correctly separated between the two mesons (blue contribution is almost equal to the black after applying signal side selection criteria).

5.2.2 Optimization of the $\Delta E/M_{bc}$ region

The quality of the reconstruction is assessed by the beam constrained mass M_{bc} and the energy difference ΔE . When interested only in the accurate reconstruction of the B_{tag} meson, a natural choice would be a narrow signal window around M_{bc} and ΔE peaks, since these events consist of well reconstructed B mesons. However, such a choice is too strict for an analysis performed on the remaining events where statistical error is expected to dominate. Events can have a well reconstructed signal region while the B_{tag} energy is inaccurate, which can be seen in Fig. 5-7, where the events with a displaced ΔE have all charged particles correctly separated between the two mesons. There are a number of possibilities where ΔE is shifted from zero, but the event still has well separated particles and fairly accurate B meson momentum. Such a case occurs for example, when a pion from the B_{tag} decay chain is misidentified as a kaon, or, a wrong photon is assigned to a π^0 decay. These effects produce the bump at lower ΔE , but they do not seriously affect the analysis.

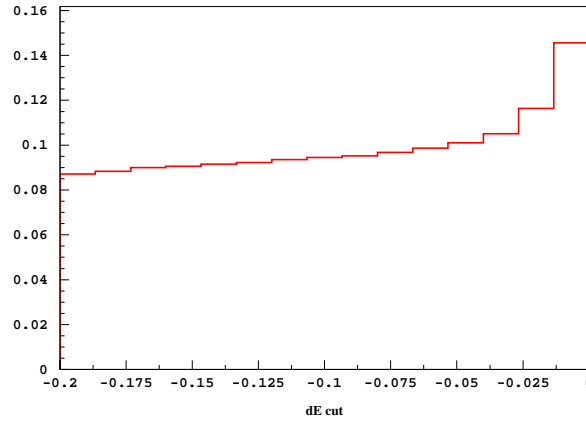


Figure 5-8. The dependence of the relative statistical counting error (see eq.5.6) on the lower limit of the ΔE selection.

We have performed an optimization of the ΔE selection according to variable:

$$\frac{\sqrt{N_{b \rightarrow u} + N_{b \rightarrow c}}}{N_{b \rightarrow u}}, \quad (5.6)$$

where $N_{b \rightarrow u}$ is the number of $b \rightarrow u$ events and $N_{b \rightarrow c}$ the number of $b \rightarrow c$ events that remain after selection. The MC estimate uses an approximate ratio of $\mathcal{B}(B \rightarrow X_c \ell \nu) / \mathcal{B}(B \rightarrow X_u \ell \nu) = 80$. The result of the estimate is presented in Fig.5-8, and it shows that the statistical error is decreasing with the decreasing lower limit of ΔE selection. The lower limit of the ΔE selection is chosen to be -200 MeV: although the improvement in the optimization variable is small

below -50 MeV, it seems in general sensible to release the selection as much as possible, since the modeling of MC is better for less stringent cuts. The upper limit is set to 50 MeV, which corresponds to the end of the peak on the positive side in Fig. 5-7 (bottom left). The effects of including a wider signal region on the properties of B_{tag} are shown in Fig. 5-9, where the wide signal region $-0.2 \text{ GeV} < \Delta E < 0.05 \text{ GeV}$ is compared to the one which includes only the peak: $-0.05 \text{ GeV} < \Delta E < 0.05 \text{ GeV}$. Including events from the bump at negative ΔE values slightly deteriorates the resolution in the angle of flight of the reconstructed B meson and the momentum ($|p_{\vec{B}}|$) resolution. All mesons are reconstructed within an angle of less than 20° ($\cos \angle(B_{\text{tag}}, B_{\text{gen}}) > 0.94$), which is the same for both B_{tag} signal region selections, the very large majority have an angle of less than 8° ($\cos \angle(B_{\text{tag}}, B_{\text{gen}}) > 0.99$).

The effect on $\Delta|p| \equiv |p_{B_{\text{tag}}} - p_{B_{\text{gen}}}|$ is shown in Fig. 5-9, left. The wide signal region includes 5% more events in the main peak of events within $\Delta|p| < 50 \text{ MeV}/c$, but there is a significant increase of the tail events. These events with the B_{tag} meson moment off by about $200 \text{ MeV}/c$ can deteriorate the quality of reconstruction of inclusive variables, so the effect was checked on $b \rightarrow c$ MC (see Fig. 5-10). The fitted resolution of the M_X variable for example changes from $150 \text{ MeV}/c^2$ to $164 \text{ MeV}/c^2$, which is acceptable.

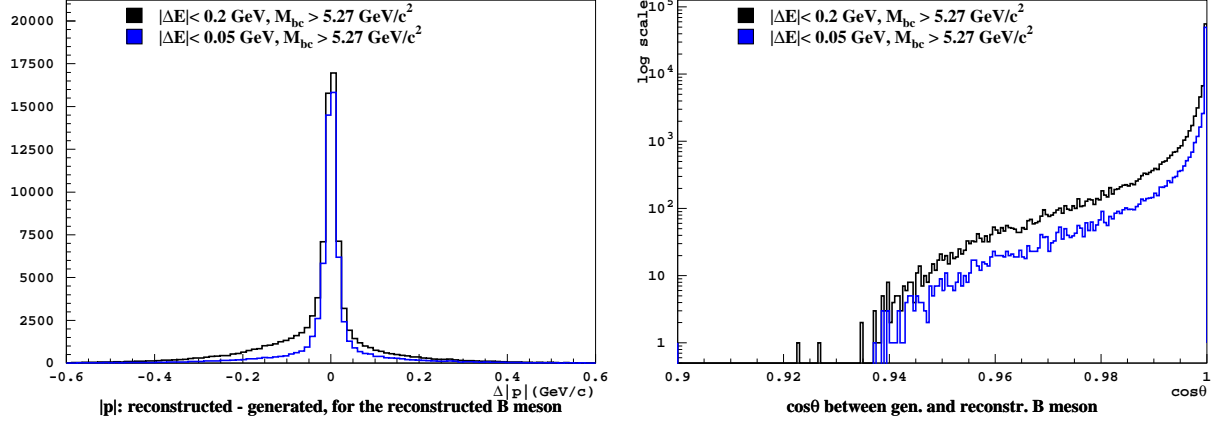


Figure 5-9. Resolution in momentum and angle of reconstructed B meson for two different cuts on M_{bc} and ΔE , for events with a lepton ($p^* \geq 1 \text{ GeV}/c$).

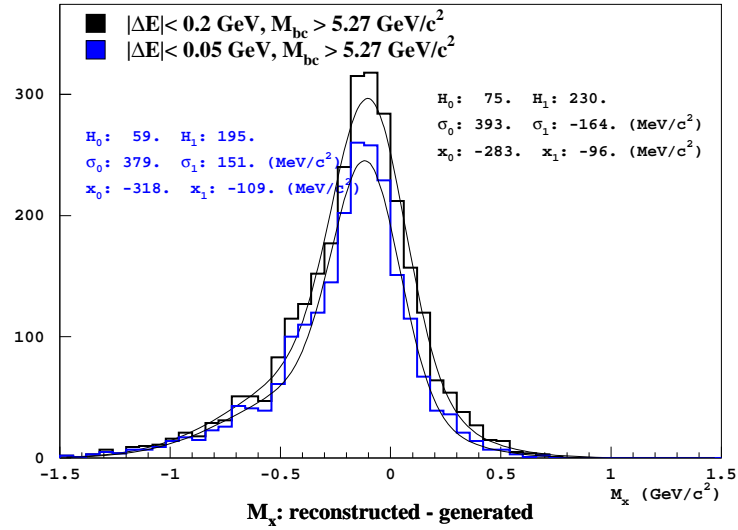


Figure 5-10. $b \rightarrow c$ MC: Difference of the reconstructed and generated M_X for two different cuts on M_{bc} and ΔE and all event selection cuts (see Sec. 6.2). The resolution for the tighter set of M_{bc} and ΔE is about $150 \text{ MeV}/c^2$, while for the looser set is about $170 \text{ MeV}/c^2$.

Selection of charmless semileptonic decays

The key element of the $|V_{ub}|$ measurement is a successful selection of charmless semileptonic decays. They are relatively rare, since the $b \rightarrow u$ transition is governed by one of the smallest CKM matrix elements, and they are hidden among much more common $b \rightarrow c$ semileptonic decays. Since they are rare and the efficiency of B_{tag} meson reconstruction is low, the process of separation of $b \rightarrow u$ from $b \rightarrow c$ events has to spare as many $b \rightarrow u$ events as possible.

First of all, we are searching for semileptonic decays, so the lepton from the semileptonic B meson decay has to be identified to discriminate between semileptonic and more abundant hadronic B meson decays. The prompt lepton should have the largest momentum of all leptons in the event, since it comes from the B decay, and it has on average a slightly larger momentum for $b \rightarrow u$ transitions than for $b \rightarrow c$ transitions, due to a smaller mass of the u quark compared to that of the c quark. Apart from the prompt lepton momentum, other inclusive kinematical variables like the invariant masses of the leptonic and the hadronic system in the semileptonic decay are also on average different for $b \rightarrow u$ and for $b \rightarrow c$ transitions, and are used to separate out $b \rightarrow u$ decays.

The construction of such inclusive kinematical variables is only possible since we are able to separate the particles in the decay according to which B meson they are coming from, by full reconstruction of the hadronic decay of one of the B mesons. In the case of perfect B_{tag} meson reconstruction and detector resolution these kinematical variables are able to very effectively separate the two transitions, but for a realistic detector and reconstruction procedure the variables are smeared and separation deteriorates significantly. This results in a large amount of remaining $b \rightarrow c$ transitions even in the selected part of phase space in which they should be kinematically suppressed.

The procedure of the selection of charmless semileptonic decays is thus as follows:

- 1.) remove from further analysis the particles from the reconstructed B_{tag} meson,
- 2.) identify the prompt lepton if it is present in the rest of the event,
- 3.) ensure that the rest of the event is adequately reconstructed,
- 4.) in adequately reconstructed events reconstruct inclusive kinematical variables,
- 5.) obtain the number of events in a $b \rightarrow u$ favored part of the kinematical phase space,
- 6.) estimate and subtract the amount of remaining $b \rightarrow c$ transitions in the selected $b \rightarrow u$ favored part of the phase space.

Successful selection rests upon a careful particle selection and identification, optimized to accurately detect leptons and kaons which play an important role in the selection procedure, and also upon usage of variables to estimate the quality of reconstruction of the signal side of the decay, which will affect the accuracy of inclusive kinematical variables, and the optimized selection of kinematical phase space regions in which we select $b \rightarrow u$ decays.

Finally MC simulation is used to subtract the estimated number of remaining $b \rightarrow c$ events in the region of phase space in which $b \rightarrow u$ transitions are kinematically favored – the accuracy of MC simulation of background semileptonic $b \rightarrow c$ transitions is tested to ensure correct subtraction of the background.

6.1 Particle selection

6.1.1 Duplicated track rejection

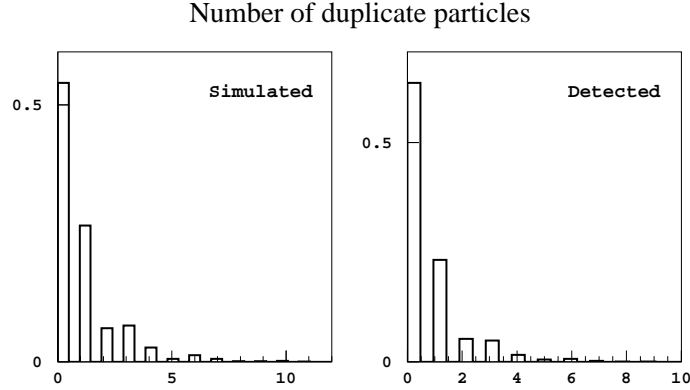


Figure 6-1. Normalized distribution of the number of simulated duplicated tracks per event for $b \rightarrow c$ MC (left) and the same distribution for detected duplicated tracks (right). Almost 50% of events have at least one duplicated track.

Tracks with low transverse momenta are difficult to reconstruct since their long curved path in the CDC offers many candidate trajectories, even such consistent with a track of an opposite charge particle. Track finder can thus produce duplicated tracks to a single particle, spoiling the resolution on the total charge of the event. Since in this analysis a severe cut on the total charge of the event is used (see Sec. 6.2.1), duplicated tracks cause the rejection of events. Almost 50% of events have at least one duplicated track (Fig. 6-1).

An attempt was made to identify duplicated tracks and select the track that corresponds better to the "real" track. The following information was used on pairs of tracks with transverse momenta smaller than $0.4 \text{ GeV}/c$ to search for duplicated tracks: angle to the z -axis ϕ for each track and the difference of the angles $\Delta\phi$ for the two tracks in a pair, difference between the sizes of their momenta $\Delta|p| = |p_1 - p_2|$ (Fig. 6-3, top), transverse momenta p_t (Fig. 6-3, bottom), angle between the two tracks θ , and their charge combination. Sharp peaks were observed both on data and MC simulation in the θ distributions (Fig. 6-2) at the angle $\theta = 0$ for same charge tracks and at $\theta = \pi$ for opposite charged tracks. A cut on $\cos\theta > 0.95$ and $\cos\theta < -0.95$, respectively, was chosen to eliminate duplicated tracks.

Simulated information was also used to chose selection criteria for selecting the "better" of the two in a pair of duplicated tracks. The following track information was considered to determine which of the two tracks corresponded better to the generated particle: χ^2 of the track fit, number of hits in the SVD and CDC and impact parameter information $|\Delta z|, |\Delta r|$. Tracks with more hits and a smaller impact parameter were in the great majority of cases having smaller $|p| - |p_{gen}|$ and smaller angle with the generated particle. The events with a larger number of hits in the detector also had a smaller impact parameter, so the number of hits in the detector did not bring any additional separating information. A χ^2 -like value $(|\Delta z|)^2 + (|\Delta r| \cdot \gamma)^2$ was constructed out of the impact parameter coordinates. By observing the dependence of the portion of correctly identified duplicated tracks ($b \rightarrow c$ MC) on its value, γ was optimized to be 5.0. Note that this also roughly corresponds to the five times better resolution in $|\Delta r|$ than in $|\Delta z|$ of the detector. The duplicated track(s) that had larger χ^2 were discarded from any further calculation.

Such duplicated particle rejection, done on fully reconstructed generic $b \rightarrow c$ MC, has 57% efficiency for finding duplicated pairs, while 25% of selected tracks are not from a duplicated pair. On a signal $b \rightarrow u$ MC the efficiency is better (due to a lower event multiplicity): 60% efficiency for finding a duplicated track with only 18% of selected duplicated tracks being wrongly tagged as duplicated.

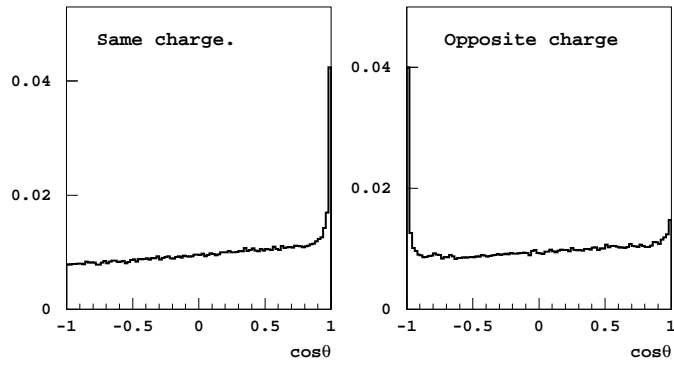


Figure 6-2. Distribution of the angle between a pair of tracks with $p_t < 0.4 \text{ GeV}/c$ (no other requirements) when having same (left) or opposite charge (right). Plots are for data.

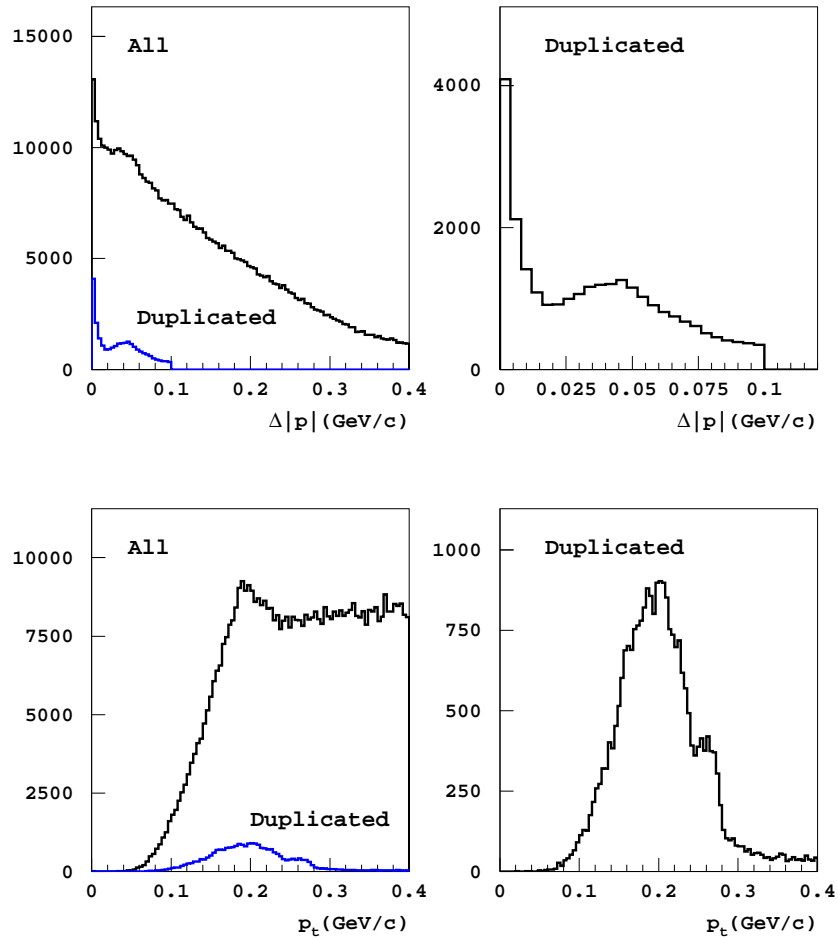


Figure 6-3. Distributions of momentum size difference $\Delta|p|$ and p_t for all pairs of particles with $p_t < 0.4 \text{ GeV}/c$ and for those tagged as duplicated. Plots are for data.

6.1.2 Selection of charged particles

After removing duplicated tracks, charged particles are reconstructed from the remaining charged tracks in order to find a fast lepton required for the selection of semileptonic $b \rightarrow u$ decays, to calculate correctly the missing mass of the event and the kinematical variables of B_{sig} . For this purpose, all the tracks within the detector acceptance are used, providing they also meet loose requirements on the impact parameter with respect to the interaction point ($|dz| < 100$ cm and $|dr| < 20$ cm). Lepton and hadron identification is then performed on the accepted tracks (Fig. 6-4, right).

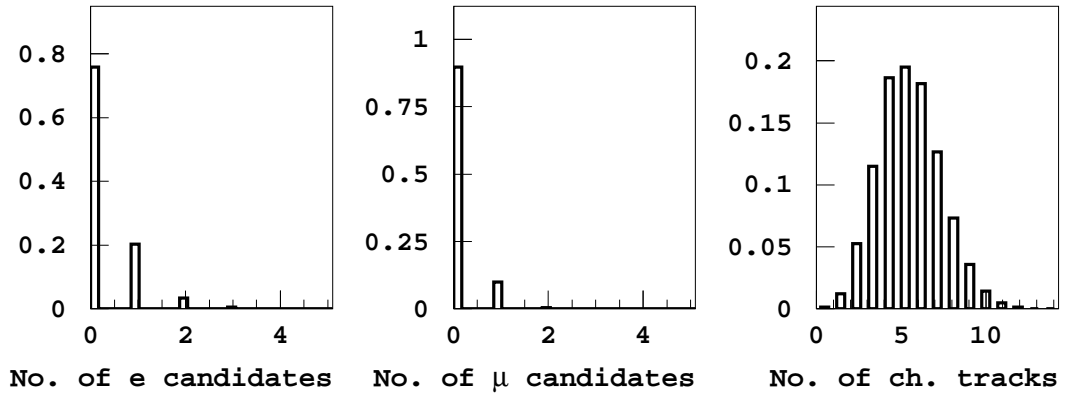


Figure 6-4. Number of electron candidates, muon candidates and tracks per event.(data)

We first select lepton candidates with a looser selection criteria and in the final instance search for the prompt lepton among the candidates. This saves CPU time of sorting the tracks according to the momentum and the quality of lepton identification; in case of mis-identification, looser selection does not seriously affect inclusive kinematical variables, since the masses of a pion (the most abundant hadron in the event), electron and muon are usually negligible compared to the particle momenta. Muon candidates are selected by requiring the value of the normalized ratio $\text{Prob}(\mu) > 0.9$. The charged tracks are identified as electrons when the electron identification probability $\text{Prob}(e)$ is above the value of 0.8. (The $\text{Prob}(x)$ hypothesis probabilities are defined in Sec. 4.5.)

Since the identified charged kaons are used for separation between the semileptonic sample into the $b \rightarrow u$ depleted and the $b \rightarrow u$ enhanced subsamples (see Sec. 6.2), accurate hadron identification is important. In addition, accurate identification of hadrons improves the resolution of kinematical variables through the assignment of correct particle masses. These selection using $\text{Prob}(K/\pi)$, defined in Sec. 4.5.3.3, minimizes pion/kaon mis-identification and offers a good performance in proton detection.

Tracks that are not previously attributed to leptons are used as hadron candidates. Tracks are identified as charged kaons, if their kaon/pion separation probability $\text{Prob}(K/\pi)$ is above 0.6, while $\text{Prob}(K/p)$ and $\text{Prob}(K/e)$ are required to be larger than 0.2. Tracks are attributed to protons when they are not identified as kaons, but still have $\text{Prob}(K/\pi) > 0.4$, $\text{Prob}(K/p) < 0.6$ and momentum below $750 \text{ MeV}/c$. All remaining charged tracks are identified as pions.

6.1.3 Selection of neutral particles

Photons, Dalitz π^0 decays, K_S , and J/ψ are reconstructed in the signal-side analysis. We do not reconstruct $\pi^0 \rightarrow \gamma\gamma$ on the signal side, for which the purity of reconstruction is too low to improve the resolution of kinematical variables.

Leptons from $J/\psi \rightarrow \ell\ell$ decays, photon conversion and Dalitz decays of neutral pions ($\pi^0 \rightarrow e^+e^-\gamma$) represent a background to our analysis, so we form a lepton selection veto based on the reconstruction of these decays. Leptons are removed from prompt semileptonic candidates on the basis of the invariant mass they form combined with opposite charge leptons ($m_{\ell\ell}$) and with an additional photon in the case of electrons ($m_{ee\gamma}$). We reject the lepton, if $m_{\ell\ell}$ lies within $\pm 4.9 \text{ MeV}/c^2$ ($\pm 5\sigma$) of the nominal J/ψ mass, m_{ee} below $100 \text{ MeV}/c^2$ or $m_{ee\gamma}$ within $\pm 32 \text{ MeV}/c^2$ ($\pm 3\sigma$) of the nominal π^0 mass. The reconstructed J/ψ candidates are shown in Fig. 6-5 (first from the right).

K_S mesons are identified using the standard criteria described in Sec. 5.1.1.1, where the invariant mass of the charged pion pair has to lie within $0.468 < M_{\pi\pi} < 0.528 \text{ GeV}/c^2$ (Fig. 6-5, first from the left).

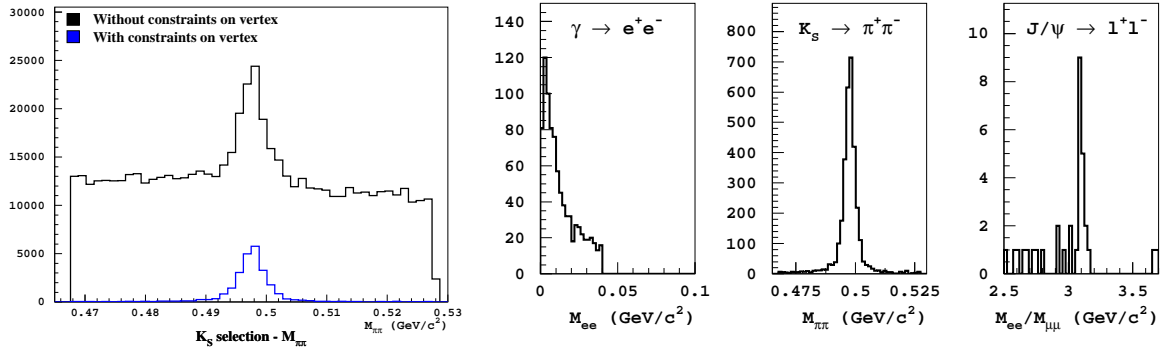


Figure 6-5. First from the left: invariant mass of the pair of tracks reconstructed to come from K_S with and without vertex constraints. Next three: invariant mass of pairs of tracks reconstructed to come from converted photon, K_S and J/ψ , respectively. Plots are for data.

Photons detected in the electro-magnetic calorimeter are included in the calculation of inclusive kinematical variables. Apart from photons also electrons and hadrons can deposit energy in the calorimeter, so the transverse shower shape parameter $e9e25 > 0.8$ is required. This variable compares the amount of energy deposited in 3×3 and 5×5 crystals (see Sec. 4.5.3.2), and helps remove energy depositions from hadrons, which are already reconstructed. The extreme forward and backward directions are polluted by photons from interactions of beams with the beam-pipe material and residual gas in the beam-pipe (beam background), so photons that fly in the direction of less than 17° or more than 162° with respect to the z direction are excluded from the analysis. The remaining part of the solid angle is divided into sections of forward, backward and barrel region (see Sec. 6.1.5.4). Forward photons having energies larger than 100 MeV , backward larger than 150 MeV and barrel photons having energy larger than 50 MeV were selected.

6.1.4 Final lepton selection

To identify semileptonic decays, prompt leptons are searched for among the lepton candidates that were not reconstructed to come from a J/ψ , converted photon or π^0 Dalitz decay. Variables used in the selection of prompt leptons are compared in Fig. 6-7 for prompt leptons and other leptons in the decays. In order to separate the two, prompt lepton candidates are required to have $|\Delta r| < 0.1 \text{ cm}$ and $|\Delta z| < 2 \text{ cm}$ (Fig. 6-7, top). The identification hypothesis

probabilities for muon candidates have to be $\text{Prob}(\mu) > 0.95$ while for electrons $\text{Prob}(e) > 0.97$ (Fig. 6-7, middle row).

The bottom row in Fig. 6-7 shows cms momentum $|p^*|$ (left) and cosine of the angle of the lepton flight direction to the z axis (right). The regions of extreme forward and backward show an increase of leptons not pertaining to the semileptonic B decay, those in the extreme forward coming mainly from beam background, and are removed by constraining lepton detection in the region of 26° to 140° to the z direction.

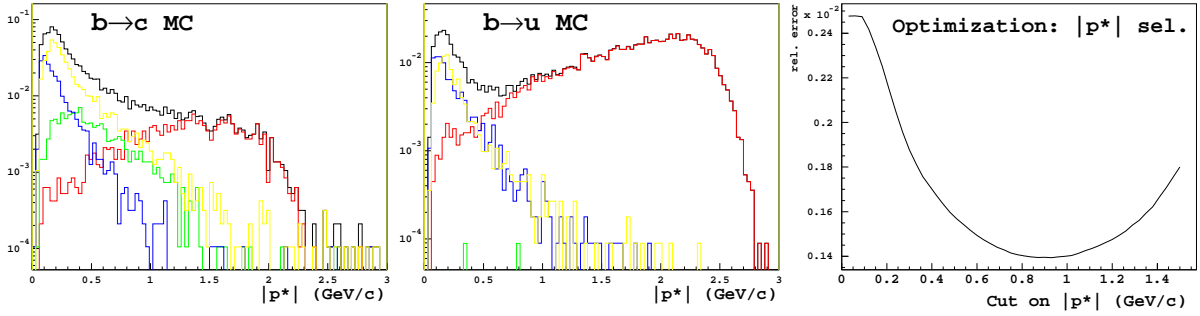


Figure 6-6. $|p^*|$ distribution for leptons (black) with the breakdown to: prompt leptons (red), leptons from photon conversion (yellow), leptons from cascade semileptonic decays (green), and other leptons (blue), for $b \rightarrow c$ (left) and $b \rightarrow u$ (middle), and the optimization of $|p^*|$ selection (right) by minimizing $\sqrt{N_{\text{prompt}} + N_{\text{other}}}/N_{\text{prompt}}$ (see the text).

The most important variable for prompt lepton selection is its momentum in cms $|p^*|$. Figs. 6-6 and 6-7 (bottom left) show the distribution of prompt leptons extending up to the endpoint of $2.3 \text{ GeV}/c$ for $b \rightarrow c$ transition and $2.6 \text{ GeV}/c$ for $b \rightarrow u$ transition, while the majority of other leptons have momenta below $1 \text{ GeV}/c$. The selection criterion of $|p^*| > 1 \text{ GeV}/c$ was optimized using variable $\sqrt{N_{\text{prompt}} + N_{\text{other}}}/N_{\text{prompt}}$, where N_{prompt} is the number of prompt leptons and N_{other} the number of other leptons remaining after the p^* requirement. The optimal selection was found to be between 0.9 and $1 \text{ GeV}/c$ (see Fig. 6-6, right), $|p^*| > 1 \text{ GeV}/c$ was decided to be the primary selection of prompt leptons.

We search for high momentum leptons above $|p^*| > 0.6 \text{ GeV}/c$ for electrons and $|p^*| > 0.8 \text{ GeV}/c$ for muons, which removes nearly all leptons other than those from prompt and cascade semileptonic decays (Fig. 6-6, left and middle).

Events can have multiple prompt lepton candidates. If two leptons are found, one with momentum $|p^*| > 1 \text{ GeV}/c$ and another with momentum $|p^*| > 0.8 \text{ GeV}/c$ (muon) or $|p^*| > 0.6 \text{ GeV}/c$ (electron), such an event was tagged as a cascade $b \rightarrow c \rightarrow s$ semileptonic decay (compare cascade lepton contributions (green) of Fig. 6-6, left and middle). Such events were excluded from the selection of charmless semileptonic decays¹.

¹They were included when obtaining the number of all semileptonic events (see Sec. 7.1.4.1)

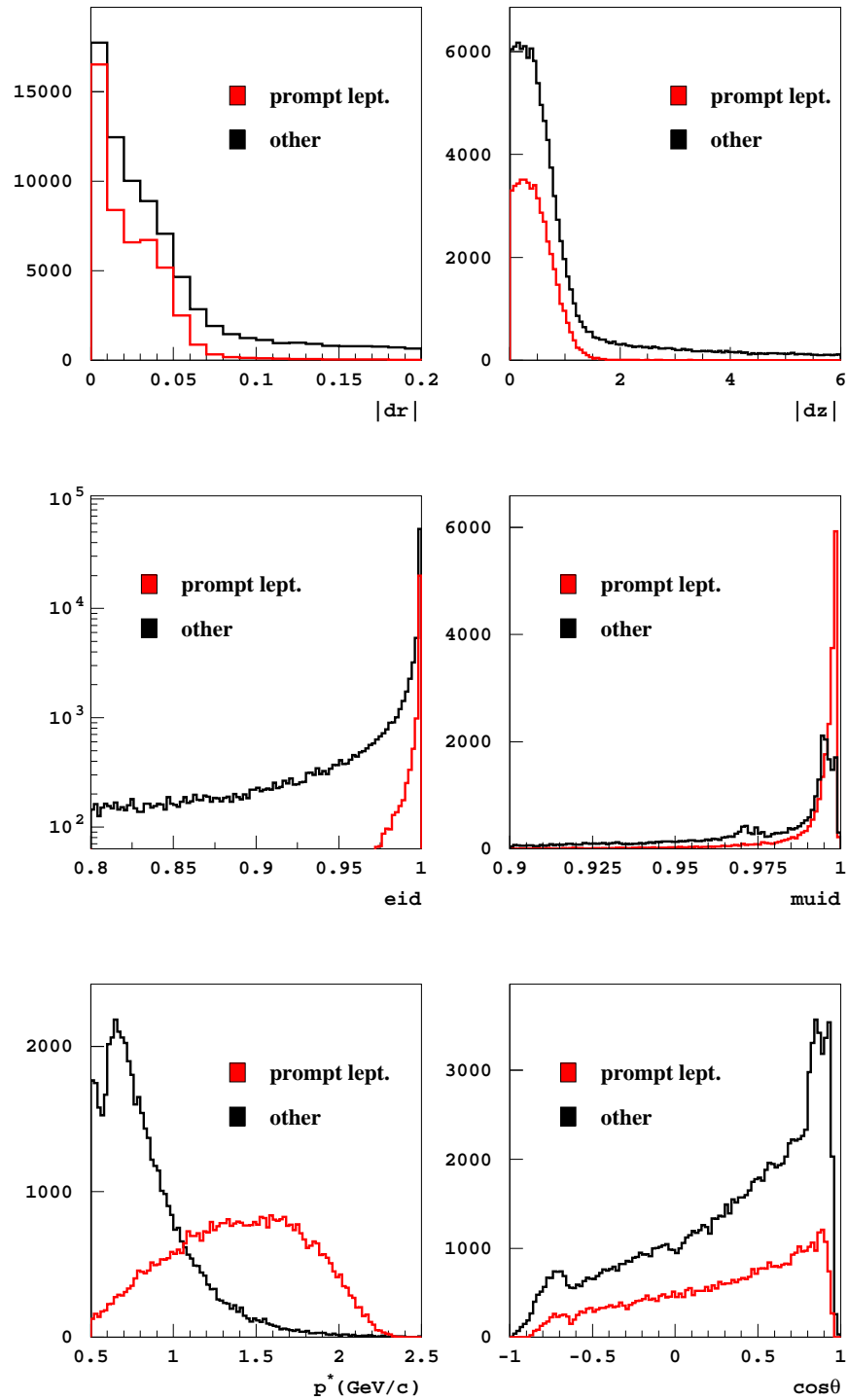


Figure 6-7. Comparison of kinematical properties for prompt leptons from a semileptonic B meson decay (red) and other leptons in the decay (black). Leptons from preselection. Plots for $b \rightarrow c$ MC.

6.1.5 Summary of particle selection

For reference the particle selection is summarized.

6.1.5.1 Duplicated tracks

each track	$p_t < 0.4 \text{ GeV}/c$
pair:	$ p_1 - p_2 < 100 \text{ MeV}/c$
same charge	$\cos \theta_{p_1, p_2} > +0.95$
opp. charge	$\cos \theta_{p_1, p_2} < -0.95$

Rejected: the one with larger $(|\Delta z|)^2 + (|\Delta r| \cdot \gamma)^2$ with $\gamma = 5$.

6.1.5.2 Charged tracks

Passed duplicated track rejection and have $|\Delta z| < 100 \text{ cm}$ and $|\Delta r| < 20 \text{ cm}$. Identification:

ID	cuts
μ	$\text{Prob}(\mu) > 0.9$
e	$(! \mu) \& \text{Prob}(e) > 0.8$
K	$(! \mu) \& (! e) \& (\text{Prob}(K/\pi) > 0.6) \& (\text{Prob}(K/p) > 0.2) \& (\text{Prob}(K/e) > 0.2)$
p	$(! \mu) \& (! e) \& (! K) \& (\text{Prob}(K/\pi) > 0.4) \& (\text{Prob}(K/p) < 0.6) \& (p < 0.75 \text{ GeV}/c)$
π	rest

Explanation: $(!x)$ means "not identified as particle x ".

6.1.5.3 Neutral particles

ID	M_{ab} cuts	vertex
K_S	$0.468 \text{ GeV}/c^2 < M_{\pi^+\pi^-} < 0.528 \text{ GeV}/c^2$	yes
γ	$M_{l+l^-} < 0.04 \text{ GeV}/c^2$	no
J/ψ	$3.05 \text{ GeV}/c^2 < M_{l+l^-} < 3.12 \text{ GeV}/c^2$	no
$\pi^0(\text{Dalitz})$	$100 \text{ MeV}/c^2 < M_{l+l^- \gamma} < 170 \text{ MeV}/c^2$	no

Pairs of pions and pairs of leptons with opposite charge are combined to reconstruct a K_S meson, converted photons, J/ψ and, in combination with an additional photon, the Dalitz decay of π^0 . If the invariant mass of the combination lies within the specified region of invariant mass, the reconstruction is successful. The additional requirements on the vertex of combined tracks in case of the K_S meson are defined in Sec. 5.1.1.1.

6.1.5.4 Selection of photons

which photons	θ region	cuts
all		$162^\circ > \theta > 17^\circ$
all		$e9e25 > 0.8$
Forward	$35^\circ > \theta > 17^\circ$	$E_\gamma > 100 \text{ MeV}$
Backward	$150^\circ > \theta > 125^\circ$	$E_\gamma > 150 \text{ MeV}$
Barrel	$125^\circ > \theta > 35^\circ$	$E_\gamma > 50 \text{ MeV}$

Table 1: Cuts on photons.

Angle θ is the angle between the reconstructed photon track and the z-axis of the detector; e9e25 is the transverse shower shape parameter.

6.1.5.5 High momentum lepton candidates

Leptons from J/ψ , γ conversion and Dalitz π^0 decay are excluded from high momentum lepton candidates.

	ID: μ	ID: e
	$\text{Prob}(\mu) > 0.95$	$\text{Prob}(e) > 0.97$
θ	$26^\circ < \theta < 140^\circ$	$26^\circ < \theta < 140^\circ$
$ \Delta r $	$< 0.1 \text{ cm}$	$< 0.1 \text{ cm}$
$ \Delta z $	$< 2 \text{ cm}$	$< 2 \text{ cm}$
$ p^* $	$> 0.6 \text{ GeV}/c$	$> 0.8 \text{ GeV}/c$

Angle θ is the angle between the reconstructed lepton track and the z-axis of the detector. All leptons that satisfy the criteria are regarded as high momentum lepton candidates. There can be more than one per event.

6.2 Event selection

After tracks are selected and identified, semileptonic events are searched for using the properties of high momentum lepton candidates. The final measured results will be normalized to the number of semileptonic decays, so a selection of a semileptonic sample are the starting point of event selection. The properties of each event of the semileptonic sample is evaluated to ensure that the events are reconstructed sufficiently well to enable accurate $b \rightarrow u$ extraction and events with poor quality of reconstruction are rejected.

The event selection has thus three scopes:

- 1.) select semileptonic decays,
- 2.) remove poorly reconstructed events,
- 3.) reduce the fraction of events with $b \rightarrow c$ decays in favor of $b \rightarrow u$ decays.

Poorly reconstructed events are removed using information on the missing momentum and the total charge of the event; indications of a $b \rightarrow c$ transition, like reconstructed kaons and D^* mesons, are used to reduce the fraction of $b \rightarrow c$ decays in the sample that is in the final instance used to extract $b \rightarrow u$ decays. We construct two samples, called the *$b \rightarrow u$ enhanced sample* and the *$b \rightarrow u$ depleted sample*; events that pass all selection criteria and have no identified charged kaon or reconstructed K_S meson in the B_{sig} decay constitute the *$b \rightarrow u$ enhanced sample*, while events passing all selection criteria and having at least one charged kaon or a reconstructed K_S meson constitute the *$b \rightarrow u$ depleted sample*.

The presence of a kaon is an indication of a cascade $b \rightarrow c \rightarrow s$ transition, while events with no kaons are either $b \rightarrow u$ decays or $b \rightarrow c$ decays where a kaon was for some reason not reconstructed. We do not expect to see a significant contribution from $b \rightarrow u$ decays to the depleted sample, since the $b \rightarrow u$ decays involving kaons are rare and kaon misidentification is at the level of a few percent. The *$b \rightarrow u$ depleted sample* thus represents a relatively clean $b \rightarrow c$ sample and is used to check the reliability of $b \rightarrow c$ MC simulation, while the *$b \rightarrow u$ enhanced sample* is used for the extraction of $b \rightarrow u$ decays.

Efficiencies for different samples of data and MC to pass selection criteria are summarized in Sec. 6.2.7.

6.2.1 Selection of semileptonic decays

Selected high momentum leptons come from either semileptonic decays or non- $B\bar{B}$ (continuum) processes. The latter are greatly suppressed by the full reconstruction of B_{tag} meson, while the remaining continuum background is determined using fully reconstructed off-resonance data. We can therefore use the result of the optimization from 6.1.4 and regard leptons with $|p^*| > 1 \text{ GeV}/c$ as a clear indication of a semileptonic decay.

The information on the flavor of the reconstructed B meson can be exploited to ensure that the lepton has a charge consistent with the flavor of B_{sig} meson. In case the tagging B meson is B^+ , the lepton from the semileptonic decay of B_{sig} is negatively charged (right charge). In case of a cascade $b \rightarrow c \rightarrow s$ transition in the signal side, the lepton arising from the charmed meson semileptonic decay carries a positive charge (wrong charge). Hence by requiring a charge of the lepton to be consistent with the charge of the B_{tag} we can additionally suppress cascade semileptonic decays. Fractions of leptons from semileptonic B meson decays and of other leptons with right or wrong charge are shown in Tab. 6-1. Due to possible mixing of the neutral B meson it was assessed that the constraint eliminates too many events where the correct lepton was identified as the prompt lepton (see Tab. 6-1) and the charge consistency constraint is not used in the neutral B meson case.

	B^0		B^\pm	
	right lept.	wrong lept.	right lept.	wrong lept.
right charge	82%	40%	97%	48%
wrong charge	18%	60%	3%	52%

Table 6-1. Relative portion of leptons from the semileptonic B decay (right lept.) and all other high energy lepton candidates (wrong lept.) that have charge consistent (right charge) with the flavor of reconstructed B meson. Separate results for B^0 and B^\pm . All other event cuts applied.

The semileptonic sample consists of events with a lepton with $|p^*| > 1 \text{ GeV}/c$ and its charge consistent with that of the flavor of B_{sig} in the case of a charged B meson. It includes semileptonic $b \rightarrow c$ and $b \rightarrow u$ decays and decays where a track was incorrectly assigned to the prompt lepton. The MC simulation is used to correct for the "fake" semileptonic events when obtaining the number of semileptonic decays, which is later used for the normalization of results (see Sec. 7.1.4.1).

For the semileptonic $b \rightarrow u$ selection additional constraints on leptons are applied to remove decays that indicate a $b \rightarrow c$ transition. After removing the leptons from vetoed decays, no other lepton should be detected in the $b \rightarrow u$ semileptonic decay. Other identified leptons come from either cascade $b \rightarrow c \rightarrow s$ decays or mis-identified hadrons, like kaons that were misidentified as muons, both of which signal a $b \rightarrow c$ transition; we remove events with additional leptons from the $b \rightarrow u$ enhanced sample. Since the MC simulation of low momentum leptons is not reliable enough, and a selection based on leptons of momenta below $0.5 \text{ GeV}/c$ would introduce a bias in MC simulation, additional leptons are only searched for among electron candidates with $|p^*| > 0.6 \text{ GeV}/c$ and muon candidates with $|p^*| > 0.8 \text{ GeV}/c$.

6.2.2 Net charge of the event

Since the hermeticity of the Belle detector [40] ensures a good coverage of the solid angle, no charged particles should escape detection and the net charge of the event has to be zero. The net charge of the event is a measure of the quality of charged particle reconstruction; the comparison of event charge distribution for data, $b \rightarrow c$ MC and $b \rightarrow u$ MC is shown in (Fig. 6-8, left). Semileptonic $b \rightarrow u$ decays have the best net charge distribution due to a smaller number

of tracks (Fig. 6-8, left). Data and $b \rightarrow c$ MC simulation agree very well, so the cut on charge should not bring any additional bias. To select events where all charged particles were successfully reconstructed, we require that the net charge of the event be zero.

Note that the rejection of duplicated tracks improved the event charge distribution considerably, as can be seen from the Fig. 6-8 (right).

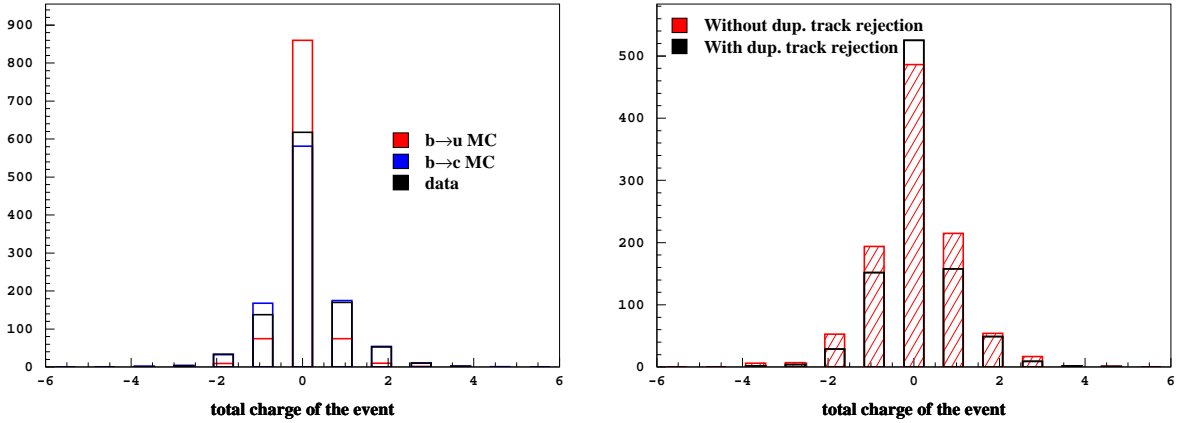


Figure 6-8. Left: the total charge of the event for data (black), $b \rightarrow u$ MC (red) and $b \rightarrow c$ MC (blue). Right: the comparison of the total charge distribution for data with (black) and without (red) duplicated tracks rejection. Both plots for samples after event selection, except that of the net charge.

6.2.3 Number of detected kaons

Presence of a kaon in the semileptonic B meson decay is a clear indication of a $b \rightarrow c$ transition: although decays of mesons composed of u and d quarks into kaons were observed, such decays are about 50 times less common compared to $b \rightarrow c \rightarrow s$ kaon producing decays.

The number of identified charged kaons and reconstructed K_S mesons is therefore used to separate $b \rightarrow u$ and $b \rightarrow c$ decays; by selecting only events with no reconstructed kaons we greatly reduce the fraction of $b \rightarrow c$ transitions while not affecting much the events with $b \rightarrow u$ transitions. The MC estimate shows that 44% of B^+ and 49% of B^0 semileptonic decays with charm are rejected, compared to 8% of charmless semileptonic decays (see Sec. 6.2.7).

In Fig. 6-9 the distribution of events according to the number of reconstructed charged and neutral kaons is shown for events with hadronic invariant mass above $M_X > 1.5 \text{ GeV}/c^2$, where charmless decays are suppressed and a comparison with $b \rightarrow c$ MC is accurate. Since we categorize events by the number of reconstructed kaons, an accurate Monte Carlo simulation of kaon reconstruction is crucial. We have tested the hypothesis that the amount of the observed disagreement is produced by statistical fluctuations alone.

A χ^2 test was used: a sample of 10000 pairs of distributions were generated corresponding to a multinomial distribution with bin probabilities calculated from the original two distributions. The fraction of pairs of generated distributions that had χ^2 larger than the compared (original) pair was the measure of the probability that the disagreement due to statistical fluctuation can be equal or larger than the one observed. The probability (together with the p.d.f.) is plotted in the upper right corner of the distribution graph in Fig. 6-2.

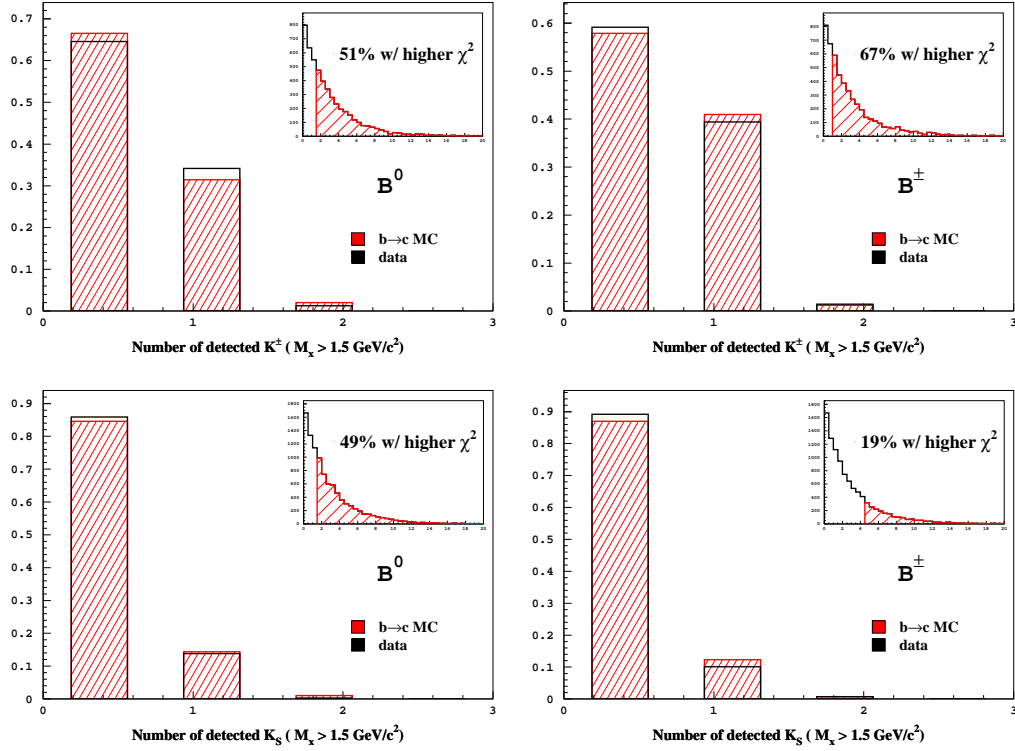


Figure 6-9. Fractions of events with different number of detected charged kaons (top) and K_S (bottom) for data (black) and $b \rightarrow c$ MC (red). All plots for $M_X > 1.5 \text{ GeV}/c^2$, where there should be no considerable contribution of $b \rightarrow u$ events. The distributions are normalized to 1.

	B^0		B^\pm	
	K^+	K_S	K^+	K_S
$\text{Prob}(\chi^2 > \chi_0^2)$	51%	49%	67%	19%

Table 6-2. Statistical estimate of the probability $\text{Prob}(\chi^2 < \chi_0^2)$ that a χ^2 discrepancy of two distributions would be larger than the one observed (χ_0^2).

The size of the observed fluctuations is within the probable range of statistical fluctuations (see Tab. 6-2); we conclude that the detected kaon number distributions for $b \rightarrow c$ MC simulation and data are consistent within statistical uncertainty.

The $b \rightarrow u$ events, rejected by the kaon veto, are accounted for in the signal efficiency. The process responsible for kaon production in $b \rightarrow u$ events proceeds mainly through gluon splitting into an $s\bar{s}$ pair (the gluon $s\bar{s}$ "popping") and is simulated in $b \rightarrow u$ MC. The effect of imperfect simulation of this contribution is estimated and included in the systematic error of $b \rightarrow u$ modeling (see Sec. 7.2.3.3).

6.2.4 K_L contribution

Events with K_L mesons in the signal side come mainly from $b \rightarrow c \rightarrow s$ kaon producing decays. The presence of a K_L meson is therefore, in the same way as the presence of a charged kaon or a K_S meson, a tag for a $b \rightarrow c$ decay. The Belle detector has limited capabilities for detecting K_L mesons [40]. The KLM detector provides some information about the direction of the candidate K_L momentum, but is not capable of measuring its energy. To illustrate how the events with K_L mesons are distributed, their contribution in hadronic invariant mass M_X and missing mass squared m_{miss}^2 (introduced in Secs. 6.3.1 and 6.2.6, respectively) is shown in Fig. 6-10. The majority of events with K_L mesons has due to the unreconstructed K_L meson a large missing mass squared (Fig. 6-10, right) and is removed from further calculation by the restriction on missing mass squared (see Sec. 6.2.6), but from the events passing the m_{miss}^2 selection, events with K_L still represent about 52% of all $b \rightarrow c$ events in the kinematic region of measurement (see Fig. 6-10, middle).

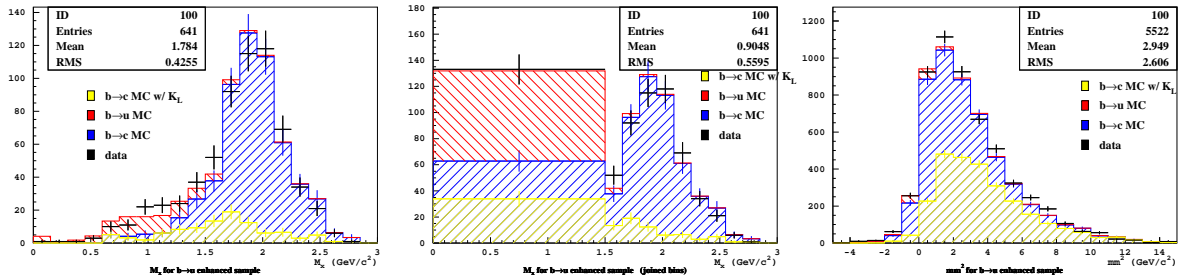


Figure 6-10. Distributions of M_X (left, middle) and missing mass (right) with the contribution of events where K_L was present (yellow) on the signal side (MC generation information). In the region of measurement 52% of the background $b \rightarrow c$ events have a K_L meson in the signal side (middle, first bin). Plots for data (black crosses), $b \rightarrow c$ MC (blue, yellow) and $b \rightarrow u$ MC (red).

The quality of the candidate K_L meson cannot be assessed by calculating its invariant mass, so the direction information is used to calculate the angle between the candidate K_L meson and missing mass direction. If the candidate K_L meson corresponds to a true K_L meson, its momentum contributes to the missing momentum and the missing momentum direction should point towards the direction of the K_L candidate. We remove events where the cosine of this angle ($\cos(\angle(K_L, P_{\text{miss}}))$) is larger than 0.9 as obtained from the optimization the selection.

6.2.5 Partial reconstruction of a D^* meson

Presence of a D^* meson in the signal side is an indication of a $b \rightarrow c$ transition ($B \rightarrow D^* \ell \nu$). A charged D^* meson decays 67.7% of times to a $D^0 \pi^\pm$ pair [10], where the available energy in a $D^* \rightarrow D^0$ transition is just a bit larger than needed for the creation of a pion; the pion is thus "slow" and flies nearly collinearly with the D^{*+} meson. From the collinearity we can derive an approximate formula that connects the energy of the pion to the energy of the D^* :

$$E_{D^{*+}} \approx \frac{m_{D^*}}{m_{D^*} - m_D} E_\pi \quad . \quad (6.1)$$

Using Eq. 6.1 and the collinearity assumption, the four-momentum of the D^{*+} can be reconstructed using only slow π^+ from the $D^* \rightarrow D\pi$ decay. The D^* momentum reconstruction using this method is illustrated in Fig. 6-11 (bottom left). The candidate for the low-momentum pion was selected among pions with charge opposite to the one of the

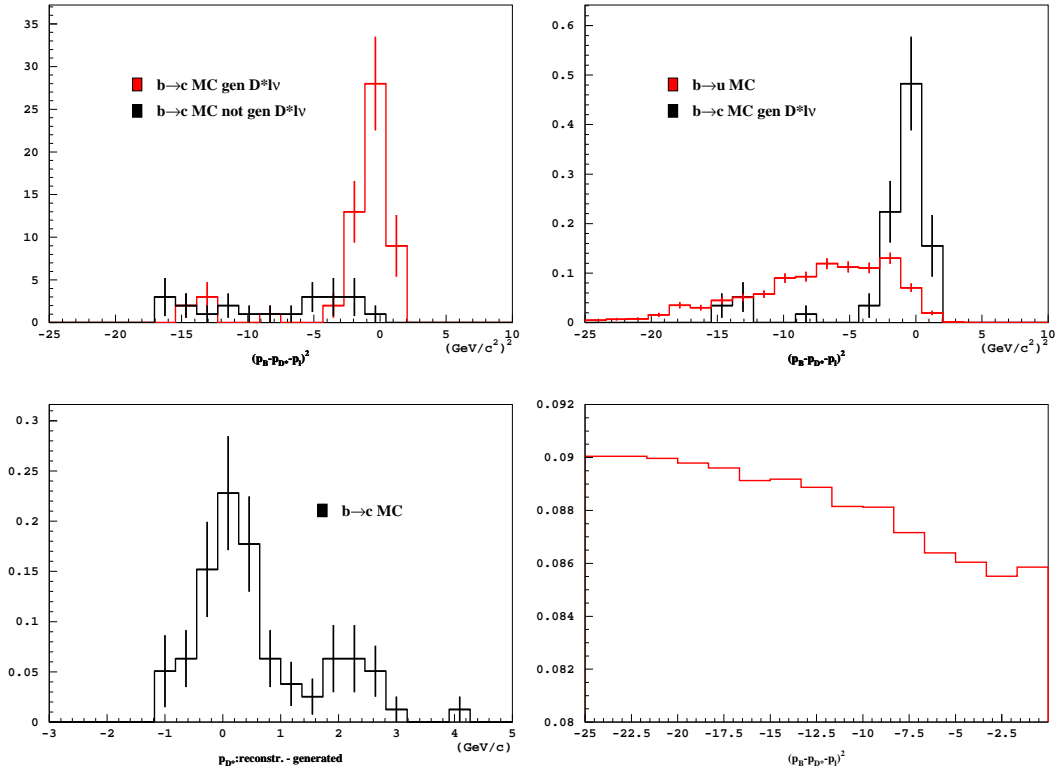


Figure 6-11. Top left: comparison of $m_{\text{miss}}^2(D^*)$ for events with and without a D^{*+} meson. Top right: comparison of $m_{\text{miss}}^2(D^*)$ for $b \rightarrow u$ events and events with D^{*+} meson. Bottom left: The difference between the reconstructed and generated D^* momentum. Bottom right: optimization of $m_{\text{miss}}^2(D^*)$ selection using $\sqrt{N_{b \rightarrow u} + N_{b \rightarrow c}}/N_{b \rightarrow u}$. Obtained minimum at $m_{\text{miss}}^2(D^*) \approx -3 \text{ GeV}^2/c^4$.

lepton, with momentum in the cms satisfying $50 \text{ MeV}/c < |p^*| < 220 \text{ MeV}/c$ and with $|\Delta z| < 2 \text{ cm}$, $|\Delta r| < 1 \text{ cm}$.

The reconstruction is possible only for the charged D^* meson, since the neutral one decays to a slow π^0 ($D^{*0} \rightarrow D^0 \pi^0$), and the purity of reconstructing the decay of a slow neutral pion ($\pi^0 \rightarrow \gamma \gamma$) is very low.

Not to introduce any bias, events with a D^{*+} meson need to be rejected as inclusively as possible, so the missing mass squared of the B_{sig} meson ($m_{\text{miss}}^2(D^*)$) is calculated based only on the four-momenta of the slow pion, the prompt

lepton and the B_{tag} meson:

$$m_{\text{miss}}^2(D^*) \equiv (P_{\mathcal{R}(4S)} - P_{B_{\text{tag}}} - P_{D^*} - P_\ell)^2 \quad . \quad (6.2)$$

Since for $B \rightarrow D^* \ell \nu$ decays the missing momentum is that of the neutrino, the consistency of missing mass squared ($m_{\text{miss}}^2(D^*)$) with zero is taken as a measure of the quality of D^* reconstruction. The distribution of $m_{\text{miss}}^2(D^*)$ is shown in Fig. 6-11(top), comparing the $b \rightarrow c$ events where a D^{*+} meson was present and those where it was not (left), and $m_{\text{miss}}^2(D^*)$ distribution for $b \rightarrow u$ events and $b \rightarrow c$ events where a D^{*+} meson was present. For $b \rightarrow u$ events and those where D^{*+} was not present the distribution is relatively flat and extending down to $-20 \text{ GeV}^2/c^4$, while for events where a D^{*+} meson was present there is a clear peak accumulated around zero. The $m_{\text{miss}}^2(D^*)$ selection was optimized by minimizing $\sqrt{N_{b \rightarrow u} + N_{b \rightarrow c}}/N_{b \rightarrow u}$, where $N_{b \rightarrow u}$ was the number of $b \rightarrow u$ events and $N_{b \rightarrow c}$ the number of $b \rightarrow c$ events after D^* rejection as a function of the lower $m_{\text{miss}}^2(D^*)$ cut (all other event selection criteria are applied). It has a minimum at $m_{\text{miss}}^2(D^*) = -3 \text{ GeV}^2/c^4$ (see Fig. 6-11, bottom right). The events with missing mass greater than $m_{\text{miss}}^2(D^*) > -3 \text{ GeV}^2/c^4$ were rejected.

6.2.6 Missing mass (neutrino reconstruction)

The reconstruction of the semileptonic decay chain of the B_{sig} meson is made difficult by the absence of the neutrino, which can be mimicked by other particles that escaped detection, such as the K_L meson. Missing particles deteriorate the ability to correctly reconstruct inclusive kinematical variables, which are used for extraction of $b \rightarrow u$ decays. To remove events where particles are missing, the missing mass squared m_{miss}^2 of the events is calculated from missing four-momentum P_{miss} , where $m_{\text{miss}}^2 = P_{\text{miss}}^2/c^2$, and used for event rejection. Missing momentum is estimated from four-momenta of B_{tag} and all reconstructed charged particles and photons that pass selection criteria on the signal side:

$$P_{\text{miss}} = P_{\mathcal{R}(4S)} - P_{B_{\text{tag}}} - \sum_{\text{ch.par.}} P - \sum_{\gamma} P \quad . \quad (6.3)$$

If missing momentum comes solely from the neutrino, m_{miss} should be consistent with 0. Possible additional missing momentum comes from other undetected particles, additional particles from beam background and duplicated particles, which result in a non-zero missing mass. The difference between the reconstructed missing momentum and generated neutrino momentum P_{miss} , and between reconstructed missing energy (E_{miss}) and neutrino energy as estimated from $b \rightarrow u$ and $b \rightarrow c$ MC, can be seen in Fig. 6-12. The comparison of P_{miss} and E_{miss} shows that the resolution of the missing momentum is much better than that of the missing energy, since it is not affected by mis-identification. The resolution of the missing momentum is estimated to be $250 \text{ MeV}/c$ for $b \rightarrow c$ transition and $70 \text{ MeV}/c$ for $b \rightarrow u$ transition.

The selection of m_{miss}^2 used in the extraction of charmless semileptonic decays was optimized by minimizing total extraction error, where $\sqrt{N_{b \rightarrow u} + N_{b \rightarrow c}}/N_{b \rightarrow u}$ was used as the estimate for statistical error and systematic and theoretical uncertainty contributions were estimated as described in 6.3.2. The $b \rightarrow u$ and $b \rightarrow c$ contributions normalized to equal number of entries are shown in Fig. 6-13, left, as well as the $b \rightarrow u$ contribution in a realistic scale reflecting the dominance of the $b \rightarrow c$ transition. Lower limit at negative m_{miss}^2 was set at $-1 \text{ GeV}^2/c^4$, while the upper limit of m_{miss}^2 achieved the minimum of total error at $0.5 \text{ GeV}^2/c^4$ (see Fig. 6-13, right). The missing mass squared selection was chosen to be $-1 \leq m_{\text{miss}}^2 \leq 0.5 \text{ GeV}^2/c^4$.

If the missing momentum points in the extreme forward or backward direction, which are not covered by detector elements, it can indicate that other particles apart from the neutrino might have escaped detection. Therefore the events with the missing momentum direction at an angle of less than 18° to the beam-pipe are rejected.

It is worth noting that $b \rightarrow c$ transitions in the $b \rightarrow u$ *enhanced sample* (events where no kaons were reconstructed) are badly reconstructed $b \rightarrow c$ events. More than 95% of them had a kaon in the decay chain that either escaped

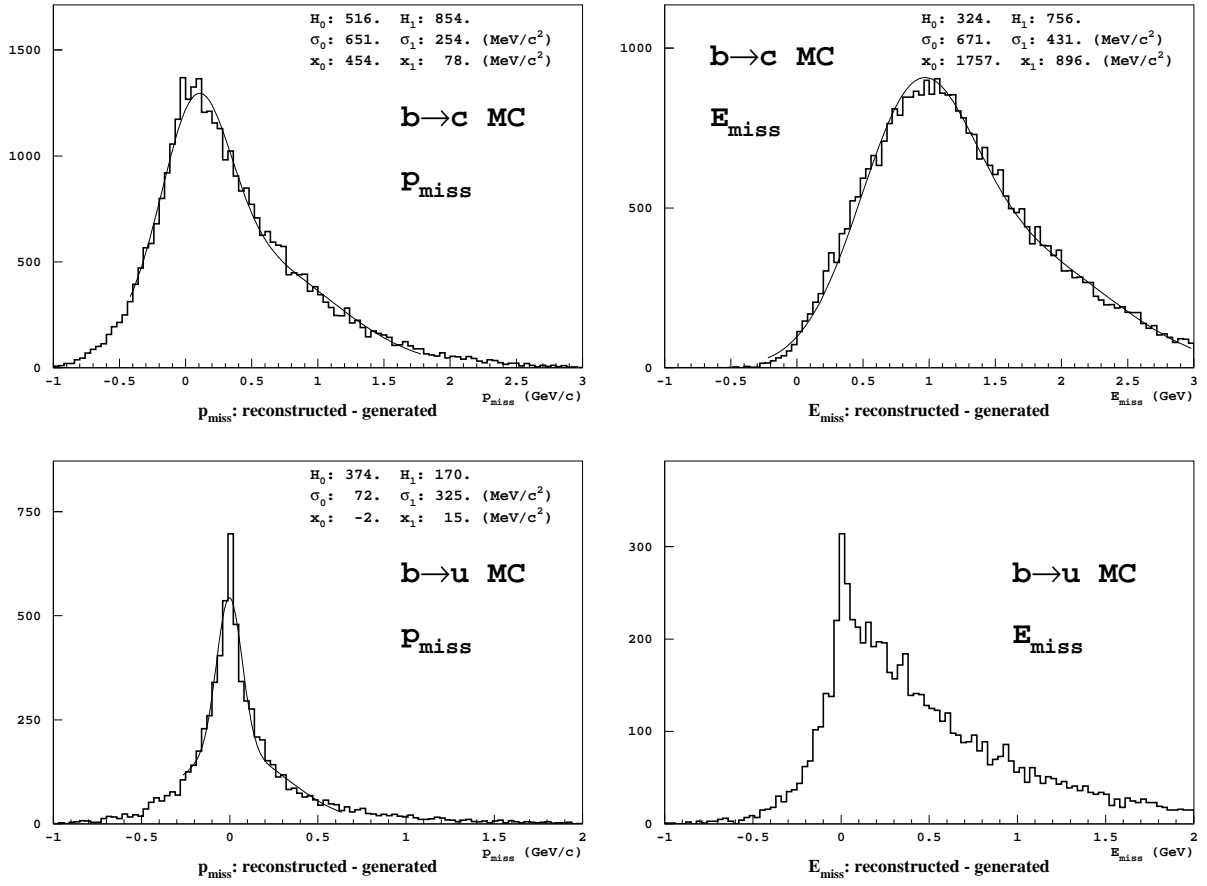


Figure 6-12. The difference between detected and generated missing momentum (left) and missing energy (right) for $b \rightarrow c$ MC (top) and $b \rightarrow u$ MC (bottom). No constraint on missing mass m_{miss} .

detection (mainly K_L mesons), was not reconstructed (for example $K_S \rightarrow \pi^0 \pi^0$), or was misidentified (for example a charged kaon as a pion). The missing mass distribution reflects this fact, the m_{miss}^2 distribution on the $b \rightarrow u$ depleted sample (detected kaon) being much more narrow.

To estimate the level of accuracy in MC simulation of the process, we plot the reconstructed m_{miss}^2 distribution for the $b \rightarrow u$ enhanced sample in Fig. 6-14. The normalization of the simulated contributions for $b \rightarrow u$ and $b \rightarrow c$ transitions is obtained from the fit to the data. The $b \rightarrow c$ contribution is then subtracted from data to enable comparison to the MC simulated $b \rightarrow u$ transition (Fig. 6-14, right).

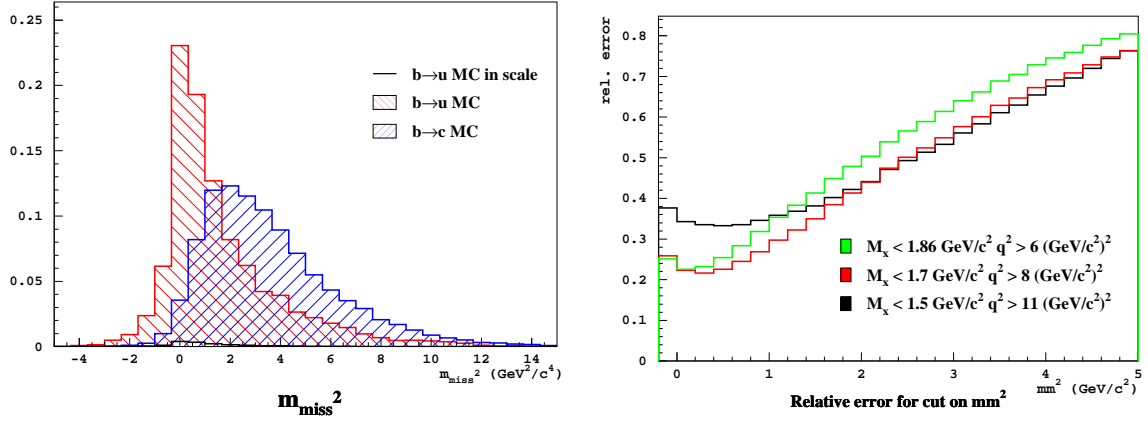


Figure 6-13. Left: comparison of missing mass m_{miss}^2 distributions for $b \rightarrow c$ MC and $b \rightarrow u$ MC (normalized to equal number of entries). Right: relative total error of $b \rightarrow u$ determination for different cuts on m_{miss}^2 ($m_{\text{miss}}^2 < x_{\text{value}}$) plotted separately for the three regions of M_X and q^2 : ($M_X < 1.5 \text{ GeV}/c^2, q^2 > 11 \text{ GeV}^2/c^2$), ($M_X < 1.7 \text{ GeV}/c^2, q^2 > 8 \text{ GeV}^2/c^2$), ($M_X < 1.86 \text{ GeV}/c^2, q^2 > 6 \text{ GeV}^2/c^2$).

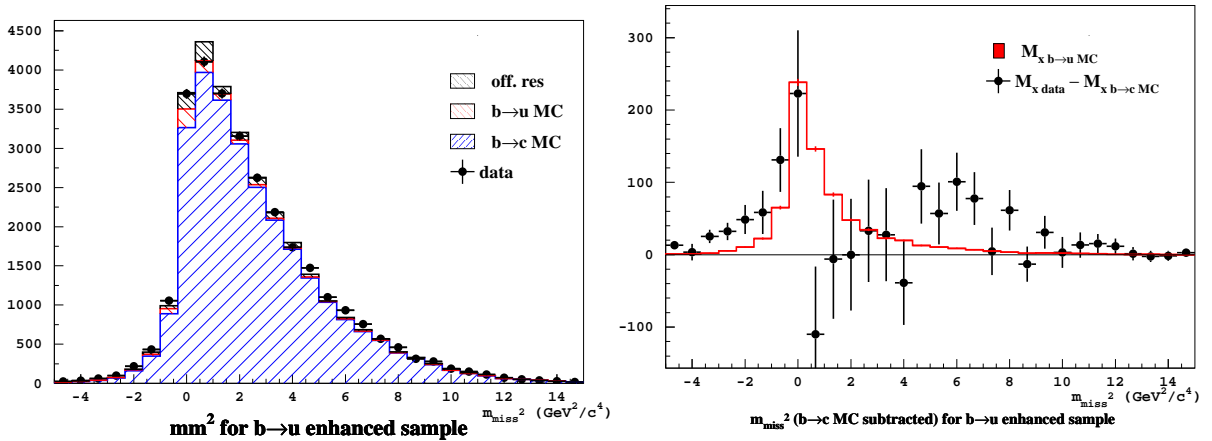


Figure 6-14. Left: Reconstructed missing mass m_{miss}^2 distribution for data, with fitted contributions from $X_c \ell \nu$ and $X_u \ell \nu$ MC simulation: (left) before, and (right) after subtracting the $X_c \ell \nu$ contribution (symbols with error bars), compared to the prediction for $b \rightarrow u$ MC (histogram).

6.2.7 Efficiency of selection criteria

The summary of both cumulative and single efficiencies with their relative errors is presented for different selection criteria. The starting selection is with at least one fast lepton. The criteria are as follows:

cut	description
lept	lepton with $p^* \geq 1 \text{ GeV}/c$
1 lept	no other leptons in the event
ℓ^\pm/B^\pm	lepton charge correlation in case of B^\pm
$\Delta q = 0$	charge of the event is zero
$\cos \theta_{mm}$	missing momentum should not point in the beam direction
$N(K) = 0$	no detected kaons
M_{mm}^2 cut	$-1 \leq m_{miss}^2 \leq 0.5 \text{ GeV}^2/c^4$
D^* recon	partial recon. of D^* , $m_{miss(D^*)}^2 > -3 \text{ GeV}^2/c^4$

6.2.7.1 Cumulative efficiency

The cumulative efficiency for passing a set of selection criteria is presented. The order of applying selection criteria follows that in the table. (The values in brackets are relative statistical errors of the estimated efficiency.)

	cut	on res.	$b \rightarrow c$ MC	$b \rightarrow u$ MC	off res.
B^+	lept	1.000(0.47%)	1.000(0.42%)	1.000(1.97%)	1.000(8.01%)
	1 lept	0.887(0.49%)	0.873(0.43%)	0.945(2.00%)	0.894(8.24%)
	ℓ^\pm/B^\pm	0.803(0.50%)	0.789(0.45%)	0.927(2.01%)	0.670(8.94%)
	$\Delta q = 0$	0.471(0.59%)	0.470(0.52%)	0.625(2.25%)	0.356(11.05%)
	$\cos \theta_{mm}$	0.459(0.59%)	0.458(0.53%)	0.610(2.26%)	0.340(11.24%)
	$N(K) = 0$	0.235(0.76%)	0.235(0.68%)	0.565(2.32%)	0.212(13.55%)
	M_{mm}^2 cut	0.045(1.61%)	0.045(1.42%)	0.255(3.09%)	0.045(27.32%)
	D^* recon	0.045(1.61%)	0.045(1.42%)	0.255(3.09%)	0.045(27.32%)

	cut	on res.	$b \rightarrow c$ MC	$b \rightarrow u$ MC	off res.
B^0	lept	1.000(0.61%)	1.000(0.54%)	1.000(2.51%)	1.000(9.13%)
	1 lept	0.867(0.63%)	0.853(0.56%)	0.942(2.55%)	0.867(9.47%)
	ℓ^\pm/B^\pm	0.867(0.63%)	0.853(0.56%)	0.942(2.55%)	0.867(9.47%)
	$\Delta q = 0$	0.425(0.79%)	0.437(0.69%)	0.613(2.88%)	0.404(12.03%)
	$\cos \theta_{mm}$	0.414(0.80%)	0.426(0.70%)	0.602(2.90%)	0.392(12.17%)
	$N(K) = 0$	0.247(0.97%)	0.251(0.85%)	0.563(2.96%)	0.287(13.66%)
	M_{mm}^2 cut	0.044(2.10%)	0.045(1.84%)	0.259(3.92%)	0.079(23.83%)
	D^* recon	0.036(2.31%)	0.035(2.07%)	0.250(3.97%)	0.075(24.44%)

6.2.7.2 Single efficiency

The efficiency for passing each selection criterion, starting from a sample with at least one lepton with $p^* \geq 1 \text{ GeV}/c$. (The values in brackets are relative statistical errors of the estimated efficiency.)

	cut	on res.	$b \rightarrow c$ MC	$b \rightarrow u$ MC	off res.
B^+	lept	1.000(0.47%)	1.000(0.42%)	1.000(1.97%)	1.000(8.01%)
	1 lept	0.887(0.49%)	0.873(0.43%)	0.945(2.00%)	0.894(8.24%)
	ℓ^\pm/B^\pm	0.899(0.48%)	0.896(0.43%)	0.978(1.98%)	0.737(8.69%)
	$\Delta q = 0$	0.570(0.55%)	0.582(0.49%)	0.659(2.21%)	0.487(9.89%)
	$\cos \theta_{mm}$	0.970(0.47%)	0.970(0.42%)	0.975(1.98%)	0.958(8.09%)
	$N(K) = 0$	0.544(0.56%)	0.559(0.49%)	0.916(2.02%)	0.619(9.16%)
	M_{mm}^2 cut	0.246(0.75%)	0.252(0.66%)	0.361(2.70%)	0.343(11.20%)
	D^* recon	1.000(0.47%)	1.000(0.42%)	1.000(1.97%)	1.000(8.01%)

	cut	on res.	$b \rightarrow c$ MC	$b \rightarrow u$ MC	off res.
B^0	lept	1.000(0.61%)	1.000(0.54%)	1.000(2.51%)	1.000(9.13%)
	1 lept	0.867(0.63%)	0.853(0.56%)	0.942(2.55%)	0.867(9.47%)
	ℓ^\pm/B^\pm	1.000(0.61%)	1.000(0.54%)	1.000(2.51%)	1.000(9.13%)
	$\Delta q = 0$	0.496(0.75%)	0.519(0.65%)	0.648(2.83%)	0.425(11.82%)
	$\cos \theta_{mm}$	0.970(0.61%)	0.971(0.54%)	0.979(2.53%)	0.954(9.24%)
	$N(K) = 0$	0.597(0.70%)	0.610(0.62%)	0.920(2.57%)	0.650(10.28%)
	M_{mm}^2 cut	0.235(0.99%)	0.234(0.88%)	0.380(3.39%)	0.342(12.79%)
	D^* recon	0.738(0.66%)	0.737(0.59%)	0.903(2.58%)	0.779(9.75%)

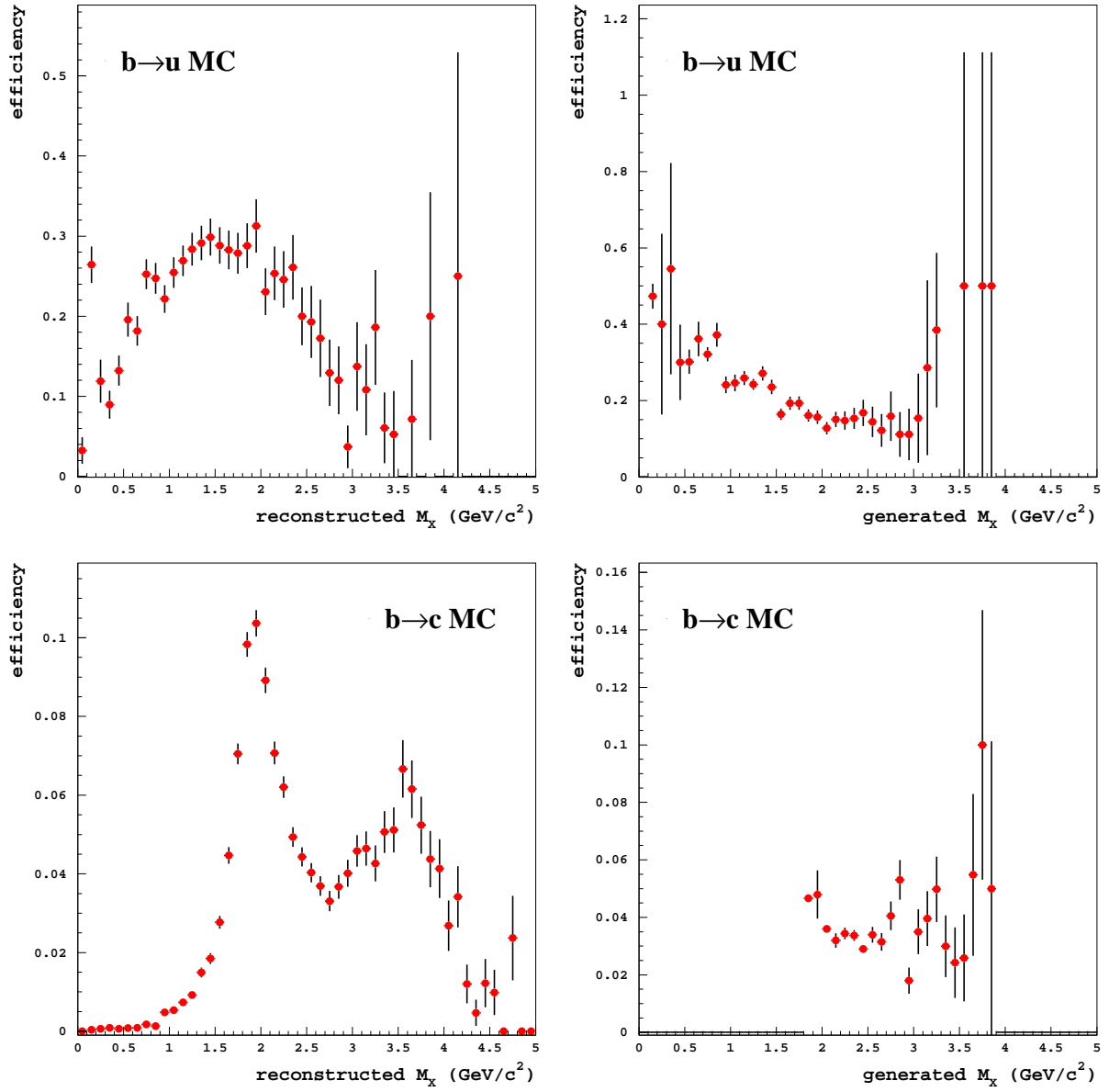


Figure 6-15. The efficiency of selection criteria as a function of reconstructed (left) and generated (right) invariant hadronic mass M_X : top for $b \rightarrow u$ MC and bottom for $b \rightarrow c$ MC.

6.3 Separation using inclusive kinematical variables

In previous sections particles were identified and selected in a way to offer optimized reconstruction of inclusive kinematical variables and then the quality of event reconstruction was estimated to remove badly reconstructed events. In the remaining events the inclusive kinematical variables are reconstructed, and kinematical regions are chosen in which the $b \rightarrow u$ transition is enhanced (with respect to $b \rightarrow c$) to extract its contribution as accurately as possible.

6.3.1 Inclusive kinematical variables

A semileptonic transition of a b quark into a c or a u quark proceeds by emitting a charged lepton and its neutrino: a B meson therefore decays into a lepton pair and one or more hadrons. No specific hadronic decay products are reconstructed in an inclusive analysis and the kinematics of the hadronic part of the decay is described only by its total hadronic four-momentum P_X . We reconstruct two inclusive hadronic variables from P_X , the hadronic invariant mass $M_X^2 = P_X^2/c^2$ and the proposed variable $P_+ = E_X/c - |\vec{p}|_X$ [2], where E_X is the energy and \vec{p}_X the vector momentum of the hadronic part, as measured in the rest frame of the B meson. Since the neutrino momentum is missing, we can reconstruct the total leptonic four-momentum q only indirectly, by noting that the sum of the hadronic and the leptonic four-momenta have to add into the four-momentum of the B_{sig} meson.

In the next sections we describe the construction of the inclusive variables M_X , P_+ and q and estimate the quality of reconstruction based on MC simulation. We optimize the selection criteria for extracting the $b \rightarrow u$ decays and present the obtained kinematical variable distributions.

6.3.1.1 M_X distribution

Hadronic invariant mass M_X seems to be the most suitable variable for separating between $b \rightarrow u$ and $b \rightarrow c$ transitions (see Fig. 6-16). Due to the fact that a c quark is much heavier than a u quark, the presence of a D meson in the $b \rightarrow c$ transition results in a large hadronic invariant mass $M_X \geq M_D$, while 80% of the $b \rightarrow u$ decays should have the hadronic invariant mass below the mass of the lightest charm meson. The imperfect reconstruction of M_X due to lost particles, inaccurate B_{tag} reconstruction or particle mis-identification smears the distributions of M_X for $b \rightarrow u$ and $b \rightarrow c$ transitions and the overlap becomes much larger (see Fig. 6-16, top).

Invariant hadronic mass is calculated from the hadronic four-momentum P_X ($M_X^2 = P_X^2/c^2$), where P_X is obtained from four-momenta of all reconstructed charged particles and photons that pass selection criteria, except that of the prompt lepton (P_ℓ):

$$P_X = \sum_{\text{ch.par.}} P + \sum_{\gamma} P - P_\ell \quad (6.4)$$

The hadronic invariant mass M_X for $b \rightarrow u$ and $b \rightarrow c$ transitions, as obtained from MC simulation, is shown in Fig. 6-16 (top), illustrating the possibility for separation of the two transitions using this variable.

6.3.1.2 Momentum transfer distribution

Momentum transfer q is the four-momentum of the lepton pair produced in the semileptonic decay. Due to a larger mass of the c quark the magnitude of q^2 is in general larger for $b \rightarrow u$ transition than for $b \rightarrow c$ transitions (see Fig. 6-17). The total four-momentum of the B meson in semileptonic decays is the sum of the hadronic and leptonic contribution: $P_B = P_X + q$. It follows that for $b \rightarrow c$ transition $q^2/c^2 \leq (M_B - M_D)^2$ (neglecting the product of momenta due to large mass), setting the kinematical limit for $b \rightarrow c$ at $q^2 \approx 12.5 \text{ GeV}^2/c^2$, while q^2 in $b \rightarrow u$

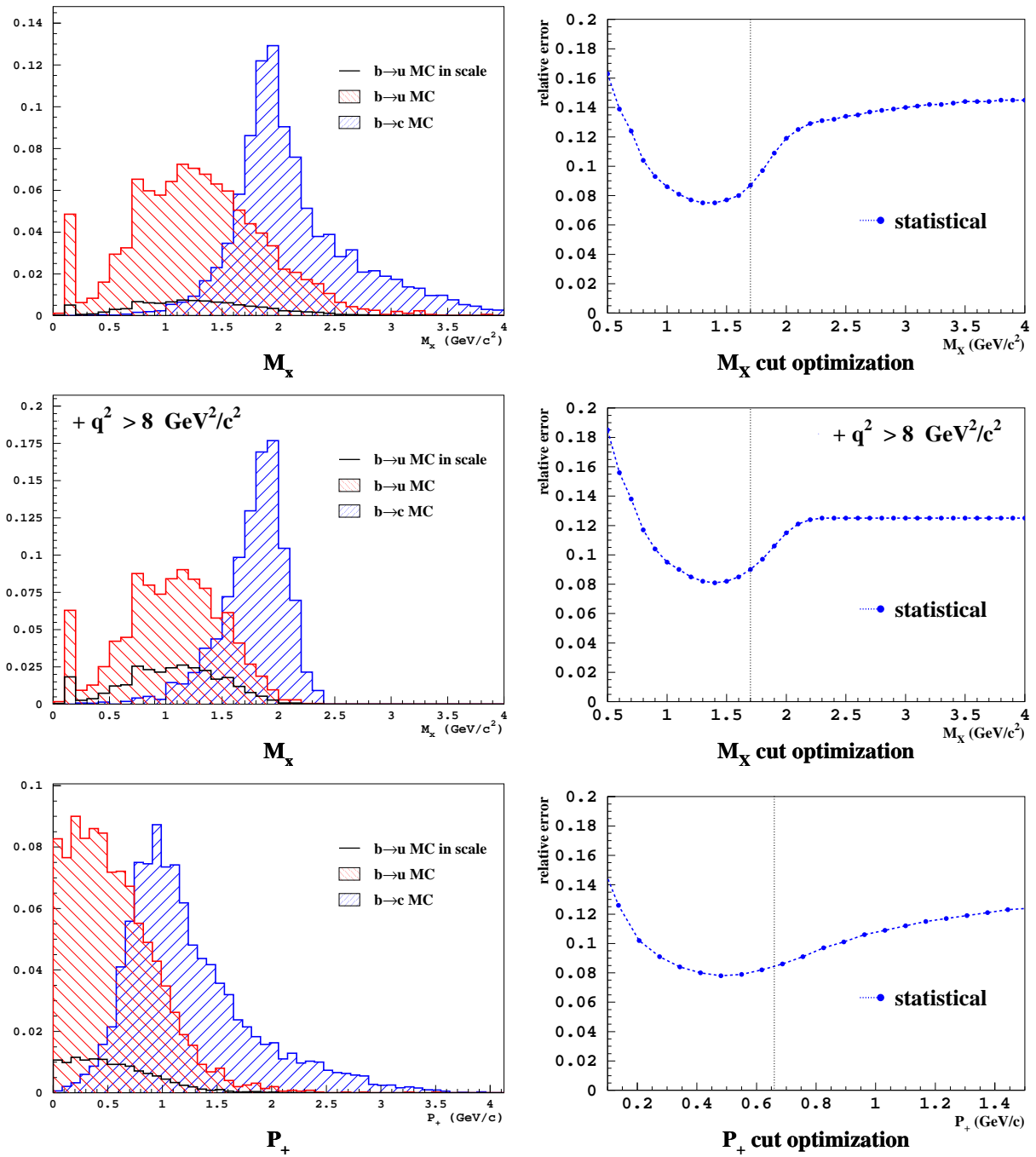


Figure 6-16. Left: comparison of inclusive kinematical distributions for $b \rightarrow c$ MC and $b \rightarrow u$ MC (normalized to equal number of entries). Plots for M_X (top), M_X with additional $q^2 > 8 \text{ GeV}^2/c^2$ (middle), and P_+ (bottom). Right: comparison of the estimated relative statistical errors for $b \rightarrow u$ extraction using each variable on the left.

transitions can take higher values (see Fig.6-17, left). Momentum transfer can thus be used for the separation of the two transitions, although there is a significant overlap of q^2 for the two transitions, and only about 20% of the $b \rightarrow u$ phase space is in the region where $b \rightarrow c$ is kinematically suppressed. Nevertheless, a selection using q^2 is favored from the point of view of the theoretical calculation, since it reduces the theoretical sensitivity to non-perturbative effects. A moderate selection of $q^2 > 8 \text{ GeV}^2/c^2$ was proposed [1] in combination with the M_X selection, and is in this analysis compared to the kinematical signal region selection using only M_X .

The momentum transfer is obtained by subtracting four-momenta for which energy and momentum were obtained separately:

$$q = P_{Y(4S)} - P_{B_{\text{tag}}} - \sum_{\text{ch.par.}} P - \sum_{\gamma} P + P_{\ell} = P_{B_{\text{sig}}} - P_X \quad , \quad (6.5)$$

and therefore q^2 can have a negative value. Since the value of q^2 does not have a distinct interpretation like M_X (where it can be compared to the masses of different mesons) the momentum transfer squared q^2 is used in the selection, instead.

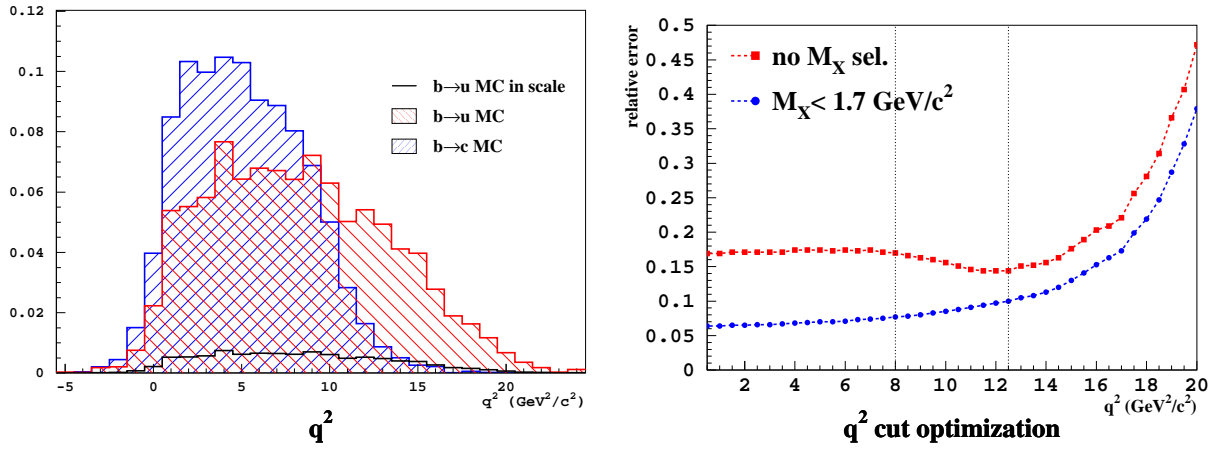


Figure 6-17. Left: comparison of q^2 distributions for $b \rightarrow c$ MC and $b \rightarrow u$ MC (normalized to equal number of entries). Right: comparison of estimated relative statistical errors for $b \rightarrow u$ separation with $q^2 > x_{\text{cut}}$ selection with and without the $M_X < 1.7 \text{ GeV}/c^2$.

The effect of the proposed additional q^2 selection on the M_X is shown in Fig. 6-16 (middle).

6.3.1.3 P_+ distribution

Tightly connected to M_X ($M_X^2 = P_+ P_- / c^2$) the variables $P_{\pm} = E_X \mp |\vec{p}_X|$ also have power to separate between $b \rightarrow u$ and $b \rightarrow c$ transitions. A selection using P_+ was proposed [2] to have an advantage in the theoretical treatment, and since compared to M_X selection the $b \rightarrow c$ background should start much more gradually due to a buffer zone between a P_+ selection and the part of phase space occupied by $b \rightarrow c$ events (see Fig.3-4). The kinematical limit for $b \rightarrow c$ (disregarding experimental effects) is

$$P_+/c \geq \frac{M_D^2}{M_B} \approx 0.66 \text{ GeV}/c \quad (6.6)$$

The distribution of P_+ for $b \rightarrow u$ and $b \rightarrow c$ transitions, as obtained from MC simulation, is shown in Fig. 6-16 (bottom), where its separation capability can be compared with the M_X distributions with and without the additional q^2 selection (Fig. 6-16 top and middle).

6.3.2 Signal region optimization

We would like to extract the number of $b \rightarrow u$ events from three kinematical phase space selections in which $b \rightarrow u$ decays are enhanced compared to $b \rightarrow c$ decays. The three choices include (1) a selection using M_X , (2) a selection using M_X and q^2 , and (3) a selection using P_+ , which we will denote as M_X , M_X/q^2 and P_+ signal region, respectively.

The three selections are highly correlated with each other, M_X/q^2 for example being a complete sub-sample of the M_X signal region. Therefore, we will not attempt to average the three measurements, since the correlations of systematic errors will be hard to estimate correctly and due to high correlation the improvement will not be significant. The high correlation of measurements on the other hand is ideal for comparison of the three selections, since the measurement will be done on the same particle and event selection, and will directly address the possible advantages of each signal region selection.

An optimization of signal region selections was performed by minimizing the total error of such extraction. Total error was composed of statistical, systematic and theoretical errors, added in quadrature:

$$\sigma_{\text{tot}}^2 = \sigma_{\text{stat}}^2 + \sigma_{\text{syst}}^2 + \sigma_{\text{theo}}^2 \quad . \quad (6.7)$$

The relative statistical error was approximated by

$$\sigma_{\text{stat}} = \frac{\sqrt{N_{b \rightarrow u} + N_{b \rightarrow c}}}{N_{b \rightarrow u}} \quad (6.8)$$

which represents the relative statistical fluctuation of a sample with $N_{b \rightarrow u}$ signal events over $N_{b \rightarrow c}$ background events. The branching fractions for $B \rightarrow X_u \ell \nu$ and $B \rightarrow X \ell \nu$ decays were taken to be $\mathcal{B}(B \rightarrow X_u \ell \nu) = 2 \times 10^{-3}$ and $\mathcal{B}(B \rightarrow X \ell \nu) = 10.7 \times 10^{-2}$, while the efficiencies for reconstruction selections were taken from MC simulation.

The relative systematic error used for the optimization of the signal region was estimated using systematic error estimation results from a previous $|V_{ub}|$ analysis at Belle [61]. It was found that for the signal-to-background ratio of the published analysis $R_{\text{SB}}^0 = N_{b \rightarrow u}^0/N_{b \rightarrow c}^0 = 0.18$ the relative systematic error was $\sigma_{\text{syst}}^0 = 0.186$. The relative systematic error of $b \rightarrow c$ contribution estimation of course increases with $N_{b \rightarrow c}$, and decreases with $N_{b \rightarrow u}$; the functional relation was estimated to be proportional to $N_{b \rightarrow c}$ and inversely proportional to $N_{b \rightarrow u}$. After correcting the systematic error σ_{syst}^0 for a smaller $b \rightarrow c$ MC statistics in the current analysis due to small B_{tag} reconstruction efficiency, $\sigma_{\text{syst}}^0 \rightarrow 0.22$, we parameterize the relative systematic error as:

$$\sigma_{\text{syst}} = \sigma_{\text{syst}}^0 \cdot \frac{R_{\text{SB}}^0}{R_{\text{SB}}} = 0.22 \cdot 0.18 \cdot \frac{N_{b \rightarrow c}}{N_{b \rightarrow u}} \quad (6.9)$$

The theoretical error was composed of two contributions, the perturbative error contribution due to truncating the perturbation expansion (see Sec. 3.2.1), and the nonperturbative contribution from shape function parameter determination. The latter is experimental in nature, since the parameters are obtained from experiment, but it nevertheless represents an uncertainty in the theoretical estimation. The two contributions are estimated using an inclusive generator with implemented theoretical calculations from Ref. [3]: the uncertainty due to truncation was estimated by varying the mass scales of the theoretical prescriptions used [3], while the shape function parameter determination uncertainty was estimated by varying the shape function parameters within their respective errors and by varying the functional models used in shape function parameterization (see Sec. 3.1.3).

The statistical error dependence on the lower limit of q^2 selection with and without an additional M_X selection is shown in Fig. 6-17. Statistically there is a weak preference for a selection of $q^2 > 12.5 \text{ GeV}^2/c^2$ (right vertical line), which corresponds to the kinematical q^2 limit of $b \rightarrow c$ decays. When an additional signal region selection $M_X < 1.7 \text{ GeV}/c^2$ is applied, statistical error prefers the removal of a lower q^2 limit (the obtained minimum is at

$q^2 = 0$). Despite this fact a moderate selection of $q^2 > 8 \text{ GeV}^2/c^2$ (left vertical line) was chosen to help reduce the theoretical uncertainty due to the shape function parameter determination.

The statistical error dependence on the upper limits of M_X and P_+ in the M_X , M_X/q^2 and P_+ signal regions can be seen in Fig. 6-16 (right, respectively from top). Judging from the minimization of statistical error only, there is a clear preference for a signal region selection using an upper limit on M_X or P_+ .

When taking into account also the systematic and theoretical errors, the optimal selection is shifted towards higher values of upper limits of M_X and P_+ (see Fig. 6-18). The selected signal regions are (1) $M_X < 1.7 \text{ GeV}/c^2$, (2) $M_X < 1.7 \text{ GeV}/c^2$ with $q^2 > 8 \text{ GeV}^2/c^2$ and (3) $P_+ < 0.66 \text{ GeV}/c$.

The result of the optimization are the following conclusions: the optimal value of M_X is practically not affected by the additional q^2 selection; without it the minimum is at $M_X \approx 1.6 \text{ GeV}/c^2$ and with it at $M_X \approx 1.7 \text{ GeV}/c^2$. While the total error is larger for the case of additional q^2 requirement, taking into account that this is an approximation we conclude they are too close to have a clear preference for one or the other. Although the strict minimum for the case with no q^2 corresponds to $M_X \approx 1.6 \text{ GeV}/c^2$, we decide to use the same M_X selection of $M_X \approx 1.7 \text{ GeV}/c^2$ for both M_X and M_X/q^2 signal regions, which will enable us to discern the effect of applying the additional q^2 selection. The selection of $M_X \approx 1.7 \text{ GeV}/c^2$ was also used for $|V_{ub}|$ determination by the previous Belle analysis [61].

The optimized selection for M_X lies $\approx 160 \text{ MeV}/c^2$ below the kinematical limit of M_X for $b \rightarrow c$ decays $M_X = M_{D^0} \approx 1864 \text{ MeV}/c^2$, which is caused by experimental effects of finite detector resolution and undetected particles. Optimal P_+ selection on the other hand corresponds to the kinematical limit $P_+/c \approx M_D^2/M_B$. The total errors from all three signal region selections can be compared in Fig. 6-18 (bottom right), where the total error distributions are plotted on the same plot and the x -axis presents both M_X and P_+ . The three total errors in minima are comparable in size, with the one from M_X being slightly smaller. The simulation shows that the three signal regions are all competitive selections for extraction of signal $b \rightarrow u$ events.

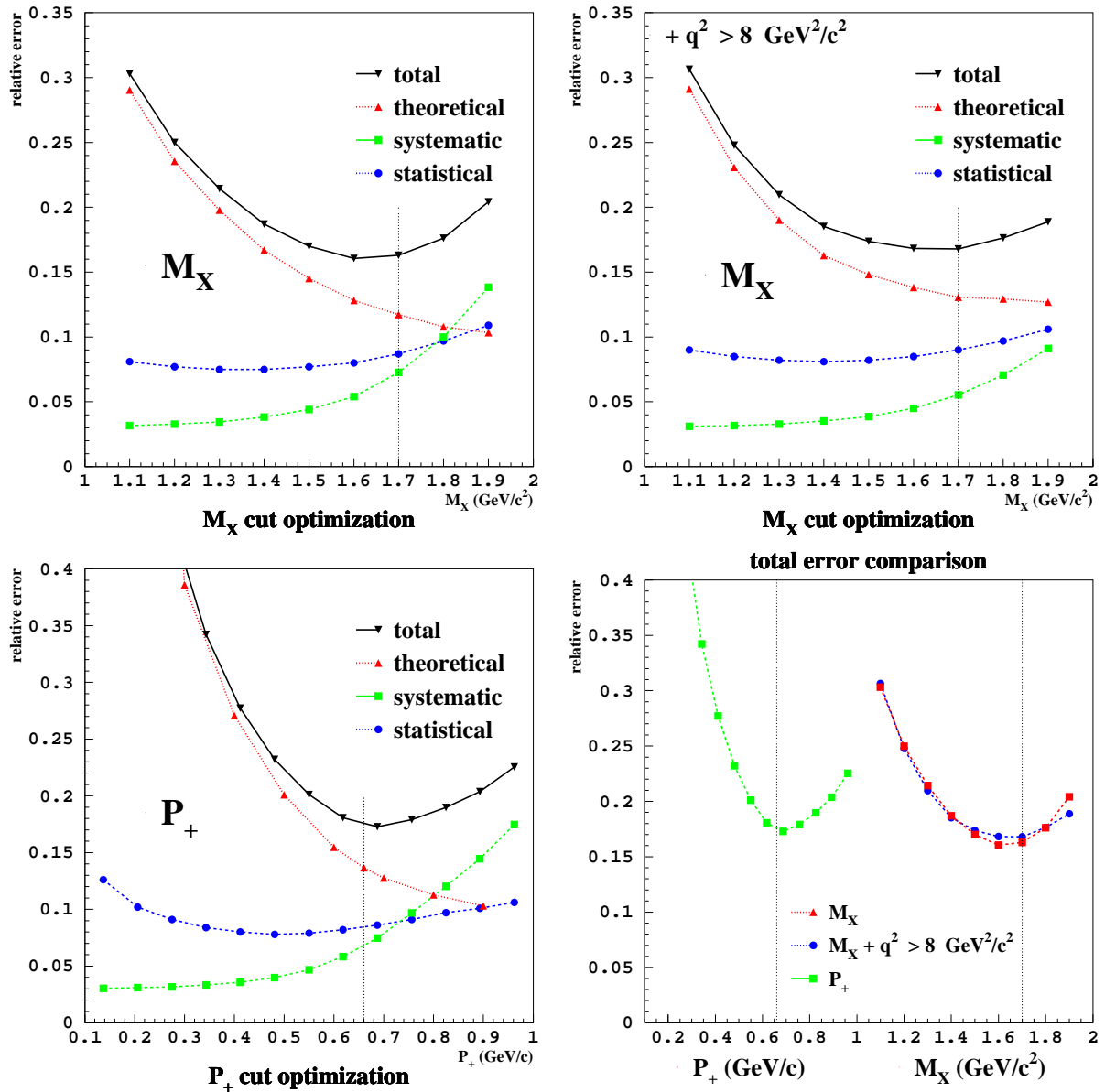


Figure 6-18. Break-down of estimated uncertainties for the M_X (top left), M_X with additional $q^2 > 8 \text{ GeV}^2/c^2$ (top right), and P_+ (bottom left), for different choices of cuts. Bottom right: the comparison of the total errors for the three signal regions using different choices of cuts.

6.3.3 Resolution of reconstructed variables

One of the important estimates of inclusive variable reconstruction quality is the resolution of the variables. It is estimated from the difference between reconstructed and generated values of a variable: the difference is fitted with two Gaussians and the width of the narrow (σ_{narrow}) and the wide (σ_{wide}) Gaussian are taken as the measure for the reconstruction resolution (see Fig. 6-19). The fraction of events in one and the other is also an important indicator of reconstruction condition. The information on reconstruction resolution is summarized in Tab. 6-3.

M_X	σ_{narrow} (MeV/ c^2)	σ_{wide} (MeV/ c^2)	$\mathcal{F}_{\text{narrow}}$	x_0 (MeV/ c^2)	x_1 (MeV/ c^2)
$b \rightarrow c$	179 ± 10	342 ± 10	0.64	-112	-451
$b \rightarrow u$	37 ± 10	256 ± 10	0.27	-3	60

q^2	σ_{narrow} (MeV ² / c^4)	σ_{wide} (MeV ² / c^4)	$\mathcal{F}_{\text{narrow}}$	x_0 (MeV ² / c^4)	x_1 (MeV ² / c^4)
$b \rightarrow c$	983 ± 10	2618 ± 10	0.58	938	4112
$b \rightarrow u$	302 ± 10	1309 ± 10	0.27	116	355

P_+	σ_{narrow} (MeV/ c)	σ_{wide} (MeV/ c)	$\mathcal{F}_{\text{narrow}}$	x_0 (MeV/ c)	x_1 (MeV/ c)
$b \rightarrow c$	133 ± 10	416 ± 10	0.47	-53	-4
$b \rightarrow u$	7 ± 10	165 ± 10	0.24	0	57

Table 6-3. Summary of reconstruction resolutions for M_X (top), q^2 (middle), and P_+ (bottom). $\mathcal{F}_{\text{narrow}}$ is the fraction of events that correspond to reconstruction resolution σ_{narrow} ($\mathcal{F}_{\text{wide}} \equiv 1 - \mathcal{F}_{\text{narrow}}$). Values of x_0 and x_1 are the positions of the peak in narrow and wide contributions, respectively.

Some interesting conclusions can be drawn from the fits presented in Fig. 6-19: the contribution to the longer tail at negative values of $\Delta M_X = M_X^{\text{rec.}} - M_X^{\text{gen.}}$ for $b \rightarrow c$ events is entirely due to events with M_X reconstructed below $1.7 \text{ GeV}/c^2$ (top left, red), where there should be no $b \rightarrow c$ contribution. For events with $M_X > 1.7 \text{ GeV}/c^2$ the ΔM_X can be described with a single Gaussian with a resolution of $\sigma = 140 \text{ MeV}/c^2$: $b \rightarrow c$ events with M_X in the $b \rightarrow c$ region have a relatively well reconstructed M_X , which is important for an accurate normalization of $b \rightarrow c$ background. This is not the case for q^2 distribution ($b \rightarrow c$), where events with $q^2 > 12 \text{ GeV}^2/c^4$ are only a part of the bump at high $\Delta q^2 = q^2_{\text{rec.}} - q^2_{\text{gen.}}$ (middle left, red). The reason is that the reconstructed M_X does not depend on the momentum of B_{tag} ($P_{B_{\text{tag}}}$), while q^2 does.

The resolution crucially depends on the separation of detected particles between the tagging and signal sides and on the hermeticity of the detector. The narrow contribution in the $b \rightarrow u$ plot for P_+ with a resolution of $\approx 60 \text{ GeV}/c^2$ represents events where all particles are detected and correctly assigned to B_{tag} and B_{sig} mesons, which happens in 27% of the cases.

6.3.4 Reconstructed kinematical variables

We reconstruct the M_X , q^2 and P_+ distributions in data and compare them to the expected distributions obtained from $b \rightarrow u$ and $b \rightarrow c$ MC simulation. Both MC distributions are fitted to the distribution in data to obtain their relative normalization. The $b \rightarrow c$ MC contribution is then subtracted to obtain the distribution of excess events, which is compared to the estimated MC contribution. The Fig. 6-20 (left) shows the data distribution with the two superimposed

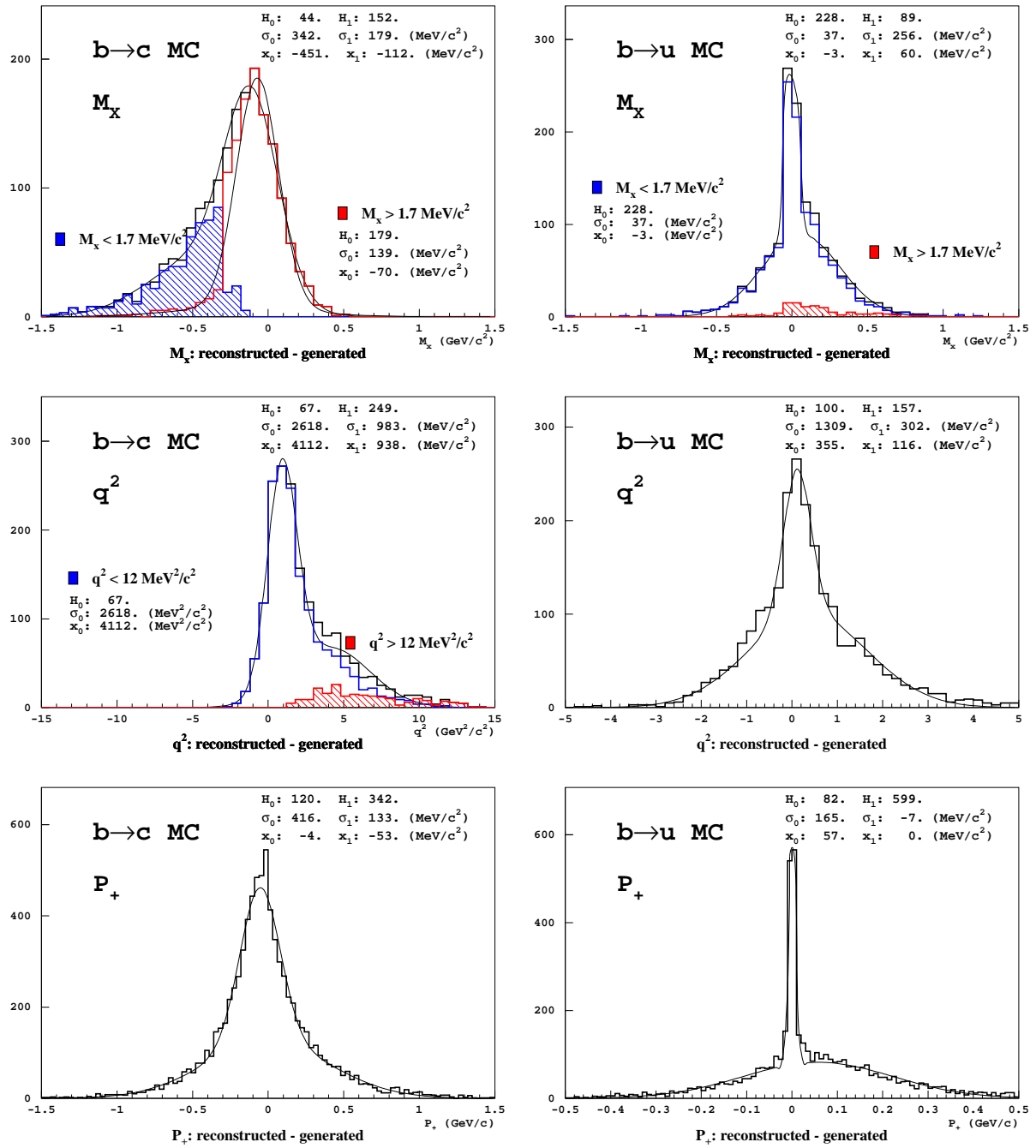


Figure 6-19. Resolution of inclusive kinematical variables M_X (top), q^2 (middle) and P_+ (bottom) estimated from the distribution of the difference between the reconstructed and generated value of the quantity. Plots for $b \rightarrow c$ MC (left) and the same distribution for $b \rightarrow u$ MC (right), all plots for the “ $b \rightarrow u$ enhanced” sample.

MC contributions. In Fig. 6-20 (left) the subtracted distribution is compared to the $b \rightarrow u$ MC simulation. The limits of the signal regions, determined by optimization in Sec. 6.3.2, are denoted by a vertical line. Within the signal regions the subtracted distributions show a good agreement with $b \rightarrow u$ MC simulation.

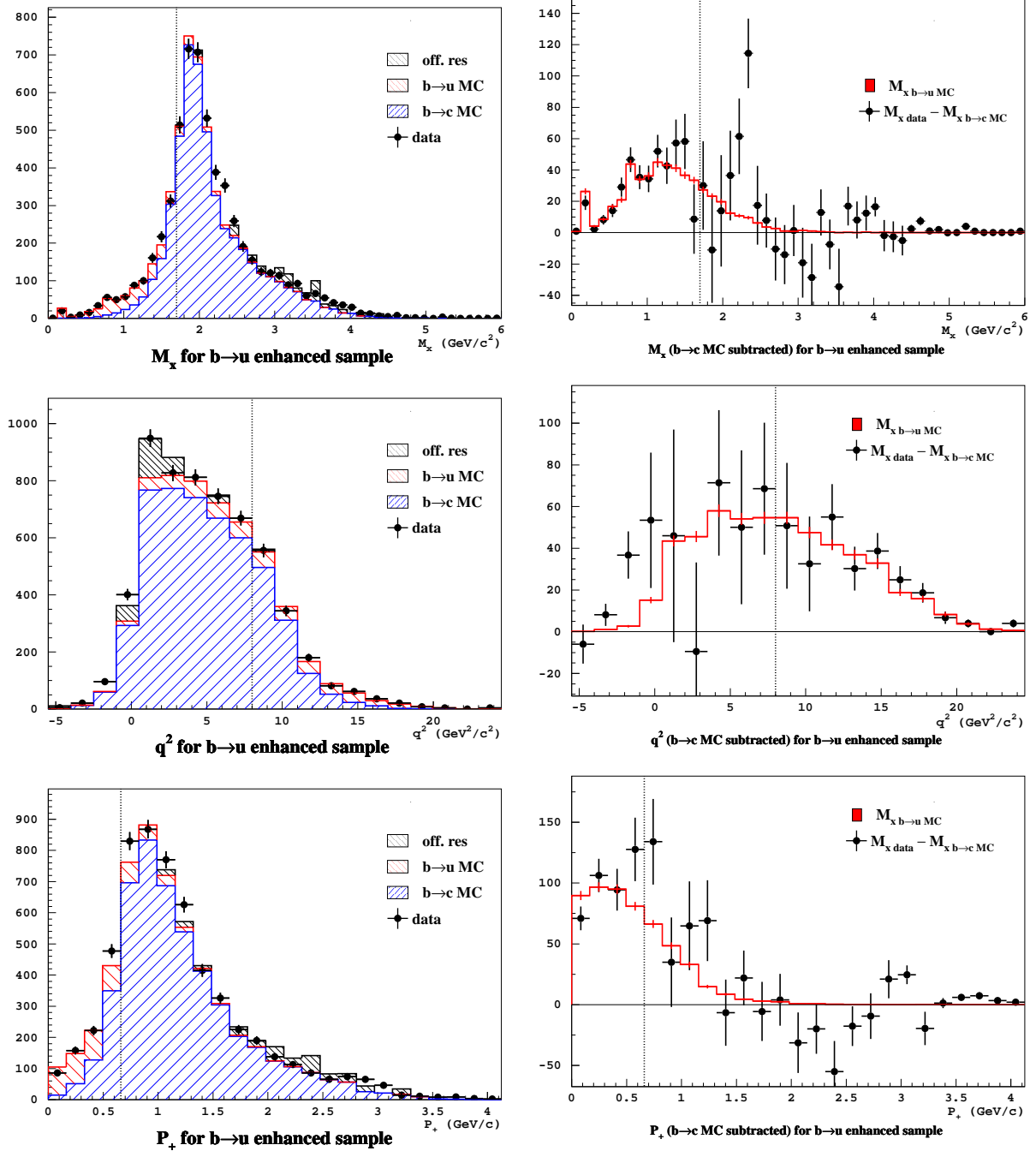


Figure 6-20. Inclusive kinematical distributions M_X (top), q^2 (middle) and P_+ (bottom) with fitted contributions from $X_c \ell \nu$ and $X_u \ell \nu$ MC simulation: (left) before, and (right) after subtracting the $X_c \ell \nu$ contribution (symbols with error bars), shown with the prediction for $b \rightarrow u$ MC (histogram).

6.3.5 Monte Carlo simulation of $b \rightarrow c$ decays

The measurement of $|V_{ub}|$ is highly dependent on an accurate MC simulation of the $b \rightarrow c$ transition, since it is used to estimate the remaining contribution of $b \rightarrow c$ decays in the signal region. The MC generation is a lengthy process and it would not be rational to re-generate the whole amount of MC whenever the values of the input parameters change with a more accurate determination. Instead, the MC distributions are reweighted to correspond to the most recent values.

The tuned simulation is compared to the data on the $b \rightarrow u$ depleted sample, where the contribution of $b \rightarrow u$ is highly suppressed.

6.3.5.1 Fine-tuning of $b \rightarrow c$ MC simulation

Generated form factors used in the decay of $D\ell\nu$ were calculated according to the ISGW2 model [38]. For the purpose of this analysis the MC simulation was reweighted to a HQET-based parameterization following [62], with the form factor slope parameter $\rho_D^2 = 1.15 \pm 0.16$ [63, 10].

For the form factors in the decay of $D^*\ell\nu$ a linear approximation was used, which turned out to be not accurate enough, and was changed to a nonlinear one with slope at zero recoil $\rho^2 = 1.51 \pm 0.13$ [64]. The vector and axial form factor ratios $R_1 = 1.18$ and $R_2 = 0.71$ were set according to [63]. The generated q^2 distributions were rescaled according to corrected form factor models (see Fig. 6-21).

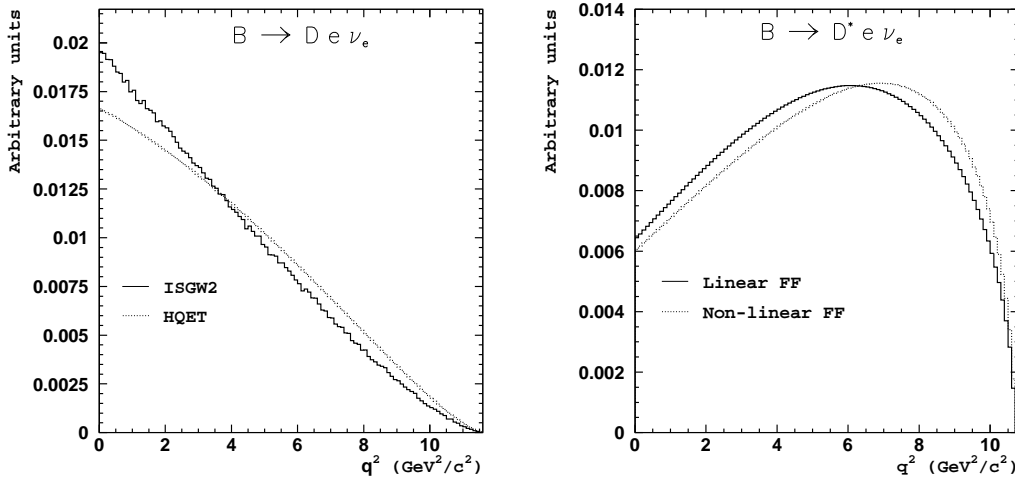


Figure 6-21. The comparison of q^2 distributions for the ISGW2 model and a HQET-based parameterization for $D\ell\nu$ decays (left) and for the linear and nonlinear approximations of form factors of $D^*\ell\nu$ decays (right). From Ref. [65].

The relative proportions of $D^{**}\ell\nu$ sub-components were also rescaled to satisfy

$$\frac{\mathcal{B}(B \rightarrow D_1(2420)\ell\nu) + \mathcal{B}(B \rightarrow D_2^*(2460)\ell\nu)}{\mathcal{B}(B \rightarrow D^{**}\ell\nu)} = 0.35 \pm 0.23 \quad , \quad (6.10)$$

using the values from Ref. [10] and following the prescription in Refs. [65, 61].

The relative branching fractions of $D^*l\nu$ and $Dl\nu$ were updated to the world average from [10],

$$\frac{\mathcal{B}(B \rightarrow D^*l\nu)}{\mathcal{B}(B \rightarrow Dl\nu)} = 2.78 \pm 0.23 \quad .$$

The dominant semileptonic $b \rightarrow c$ modes with their relative contributions to the kinematical variables are shown in Fig. 6-22.

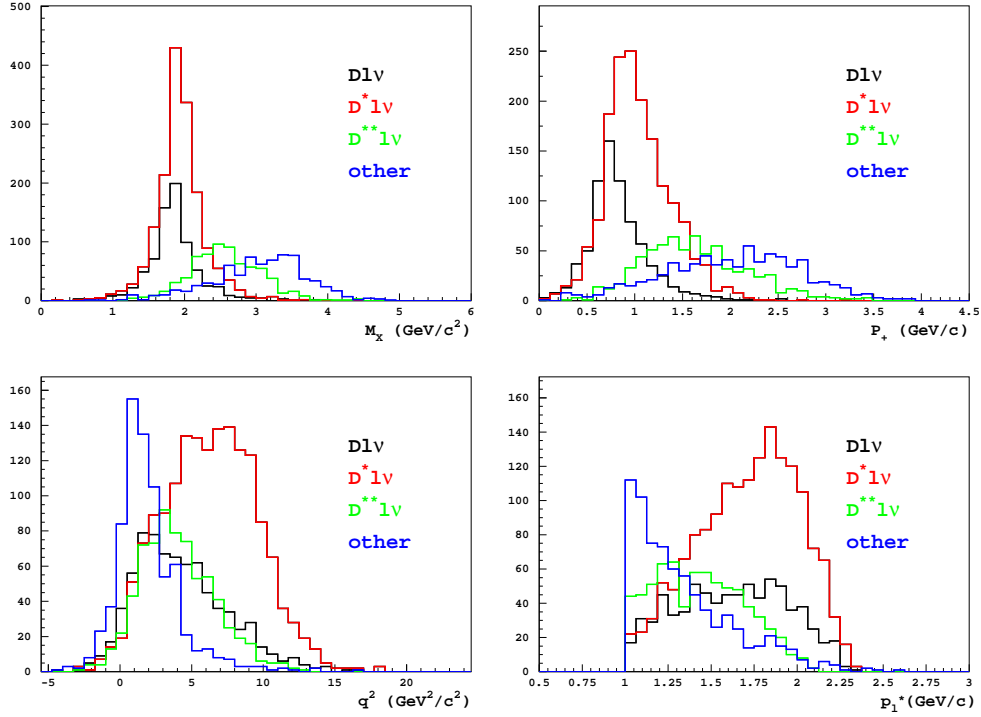


Figure 6-22. The breakdown of $b \rightarrow c$ semileptonic mode contributions in $b \rightarrow c$ MC to the inclusive kinematical variables: M_X (top left), P_+ (top right), q^2 (bottom left) and the moment in cms of the prompt lepton p_l^* (bottom right).

6.3.5.2 Kaon background composition

The estimated contribution from different backgrounds in the signal regions due to kaon reconstruction has been estimated from the MC simulation. We quote the following effects:

- **Non-reconstructed K^+ :** The charged kaon tracks that were not successfully reconstructed.
- **Misidentified K^+ :** Charged kaons that were misidentified as pions.
- **Non-reconstructed $K_S \rightarrow \pi^0\pi^0$:** Since π^0 is not reconstructed on the signal side, $K_S \rightarrow \pi^0\pi^0$ are not reconstructed. Their momentum is included through the photon energy deposits in ECL.
- **Non-reconstructed $K_S \rightarrow \pi^-\pi^+$:** K_S mesons where the decay mode $K_S \rightarrow \pi^-\pi^+$ was not reconstructed. Their momentum is included through the momenta of charged pions.
- **Non-reconstructed K_L :** K_L meson is not reconstructed.

The fractions of each contribution are given in the following table:

	B^0			B^+		
	M_X/q^2	M_X	P_+	M_X/q^2	M_X	P_+
Non-reconstructed \bar{K}^+ :	13.0%	12.5%	12.7%	19.3%	18.6%	18.8%
Misidentified K^+ :	10.3%	9.5%	9.7%	7.7%	8.3%	8.3%
Non-reconstructed $\bar{K}_S \rightarrow \pi^- \pi^+$:	5.2%	6.7%	6.0%	3.4%	4.1%	4.4%
$K_S \rightarrow \pi^0 \pi^0$:	26.3%	27.2%	26.5%	10.6%	12.1%	11.9%
Non-reconstructed K_L :	30.1%	30.0%	30.2%	30.0%	29.0%	29.6%

6.3.5.3 Test on the $b \rightarrow u$ depleted sample

The sample where at least one charged or neutral kaon was reconstructed has a very small contribution of $b \rightarrow u$ decays, since the kaon-producing decays are rare and pion-kaon misidentification is small; it is therefore called the "b \rightarrow u depleted sample". The distributions should be mainly consisted of $b \rightarrow c$ decays, which enables us to compare the $b \rightarrow c$ MC simulation to data.

It is worth re-iterating that the distributions on the depleted sample should be the measure of the reconstruction quality of $b \rightarrow c$ events at the fully reconstructed sample (since the kaons are present in nearly every $b \rightarrow c$ transition). The $b \rightarrow c$ decays in the "b \rightarrow u enhanced sample" are therefore badly reconstructed $b \rightarrow c$ events.

Tests on the depleted sample presuppose that the kaon reconstruction and identification in MC simulation is accurate: the analysis in Sec. 6.2.3 tested this hypothesis and established that the distributions of reconstructed kaons on data and MC agree within the statistical uncertainty.

Figs. 6-23 and 6-24 show the modeling of $b \rightarrow c$ simulation: some inconsistency due to D^{**} modeling is observed around $P_+ \approx 1.5$ GeV/c and the over-subtraction in the region of $P_+ \approx 2.5$ GeV/c. These regions are outside the signal region, where the modeling is accurate. We estimate the effect of inaccurate modeling of $b \rightarrow c$ decays in the systematic error (See Sec. 7.2.2.3).

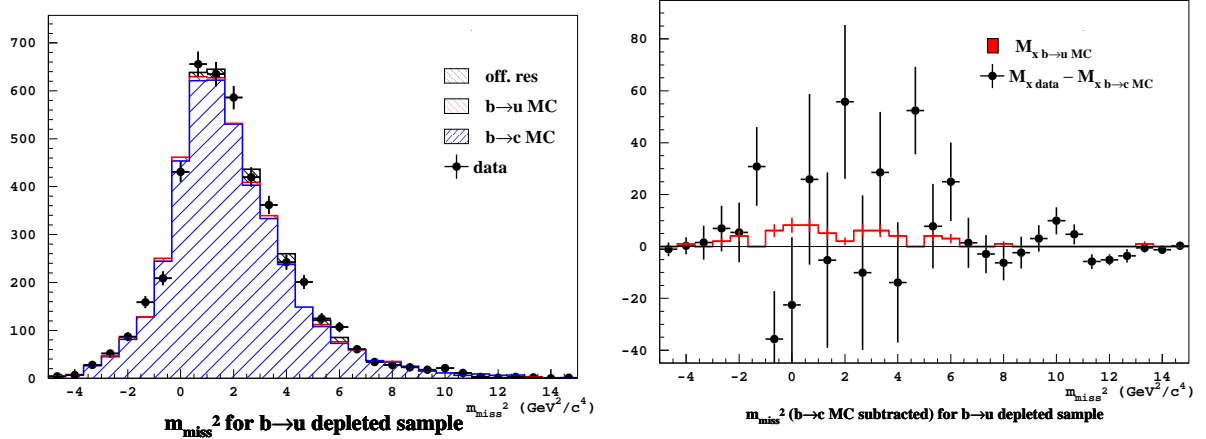


Figure 6-23. Plots for the $b \rightarrow u$ depleted sample: missing mass squared m_{miss}^2 distribution with fitted contributions from $X_c \ell \nu$ and $X_u \ell \nu$ MC simulation: (left) before, and (right) after subtracting the $X_c \ell \nu$ contribution (symbols with error bars), shown with the prediction for $b \rightarrow u$ MC (histogram).

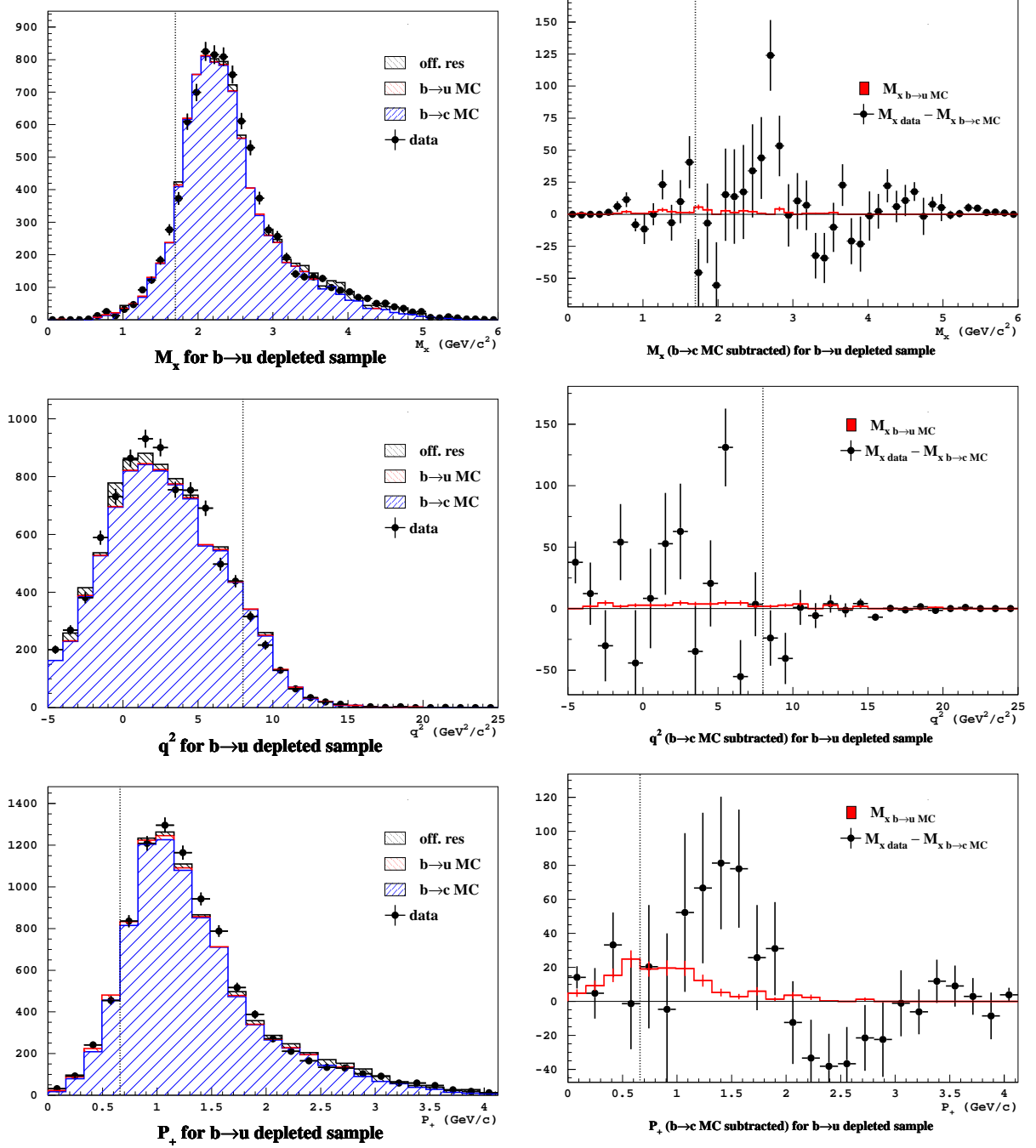


Figure 6-24. Plots for the $b \rightarrow u$ depleted sample: inclusive kinematical distributions M_X (top), q^2 (middle) and P_+ (bottom) with fitted contributions from $X_c \ell \nu$ and $X_u \ell \nu$ MC simulation: (left) before, and (right) after subtracting the $X_c \ell \nu$ contribution (symbols with error bars), shown with the prediction for $b \rightarrow u$ MC (histogram).

Measurement of $|V_{ub}|$

In the preceding chapters we describe the full reconstruction of the B_{tag} meson and particle selection procedure which lead to extraction of semileptonic decays. Additional selection of events is applied to ensure a satisfactory reconstruction of B_{sig} meson decays, enabling the construction of inclusive kinematical variables. Since the kinematics of $b \rightarrow c$ and $b \rightarrow u$ decays is different due to different masses of c and u quarks, these variables are used to extract $b \rightarrow u$ decays.

In Sec. 6.3.2 the optimization of kinematical selection was performed by minimizing the estimated total error of the $b \rightarrow u$ extraction. Three kinematical "signal regions" ($\Delta\Phi$, regions of kinematical phase space) are selected, labeled M_X , M_X/q^2 and P_+ , in which excess events over the estimated number of $b \rightarrow c$ transitions are counted. The selected signal regions are (1) $M_X < 1.7 \text{ GeV}/c^2$, (2) $M_X < 1.7 \text{ GeV}/c^2$ with $q^2 > 8 \text{ GeV}^2/c^2$ and (3) $P_+ < 0.66 \text{ GeV}/c$, for events where a lepton with $p^* \geq 1 \text{ GeV}/c$ was found.

The resulting number of excess events within $\Delta\Phi$ is normalized to the number of semileptonic decays obtained from the same fully reconstructed sample, and is corrected for the reconstruction efficiency of event selection on the signal side and for the difference in the estimated efficiencies for lepton selection and full reconstruction for the semileptonic and $b \rightarrow u$ semileptonic samples (see Eq. 7.2).

The experimental result is thus the ratio of the number of $b \rightarrow u$ semileptonic decays and all semileptonic decays $W(\Delta\Phi)$ for each of the three signal regions. As both the numerator and the denominator of $W(\Delta\Phi)$ have been obtained from the same fully reconstructed sample, after efficiency correction the ratio of the number of charged and neutral B mesons is the same, and $W(\Delta\Phi)$ has no dependence on B^+ and B^0 lifetimes. This means that $W(\Delta\Phi)$ presents both the ratio of branching fractions and the ratio of rates:

$$W(\Delta\Phi) = \frac{\Delta\Gamma_{ul\nu}(\Delta\Phi)}{\Gamma(X\ell\nu)} = \frac{\Delta\mathcal{B}_{ul\nu}(\Delta\Phi)}{\mathcal{B}(X\ell\nu)} . \quad (7.1)$$

Since the theoretical treatment described in Sec. 3.2 calculates the partial rate $\Delta\Gamma_{ul\nu}(\Delta\Phi)$ directly, $W(\Delta\Phi)$ is turned into $\Delta\Gamma_{ul\nu}(\Delta\Phi)$ using the average experimentally obtained value for $\Gamma(X\ell\nu)$.

7.1 Partial charmless semileptonic rate $\Delta\Gamma_{ul\nu}(\Delta\Phi)$

The experimental result of this analysis is the relative partial rate $W(\Delta\Phi)$, obtained as:

$$W(\Delta\Phi) = \frac{\Delta\Gamma_{ul\nu}(\Delta\Phi)}{\Gamma(X\ell\nu)} = \frac{N_{b \rightarrow u}^{\text{raw}}}{N_{\text{sl}}} \times \frac{F}{\varepsilon_{\text{sel}}^{b \rightarrow u}} \times \frac{\varepsilon_{\text{freq}}^{\text{sl}}}{\varepsilon_{\text{freq}}^{b \rightarrow u}} \times \frac{\varepsilon_{\ell}^{\text{sl}}}{\varepsilon_{\ell}^{b \rightarrow u}} . \quad (7.2)$$

The explanation of quantities follows:

$N_{b \rightarrow u}^{\text{raw}}$: the number of excess events after subtracting the estimated level of $b \rightarrow c$ background. (Obtained in Sec. 7.1.1.)

F : the correction factor that unfolds the measured kinematical region $\Delta\Phi$ into the true $\Delta\Phi$, by estimating the amount of events that should be detected within $\Delta\Phi$ but were not due to detector resolution, and events that were detected within $\Delta\Phi$ but belong to the region outside $\Delta\Phi$. (Obtained in Sec. 7.1.2.)

$\varepsilon_{\text{sel}}^{b \rightarrow u}$: the efficiency of events with $b \rightarrow u$ transitions to pass the event selection after already being selected as semileptonic decays. (Obtained in Sec. 7.1.3.)

N_{sl} : the estimated number of semileptonic events in the fully reconstructed sample (having at least one lepton with $p^* \geq 1 \text{ GeV}/c$) corrected for possible "fake" events. (Obtained in Sec. 7.1.4.1.)

$\varepsilon_{\text{rec}}^{\text{sl}}/\varepsilon_{\text{rec}}^{b \rightarrow u}$: factor accounting for a possible difference in the B_{tag} reconstruction efficiency in the presence of a semileptonic or a $B \rightarrow X_u \ell \nu$ decay. (Obtained in Sec. 7.1.4.2.)

$\varepsilon_{\ell}^{\text{sl}}/\varepsilon_{\ell}^{b \rightarrow u}$: the ratio of efficiencies for the prompt lepton selection in the case of a semileptonic and a $b \rightarrow u$ semileptonic decay, taking into account that the decay in $b \rightarrow u$ lepton selection is only for the decays within the selected kinematical signal region $\Delta\Phi$. (Obtained in Sec. 7.1.4.2.)

All quantities are obtained using fully reconstructed samples of data and MC simulation, where a fraction of events within the $\Delta E/M_{bc}$ signal region selected for full reconstruction (5.2.2) has a B_{tag} meson reconstructed from random particles that accidentally correspond to appropriate ΔE and M_{bc} . Since the contribution from such combinatorial background is accurately parameterized by the ARGUS function (Eq. 5.3, in line with the observation in Sec. 5.1.3.2)), we remove this background by fitting the M_{bc} distributions with the empirical form of signal (Eqs. 5.4, 5.5) and background (Eq. 5.3). The values are then calculated only from events represented by the empirical signal distribution, which lie inside $-0.2 \text{ GeV} < \Delta E < 0.05 \text{ GeV}$ and $M_{bc} \geq 5.27 \text{ GeV}/c^2$.

In case of signal yield extraction ($N_{b \rightarrow u}^{\text{raw}}$), the yield in each bin of the kinematical variables M_X and P_+ is obtained by fitting the appropriate M_{bc} distribution. This is justified by the observation that the quality of reconstruction of B_{tag} depends on the kinematics of the B_{sig} decay, and the combinatorial background of B_{tag} reconstruction is different for different bins of kinematical variables (see Fig. 7-3).

In the final instance the partial rate within the signal region $\Delta\Phi$ is obtained from the relative partial rate using the world average values for τ_B and $\mathcal{B}(X\ell\nu)$ (see Sec. 7.1.5):

$$\Delta\Gamma_{u\ell\nu}(\Delta\Phi) = W(\Delta\Phi) \times \Gamma(X\ell\nu) = W(\Delta\Phi) \times \frac{\mathcal{B}(X\ell\nu)}{\tau_B} . \quad (7.3)$$

7.1.1 Signal yield

The beam-constrained mass M_{bc} is fitted for each bin of the obtained distributions of kinematical variables M_X and P_+ to remove the amount of combinatorial background to B_{tag} full reconstruction. By fitting the beam-constrained mass and obtaining the yield from the empirical parameterization of signal we correct the M_X and P_+ distributions for the background of full reconstruction.

Since different kinematical regions of M_X and P_+ contain events with different number of particles and with momenta dependent on the kinematical region, the purity of full reconstruction of B_{tag} meson also depends on the M_X and P_+ of the B_{sig} meson. For example if a neutral B_{sig} meson decays semileptonically to a charged pion ($B^0 \rightarrow \pi^- \ell^+ \nu$), the decay of the signal side includes only two charged particles, one of which is a high momentum lepton, and the combinatorial background of full reconstruction of such event is small. A semileptonic decay to a D^* meson on the other hand, with a slow pion and a number of particles from the consequent D meson decay, offers more opportunities for an unsuccessful reconstruction. The increase of combinatorial background with increasing M_X and P_+ can be seen on Figs. 7-1, 7-3 and 7-5.

The shape of the signal is chosen empirically to describe adequately the data, but different choices of signal shape parameterization give a slightly different signal yield. The region of disagreement is the tail below $M_{bc} = 5.27 \text{ GeV}/c^2$ produced by not fully contained π^0 mesons in the reconstruction (see 5.1.3.2). Therefore only the yield in the empirical signal of M_{bc} above $M_{bc} = 5.27 \text{ GeV}/c^2$ is used, where the remaining discrepancy between different signal parameterizations was found to be small enough to be neglected.

The first bin corresponds to the kinematical region $\Delta\Phi$, for which the yield is obtained by one M_{bc} fit. The same binning and yield extraction is used for $b \rightarrow u$ and $b \rightarrow c$ MC simulation. The normalization of $b \rightarrow c$ background contribution is obtained by fitting the distribution obtained on data with the sum of expected distributions for $b \rightarrow u$ and $b \rightarrow c$ decays. The contributions of each transition are fitted parameters, the total number of events is not fixed in the fit.

The obtained excess events after fitted $b \rightarrow c$ background subtraction ($N_{b \rightarrow u}^{\text{raw}}$) are summarized in Tab. 7-1. The M_{bc} fits in M_X and P_+ bins and the resulting distribution of M_X and P_+ used in the signal yield extraction are summarized in the following three sections for M_X/q^2 , M_X , and P_+ signal regions, respectively.

	M_X/q^2	M_X	P_+
$N_{b \rightarrow u}^{\text{raw}}$	268	404	340
$N_{b \rightarrow u}^{\text{raw}}/N_{b \rightarrow c}$	1.0	0.65	0.7
stat. err.	10.0%	9.1%	9.4%
MC stat. err.	6.5%	5.0%	5.8%

Table 7-1. The summary of fit results: the signal yield $N_{b \rightarrow u}^{\text{raw}}$ for the three signal regions $\Delta\Phi$.

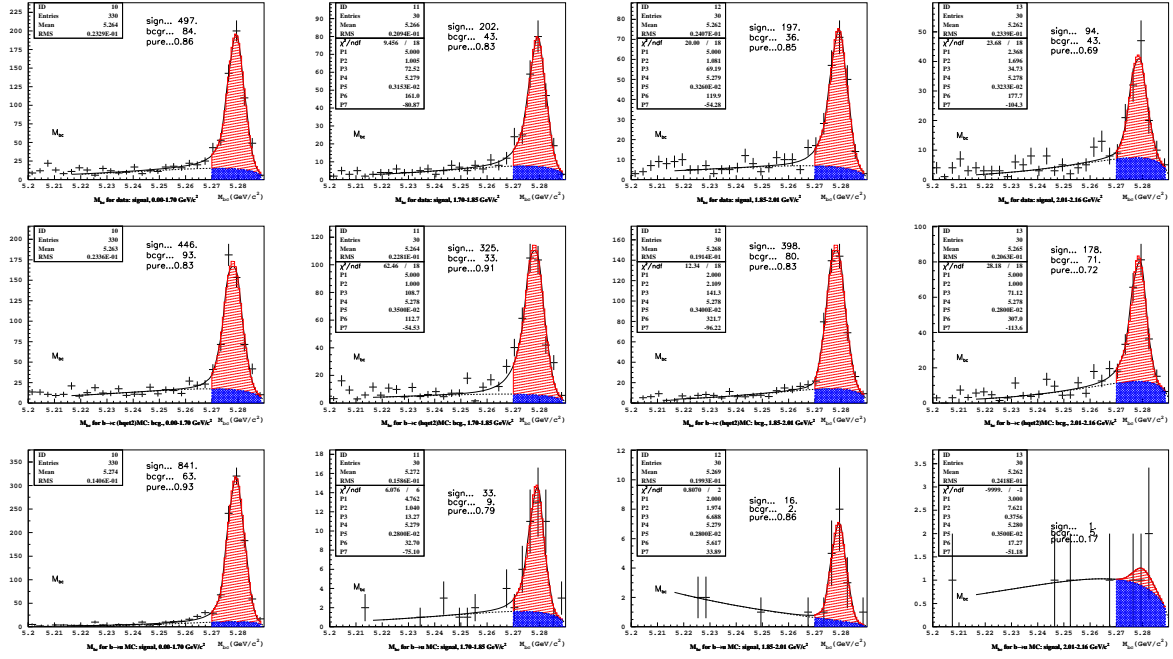
7.1.1.1 M_X/q^2 

Figure 7-1. M_{bc} fit for events with $q^2 > 8 \text{ GeV}^2/c^2$, to obtain the yield in the bins of the M_X distribution for data (top), $b \rightarrow c$ MC (middle) and $b \rightarrow u$ MC (bottom). Only the plots for the first four bins are shown: first bin covers the region below $M_X = 1.7 \text{ GeV}/c^2$, the next bins are equidistant with a width of $150 \text{ MeV}/c^2$.

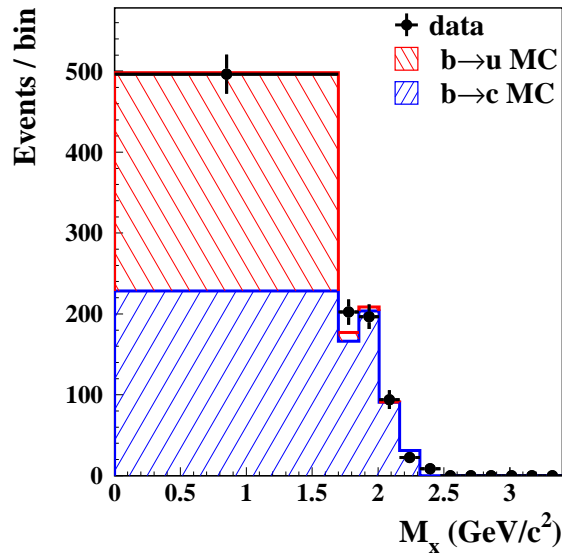


Figure 7-2. M_X distribution for events with $q^2 > 8 \text{ GeV}^2/c^2$, obtained by fitting M_{bc} in each bin (see Fig. 7-1). The MC expected distributions are superimposed: $b \rightarrow c$ MC (blue) and $b \rightarrow u$ MC (red), their relative contributions are obtained by a χ^2 fit to the data.

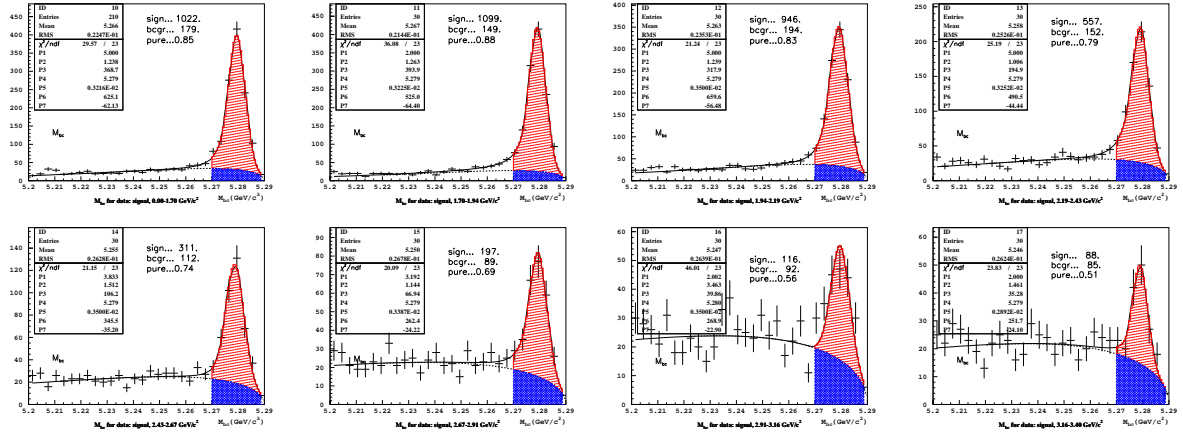
7.1.1.2 M_X 

Figure 7-3. M_{bc} fit for different M_X bins. The M_{bc} distribution for the eight bins of the M_X distribution (see Fig. 7-4) for data is shown. The fraction of the background component increases with bins, justifying the separate background component subtraction for each bin. First bin covers the region below $M_X = 1.7 \text{ GeV}/c^2$, the next bins are equidistant with a width of $150 \text{ MeV}/c^2$.

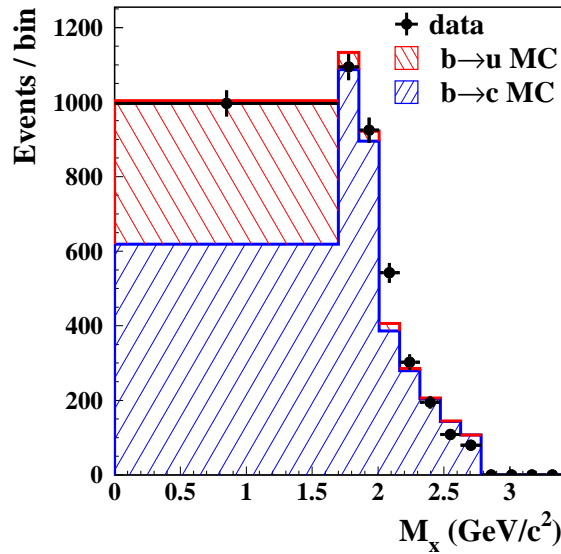


Figure 7-4. M_X distribution, obtained by fitting M_{bc} in each bin (see Fig. 7-3). The MC expected distributions are superimposed: $b \rightarrow c$ MC (blue) and $b \rightarrow u$ MC (red), their relative contributions are obtained by a χ^2 fit to the data.

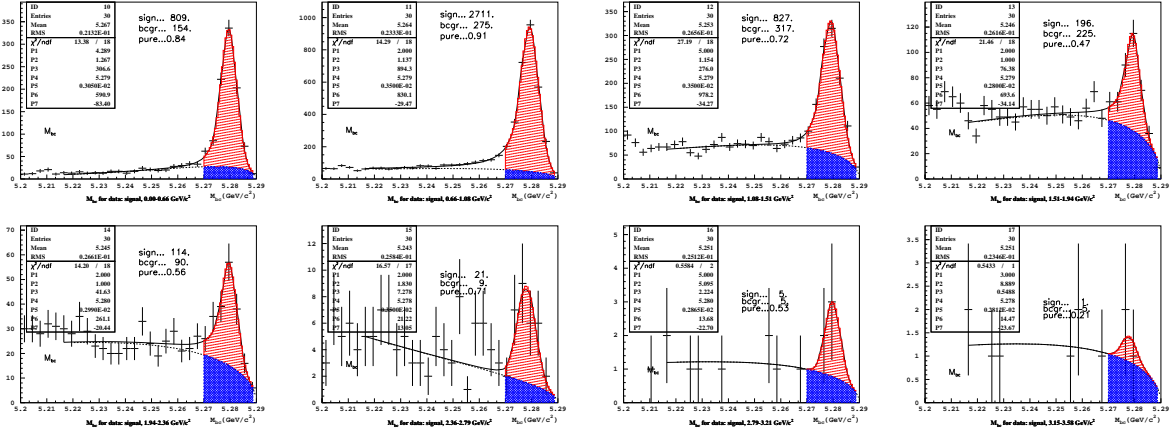
7.1.1.3 P_+ 

Figure 7-5. M_{bc} fit for different P_+ bins. The M_{bc} distribution for the eight bins of P_+ distribution for data (see Fig. 7-6) is shown. The amount of not well reconstructed events again depends on the kinematics (and thus P_+), justifying the separate background component subtraction for each bin. Bins are equidistant with a width of 660 MeV/c.

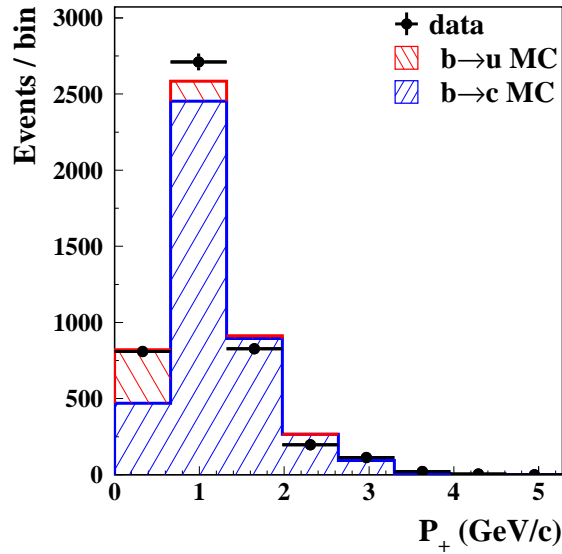


Figure 7-6. P_+ distribution, obtained by fitting M_{bc} in each bin (see Fig. 7-5). The MC expected distributions are superimposed: $b \rightarrow c$ MC (blue) and $b \rightarrow u$ MC (red), their relative contributions are obtained by a χ^2 fit to the data.

7.1.2 Efficiency and unfolding

To correct for the imperfect reconstruction of the kinematical variables due to detector smearing and effect of lost particles, we estimate the amount of events that were detected outside of their true kinematical region. The amount of events that migrated in or out of the M_X , q^2 and P_+ region is estimated on fully reconstructed $b \rightarrow u$ MC. The correction is applied by multiplying the obtained number of events with factor a F , where inside and outside refer to the region of measurement:

$$N_{\text{gen. inside}} = F \times N_{\text{rec. inside}} \quad (7.4)$$

Factor F can be decomposed to $F = 1 + F_{\text{add}} - F_{\text{sub}}$:

$$F_{\text{add}} = \frac{N_{\text{rec. outside}}^{\text{gen. inside}}}{N_{\text{rec. inside}}}, \quad F_{\text{sub}} = \frac{N_{\text{rec. inside}}^{\text{gen. outside}}}{N_{\text{rec. inside}}} \quad (7.5)$$

F_{sub} and F_{add} are fractions of events that migrated in and out of the true signal region $\Delta\Phi$, respectively, normalized to the number of reconstructed events in the kinematical region. The yields are obtained by fitting the M_{bc} distributions (see Fig. 7-7).

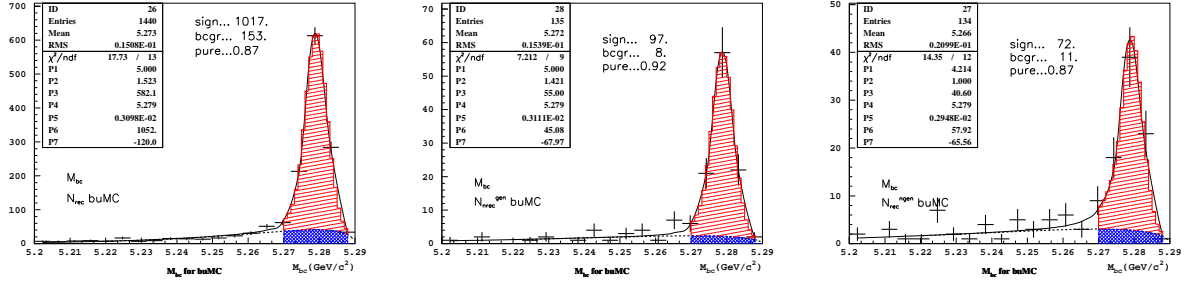


Figure 7-7. M_{bc} fits for the unfolding factor for events in the kinematical region of $M_X < 1.7 \text{ GeV}/c^2$ and $q^2 > 8 \text{ GeV}^2/c^2$ is obtained. From left: $N_{\text{rec. inside}}$, $N_{\text{rec. outside}}$, $N_{\text{rec. inside}}$.

We find the unfolding factors for different signal regions to be:

	M_X/q^2	M_X	P_+
F	$1.025(1 \pm 0.014)$	$1.07(1 \pm 0.01)$	$1.01(1 \pm 0.01)$

Table 7-2. The unfolding factor F for different signal regions.

7.1.3 Signal efficiency

We define $\varepsilon_{\text{sel}}^{b \rightarrow u}$, the efficiency for $b \rightarrow u$ events from the kinematical region $\Delta\Phi$ to pass event selection after having been already selected as semileptonic decays. The efficiency corrects for the event selection without extrapolating from $\Delta\Phi$ to the full available phase space.

The efficiencies are estimated on a fully reconstructed $b \rightarrow u$ MC. The shape function parameters $m_b^{\text{pole}} = 4.62 \text{ GeV}/c^2$ ($\bar{\Lambda}^{SF} = 0.66 \text{ GeV}/c^2$) and $\lambda_1^{SF} = -0.40 \text{ GeV}^2/c^2$, obtained by the fit to the $B \rightarrow X_s \gamma$ photon energy spectrum (see Sec.7.4.1), differ from the ones used in MC simulation. Since the values of m_b^{pole} and $\bar{\Lambda}^{SF}$ directly affect the size of $\varepsilon_{\text{sel}}^{b \rightarrow u}$, we tried to correct for the difference due to the used shape function parameters. We have compared the

relative difference of the efficiency between the default sample ($m_b^{\text{pole}} = 4.80 \text{ GeV}/c^2, \lambda_1^{SF} = -0.30 \text{ GeV}^2/c^2$) and the sample with ($m_b^{\text{pole}} = 4.65 \text{ GeV}/c^2, \lambda_1^{SF} = -0.52 \text{ GeV}^2/c^2$). We do a linear intrapolation to estimate the change in the efficiency from $\lambda_1^{SF} = -0.52 \text{ GeV}^2/c^2$ to $\lambda_1^{SF} = -0.40 \text{ GeV}^2/c^2$, by using the results from section 7.2.3.3. We scale the increase of the partial rate due to $\Delta\lambda_1^{SF} = 0.15 \text{ GeV}^2/c^2$ (see Tab. 7-12) to $\Delta\lambda_1^{SF} = 0.12 \text{ GeV}^2/c^2$ to obtain f_{cor}^{SF} .

	M_X/q^2	M_X	P_+
$\varepsilon_{\text{sel}}^{b \rightarrow u}$	0.282	0.309	0.275
rel. stat. error of $\varepsilon_{\text{sel}}^{b \rightarrow u}$	4%	3%	3%
f_{cor}^{SF}	6.1%	7.1%	7.1%
$\varepsilon_{\text{sel}}^{b \rightarrow u}(1 - f_{\text{cor}}^{SF})$	0.265	0.287	0.275

Table 7-3. The summary of $b \rightarrow u$ efficiency estimation.

7.1.4 Normalization to the number of the semileptonic decays

Absolute branching fraction measurement on a sample of fully reconstructed events needs to take into account that the reconstruction efficiency is sensitive to the number and type of charged particles in the decay of the B_{sig} . Normalization to the overall number of reconstructed events would need to correct for such effects. Since the measurement of inclusive semileptonic branching fraction is a precision measurement with a few percent errors, it is wise to exploit the similarities to cancel out some effects leading to systematic errors due to lepton selection and full reconstruction.

For the relative measurement, the semileptonic decays have to be counted and corrected for the fraction of "fake" leptons. The ratio of lepton selection and full reconstruction efficiencies for charmless semileptonic to semileptonic decays is estimated and used in the calculation of the relative partial rate $W(\Delta\Phi)$.

7.1.4.1 Number of semileptonic decays

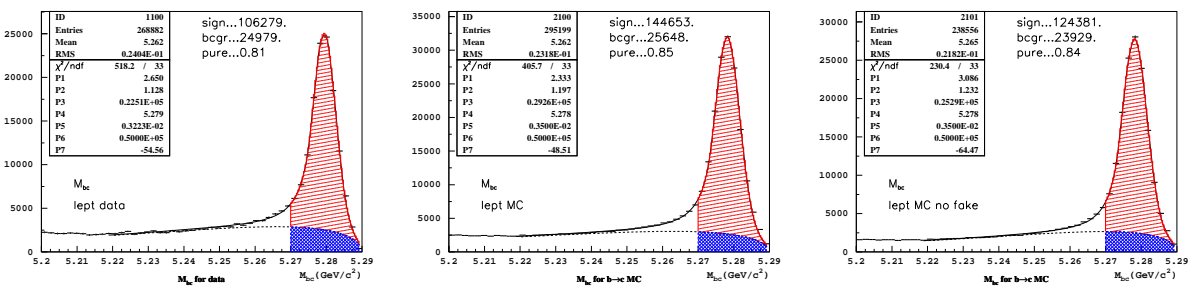


Figure 7-8. M_{bc} distributions for events that passed lepton selection requirements. Left: data; middle: $b \rightarrow c$ MC; right: events where the correct track was assigned to the lepton coming from a semileptonic B decay ($b \rightarrow c$ MC).

Semileptonic event candidates were obtained by a fit to the M_{bc} distribution for events that had at least one lepton with $p^* \geq 1 \text{ GeV}/c$ and the charge consistent with the flavour of B meson, counting only the number of fitted signal events within $M_{bc} \geq 5.27 \text{ GeV}/c^2$ and $-0.2 \text{ GeV} < \Delta E < 0.05 \text{ GeV}$ (Fig. 7-8, left). From the fit we determine $N_{\text{sl}}^{\text{counted}} = 106279(1 \pm 0.003)$ signal events. The fraction of events where the lepton is correctly reconstructed

and tagged was assessed on $b \rightarrow c$ MC (Fig. 7-8, right) to be $P_{\text{true}} = 0.860(1 \pm 0.004)$. The obtained fraction of true semileptonic events on MC was used to determine the number of true reconstructed semileptonic events with $p^* \geq 1 \text{ GeV}/c$ in the fully reconstructed data sample:

$$N_{\text{sl}} = N_{\text{sl}}^{\text{counted}} \times P_{\text{true}} = 91400(1 \pm 0.005) \quad . \quad (7.6)$$

7.1.4.2 Determination of efficiency ratios

We correct for the difference in the lepton selection and full reconstruction efficiencies between the cases when the signal B meson decayed into a charmless semileptonic decay or a semileptonic decay with charm, by calculating the ratio of efficiencies $\varepsilon_{\text{frec}}^{\text{sl}}/\varepsilon_{\text{frec}}^{b \rightarrow u}$ and $\varepsilon_{\ell}^{\text{sl}}/\varepsilon_{\ell}^{b \rightarrow u}$. $W(\Delta\Phi)$ is obtained for leptons with $p^* \geq 1 \text{ GeV}/c$; the lepton momentum distribution for $b \rightarrow c$ semileptonic decays is relatively well known and $b \rightarrow c$ MC can be used to correct for the lepton selection efficiency on the semileptonic decays. For the $b \rightarrow u$ decays the efficiencies need to be calculated only for the events that are within the signal region $\Delta\Phi$. The ratio of efficiencies $r_{b \rightarrow u}^{\text{sl}} \equiv \varepsilon_{\text{frec}}^{\text{sl}}/\varepsilon_{\text{frec}}^{b \rightarrow u} \times \varepsilon_{\ell}^{\text{sl}}/\varepsilon_{\ell}^{b \rightarrow u}$ is thus:

$$r_{b \rightarrow u}^{\text{sl}} \equiv \frac{\varepsilon_{\text{frec}}^{\text{sl}}}{\varepsilon_{\text{frec}}^{b \rightarrow u}} \times \frac{\varepsilon_{\ell}^{\text{sl}}}{\varepsilon_{\ell}^{b \rightarrow u}} = \frac{N_{b \rightarrow c \text{ MC}}(p^* \geq 1 \text{ GeV}/c)}{N_{b \rightarrow c \text{ MC}}^{\text{generated}}} \times \frac{N_{b \rightarrow u \text{ MC}}^{\text{generated}}(\Delta\Phi)}{N_{b \rightarrow u \text{ MC}}(\Delta\Phi)} \quad . \quad (7.7)$$

The $N^{\text{generated}}$ is the number of generated events before full reconstruction for both MC samples. The argument in the parenthesis represents the kinematical region in which the value is obtained. For $b \rightarrow u$ MC the ratio is obtained for the kinematical region of measurement (both in the denominator and numerator), while for $b \rightarrow c$ MC the ratio corrects for the limited lepton momentum phase space (we divide with all MC events before reconstruction). We obtain the value of the ratio $r_{b \rightarrow u}^{\text{sl}}$ without separately determining $\varepsilon_{\text{frec}}^{\text{sl}}/\varepsilon_{\text{frec}}^{b \rightarrow u}$ and $\varepsilon_{\ell}^{\text{sl}}/\varepsilon_{\ell}^{b \rightarrow u}$ to avoid double-counting of systematic and statistical errors:

	M_X/q^2	M_X	P_+
$r_{b \rightarrow u}^{\text{sl}}$	0.687 ± 0.014	0.700 ± 0.011	0.700 ± 0.012

Table 7-4. Ratio of the lepton selection and full reconstruction efficiencies for $b \rightarrow u$ semileptonic and semileptonic decays.

7.1.5 Extraction of $\Delta\Gamma_{u\ell\nu}(\Delta\Phi)$

Inserting the measured values in Eq. 7.2, we obtain the three relative partial rates $W(\Delta\Phi)$. Multiplying $W(\Delta\Phi)$ by the average measured semileptonic rate gives the charmless semileptonic partial rate $\Delta\Gamma_{u\ell\nu}(\Delta\Phi)$:

$$\Delta\Gamma_{u\ell\nu}(\Delta\Phi) = W(\Delta\Phi) \times \Gamma(X\ell\nu) = W(\Delta\Phi) \times \frac{\mathcal{B}(X\ell\nu)}{\tau_B} . \quad (7.8)$$

7.1.5.1 Average semileptonic branching fraction and the inclusive B meson lifetime

The measurement of $W(\Delta\Phi)$ is an average over charged and neutral B mesons. The average measurement is performed because this analysis is still limited by the size of the fully reconstructed sample and a separate measurement for charged and neutral B mesons is not feasible yet (see Sec. 7.3). The reasons are on the one hand that the statistical error smears out any difference between the results on the charged and neutral B meson sub-set, and on the other hand, since by separating the measurements we introduce new systematical errors of cross-feeds between the charged and the neutral sample. In the present analysis the full reconstruction is used primarily for the separation of particles according to the B meson they come from, which enables us to use the inclusive kinematical variables of B_{sig} without the need to explicitly separate the charged and neutral B meson samples.

As already mentioned, in $W(\Delta\Phi)$ the ratio of the number of charged and neutral B mesons is equal in the denominator and the numerator (after correcting for selection efficiencies), and thus in essence $W(\Delta\Phi)$ does not depend on this ratio. We can therefore use the average B meson semileptonic rate to extract the partial rate $\Delta\Gamma_{u\ell\nu}(\Delta\Phi)$.

The average semileptonic rate can be calculated from the world average for the semileptonic branching fraction $\mathcal{B}(B \rightarrow X\ell\nu)$ under the assumption that an equal admixture of charged and neutral B mesons is produced in decays of $\Upsilon(4S)$: ($f_{00} = f_{+-}$). The rates of charged and neutral B mesons are thus the same:

$$\Gamma(B^0 \rightarrow X\ell\nu) = \Gamma(B^+ \rightarrow X\ell\nu) = \Gamma_{\text{sl}} , \quad (7.9)$$

and the average semileptonic branching fraction is therefore equal to:

$$\mathcal{B}(B \rightarrow X\ell\nu) = \frac{1}{2} \left(\frac{\Gamma_{\text{sl}}}{\Gamma_{B^0}} + \frac{\Gamma_{\text{sl}}}{\Gamma_{B^+}} \right) = \frac{1}{2} (\tau_{B^0} + \tau_{B^+}) \times \Gamma_{\text{sl}} = \Gamma_{\text{sl}} \times \tau_B , \quad (7.10)$$

where τ_B is the so-called inclusive B meson lifetime:

$$\tau_B = \sum_i f_i \times B_i . \quad (7.11)$$

The sum goes over all B meson flavors produced in the decays; in the case of $\Upsilon(4S)$ $\tau_B = \frac{1}{2}(\tau_{B^0} + \tau_{B^+})$, as can be seen from Eq.7.10. Since charged and neutral B mesons are different particles with different lifetimes, such an average does not have a deeper meaning, it is a quantity that is useful when performing averages.

quantity	world average
τ_{B^+}	1.671 ± 0.018 ps
τ_{B^0}	1.536 ± 0.014 ps
$\mathcal{B}(B \rightarrow X\ell\nu)$	0.1073 ± 0.0028

Table 7-5. World averages from Ref. [10] used in the calculation of $\Delta\Gamma_{u\ell\nu}(\Delta\Phi)$.

The obtained value of the average inclusive B meson lifetime, using the values from Tab. 7-5, is $\tau_B = 1.604 \pm 0.016$ ps, where the errors of τ_{B^+} and τ_{B^0} are added linearly to conservatively account for possible correlation between τ_{B^+} and τ_{B^0} measurements.

The average semileptonic B meson rate is thus equal to:

$$\Gamma(B \rightarrow X\ell\nu) = 0.067 \pm 0.002 \text{ ps}^{-1} \quad . \quad (7.12)$$

The partial semileptonic rate $\Delta\Gamma_{u\ell\nu}(\Delta\Phi)$ for different signal regions with relative errors are given in Table 7-6.

$\Delta\Phi$	$\Delta\Gamma_{u\ell\nu}(\Delta\Phi)$	rel. stat. error
M_X/q^2	$5.24 \times 10^{-4} \text{ ps}^{-1}$	10.0%
M_X	$7.71 \times 10^{-4} \text{ ps}^{-1}$	9.1%
P_+	$6.89 \times 10^{-4} \text{ ps}^{-1}$	9.4%

Table 7-6. Partial rates to the three kinematic signal regions with the relative statistical error.

7.2 Error estimation

The accuracy of the partial rate measurement is estimated by recognizing different sources of error and grouping them into logical units. First, the errors are separated according to the sample they come from, and then according to the part of the measurement process where they arise. The errors are finally grouped into four categories: statistical, systematic, $b \rightarrow c$ modeling and $b \rightarrow u$ modeling.

Statistical error comes only from data statistics, while statistical fluctuations from MC samples are counted as a systematic error. Systematic error also includes the error due to imperfect detector simulation, the effect of binning in the fits and the uncertainty in the world average semileptonic rate $\Gamma(B \rightarrow X \ell \nu)$ used to obtain $\Delta\Gamma_{u\ell\nu}(\Delta\Phi)$.

The uncertainty of the modeling of $b \rightarrow u$ and $b \rightarrow c$ decays is, in accordance with the previous $|V_{ub}|$ measurement at Belle [61], given separately.

7.2.1 Data

Statistical fluctuations in the data sample affect the signal yield extraction both directly in the kinematical measurement region and indirectly in other bins through background normalization. In addition a much smaller error contribution coming from the determination of the number of semileptonic decays in both on resonance and in off-resonance data sample is also estimated.

	M_X/q^2	M_X	P_+
data statistics	10.0%	9.1%	9.4%

Table 7-7. The relative statistical uncertainty of the partial rate.

7.2.2 Background $b \rightarrow c$ MC

7.2.2.1 Systematics: Monte Carlo statistics

The amount of $b \rightarrow c$ MC sample corresponds to 263 fb^{-1} of data. Statistical fluctuations due to a limited MC sample affect signal yield extraction both directly in the kinematical measurement region and indirectly through MC normalization. The contribution of MC statistical fluctuations in determination of the number of semileptonic decays is also estimated.

	M_X/q^2	M_X	P_+
$b \rightarrow c$ MC statistics	6.5%	5.0%	5.8%

Table 7-8. Relative uncertainty of the partial rate $\Delta\Gamma_{u\ell\nu}(\Delta\Phi)$ due to a limited $b \rightarrow c$ MC simulation sample.

7.2.2.2 Systematics: detector simulation and K_L contamination

The discrepancy between data and MC due to detector simulation was studied by varying tracking, cluster finding and particle identification efficiencies. For the tracking efficiency study 2% of tracks were removed, and 5% of reconstructed photon clusters to estimate the uncertainty due to imperfect simulation of the photon cluster finding efficiency. For the lepton detection efficiency, from 1% to 5% of detected leptons were removed according to their angle of flight.

The error due to imperfect simulation of charged kaon identification was estimated due to the charged kaon veto applied in the measurement. Both kaon detection efficiency was reduced by 1% (resulting in 50% increase of the pion fake rate) and the kaon fake rate was increased by 25%, by additionally identifying 2% of pions as kaons.

The resulting effect on the partial rate is combined with the effect of the detector simulation in $b \rightarrow u$ decays to take into account the correlation of effects on both MC simulations. The combined result is presented in Tab. 7-13.

The imperfect simulation of a K_L meson deposit in ECL is estimated by varying the energy deposited by K_L in MC by 15%. The resulting effect is given in Tab. 7-9.

	M_X/q^2	M_X	P_+
K_L simulation	1.5%	2.8%	2.8%

Table 7-9. Relative uncertainty of the partial rate $\Delta\Gamma_{u\ell\nu}(\Delta\Phi)$ due to simulation of energy deposits by the K_L mesons.

7.2.2.3 Systematics: Monte Carlo modeling

The uncertainty in the branching fractions of D decays was obtained by varying the branching fractions in MC within the errors of their world averages [10]. The relative fraction of narrow states D_1 and D_2^* in the make-up of $D^{**}\ell\nu$ was varied within errors to estimate the modeling error of the D^{**} region.

The effect of form factor modeling in $D\ell\nu$ and $D^*\ell\nu$ was studied by varying the parameters $\rho_D^2 = 1.15 \pm 0.16$ and $\rho^2 = 1.51 \pm 0.13$ within their errors [10]. There are two additional parameters of the form factors in $D^*\ell\nu$ decays, R_1 and R_2 [10]. The errors of ρ , R_1 and R_2 are highly correlated and the world average result for ρ^2 was obtained taking into account the correlations in R_1 and R_2 , so varying the models within the error of ρ^2 already includes the effect of our limited knowledge of parameters R_1 and R_2 .

The variation of MC parameters was done by re-weighting the shapes of distributions.

	D^*/D form factors		branching fractions		Σ
	FF par.	Evtgen / QQ98	D/D^*	D^{**}	
M_X	0.8%	0.6%	1.0%	1.7%	2.2%
M_X/q^2	3.8%	3.6%	1.0%	0.1%	5.3%
P_+	4.8%	6.4%	2.0%	2.8%	8.7%

Table 7-10. Summary of the relative uncertainty of $N_{b \rightarrow u}$ due to uncertainty of background $b \rightarrow c$ MC modeling. For the " D^*/D form factors" entry the first error comes from the form factor parameter variation while the second comes from the difference in $N_{b \rightarrow u}$ when the expected number of $b \rightarrow c$ events is estimated by QQ98 or evtgen. The modeling error (Σ) is the quadratic sum of the contributions.

7.2.3 Signal $b \rightarrow u$ MC

7.2.3.1 Systematics: Monte Carlo statistics

Statistical fluctuations from a limited sample of $b \rightarrow u$ MC affect mainly the $\varepsilon_{\text{sel}}^{b \rightarrow u}$ determination and indirectly the $N_{b \rightarrow u}^{\text{raw}}$ value. The effect is estimated to be:

	M_X/q^2	M_X	P_+
$b \rightarrow u$ MC statistics	2.9%	2.0%	2.5%

Table 7-11. Relative uncertainty of the partial rate $\Delta\Gamma_{u\ell\nu}(\Delta\Phi)$ due to a limited $b \rightarrow u$ MC simulation sample.

7.2.3.2 Systematics: detector simulation

The study of the inaccuracy of the obtained results due to imperfect detector simulation was performed on signal $b \rightarrow u$ MC as well. The same effects of the imperfect detector simulation on $b \rightarrow u$ MC and $b \rightarrow c$ MC have opposite result, and are expected to partially cancel out. The study of the detector simulation was therefore performed on $(N_{b \rightarrow u}/\varepsilon_{\text{sel}}^{b \rightarrow u})$ simulateneously for both MCs.

As in the $b \rightarrow c$ case, the tracking and photon cluster reconstruction efficiency errors were estimated by removing 2% of the tracks and 5% of the photon clusters. For lepton detection efficiency, leptons were removed according to their angle of flight, the removal fraction was from 1% to 5%. For the uncertainty due to the difference in the efficiency for kaon detection, both kaon detection efficiency was reduced by 1% (50% increase in pion fake rate) and the kaon fake rate was increased by 25%, by additionally identifying 2% of pions as kaons.

7.2.3.3 Systematics: Monte Carlo modeling

The number of excess events $N_{b \rightarrow u}^{\text{raw}}$, the unfolding factor F and the efficiency $\varepsilon_{\text{sel}}^{b \rightarrow u}$ are obtained with $b \rightarrow u$ MC and their values are affected by the uncertainty in the $b \rightarrow u$ MC modeling. The effect on $N_{b \rightarrow u}^{\text{raw}} \times F/\varepsilon_{\text{sel}}^{b \rightarrow u}$ is estimated by varying the shape function parameters within the range of their uncertainty¹: ($(m_b^{\text{pole}} = 4.65 \text{ GeV}/c^2, \lambda_1^{SF} = -0.52 \text{ GeV}^2/c^2)$, ($m_b^{\text{pole}} = 4.95 \text{ GeV}/c^2, \lambda_1^{SF} = -0.14 \text{ GeV}^2/c^2$)). In Tab. 7-12 we quote the largest observed effect on the partial rate² (separate λ_1^{SF} variation is also estimated). The effect of modeling is estimated

	M_X/q^2	M_X	P_+
$\lambda_1^{SF} - 0.15 \text{ GeV}^2/c^2$	-2.8%	-3.4%	-3.6%
$\lambda_1^{SF} + 0.15 \text{ GeV}^2/c^2$	2.4%	4.6%	4.8%
$g \rightarrow s\bar{s}$	1.5%	1.5%	1.5%
$b \rightarrow u$ MC modeling	6.2%	6.1%	6.4%

Table 7-12. Break-down of $b \rightarrow u$ modeling uncertainty contributions.

relative to the default MC values of shape function parameters, although the latest obtained values differ from them

¹The shape function parameters at the two edges on the major axis of the $\chi^2 = 1$ contour ellipse of the fit to the $B \rightarrow X_s \gamma$ photon spectrum [39], where the effects on the partial rate should be largest

²At $(m_b^{\text{pole}} = 4.95 \text{ GeV}/c^2, \lambda_1^{SF} = -0.14 \text{ GeV}^2/c^2)$

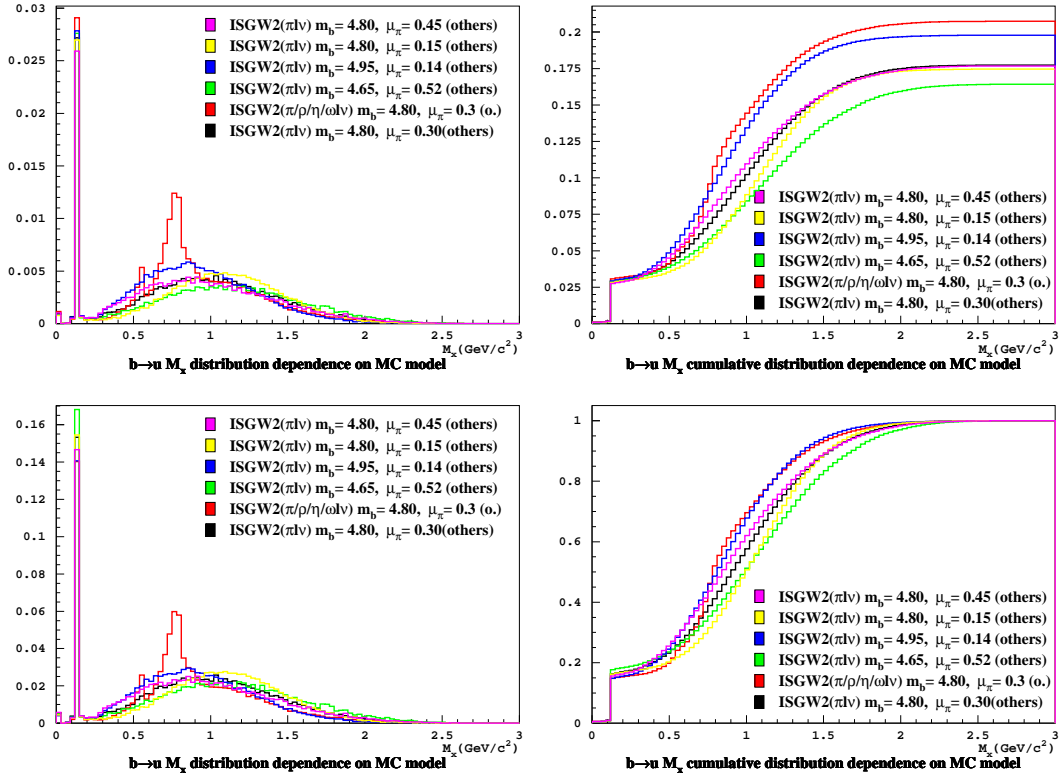


Figure 7-9. Top: comparison of M_X distributions for different models, normalized to equal entries **before** applying signal side cuts. Right: cumulative distribution. Bottom: comparison of M_X distributions for different models, normalized to equal entries **after** applying signal side cuts. Right: cumulative distribution.

(the currently best determination of the shape function parameters $m_b(SF) = (4.60 \pm 0.04) \text{ GeV}/c^2$ and $\mu_\pi^2(SF) = (0.20 \pm 0.04) \text{ GeV}^2/c^2$ that are used in obtaining $|V_{ub}|$ (see section 7.4.1.7) corresponds to $m_b^{\text{pole}} = 4.62 \text{ GeV}/c^2$ ($\bar{\Lambda}^{SF} = 0.66 \text{ GeV}/c^2$) and $\lambda_1^{SF} = -0.40 \text{ GeV}^2/c^2$). The presupposition is that the effect of variation on one pair of central values is comparable to the effect on the other pair.

We estimate the effect of imperfect simulation of the kaon production in $B \rightarrow X_u \ell \nu$ decays (mainly gluon splitting into an $s\bar{s}$ pair) by varying the contribution of events with a kaon in the final state by 25%, to be around 1.5% on the branching fraction. This contribution is included in the $b \rightarrow u$ systematic error. Note that this effect is also reduced by the kinematical selection, since the $b \rightarrow u$ transitions to two kaons need to have a mass in the region near the kinematical limit used in this analysis.

7.2.4 Summary of the error estimation

We give a summary table of error contributions from previous sections (Tab. 7-13). We assign additional errors to the effect of binning in the fits, the error of obtaining $r_{b \rightarrow u}^{\text{sl}}$ and the error on the world averages used in the determination of $\Gamma(B \rightarrow X \ell \nu)$. The three contributions are assigned to the systematical error.

The effect of imperfect detector simulation is not given separately for $b \rightarrow c$ and $b \rightarrow u$ MC, since the effects are correlated for the two samples. Therefore we add the contributions from the same effect (worse tracking, worse photon cluster reconstruction, worse charged kaon identification efficiency) linearly for both MC samples, and then add the contributions from different effects in quadrature.

SOURCE	M_X/q^2	M_X	P_+
statistics	10.0	9.1	9.4
systematics:			
binning	2.0	2.0	2.0
$r_{b \rightarrow u}^{\text{sl}}$	2.4	1.9	2.0
$\mathcal{B}(X \ell \nu)/\tau_B$	3.0	3.0	3.0
$b \rightarrow c$ MC statistics	5.8	4.0	4.8
$b \rightarrow u$ MC statistics	2.9	2.0	2.5
Detector simulation	4.1	2.5	5.6
K_L simulation	1.5	2.8	2.8
total systematics	8.9	7.1	9.2
$b \rightarrow u$ modeling:			
SF related	6.0	5.9	6.2
$g \rightarrow s \bar{s}$	1.5	1.5	1.5
total $b \rightarrow u$ modeling	6.2	6.1	6.4
$b \rightarrow c$ modeling:			
D/D^* form factor modeling	5.2	1.0	8.0
$\mathcal{B}(B \rightarrow D^* \ell \nu)$	1.0	1.0	2.0
$\mathcal{B}(B \rightarrow D^{**} \ell \nu)$	0.1	1.7	2.8
total $b \rightarrow c$ modeling	5.3	2.2	8.7

Table 7-13. The summary of the relative uncertainties (in %) of the partial rate $\Delta\Gamma_{u\ell\nu}(\Delta\Phi)$ for the three sets of kinematical regions.

7.3 Tests on sub-samples

The obtained semileptonic partial rates for all selected signal regions were calculated in different subsamples to check for possible biases. The subsamples were constructed on the base of lepton and kaon selections and B meson reconstruction. For the lepton selection the sample was separated to subsamples where the reconstructed lepton was an electron or a muon. For kaon selection the results on $b \rightarrow u$ enhanced and $b \rightarrow u$ depleted samples were compared. For B meson reconstruction, the results for charged and neutral B mesons were calculated separately.

For B^0 sample, the mixing correction was performed, by obtaining excess events on a sample where the lepton had a consistent (r.c.) or inconsistent charge (w.c.) with the flavor of the B^0 meson (see Sec. 6.2.1). From the number of events with consistent and inconsistent lepton charge the number of prompt (n_p) and cascade (n_c) leptons were obtained by solving the set of equations:

$$n_{r.c.} = n_p(1 - \chi_d) + n_c\chi_d \quad (7.13)$$

$$n_{w.c.} = n_p\chi_d + n_c(1 - \chi_d) , \quad (7.14)$$

where $\chi_d = 0.186 \pm 0.004$ [10] is the B^0 mixing probability.

We observe no significant deviations from the calculated values of $\Delta\Gamma_{u\ell\nu}(\Delta\Phi)$. The results are shown in Fig. 7-10.

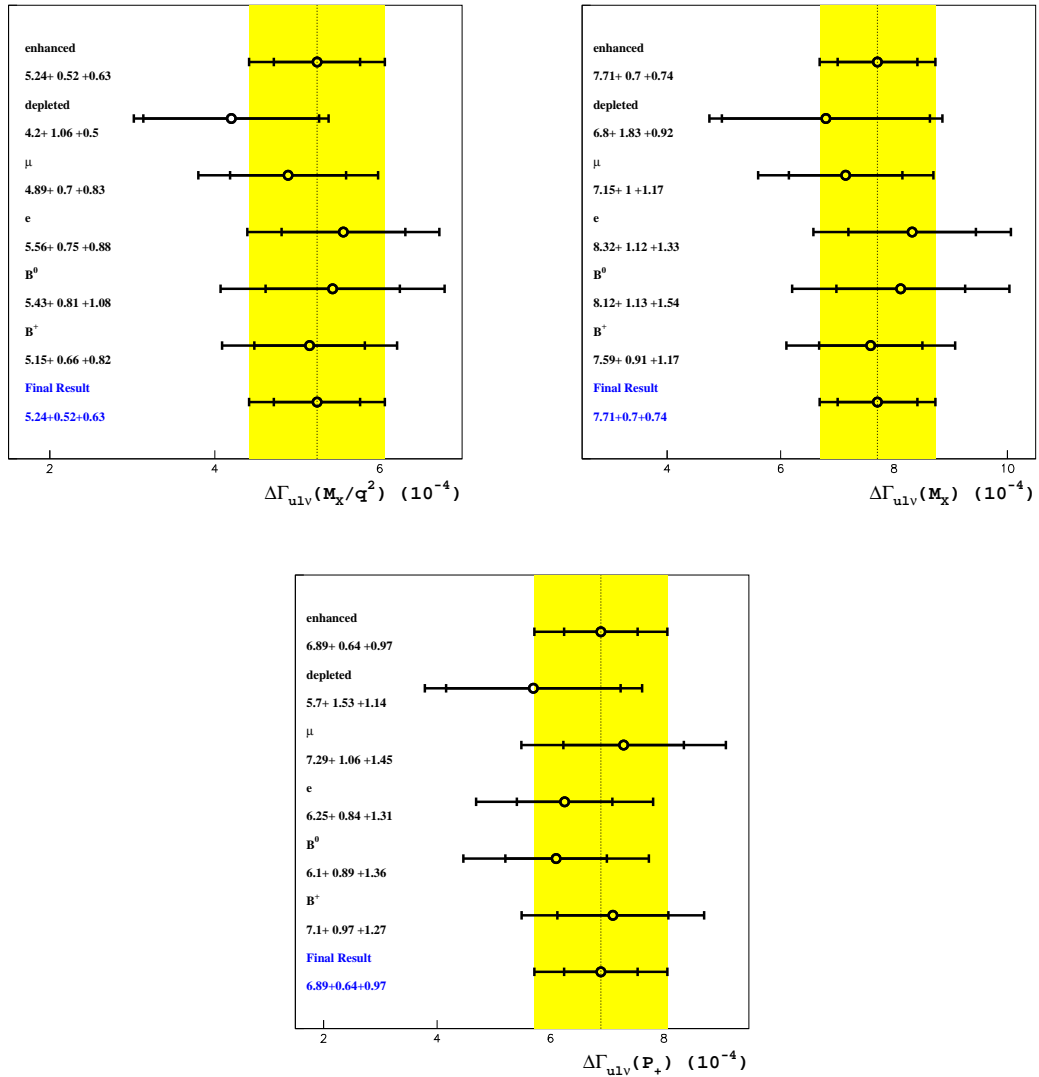


Figure 7-10. The values of $\Delta\Gamma_{u\ell\nu}(\Delta\Phi)$ calculated on subsamples, based on lepton and kaon selection, and B meson reconstruction: for M_X/q^2 signal region (top left), M_X signal region (top right), and P_+ signal region (bottom).

7.4 Extraction of $|V_{ub}|$

The obtained partial rate for B mesons to kinematical signal regions $\Delta\Phi$, with errors estimated in Sec. 7.2, are summarized in Tab. 7-14.

$\Delta\Phi$	$\Delta\Gamma_{ul\nu}(\Delta\Phi)$	stat	syst	$b \rightarrow u$	$b \rightarrow c$
M_X/q^2	$5.24 \times 10^{-4} \text{ ps}^{-1}$	10.0	8.9	6.2	5.3
M_X	$7.71 \times 10^{-4} \text{ ps}^{-1}$	9.1	7.1	6.1	2.2
P_+	$6.89 \times 10^{-4} \text{ ps}^{-1}$	9.4	9.3	6.4	8.7

Table 7-14. Partial rates to the three kinematic signal regions with relative errors (in %).

The partial rate to the signal region $\Delta\Phi$ can be turned directly into $|V_{ub}|$ using $R(\Delta\Phi)$, the theoretical prediction for $\Delta\Gamma_{ul\nu}(\Delta\Phi)$, divided by $|V_{ub}|^2$:

$$|V_{ub}| = \sqrt{\frac{\Delta\Gamma_{ul\nu}(\Delta\Phi)}{R(\Delta\Phi)}}. \quad (7.15)$$

The predicted rate $R(\Delta\Phi)$ is in essence a purely theoretical quantity, but can be obtained much more reliably if the non-perturbative contributions to the calculations are separated out and obtained experimentally. The non-perturbative contribution is parameterized with the help of a shape function, the parameterized hadronic structure function, describing the inner structure of the B meson. $R(\Delta\Phi)$ thus depends not only on the $\Delta\Phi$ selection, but also on the two shape function parameters $m_b(SF)$ and $\mu_\pi^2(SF)$, and finally on the choice of the parameterization function of the shape function [3].

A method for obtaining shape function parameters by fitting the shape of the photon energy distribution in inclusive $B \rightarrow X_s\gamma$ decays was proposed [3]. Since the uncertainty from shape function parameters is one of the key contributions to the total $|V_{ub}|$ error, a determination of the shape function parameters was performed by fitting the shape of the $B \rightarrow X_s\gamma$ photon energy distribution obtained on the Belle detector [34].

7.4.1 Determination of shape function parameters

7.4.1.1 Procedure

We used a method based on that devised by the CLEO Collaboration [66]. We fit MC simulated spectra to the raw photon energy spectrum. ‘‘Raw’’ refers to the spectra that are obtained after the application of the $B \rightarrow X_s\gamma$ analysis cuts [34]. The use of ‘‘raw’’ spectra correctly accounts for Lorentz boost from the B rest frame to the center of mass system, energy resolution effects and avoids unfolding. The method is as follows:

1. Assume a shape function model.
2. Simulate the photon energy spectrum for a certain set of parameters; $(m_b(SF), \mu_\pi^2(SF))$.
3. Perform a χ^2 fit of the simulated spectrum to the data, where only the normalization of the simulated spectrum is floated, and keep the resultant χ^2 value.
4. Repeat steps 2-3 for different sets of parameters to construct a two dimensional grid of χ^2 values.
5. Find the minimum χ^2 on the grid and all the points on the grid that are one unit of χ^2 above the minimum.
6. Repeat steps 1-5 for the three shape function functional forms (Table 3-1).

7.4.1.2 Monte Carlo simulated photon energy spectrum

We generate $B \rightarrow X_s \gamma$ MC events according to the prescription in Ref. [3] for each set of the shape function parameter values. The generated events are simulated for the detector performance using the Belle detector simulation and the $B \rightarrow X_s \gamma$ analysis cuts are applied to the MC events to obtain the raw photon energy spectrum in the $\Upsilon(4S)$ rest frame [34].

7.4.1.3 Fitting the spectrum

For a given set of shape function parameters, a χ^2 fit of the MC simulated photon spectrum to the raw data spectrum is performed in the interval $1.8 < E_\gamma^* < 2.8$ GeV, where the * denotes the $\Upsilon(4S)$ rest frame. Although in the Ref. [39] the fitting was performed in the interval between 1.5 GeV and 2.8 GeV, the data below 1.8 GeV are not used in the present analysis since the models we use do not model accurately the tails below 1.8 GeV [67].

The normalization parameter is floated in the fit. The raw spectrum is plotted in Figure 7-11, the errors include both statistical and systematic errors. The latter are dominated by the estimation of the $B\bar{B}$ background and are 100% correlated. Therefore the covariance matrix is constructed as:

$$V_{ij} = \sigma_{d_i}^{\text{stat}} \sigma_{d_j}^{\text{stat}} \delta_{ij} + \sigma_{d_i}^{\text{sys}} \sigma_{d_j}^{\text{sys}}, \quad (7.16)$$

where $\sigma_{d_i}^{\text{sys}}$ is the error in the i -th data bin, and indices can be $i, j = 1, 2, \dots, 10$. Then the χ^2 used in the fitting is given by

$$\chi^2 = \sum_{ij} (d_i - f_i)(V^{-1})_{ij}(d_j - f_j), \quad (7.17)$$

where d_i is the content in i -th data bin, f_i is the content in the i -th bin of the simulated MC spectrum, and $(V^{-1})_{ij}$ denotes the ij^{th} element of the inverted covariance matrix. The χ^2 value of the fit is used to determine a map of χ^2 as a function of the shape function parameters.

7.4.1.4 The best fit and $\Delta\chi^2$ contour

The best fit parameters are associated to the minimum chi-squared case, χ_{min}^2 . The error ‘‘ellipse’’ is defined as the contour which satisfies $\Delta\chi^2 \equiv \chi^2 - \chi_{\text{min}}^2 = 1$. The contours are found to be well approximated by the modified ellipse [68]:

$$\Delta\chi^2(m_b(SF), \mu_\pi^2(SF)) = \left(\frac{\mu_\pi^2(SF) + a(m_b(SF))^2 + b}{c} \right)^2 + \left(\frac{(m_b(SF))^2 + d}{e} \right)^2. \quad (7.18)$$

The parameters $a, b, c, d,$ and e are determined by fitting the function to the parameter points that lie on the contour.

7.4.1.5 Results

The best fit parameters are given in Table 7-15. The parameter values are found to be consistent across all three shape function forms. The minimum χ^2 fit for each shape function model is displayed in Figure 7-12. The fits to the contour with $\Delta\chi^2 = 1$ points are shown in Figs. 7-12 and 7-13.

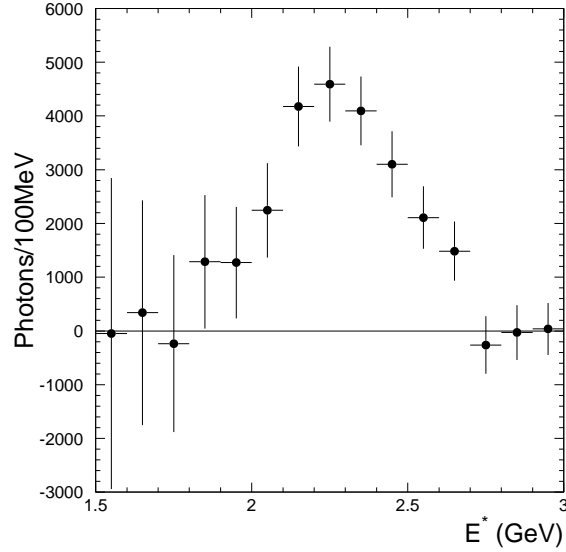


Figure 7-11. Raw $B \rightarrow X_s \gamma$ photon energy spectra in the $\Upsilon(4S)$ frame as acquired from data. The errors include both statistical and systematic errors. Raw refers to spectra as measured after the application of Belle $B \rightarrow X_s \gamma$ analysis cuts.

Shape	χ^2_{\min}	$m_b(SF)$ GeV/ c^2	$\mu_\pi^2(SF)$ GeV $^2/c^2$
exponential	4.32	4.52 ± 0.07	0.27 ± 0.13
gaussian	3.78	4.54 ± 0.07	0.25 ± 0.13
hyperbolic	4.41	4.52 ± 0.07	0.27 ± 0.13

Table 7-15. The best fit shape function parameter values. The three functional forms used for shape function parameterization are from Ref. [3] and are defined in Tab. 3-1.

7.4.1.6 Summary

The b -quark leading shape function parameters in the shape function scheme, $m_b(SF)$ and $\mu_\pi^2(SF)$, were determined from fits of Monte Carlo simulated spectra, generated by the prescription in Ref. [3], to the raw Belle measured $B \rightarrow X_s \gamma$ photon energy spectrum. Three functional forms for the leading shape function were used: exponential, gaussian and hyperbolic, while the default model from Ref. [3] was used for the subleading shape function, where the reference scale is chosen to be 1.5 GeV [3]. The obtained best fit parameters are: $(m_b(SF), \mu_\pi^2(SF))_{\text{exp}} = (4.52, 0.27)$, $(m_b(SF), \mu_\pi^2(SF))_{\text{gauss}} = (4.54, 0.25)$, and $(m_b(SF), \mu_\pi^2(SF))_{\text{hyp}} = (4.52, 0.27)$, where $m_b(SF)$ and $\mu_\pi^2(SF)$ are measured in units of GeV/ c^2 and GeV $^2/c^2$ respectively. We have also determined the $\Delta\chi^2 = 1$ contours in the $(m_b(SF), \mu_\pi^2(SF))$ parameter space for each of the assumed models, which determine the error of the shape function parameter determination.

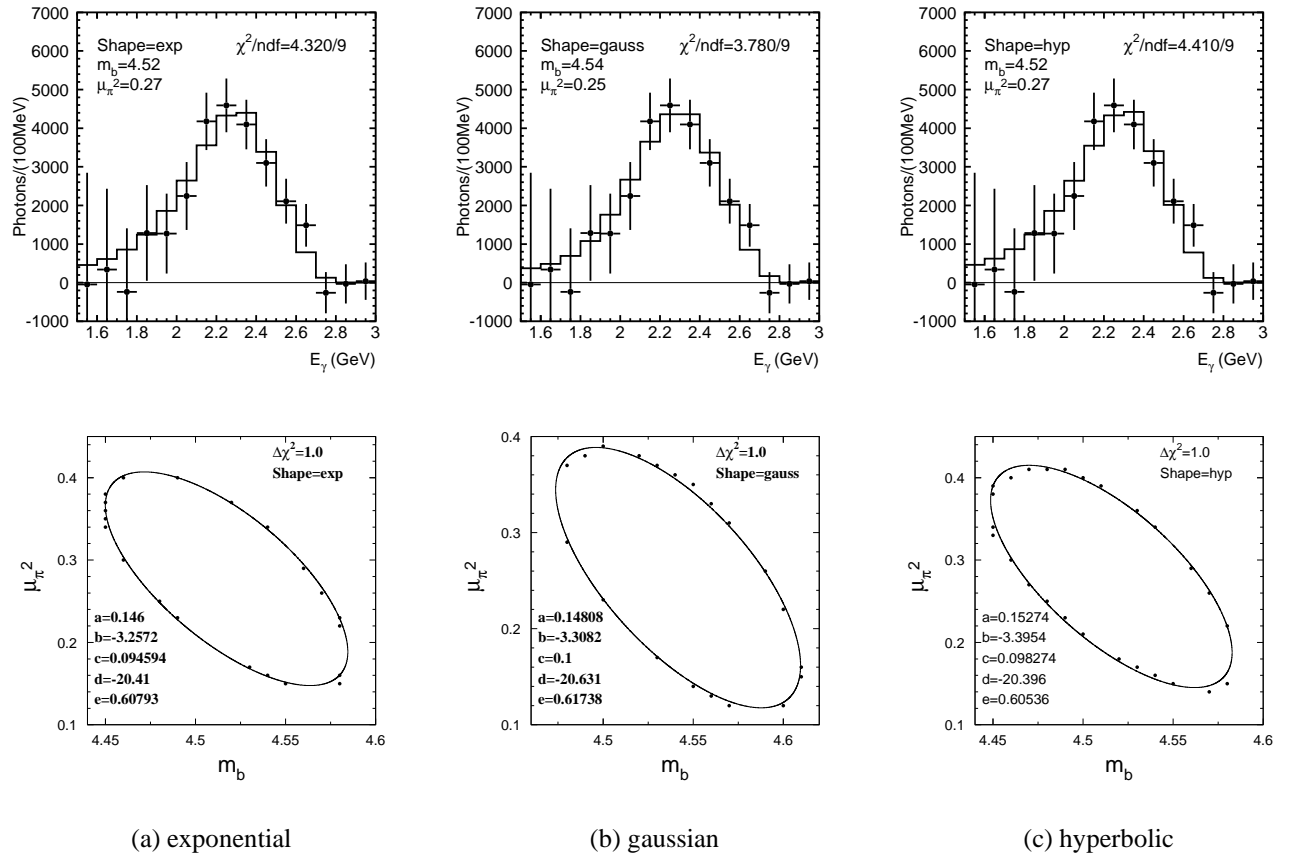


Figure 7-12. Top: Minimum χ^2 fits of MC simulated spectra to the raw data for each shape function model. Bottom: The fitted $\Delta\chi^2 = 1$ contours for each shape function model.

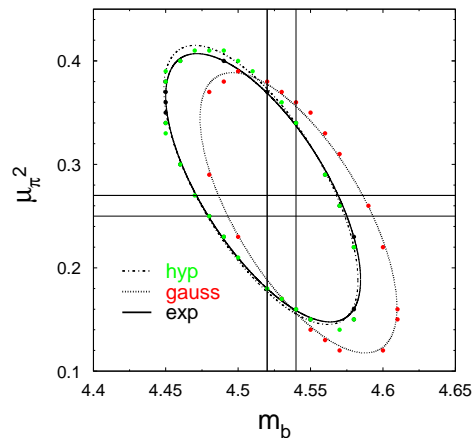


Figure 7-13. Comparison of the fitted $\Delta\chi^2 = 1$ contours for all shape function models. The contours for the exponential, gaussian and hyperbolic model are shown by the solid, dotted and dash-dotted curves, respectively. The vertical and horizontal lines mark the central values of the three fits.

7.4.1.7 Improved determination of shape function parameters

Recently, an improved simultaneous determination of shape function parameters was performed, using all the moment measurements (where correlation matrices are available) of the invariant hadronic mass and lepton energy distribution in $B \rightarrow X_c \ell \nu$ decays and photon energy distribution of $B \rightarrow X_s \gamma$ decays [69].

The fit was performed using parameters defined in the so-called kinetic scheme, and later transformed into the shape function scheme [3]. The resulting $\Delta\chi^2 = 1$ ellipses in the kinetic scheme are used to determine the uncertainty of the shape function parameters, and are shown separately for the moment measurements from $B \rightarrow X_s \gamma$ and $B \rightarrow X_c \ell \nu$ in Fig. 7-14 (left).

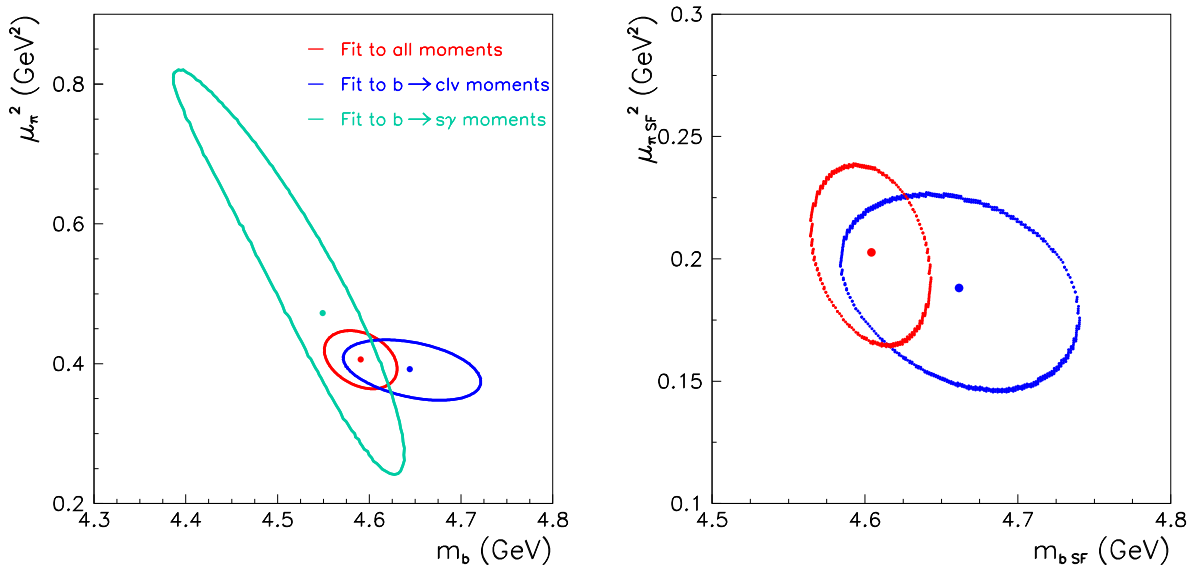


Figure 7-14. The $\Delta\chi^2 = 1$ ellipse used to determine the uncertainty of the shape function parameters. Left: the ellipses in the kinetic scheme. Right: the ellipses in the shape function scheme from the fit of $B \rightarrow X_c \ell \nu$ moments alone (blue) and the combined fit to the moment measurements from $B \rightarrow X_s \gamma$ and $B \rightarrow X_c \ell \nu$ (red). From Ref. [69].

The obtained shape function parameters of relevance to this analysis were determined to be $m_b(SF) = (4.60 \pm 0.04)$ GeV/ c^2 and $\mu_\pi^2(SF) = (0.20 \pm 0.04)$ GeV²/ c^2 . The resulting accuracy of 40 MeV/ c^2 in $m_b(SF)$ should be compared to the accuracy of 70 MeV/ c^2 , obtained from fitting the shape of the photon energy distribution in $B \rightarrow X_s \gamma$ (see Tab. 7-15). Since the uncertainty of $m_b(SF)$ contributes significantly to the uncertainty of the $|V_{ub}|$ measurement, the result from [69] will be used in the final determination of $|V_{ub}|$. The obtained $\Delta\chi^2 = 1$ ellipse for this result in the shape function scheme is shown in Fig. 7-14 (right), where the blue ellipse is the result obtained from fits of $B \rightarrow X_c \ell \nu$ moments alone, while the result from the combined fit to moment measurements from $B \rightarrow X_s \gamma$ and $B \rightarrow X_c \ell \nu$ is shown in red.

7.4.2 $|V_{ub}|$ result

The values of $R(\Delta\Phi)$, the theoretical prediction for the partial rate $\Delta\Gamma_{u\ell\nu}(\Delta\Phi)$, divided by $|V_{ub}|^2$, were calculated using the theoretical prescriptions from Ref. [3], by inserting the shape function parameters $m_b(SF) = (4.60 \pm 0.04)$ GeV/ c^2 and $\mu_\pi^2(SF) = (0.20 \pm 0.04)$ GeV $^2/c^2$ from Ref. [69]. The sources of the uncertainty in $R(\Delta\Phi)$ estimation are of two types; the so-called theoretical uncertainty (theo) includes the contributions from matching scale variation and the contribution from the weak annihilation diagram (see Sec. 3.2.1), while shape function parameter determination uncertainty (SF) includes the dependence of the result on the uncertainty in the shape function parameters and on the choice of the specific parameterization of the shape function. As can be seen from the comparison in Tab. 7-16, the determination using $B \rightarrow X_s \gamma$ shape (see Sec. 7.4.1), have nearly twice as large $m_b(SF)$ errors, which translates directly into twice as large SF dependence. For $|V_{ub}|$ determination we have used the values obtained in Ref. [69].

$\Delta\Phi$	$m_b(SF)$, $\mu_\pi^2(SF)$ (4.60 \pm 0.04) , (0.20 \pm 0.04)			$m_b(SF)$, $\mu_\pi^2(SF)$ (4.52 \pm 0.07) , (0.27 \pm 0.13)		
	$R(\Delta\Phi)$	SF	theo	$R(\Delta\Phi)$	SF	theo
M_X/q^2	23.7 ps	8.5	$^{+10.4}_{-9.5}$	21.7 ps	18.7	$^{+11.0}_{-10.0}$
M_X	46.1 ps	9.0	$^{+7.6}_{-6.9}$	40.9 ps	18.3	$^{+7.8}_{-7.1}$
P_+	39.4 ps	11.5	$^{+7.0}_{-6.8}$	33.2 ps	20.5	$^{+7.0}_{-6.8}$

Table 7-16. Obtained values of $R(\Delta\Phi)$ for the three kinematical signal regions with relative errors, given in %. Left: the determination from Ref. [69]. Right: the determination from Sec. 7.4.1.

While the dependence of $R(\Delta\Phi)$ on $\mu_\pi^2(SF)$ is small ($\sim 1.3\%$ for the values within the uncertainty of $\mu_\pi^2(SF)$), the dependence on $m_b(SF)$ was found using calculations from Ref. [3] to be linear in a wide range:

$$\frac{R}{R(m_b^0)} = 1 + k(\Delta\Phi) \left(\frac{m_b}{m_b^0} - 1 \right), \quad (7.19)$$

where $m_b^0 = 4.60$ GeV/ c^2 and $k(\Delta\Phi)$ is found to be 2.09, 2.29 and 3.00 for the M_X/q^2 , M_X and P_+ signal regions, respectively.

The dependence of $R(\Delta\Phi)$ on the specific parameterization of the shape function was estimated by comparing the calculated result when using the exponential and gaussian parameterizations (see Tab. 3-1). The two effects are added in quadrature to form the SF error.

The values of $R(\Delta\Phi)$ with the errors are summarized in Tab. 7-16. Note that the bounds of the uncertainty are inverse on $R(\Delta\Phi)$ and $|V_{ub}|$. The final result of $|V_{ub}|$ determination using the three kinematical signal regions $\Delta\Phi$ are given in Tab. 7-17. The total error on $|V_{ub}|$ is 10%, 9% and 11% for M_X/q^2 , M_X and P_+ regions, respectively.

$\Delta\Phi$	$ V_{ub} \times 10^3$	stat	syst	$b \rightarrow u$	$b \rightarrow c$	SF	th.
M_X/q^2	4.70	5.0	4.4	3.1	2.7	4.2	$^{+4.8}_{-5.2}$
M_X	4.09	4.6	3.5	3.1	1.1	4.5	$^{+3.5}_{-3.8}$
P_+	4.19	4.7	4.6	3.2	4.4	5.8	$^{+3.4}_{-3.5}$

Table 7-17. Values for $|V_{ub}|$ with relative errors (in %) for the three kinematic signal regions. Shape function parameters used in the calculation are $m_b(SF) = (4.60 \pm 0.04)$ GeV/ c^2 and $\mu_\pi^2(SF) = (0.20 \pm 0.04)$ GeV $^2/c^2$.

Interpretation of the results

From the measurements using three signal regions, M_X , M_X/q^2 and P_+ (each of them chosen for the proposed advantages they have over other selections) we obtain three $|V_{ub}|$ values. Since the results are obtained on a common data sample and share particle and event selection, this analysis offers an opportunity to compare face to face the outreach of the three selected signal regions.

The main motivation for a $|V_{ub}|$ measurement is to constrain the upper vertex of the unitarity triangle; we have estimated the level of constraint on the $\rho - \eta$ plane due to the $|V_{ub}|$ value obtained by this analysis and confronted it with the constraints from the measurements of other parameters of the Standard Model.

The comparison with the results from other $|V_{ub}|$ analyses shows that the current result has the smallest overall uncertainty and is in agreement with the previous $|V_{ub}|$ results. The work on $|V_{ub}|$ should not stop here, since there is a lot of room for improvement: in the final instance we present the possible future improvements of V_{ub} determination, offered by the fully reconstructed sample.

8.1 Comparison of the results

The three obtained $|V_{ub}|$ results are presented in Fig. 8-1. Although the total errors are larger than the difference between the measurements, the three analyses are correlated by a common particle and event selection and the three signal regions overlap significantly (M_X/q^2 is for example a complete sub-sample of M_X), so a difference between results needs to be compared after the correlation between the measurements has been taken into account.

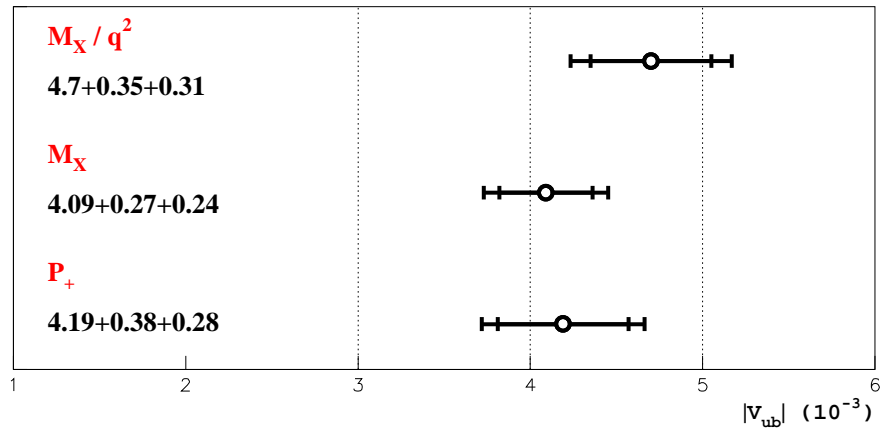


Figure 8-1. Comparison of the $|V_{ub}|$ results from the three signal regions.

8.1.1 Are the results consistent with each other?

The largest difference between obtained values of $|V_{ub}|$ is observed for the M_X and M_X/q^2 signal regions. The selections of the two signal regions differ only for the additional $q^2 > 8 \text{ GeV}^2/c^2$ constraint: this enables us to compare the results from these two signal regions by taking into account the statistical and theoretical correlations. The correlation of the uncertainty due to the shape function parameter determination is observed to be nearly 100% correlated. We also take the systematic uncertainty to be 100% correlated, since the exact level of correlation is hard to estimate. The problem is that a single event does not carry the information on the final $|V_{ub}|$, which is obtained after subtraction of the estimated $b \rightarrow c$ background.

We find a difference of $\Delta|V_{ub}| = (0.61 \pm 0.22(\text{stat}) \pm 0.06(\text{theo})) \times 10^{-3}$ between the measurements of M_X and M_X/q^2 regions. Thus, taking correlations into account, we find that the difference has a 2.8σ statistical significance and 2.7σ total error significance. From the observed significance we conclude that the results are consistent within errors, but we do not rule out possible effects of duality violation or weak annihilation contribution, which should be different for the two selections.

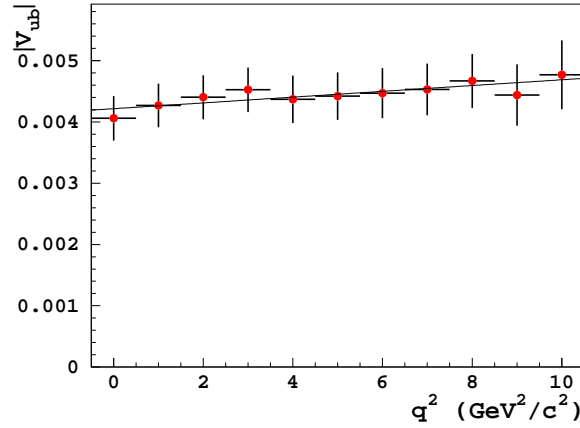


Figure 8-2. Values of $|V_{ub}|$, obtained by varying the lower limit of the q^2 signal selection. The shown total error of each point is correlated between measurements for different q^2 values. A linear fit to the points is also shown, parameterized by Eq. 8.1.

To search for a possible discrepancy, the $|V_{ub}|$ value is obtained as a function of the lower limit of the q^2 signal selection. The result is presented in Fig. 8-2. We find a slight dependence of the $|V_{ub}|$ result on the q^2 selection, which can be in the tested range of the q^2 region ($0 - 10 \text{ GeV}^2/c^2$) described by a linear function :

$$|V_{ub}| = 4.22 \cdot 10^{-3} + 4.72 \cdot 10^{-5} \times \frac{q^2}{1 \text{ GeV}^2/c^2} . \quad (8.1)$$

The running of the $|V_{ub}|$ value can have an experimental cause (see the discussion in Sec. 8.1.2). To test if the effect is caused by the theoretical treatment used in the $|V_{ub}|$ extraction, we estimate the consistency of the obtained q^2 distribution from data to the simulated shapes. The observed discrepancy of the $|V_{ub}|$ results should be seen as a disagreement of the theoretical prediction with the data distributions, from which the $b \rightarrow c$ contribution has been subtracted. The plots in Fig. 8-3 show q^2 distributions for events with $M_X < 1.7 \text{ GeV}/c^2$: in Fig. 8-3 (left), the whole distribution corresponds to the M_X signal region, while the events with $q^2 > 8 \text{ GeV}^2/c^2$ correspond to the M_X/q^2 signal region. No significant difference can be observed. Since different theoretical models were used for $b \rightarrow u$ MC simulation and for final $|V_{ub}|$ extraction, the generated distributions for both models are compared in

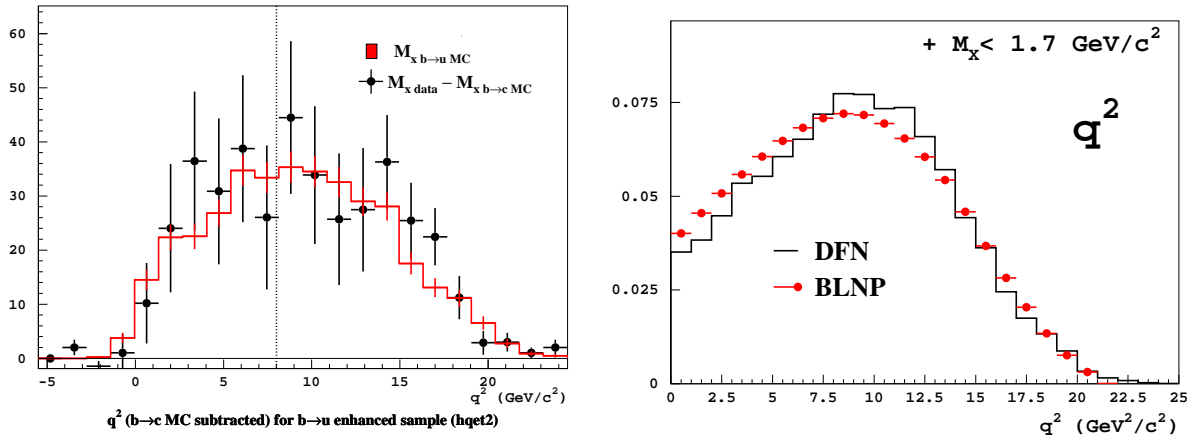


Figure 8-3. Left: The q^2 distribution after subtraction of the $b \rightarrow c$ contribution for events with $M_X < 1.7$ GeV $^2/c^2$ in the $b \rightarrow u$ enhanced sample. No significant discrepancy can be seen for events below and above $q^2 = 8$ GeV $^2/c^2$. Right: comparison of generated q^2 distributions for DFN model [31] used for $b \rightarrow u$ MC simulation and BLNP model [3] used for $|V_{ub}|$ extraction.

Fig. 8-3 (right). We find a slight difference in the fractions below and above $q^2 = 8$ GeV $^2/c^2$, which affects the result by 1%.

8.1.2 The M_X distribution

The obtained hadronic invariant mass distribution for the $b \rightarrow u$ decays is an important result that can help evaluate the successfulness of the analysis. It is obtained by subtracting the simulated $b \rightarrow c$ contribution from the data. The normalization of both $b \rightarrow c$ background and $b \rightarrow u$ signal simulation is obtained by a direct fit of the estimated contributions to the data. In Fig. 8-4 we show the obtained distribution for both the $b \rightarrow u$ *enhanced sample* (left) and $b \rightarrow u$ *depleted sample* (right) samples and compare it to the expected distribution from the $b \rightarrow u$ simulation (normalization from the aforementioned fit). The result in the signal region of $M_X < 1.7 \text{ GeV}/c^2$ (the region left of the vertical line) agrees well with the simulated $b \rightarrow u$ distribution, and the $B \rightarrow \pi\ell\nu$ and $B \rightarrow \rho\ell\nu$ components are clearly seen.

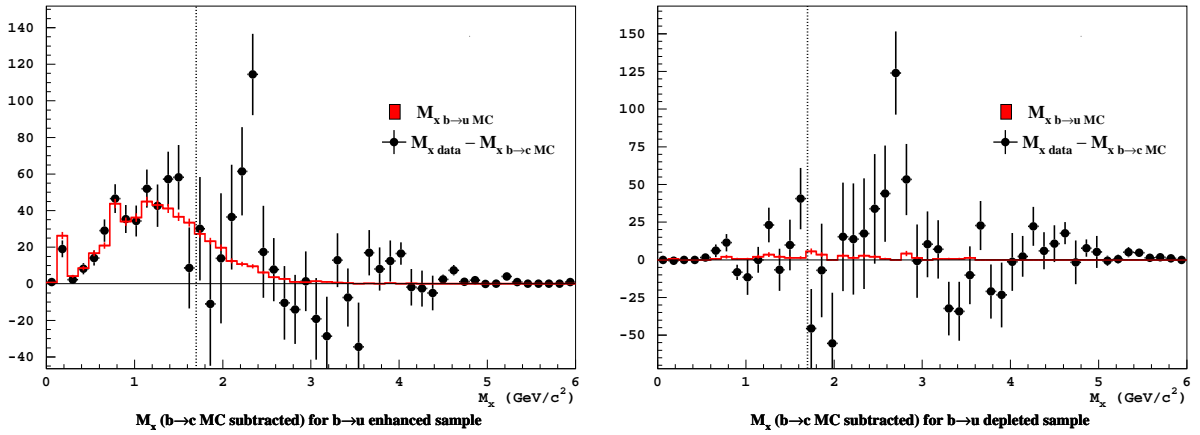


Figure 8-4. The M_X distribution obtained by subtracting the simulated $b \rightarrow c$ contribution from the data. The normalization of $b \rightarrow c$ and $b \rightarrow u$ contributions is obtained by a fit to the data. The subtracted distribution is compared to the fitted simulated $b \rightarrow u$ distribution. Left: plot for the $b \rightarrow u$ *enhanced sample*. Right: plot for the $b \rightarrow u$ *depleted sample*.

The M_X distribution outside the signal region, where the contribution of the $b \rightarrow c$ component is dominant, shows that the $b \rightarrow c$ MC simulation is not entirely successful. The clear discrepancy of the shapes at $M_X \approx 2.2 \text{ GeV}/c^2$ in the $b \rightarrow u$ *enhanced sample* and $M_X \approx 2.7 \text{ GeV}/c^2$ in the $b \rightarrow u$ *depleted sample* is not understood yet. The difference in M_X for both observed discrepancies is $\Delta M_X \approx 500 \text{ MeV}/c^2$, which corresponds to the mass of a kaon, so the interpretation that the two discrepancies are of the same origin, where a kaon from the decay is missing or misidentified on the $b \rightarrow u$ *enhanced sample*, seems reasonable.

The better understanding of this discrepancy is essential for future $|V_{ub}|$ determinations, since it might be one of the causes of the discrepancy between the $|V_{ub}|$ values obtained in the M_X and M_X/q^2 signal regions. The q^2 selection suppresses the $b \rightarrow c$ contribution for events with higher M_X , and can thus reduce the observed discrepancy in the M_X shape, which in turn reduces the obtained normalization of the $b \rightarrow c$ MC. This can result in the observed linear increase of the $|V_{ub}|$ values when increasing the lower limit of the q^2 selection. The estimated relative deviation of the $|V_{ub}|$ result when the bin containing the discrepancy (see Fig. 7-4) is removed from the fit, is 3%, which is too small to account for the difference in the $|V_{ub}|$ results for the M_X and M_X/q^2 signal regions.

8.1.3 Comparison of the three methods

From the $|V_{ub}|$ results obtained using the three signal regions (see Tab. 7-17) we can draw the following conclusions:

- No experimental nor theoretical improvement was observed by applying the additional selection of $q^2 > 8 \text{ GeV}^2/c^2$ to the M_X analysis.
- We find that the usage of the variable P_+ is more sensitive to the $b \rightarrow c$ modeling and shape function parametrization than the other two methods and will only become competitive in the future when the theoretical error of $R(\Delta\Phi)$ dominates.

One of the expected advantages of the P_+ analysis was that the $b \rightarrow c$ background will increase more gradually than in the M_X case, where the D and D^* meson resonances introduce the background at once [3]. This "buffer zone" of gradual increase in $b \rightarrow c$ background for P_+ should reduce the effect of the $b \rightarrow c$ - related uncertainties on $|V_{ub}|$ determination. In contrary, we observe a four times larger uncertainty due to the $b \rightarrow c$ simulation of the P_+ analysis compared to the M_X case.

We think the reason for such an outcome is a very different ratio for M_X and P_+ between the width of the available $b \rightarrow c$ suppressed region and the experimental resolution of the variable.

$\Delta\Phi$	$\Delta\Phi^{\text{theo}}$	σ_{wide}	$\Delta\Phi^{\text{theo}}$ in σ_{wide}
M_X	1864 MeV/ c^2	342 MeV/ c^2	$5.5 \times \sigma_{\text{wide}}$
P_+	660 MeV/ c	416 MeV/ c	$1.6 \times \sigma_{\text{wide}}$

Table 8-1. Comparison of the regions, where $b \rightarrow c$ transitions are kinematically not allowed ($\Delta\Phi^{\text{theo}}$) and experimental resolutions (from Sec. 6.3.3) in P_+ an M_X .

Since $b \rightarrow c$ transitions that migrate into the kinematically suppressed region ($\Delta\Phi^{\text{theo}}$) are badly reconstructed decays, the resolution in the particular variable is represented by σ_{wide} (see Sec. 6.3.3). The $\Delta\Phi^{\text{theo}}$ region for P_+ is only $1.6 \times \sigma_{\text{wide}}$, compared to $5.5 \times \sigma_{\text{wide}}$ for M_X (Tab.8-1). This means that the whole $\Delta\Phi^{\text{theo}}$ is less than $2\sigma_{\text{wide}}$ away from $b \rightarrow c$ background in the P_+ case, whereas in the M_X case the region below $1 \text{ GeV}/c^2$ is shielded by $3\sigma_{\text{wide}}$ distance from the start of the $b \rightarrow c$ background.

8.1.4 Final $|V_{ub}|$ result

For the reasons that were presented in the previous section, we chose the M_X signal region result as the final $|V_{ub}|$ result of the analysis, since it includes the largest portion of the phase space and is the least affected by the uncertainties:

$$|V_{ub}| = (4.09 \pm 0.19 \pm 0.20 \begin{smallmatrix} +0.14 \\ -0.15 \end{smallmatrix} \pm 0.18) \times 10^{-3} \quad , \quad (8.2)$$

where the errors are statistical, systematic with MC modeling, theoretical and from shape function parameter determination, respectively. The total $|V_{ub}|$ error of this result is 9%.

This result is the most accurate measurement of $|V_{ub}|$ to date; using the newly determined shape function parameters it is the first one to break the 10% accuracy barrier, indicating that the measurement of the smallest CKM matrix element is, owing to continuous effort of both experimental and theoretical communities, slowly becoming a precision measurement.

The achieved precision of the $|V_{ub}|$ determination is the result of the use of larger data sample, better shape function parameter determination and improved theoretical predictions [36, 3].

8.1.4.1 Comparison with other inclusive measurements

The obtained result is compared to other inclusive measurements of $|V_{ub}|$. The $|V_{ub}|$ results with error bars are shown in Fig. 8-5, where the errors are separated according to their correlation between different results. Uncorrelated errors are consisted of the statistical and systematic errors with MC modeling, while the theoretical error and the error due to shape function parameters is correlated between experiments. The inner error bar represents the uncorrelated errors, the outer error bar presents the total error of each measurement.

The $|V_{ub}|$ average from the LEP $|V_{ub}|$ Group is obtained from four analyses, one of which was the first to use the M_X selection with a cut on the lepton momentum [70]. They also separate events into the $b \rightarrow u$ *enhanced sample* and $b \rightarrow u$ *depleted sample* based on the number of reconstructed kaons and the displacement of secondary and tertiary decay vertices of the charmed mesons.

The CLEO, BaBar and Belle endpoint analyses [22, 23, 21] extract $b \rightarrow u$ transitions from the endpoint of the charged lepton momentum. The analysis does not need a separation of particles between the two B mesons, since only the information on high momentum lepton is used.

Belle published an analysis [61] where the particles were separated between the two B mesons using a so-called simulated annealing (sim. ann.), where combinations of particles are constructed and the separation is gradually improved by exchanging particles in the combinations.

Other analyses use a fully reconstructed sample (freco), and extract charmless semileptonic decays using the combinations of kinematical variables M_X , P_+ , q^2 and E_e , the energy of the prompt electron [71, 72, 73].

The values of V_{ub} , except for the LEP average and "BaBar M_X freco" results, are recalculated using the shape function parameters used also in this analysis [69], and are averaged in the world average HFAG2005.

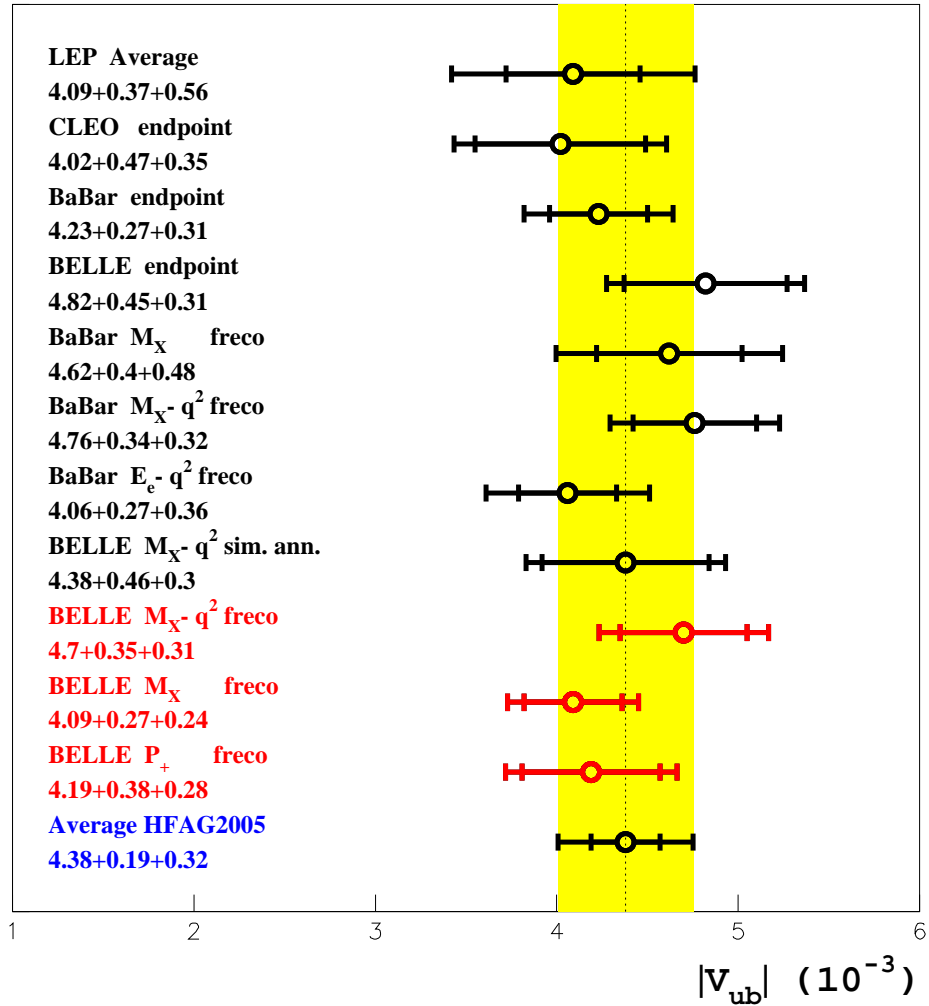


Figure 8-5. Comparison with other $|V_{ub}|$ measurements: the results from this analysis (red), other recent inclusive measurements (black), and current the world average (blue) that includes the results obtained from experiments, producing B mesons from $\Upsilon(4S)$ decays (BaBar, Belle, Cleo) [14], except the "BaBar M_X freco" result. From the results of this analysis, only " M_X freco" is used in the fit. See Sec. 8.1.4.1 for the explanation of the methods.

8.2 Constraints on the $\rho - \eta$ plane

The $|V_{ub}|$ measurement constrains the size of the side opposite to the angle ϕ_1 of the unitarity triangle, the length of which corresponds to

$$R_b = \frac{|V_{ud}V_{ub}^*|}{|V_{cd}V_{cb}^*|} . \quad (8.3)$$

The constraint on R_b in the $\rho - \eta$ plane represents a ring, centered at $(0,0)$. The constraint from this analysis is shown in Fig. 8-6, together with other constraints from the experimental world averages of the Standard Model parameters.

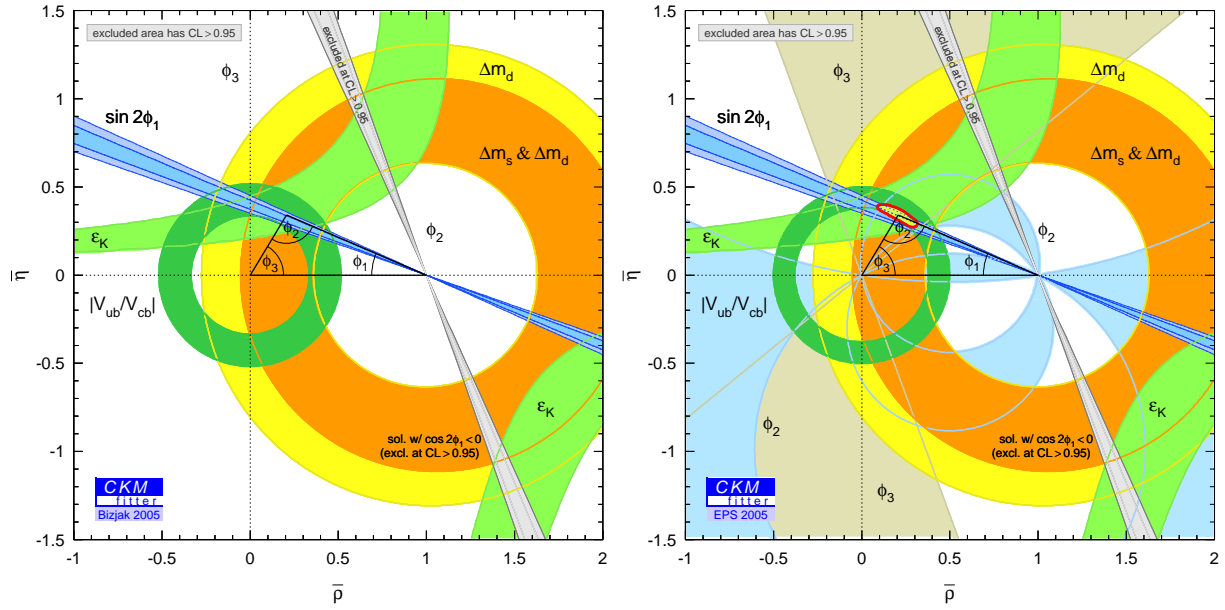


Figure 8-6. The 95% CL constraint on the upper vertex of the unitarity triangle. Left: the ring (dark green) centered at $(0,0)$ represents the $|V_{ub}|$ constraint from this analysis, other constraints are from experimental world averages of the Standard Model parameters: ϵ_K is obtained from measurements of CP violation in K mesons, Δm_d and Δm_s from $B\bar{B}$ and $B_s\bar{B}_s$ oscillations, respectively, and $\sin(2\phi_1)$ in CP-violating B meson decays like $B \rightarrow J/\psi K_S$. Right: same plot with the $|V_{ub}|$ constraint from a world average of $|V_{ub}|$ measurements, including this one (August 2005) [15].

The precision of the $|V_{ub}|$ measurements is coming to the stage where it constrains the upper vertex of the unitarity triangle to the same extent as the measurements of $\sin(2\phi_1)$ (currently the most accurately measured constraint); for now the constraints from $|V_{ub}|$ and $\sin(2\phi_1)$ overlap significantly, pointing at the internal consistency of the Standard Model (see 8.2, left).

8.3 Future improvements

The measurement of $|V_{ub}|$ has improved significantly in the last few years and achieved a total error of less than 10%. For now, the total error has equal contributions from statistics, systematic errors, theoretical errors and the uncertainty due to the determination of shape function parameters; it is therefore equally important to reduce each of the contributions.

The Belle detector will soon reach the collected luminosity of 500fb^{-1} , doubling the data sample used for current analysis and reducing the statistical error to $\sim 3\%$. The amount of background $b \rightarrow c$ MC, which contributes

significantly to the systematic uncertainty, will also increase. The $b \rightarrow c$ transition simulation should be improved by precision measurements of the properties of $B \rightarrow D\ell\nu$ and $D^*\ell\nu$ decays, specially the understanding of form-factor dependence on q^2 . The contributions to the D^{**} region should be reduced with improved measurements of branching fractions of wide and narrow D^{**} components, reducing the uncertainty on for now the least understood contribution of the $b \rightarrow c$ simulation.

There is a continuous effort by several experiments under Heavy Flavor Averaging Group (HFAG) to obtain the shape function parameters as reliably as possible, and to recalculate $|V_{ub}|$ values for different measurements with the improved parameters. For now, the most accurate determinations are the one combining the result of several experiments on moments of (1) $B \rightarrow X_s\gamma$ photon spectrum distribution, (2) $B \rightarrow X_c\ell\nu$ hadronic invariant mass distributions and (3) lepton momentum distributions. When the samples are increased, the shape function parameters will also be determined from $B \rightarrow X_u\ell\nu$ distributions.

The Soft Collinear Effective Theory seems to have developed a way to deal systematically with the decays of a heavy to a light quark. We hope that the theorists will be stimulated by improved experimental results to calculate the next order corrections to the partial rates, reducing the theoretical uncertainties, which are currently the single largest contribution to the total error for the M_X/q^2 analysis.

The sample of fully reconstructed events is able to tag the flavor of the reconstructed B meson; the reduced contributions to the uncertainty will allow for a reliable determination of semileptonic branching fractions for charged and neutral B mesons separately. A separate determination will help shed light on for now relatively unexplored issues, for example the weak annihilation of the neutral B meson. Increased fully reconstructed data sample will also revive some of the analysis methods that have been limited by large $b \rightarrow c$ background systematics, like the lepton endpoint analysis. Finally, the improved understanding of how to combine different measurements and their uncertainties will be able to provide us with the knowledge of how to chose methods of $|V_{ub}|$ determination that will offer a reliable average, and will enable us to test the predictions of the Standard Model.

9.1 Uvod

Fizika osnovnih delcev se ukvarja z razumevanjem lastnosti in interakcij osnovnih delcev. Splošno sprejeto znanje, ki smo si ga nabrali o fiziki osnovnih delcev, je zbrano v tako imenovanem Standardnem Modelu. Standardni Model je zelo uspešen pri napovedovanju fizikalnih procesov, saj se skoraj vse meritve znotraj eksperimentalnih in teoretičnih napak ujemajo z napovedmi. Kljub temu je kar nekaj znakov, da Standardni Model kot ga poznamo danes, ni končni odgovor na vsa vprašanja fizike osnovnih delcev.

Eksperimentalna fizika osnovnih delcev preverja naše razumevanje in teoretske napovedi fizike osnovnih delcev in z natančnimi meritvami spodbuditi k napredku našega razumevanja fizikalnih procesov. Področje, na katero se je osredotočilo veliko raziskav v zadnjih nekaj letih, je tako imenovana fizika okusov, torej fizika šibke interakcije, pri kateri kvarki lahko spreminjajo okus. V Standardnem Modelu je opisana z mehanizmom Kobayashija in Maskawe, ki sta leta 1973 zapisala matriko CKM (Cabibbo-Kobayashi-Maskawa). Matrika CKM je unitarna, unitarnostne pogoje matrike CKM pa zaradi tega, ker so njeni elementi lahko kompleksne vrednosti, v kompleksni ravnini pokažemo kot trikotnike. Različne meritve omogočajo določitev kotov in stranic unitarnostnih trikotnikov. Možna odstopanja napovedi Standardnega Modela od meritev bi lahko zaznali kot neujemanje pri konstrukciji trikotnikov.

Meritev kršitve simetrije CP v sistemu nevtralnih mezonov B leta 2001 je pokazala, da je matrika CKM res kompleksna, ter da je kot ϕ_1 v trikotniku, ki je lahko popolnoma določen samo z meritvami prehodov kvarka b , različen od nič. Stranica nasproti kota ϕ_1 je določena z velikostjo matričnega elementa V_{ub} , procesi, uporabljeni pri meritvi kota ϕ_1 in $|V_{ub}|$ pa se pomembno razlikujejo, zato bi se mogoča odstopanja od napovedi standardnega modela lahko pokazala prav pri primerjavi teh dveh meritev.

Namen meritve, predstavljene v tem delu, je natančna določitev velikosti matričnega elementa V_{ub} s pomočjo meritve razpadne širine mezonov B v semileptonske razpade, kjer je kvark b prešel v kvark u . Ker je semileptonski prehod kvarka b v kvark c zelo podoben, a kar 80-krat bolj pogost, je potrebno za ločevanje med semileptonskimi prehodi kvarka b v kvark u in c meritev omejiti na kinematična območja, kjer je prehod $b \rightarrow c$ kinematično prepovedan.

Za izračun kinematičnih količin, kot so hadronska invariantna masa M_X , kvadrat leptonske invariantne mase q^2 in spremenljivka $P_+ \equiv E_X/c - |\vec{p}_X|$, je potrebno ločiti delce v dogodku glede na to, iz razpada katerega mezona B prihajajo. Meritev je zato opravljena na vzorcu mezonov B , pri katerem je razpad enega od mezonov B popolnoma rekonstruiran. Zaradi majhne uspešnosti popolnega rekonstruiranja je potrebno izmeriti veliko količino mezonov B ; meritev je bila opravljena na vzorcu 275 milijonov parov mezonov B , ki so nastali pri trkih pozitronov in elektronov v detektorju Belle institutu KEK na Japonskem.

Pri teoretičnem izračunu, ki je bil uporabljen za določitev velikosti matričnega elementa V_{ub} iz izmerjenih rezultatov, so pomembni neperturbativni prispevki, ki močno omejujejo natančnost izračuna. Da bi omogočili natančno meritev $|V_{ub}|$, je neperturbativni prispevek parametriziran v tako imenovani oblikovni funkciji [3], parametri oblikovne funkcije pa so določeni s prilaganjem porazdelitev kinematičnih količin pri neodvisni meritvi.

9.2 Matrika CKM

Matriko CKM sta zapisala Kobayashi in Maskawa leta 1973 [5], ko še niso bili odkriti kvarki c , b in t . Mehanizem naj bi opisal prehode med kvarki različnih generacij.

Matrika CKM transformira stanja kvarkov z nabojem $-\frac{1}{3}$ iz stanj, v katerih imajo dobro določeno maso (d), v stanja, ki nastopajo pri šibki interakciji d' :

$$\begin{pmatrix} d' \\ s' \\ b' \end{pmatrix} = \begin{pmatrix} V_{ud} & V_{us} & V_{ub} \\ V_{cd} & V_{cs} & V_{cb} \\ V_{td} & V_{ts} & V_{tb} \end{pmatrix} \begin{pmatrix} d \\ s \\ b \end{pmatrix}, \quad (9.1)$$

Je unitarna kompleksna matrika s štirimi prostimi parametri. Ena od bolj pogostih in uporabnih parametrizacij je Wolfensteinova parametrizacija [9], ki uporablja parametre λ , A , ϱ in η :

$$\hat{V}_{\text{CKM}} = \begin{pmatrix} 1 - \frac{1}{2}\lambda^2 - \frac{1}{8}\lambda^4 & \lambda + \mathcal{O}(\lambda^7) & A\lambda^3(\varrho - i\eta) \\ -\lambda + \frac{1}{2}A^2\lambda^5[1 - 2(\varrho + i\eta)] & 1 - \frac{1}{2}\lambda^2 - \frac{1}{8}\lambda^4(1 + 4A^2) & A\lambda^2 + \mathcal{O}(\lambda^8) \\ A\lambda^3(1 - \bar{\varrho} - i\bar{\eta}) & -A\lambda^2 + \frac{1}{2}A\lambda^4[1 - 2(\varrho + i\eta)] & 1 - \frac{1}{2}A^2\lambda^4 \end{pmatrix}, \quad (9.2)$$

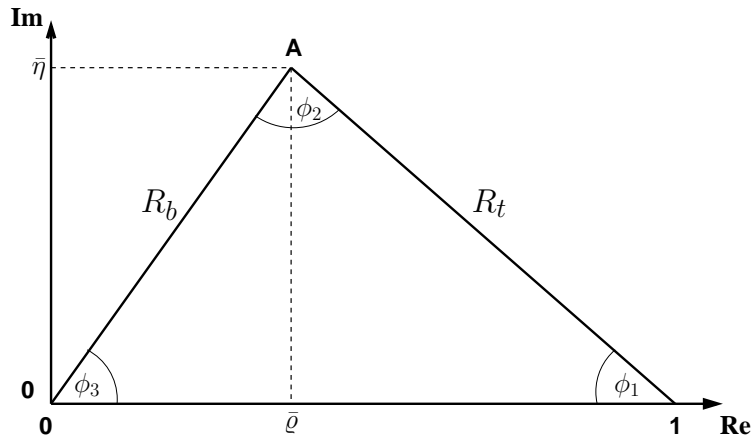
Za večjo berljivost so popravki reda λ^2 dodani v zadnja dva parametra:

$$\bar{\varrho} = \varrho \left(1 - \frac{\lambda^2}{2}\right), \quad \bar{\eta} = \eta \left(1 - \frac{\lambda^2}{2}\right). \quad (9.3)$$

Eden izmed pogojev, da je matrika CKM unitarna, je dobljen z množenjem prvega in tretjega stolpca matrike CKM:

$$V_{ud}V_{ub}^* + V_{cd}V_{cb}^* + V_{td}V_{tb}^* = 0, \quad (9.4)$$

in določa tako imenovan *unitarnostni trikotnik*. Relacijo 9.4 normiramo s členom $(V_{cd}V_{cb}^*)$, ki je v Wolfensteinovi parametrizaciji realen, tako da dobimo trikotnik na sliki 9-1.



Slika 9-1. Unitarnostni trikotnik z normirano stranico.

Stranice in kote tega trikotnika zapišemo z matričnimi elementi matrike CKM:

$$\phi_1 \equiv \left[-\frac{V_{cd}V_{cb}^*}{V_{td}V_{tb}^*} \right]; \quad \phi_2 \equiv \left[-\frac{V_{ud}V_{ub}^*}{V_{td}V_{tb}^*} \right]; \quad \phi_3 \equiv \left[-\frac{V_{cd}V_{cb}^*}{V_{ud}V_{ub}^*} \right] \equiv \pi - \phi_1 - \phi_2; \quad (9.5)$$

$$R_b \equiv \frac{|V_{ud}V_{ub}^*|}{|V_{cd}V_{cb}^*|} = \sqrt{\bar{\varrho}^2 + \bar{\eta}^2} = \left(1 - \frac{\lambda^2}{2}\right) \frac{1}{\lambda} \left| \frac{V_{ub}}{V_{cb}} \right|; \quad (9.6)$$

$$R_t \equiv \frac{|V_{td}V_{tb}^*|}{|V_{cd}V_{cb}^*|} = \sqrt{(1 - \bar{\varrho})^2 + \bar{\eta}^2} = \frac{1}{\lambda} \left| \frac{V_{td}}{V_{cb}} \right|. \quad (9.7)$$

Meritev kota ϕ_1 je ena najbolj natančnih meritev, ki določa *unitarnostni trikotnik*. Za preverjanje napovedi Standardnega Modela jo je potrebno primerjati z ostalimi meritvami. Prispevki k meritvi kota ϕ_1 vsebujejo Feynmanove diagrame z zankami, na primer škatlasti in pingvinski diagram, medtem ko meritev $|V_{ub}|$ vsebuje le diagrame drevesnega tipa. V diagramih drevesnega tipa ne pričakujemo možnih prispevkov izven Standardnega Modela, med tem ko so diagrame z zankami na možne prispevke zelo občutljivi. Primerjava meritev ϕ_1 in $|V_{ub}|$ bi torej lahko pokazala na odstopanja od napovedi Standardnega Modela, zato je izjemno pomembno določiti $|V_{ub}|$ karseda natančno, pri tem pa zmanjšati tako teoretične kot eksperimentalne napake meritve $|V_{ub}|$.

9.3 Teoretično ozadje

Celotno razpadno širino za semileptonske razpade, kjer je kvark b prešel v kvark u , lahko izračunamo s pomočjo razvoja po produktih operatorjev (OPE) [27] in efektivno teorijo težkega kvarka (HQET) [16, 17]:

$$\Gamma(B \rightarrow X_u \ell \nu) = \frac{G_F^2 |V_{ub}|^2}{192\pi^3} m_b^5 \times \left[1 - \frac{9\lambda_2 - \lambda_1}{2m_b^2} + \dots - \mathcal{O}(\alpha_s) \right] \quad (9.8)$$

kjer je G_F Fermijeva sklopitvena konstanta: $G_F = 1.166 \times 10^{-5} \text{ GeV}^{-2}$, m_b masa kvarka b in λ_1 ter λ_2 parametra HQET, ki opisujeta neperturbativne popravke, zato sta določena iz neodvisnih meritev.

Ker je potrebno ločiti semileptonske prehode $b \rightarrow u$ od prehodov $b \rightarrow c$, merimo le razpade znotraj določenega kinematičnega območja in je potrebno izračunati delno razpadno širino v določeno kinematično območje. Tak izračun je močno otežen zaradi velikih neperturbativnih prispevkov [30] (vzrok neperturbativnih prispevkov je to, da je α_s , sklopitvena konstanta močne interakcije, pri gibalnih količinah, ki se izmenjujejo v mezonu B , prevelika, da bi lahko razvijali po potencah α_s).

Neperturbativni prispevek je zato parametriziran v tako imenovani oblikovni funkciji (shape function) [3]. Oblikovna funkcija je v prvem približku neodvisna od specifičnega razpadnega kanala in je enaka za vse razpade težkega kvarka b v lahke kvarke. Parametri oblikovne funkcije so dobljeni s prilagajanjem iz porazdelitev kinematičnih količin drugih razpadov, ki so prav tako opisani z isto oblikovno funkcijo, na primer prehod $b \rightarrow s$. V analizi smo med drugim določili parametra $m_b(SF)$ in $\mu_\pi^2(SF)$ [3], ki sta potrebna za izračun neperturbativnih prispevkov k delni semileptonski razpadni širini.

Matrični element $|V_{ub}|$ je določen neposredno iz $\Delta\Gamma_{u\ell\nu}(\Delta\Phi)$, delne semileptonske razpadne širine v razpadne produkte s kvarkom u ter v kinematično območje $\Delta\Phi$, s pomočjo $R(\Delta\Phi)$, teoretičnega izračuna za $\Delta\Gamma_{u\ell\nu}(\Delta\Phi)$, deljenega z $|V_{ub}|^2$ [3]:

$$|V_{ub}| = \sqrt{\frac{\Delta\Gamma_{u\ell\nu}(\Delta\Phi)}{R(\Delta\Phi)}}. \quad (9.9)$$

9.4 Določanje s popolno rekonstrukcijo

S pomočjo rekonstrukcije razpadne verige enega od mezonov B lahko izračunamo inkluzivne količine nerekonstruiranega mezona B , ki nam omogočajo ločevanje med semileptonskimi razpadi $b \rightarrow u$ in $b \rightarrow c$. Ekskluzivno rekonstruiramo okoli 180 razpadnih kanalov, kar pomeni, da poleg mezona B rekonstruiramo tudi vse vmesne delce. Rekonstruirani razpadni kanali mezonov B so navedeni v tabeli 9-1.

razpadni kanali B^+	razvejitevno razmerje (%)	razpadni kanali B^0	razvejitevno razmerje (%)
$B^+ \rightarrow \bar{D}^0 \pi^+$	0.498 ± 0.029	$B^0 \rightarrow D^- \pi^+$	0.276 ± 0.025
$B^+ \rightarrow \bar{D}^0 \rho^+$	1.34 ± 0.18	$B^0 \rightarrow D^- \rho^+$	0.77 ± 0.13
$B^+ \rightarrow \bar{D}^0 a_1^+$	0.25 ± 0.20	$B^0 \rightarrow D^- a_1^+$	0.30 ± 0.17
$B^+ \rightarrow \bar{D}^0 D_S^+$	1.3 ± 0.4	$B^0 \rightarrow D^- D_S^+$	0.8 ± 0.3
$B^+ \rightarrow \bar{D}^0 D_S^{*+}$	0.9 ± 0.4	$B^0 \rightarrow D^- D_S^{*+}$	1.0 ± 0.5
$B^+ \rightarrow \bar{D}^{*0} \pi^+$	0.46 ± 0.04	$B^0 \rightarrow D^{*-} \pi^+$	0.276 ± 0.021
$B^+ \rightarrow \bar{D}^{*0} \rho^+$	0.98 ± 0.17	$B^0 \rightarrow D^{*-} \rho^+$	0.68 ± 0.09
$B^+ \rightarrow \bar{D}^{*0} a_1^+$	0.95 ± 0.25	$B^0 \rightarrow D^{*-} a_1^+$	0.65 ± 0.14
$B^+ \rightarrow \bar{D}^{*0} D_S^+$	1.2 ± 0.5	$B^0 \rightarrow D^{*-} D_S^+$	1.07 ± 0.29
$B^+ \rightarrow \bar{D}^{*0} D_S^{*+}$	2.7 ± 1.0	$B^0 \rightarrow D^{*-} D_S^{*+}$	1.9 ± 0.5
$B^+ \rightarrow \text{rekonstr.}$	10.5 ± 1.3	$B^0 \rightarrow \text{rekonstr.}$	7.7 ± 0.9

Tabela 9-1. Rekonstruirani razpadni kanali mezonov B z njihovimi razvejitvenimi razmerji.

Razpadni kanali, v katerih rekonstruiramo mezone D , D_s , D^* in D_s^* , so navedeni v tabelah 9-2 in 9-3.

Kvaliteta rekonstrukcije mezonov B je ocenjena z razliko energij $\Delta E = E_B^* - E_{\text{curek}}^*$, kjer je E_B^* energija mezona B v težiščnem sistemu $\Upsilon(4S)$, E_{curek}^* pa energija enega curka v težiščnem sistemu, ter z energijo curka omejena masa $M_{bc} = \sqrt{(E_{\text{curek}}^*)^2/c^4 - p_B^{*2}/c^2}$, kjer je p_B^* gibalna količina mezona B v težiščnem sistemu. Dobro rekonstruirani mezoni B imajo ΔE blizu 0, M_{bc} pa nekoliko pod E_{curek}^*/c^2 . Da bi ocenili število dobro in slabo rekonstruiranih mezonov B v nekem vzorcu, prilagajamo porazdelitvi M_{bc} empirično določeno obliko porazdelitev za dobro (En. 9.11 in 9.12) in slabo rekonstruirane mezone (En. 9.10). Porazdelitve slabo rekonstruiranih mezonov parametriziramo s funkcijo ARGUS [59]:

$$\frac{dN}{d(M_{bc})} = N \cdot (E_{\text{curek}}^*/c^2) \cdot x \cdot \sqrt{1-x^2} \cdot e^{-\beta \cdot (1-x^2)} \quad (9.10)$$

kjer je $x \equiv M_{bc}/(E_{\text{curek}}^*/c^2)$ in parameter β določa obliko ozadja, porazdelitev dobro rekonstruiranih pa s funkcijo Crystal Ball [60]:

$$M_{bc} > m_0 - \alpha \cdot \sigma:$$

$$\frac{dN}{d(M_{bc})} = A \cdot e^{-\frac{(M_{bc}-m_0)^2}{2\sigma^2}} \quad (9.11)$$

$$M_{bc} < m_0 - \alpha \cdot \sigma:$$

$$\frac{dN}{d(M_{bc})} = A \cdot \frac{e^{-\frac{\alpha}{2}}}{\left(1 - \frac{\alpha \cdot (M_{bc}-m_0)}{n \cdot \sigma} - \frac{\alpha^2}{n}\right)^n} \quad (9.12)$$

Razpadni kanal	razvejitevno razmerje (%)	masa mezona D	dovoljeno odstopanje
$\overline{D}^0 \rightarrow K^+ \pi^-$	3.80 ± 0.09	$1864.5 \text{ MeV}/c^2$	$\pm 30 \text{ MeV}/c^2$
$\overline{D}^0 \rightarrow K^+ \pi^- \pi^-$	7.46 ± 0.31	$1864.5 \text{ MeV}/c^2$	$\pm 30 \text{ MeV}/c^2$
$\overline{D}^0 \rightarrow K_S \pi^+ \pi^-$	2.05 ± 0.12	$1864.5 \text{ MeV}/c^2$	$\pm 30 \text{ MeV}/c^2$
$\overline{D}^0 \rightarrow K^+ K^-$	$0.39^{+0.12}_{-0.15}$	$1864.5 \text{ MeV}/c^2$	$\pm 30 \text{ MeV}/c^2$
$\overline{D}^0 \rightarrow K^+ \pi^- \pi^0$	13.0 ± 0.8	$1864.5 \text{ MeV}/c^2$	$\pm 45 \text{ MeV}/c^2$
$\overline{D}^0 \rightarrow K_S \pi^+ \pi^- \pi^0$	3.75 ± 0.44	$1864.5 \text{ MeV}/c^2$	$\pm 45 \text{ MeV}/c^2$
$\overline{D}^0 \rightarrow K_S \pi^0$	0.792 ± 0.075	$1864.5 \text{ MeV}/c^2$	$\pm 60 \text{ MeV}/c^2$
$D^0 \rightarrow \text{rekonstr.}$	31.2 ± 1.0		
$D^- \rightarrow K^+ \pi^+ \pi^-$	9.2 ± 0.6	$1869.4 \text{ MeV}/c^2$	$\pm 30 \text{ MeV}/c^2$
$D^- \rightarrow K_S \pi^-$	0.972 ± 0.065	$1869.4 \text{ MeV}/c^2$	$\pm 30 \text{ MeV}/c^2$
$D^- \rightarrow K_S \pi^- \pi^+ \pi^-$	2.44 ± 0.34	$1869.4 \text{ MeV}/c^2$	$\pm 30 \text{ MeV}/c^2$
$D^- \rightarrow K^+ K^- \pi^-$	0.89 ± 0.08	$1869.4 \text{ MeV}/c^2$	$\pm 30 \text{ MeV}/c^2$
$D^- \rightarrow K^+ \pi^- \pi^- \pi^0$	6.5 ± 1.1	$1869.4 \text{ MeV}/c^2$	$\pm 45 \text{ MeV}/c^2$
$D^- \rightarrow K_S \pi^+ \pi^0$	3.3 ± 1.0	$1869.4 \text{ MeV}/c^2$	$\pm 45 \text{ MeV}/c^2$
$D^- \rightarrow \text{rekonstr.}$	23.3 ± 1.6		
$D_s^- \rightarrow K^- K^+ \pi^-$	4.3 ± 1.2	$1969.0 \text{ MeV}/c^2$	$\pm 30 \text{ MeV}/c^2$
$D_s^- \rightarrow K^- K_S$	1.24 ± 0.37	$1969.0 \text{ MeV}/c^2$	$\pm 30 \text{ MeV}/c^2$
$D_s^- \rightarrow \text{rekonstr.}$	5.5 ± 1.3		

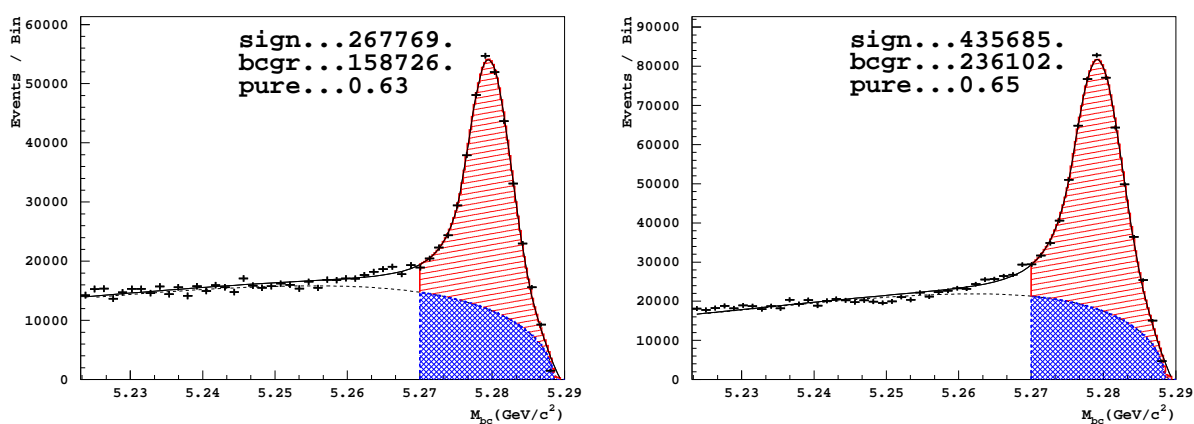
Tabela 9-2. Rekonstruirani razpadni kanali, uporabljeni pri rekonstrukciji mezonov D in D_s , njihova razvejitevna razmerja [10], ter dovoljeno odstopanje rekonstruirane mase mezona od njegove nominalne mase.

Razpadni kanal	razvejitevno razmerje(%)	$\Delta m \equiv m_{D_{(s)}^*} - m_{D_{(s)}}$	dovoljeno odstopanje
$\overline{D}^{*0} \rightarrow \overline{D}^0 \pi^0$	61.9 ± 2.9	$142.12 \text{ MeV}/c^2$	$\pm 5 \text{ MeV}/c^2$
$\overline{D}^{*0} \rightarrow \overline{D}^0 \gamma$	38.1 ± 2.9	$142.12 \text{ MeV}/c^2$	$\pm 20 \text{ MeV}/c^2$
$D^{*-} \rightarrow \overline{D}^0 \pi^-$	67.7 ± 0.5	$140.64 \text{ MeV}/c^2$	$\pm 5 \text{ MeV}/c^2$
$D^{*-} \rightarrow \overline{D}^- \pi^0$	30.7 ± 0.5	$140.64 \text{ MeV}/c^2$	$\pm 5 \text{ MeV}/c^2$
$D_s^{*-} \rightarrow D_s^- \gamma$	94.2 ± 2.5	$143.9 \text{ MeV}/c^2$	$\pm 20 \text{ MeV}/c^2$

Tabela 9-3. Rekonstruirani razpadni kanali, uporabljeni pri rekonstrukciji mezonov D^* in D_s^* , njihova razvejitevna razmerja [10], ter dovoljeno odstopanje rekonstruirane razlike med masama mezonov D^* (D_s^*) in D (D_s).

Število dobro rekonstruiranih mezonov B je enako številu delcev v prispevku, ki ustreza En. 9.11 in 9.12, hkrati pa je še znotraj $-0.2 \text{ GeV} < \Delta E < 0.05 \text{ GeV}$ in $M_{bc} \geq 5.27 \text{ GeV}/c^2$. Število dobro rekonstruiranih mezonov B v celotnem vzorcu popolnoma rekonstruiranih mezonov B , dobljenih iz prilagajanja na sliki 9-2, je podano v tabeli 9.4, kjer je čistost vzorca definirana kot $N(\text{dobro r.})/(N(\text{dobro r.}) + N(\text{slabo r.}))$.

	N(dobro r.)	N(slabo r.)	čistost	izkoristek reconstr.
B^+	435685	236102	0.65	0.30%
B^0	267769	158726	0.63	0.19%



Slika 9-2. Porazdelitev M_{bc} za podatke z $-0.2 \text{ GeV} < \Delta E < 0.05 \text{ GeV}$. Prilagajanje s funkcijo Crystal Ball za dobro rekonstruirane (rdeča polna črta) in funkcijo ARGUS (črtkana črna črta). Levo rezultat za B^0 , desno za B^+ .

9.5 Analiza dogodkov

Da bi lahko uspešno prešteli dogodke s semileptonskimi razpadi $b \rightarrow u$, moramo izbrati dogodke, kjer je prisoten lepton z veliko gibalno količino, razen nevtrina ni nezaznanih delcev, ter ni rekonstruiranih nabitih in nevtralnih kaonov. Delno rekonstruiramo tudi razpad delca D^* , ter število dodatnih leptonov v dogodku, ker sta oboje znaka za prehod $b \rightarrow c$. Rezultati so normirani na število semileptonskih razpadov, ki jih označimo z identificiranim leptonom z gibalno količino $p^* \geq 1 \text{ GeV}/c$, ter nabojem, ki mora v primeru rekonstrukcije nabitega mezona B ustrezati naboju rekonstruiranega mezona B .

opis izbornega kriterija	s.l.	$b \rightarrow u$
lepton s $p^* \geq 1 \text{ GeV}/c$	✓	✓
naboj koreliran med ℓ^\pm/B^\pm	✓	✓
natanko en lepton s $p^* \geq 0.7 \text{ GeV}/c$		✓
naboj dogodka nevtralen: $\Delta Q = 0$		✓
manjkajoča gib. ni v smeri curkov: $\cos \theta_{mm} < 0.9$		✓
manjkajoča masa: $-1 \leq m_{miss}^2 \leq 0.5 \text{ GeV}^2/c^4$		✓
ni rekon. in ident. kaonov: $N(K) = 0$		✓
zavračanje delno rekon. D^*		✓

Tabela 9-4. Izborni kriteriji za semileptonske kandidate (s.l.) in kandidate za meritev prehodov $b \rightarrow u$.

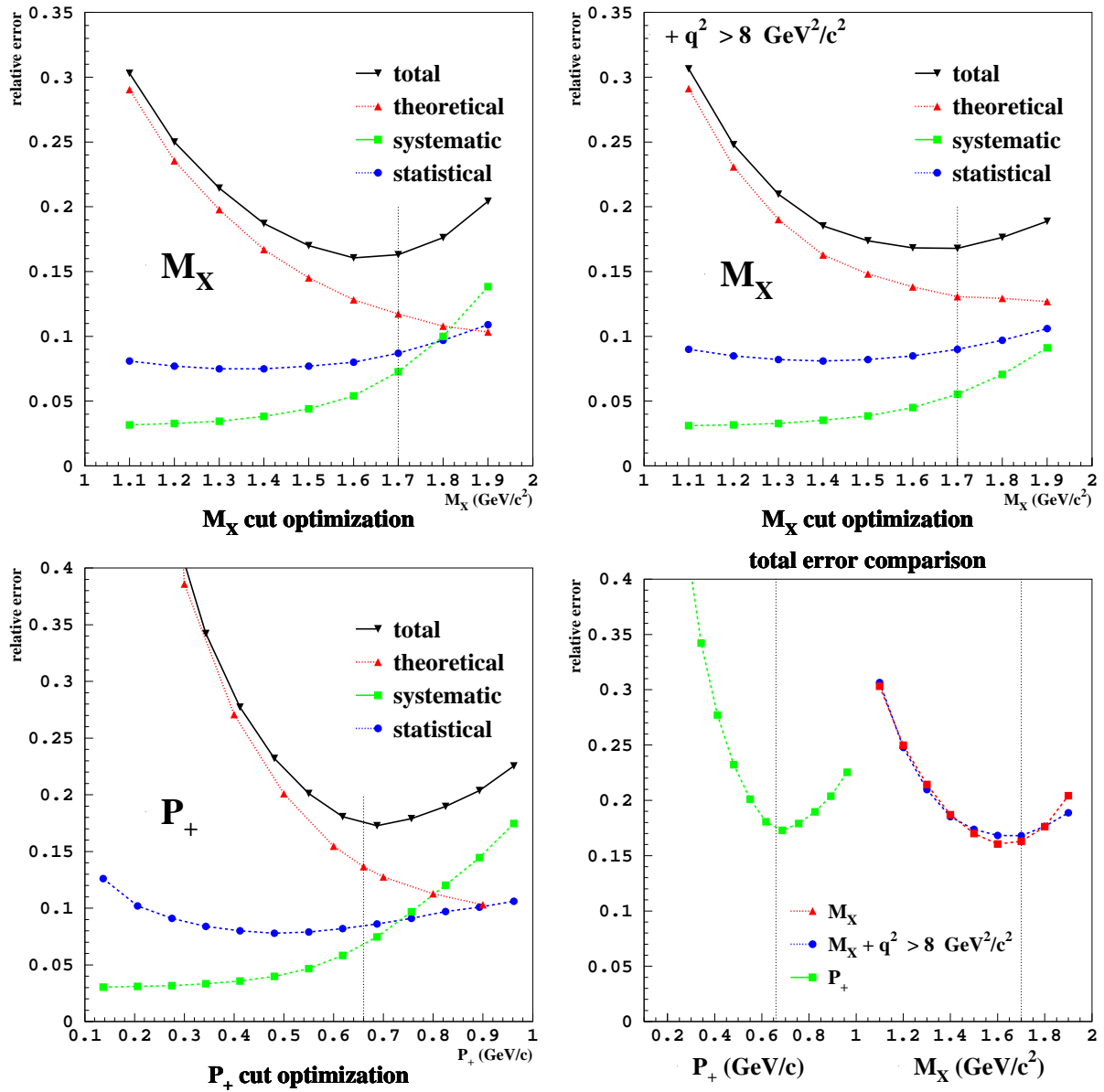
Na dogodkih, ki ustrezajo izbornim kriterijem 9-4, izračunamo inkluzivne kinematične količine: hadronsko invariantno maso $M_X = \sqrt{P_X^2/c^2}$, kvadrat četverca gibalne količine leptonskega para q^2 in spremenljivko P_+ . Za to potrebujemo četverca leptonskega (q) in hadronskega dela (P_X):

$$\begin{aligned} P_X &= \sum_{\text{nabitih delci}} P + \sum_{\gamma} P - P_\ell \\ q &= P_{\Upsilon(4S)} - P_{B_{\text{tag}}} - \sum_{\text{nabitih delci}} P - \sum_{\gamma} P + P_\ell = P_{\Upsilon(4S)} - P_{B_{\text{tag}}} - P_X \end{aligned} \quad (9.13)$$

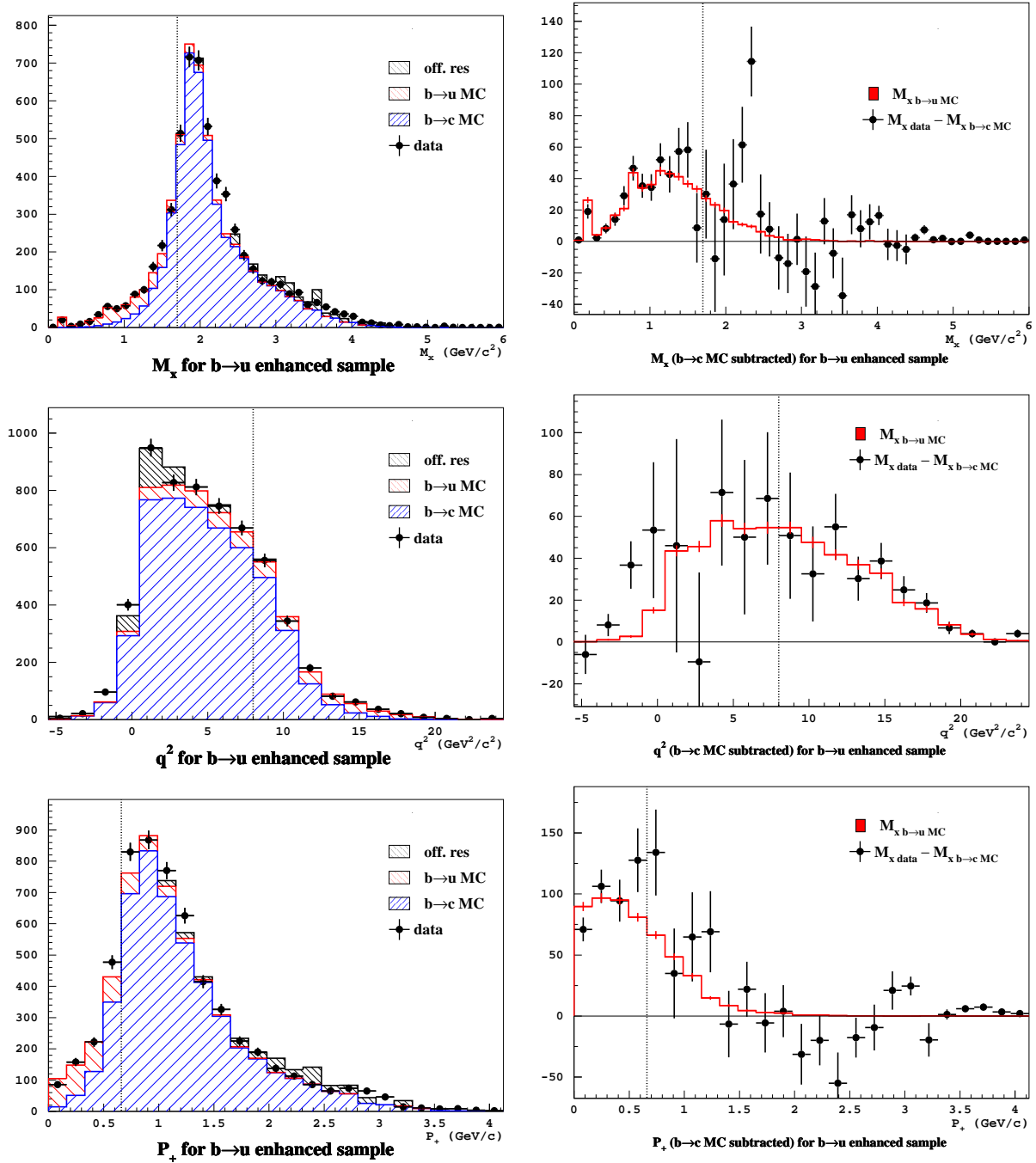
kjer so P_ℓ četverec gibalne količine hitrega leptona, $P_{\Upsilon(4S)}$ četverec gibalne količine resonance $\Upsilon(4S)$, $P_{B_{\text{tag}}}$ četverec gibalne količine rekonstruiranega mezona B , v vsotah pa seštejemo četverce gibalnih količin vseh fotonov in nabitih delcev, ki ustrezajo izbornim pogojem.

Količino P_+ sestavimo iz energije in gibalne količine hadronskega dela v sistemu mezona B : $P_+ = E_X/c - |\vec{p}]_X$. S pomočjo M_X , q^2 ter P_+ izberemo tri kinematična območja, v katerih je delež semileptonskih razpadov $b \rightarrow u$ zadosti velik glede na razpade $b \rightarrow c$, da je meritev $|V_{ub}|$ čim bolj natančna: (1) območje M_X , (2) območje M_X z dodatno omejitvijo q^2 , ter (3) območje P_+ . Natančno vrednost meja kinematičnih območij določimo z minimizacijo ocenjene skupne napake meritve. Slika 9-3 prikazuje skupno napako meritve za vsa tri območja: M_X zgoraj levo, M_X/q^2 zgoraj desno, ter P_+ spodaj levo. Vse tri izbire na eni sliki (os x je hkrati M_X in P_+) so predstavljeni na sliki 9-3 (spodaj desno).

Tako določene meje so: (1) $M_X < 1.7 \text{ GeV}/c^2$, (2) $M_X < 1.7 \text{ GeV}/c^2$ skupaj z $q^2 > 8 \text{ GeV}^2/c^2$, ter (3) $P_+ < 0.66 \text{ GeV}/c$. Rekonstruirane porazdelitve kinematičnih količin M_X , q^2 in P_+ so predstavljene na sliki 9-4.



Slika 9-3. Prispevki k skupni napaki za kinematična območja M_X (zgoraj levo) M_X z dodatno zahtevo $q^2 > 8$ GeV²/c² (zgoraj desno), in P_+ (spodaj levo), risani v odvisnosti od izbrane zgornje meje M_X in P_+ . Spodaj desno: primerjava skupnih napak za vsa tri kinematična območja, v odvisnosti od izbrane zgornje meje M_X in P_+ (os x predstavlja tako M_X kot P_+).



Slika 9-4. Porazdelitev inkluzivnih kinematičnih količin M_X (zgoraj), q^2 (v sredi) in P_+ (spodaj), s prilagajanimi prispevki simulacij za $X_c \ell \nu$ in $X_u \ell \nu$: (levo) pred, in (desno) po odštevanju prispevka $X_c \ell \nu$ (točke z napakami), prikazano skupaj s simulacijo za $b \rightarrow u$ (rdeč histogram).

9.6 Meritev matričnega elementa $|V_{ub}|$

Dogodke, kjer je eden od mezonov B semileptonsko razpadel v končna stanja brez kvarka c , smo prešteli na vzorcu, v katerem smo kinematične količine M_X , q^2 in P_+ rekonstruirali v enem od treh kinematičnih območij (poglavje 9.5). Ker je del dogodkov v izbranem območju ΔE in M_{bc} takih, kjer je bil delec B rekonstruiran iz naključnih delcev (kombinatorično ozadje), preštejemo dogodke s prilagajanjem empirične oblike porazdelitve dobro in slabo rekonstruiranih dogodkov (enačbe 9.10, 9.11 in 9.12).

Neposredni rezultat meritve je količnik $W(\Delta\Phi)$:

$$W(\Delta\Phi) = \frac{\Delta\Gamma_{ul\nu}(\Delta\Phi)}{\Gamma(X\ell\nu)} = \frac{N_{b\rightarrow u}^{\text{raw}}}{N_{\text{sl}}} \times \frac{F}{\varepsilon_{\text{sel}}^{b\rightarrow u}} \times \frac{\varepsilon_{\text{frec}}^{\text{sl}}}{\varepsilon_{\text{frec}}^{b\rightarrow u}} \times \frac{\varepsilon_{\ell}^{\text{sl}}}{\varepsilon_{\ell}^{b\rightarrow u}} . \quad (9.14)$$

Razlaga posameznih faktorjev:

$N_{b\rightarrow u}^{\text{raw}}$: Število presežnih dogodkov, ocenjenih tako, da v kinematičnem območju preštetim dogodkom na podatkih odštejemo pričakovano vrednost dogodkov s prehodom $b \rightarrow c$. Pričakovano število $b \rightarrow c$ dobimo tako, da podatkom prilagajamo simulirani porazdelitvi za prehoda $b \rightarrow u$ in $b \rightarrow c$. Rezultat prilagajanja za vsa tri kinematična območja je prikazan na sliki 9-5.

F : Korekcijski faktor, ki dobljeno število dogodkov s prehodom $b \rightarrow u$ popravi za ocenjeni delež dogodkov, ki so prešli v kinematično območje $\Delta\Phi$ ali iz njega zaradi detektorske resolucije ali slabe rekonstrukcije.

$\varepsilon_{\text{sel}}^{b\rightarrow u}$: Izkoristek za izbiro dogodkov s prehodom $b \rightarrow u$, normiran na dogodke s prehodom $b \rightarrow u$, pri katerih smo rekonstruirali lepton s $p^* \geq 1 \text{ GeV}/c$.

N_{sl} : Ocenjeno število dogodkov s semileptonskim prehodom v vzorcu popolnoma rekonstruiranih mezonov B . V številu je upoštevan pričakovani delež dogodkov, ki niso bili semileptonski, pa so bili za take določeni zaradi netočne rekonstrukcije leptona.

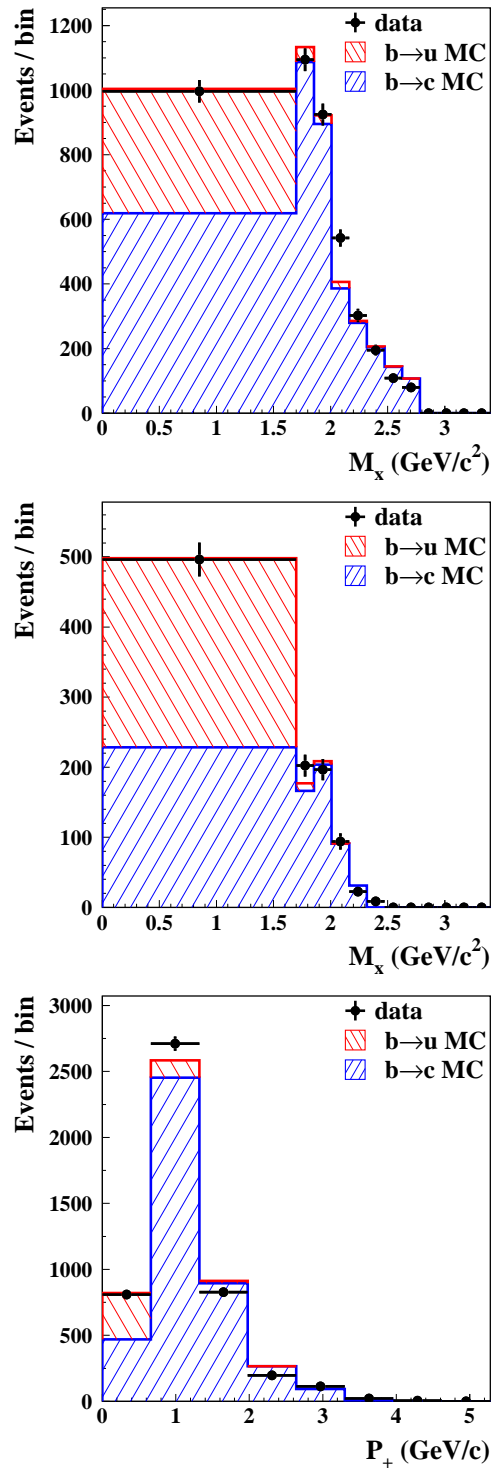
$\varepsilon_{\ell}^{\text{sl}}/\varepsilon_{\ell}^{b\rightarrow u}$: Faktor, ki upošteva razliko v izkoristku leptonske izbire med semileptonskimi prehodi brez kvarka u in vsemi semileptonskimi prehodi.

$\varepsilon_{\text{frec}}^{\text{sl}}/\varepsilon_{\text{frec}}^{b\rightarrow u}$: Faktor, ki upošteva razliko v izkoristku popolne rekonstrukcije mezona B med semileptonskimi prehodi brez kvarka u in vsemi semileptonskimi prehodi.

Ker sta tako imenovalc in števec v količniku $W(\Delta\Phi)$ dobljena (po popravku izkoristkov) na vzorcih z enakim razmerjem števila rekonstruiranih nevtralnih in nabitih mezonov B , je $W(\Delta\Phi)$ neodvisen od tega razmerja. $W(\Delta\Phi)$ torej predstavlja relativno delno razpadno širino mezona B v semileptonsko končno stanje brez kvarka c , normirano na razpadno širino v poljuben semileptonski razpad. Pridevnik delno se nanaša na to, da je $W(\Delta\Phi)$ izračunan za dogodke v določenem kinematičnem območju ($\Delta\Phi$). Delno razpadno širino mezona B v semileptonsko končno stanje brez kvarka c dobimo z množenjem $W(\Delta\Phi)$ s svetovnim povprečjem razpadne širine za semileptonski razpad [10]:

$$\Delta\Gamma_{ul\nu}(\Delta\Phi) = W(\Delta\Phi) \times \Gamma(X\ell\nu) = W(\Delta\Phi) \times \frac{\mathcal{B}(X\ell\nu)}{\tau_B} . \quad (9.15)$$

Dobljene vrednosti za $\Delta\Gamma_{ul\nu}(\Delta\Phi)$, delne razpadne širine mezona B v semileptonsko končno stanje brez kvarka c , so povzete z napakami v tabeli 9-5. Natančnejša določitev vzrokov napak ter njihovih prispevkov je podana v tabeli 9-6.



Slika 9-5. Porazdelitve kinematičnih količin, dobljenih s prilagajanjem porazdelitve M_{bc} za vsak interval posebej. Porazdelitvam za podatke nato prilagajamo simulirani porazdelitvi za prehode $b \rightarrow c$ in $b \rightarrow u$. Po vrsti od zgoraj: porazdelitev M_X , porazdelitev M_X z dodatnim pogojem $q^2 > 8 \text{ GeV}^2/c^2$, ter porazdelitev za P_+ . Prvi interval predstavlja izbrano kinematično območje meritve.

$\Delta\Phi$	$\Delta\Gamma_{ul\nu}(\Delta\Phi)$	stat.	sist.	$b \rightarrow u$	$b \rightarrow c$
M_X/q^2	$5.24 \times 10^{-4} \text{ ps}^{-1}$	10.0	8.9	6.2	5.3
M_X	$7.71 \times 10^{-4} \text{ ps}^{-1}$	9.1	7.1	6.1	2.2
P_+	$6.89 \times 10^{-4} \text{ ps}^{-1}$	9.4	9.3	6.4	8.7

Tabela 9-5. Delna razpadna širina za tri kinematična območja, z relativnimi napakami (v %): statistična, sistematična, ter modelski napaki za prehode $b \rightarrow u$ in $b \rightarrow c$.

PRISPEVEK	M_X/q^2	M_X	P_+
statistična napaka	10.0	9.1	9.4
Prispevki k sistematični napaki:			
porazdelitev intervalov	2.0	2.0	2.0
$r_{b \rightarrow u}^{\text{sl}}$	2.4	1.9	2.0
$\mathcal{B}(X\ell\nu)/\tau_B$	3.0	3.0	3.0
končen vzorec $b \rightarrow c$ MC	5.8	4.0	4.8
končen vzorec $b \rightarrow u$ MC	2.9	2.0	2.5
simulacija detektorja	4.1	2.5	5.6
simulacija K_L	1.5	2.8	2.8
sistematika skupno	8.9	7.1	9.2
modeliranje $b \rightarrow u$:			
oblikovna funkcija	6.0	5.9	6.2
$g \rightarrow s\bar{s}$	1.5	1.5	1.5
skupno modeliranje $b \rightarrow u$	6.2	6.1	6.4
modeliranje $b \rightarrow c$:			
modeliranje strukt. faktorjev D/D^*	5.2	1.0	8.0
$\mathcal{B}(B \rightarrow D^*\ell\nu)$	1.0	1.0	2.0
$\mathcal{B}(B \rightarrow D^{**}\ell\nu)$	0.1	1.7	2.8
skupno modeliranje $b \rightarrow c$	5.3	2.2	8.7

Tabela 9-6. Povzetek prispevkov (v % od $\Delta\Gamma_{ul\nu}(\Delta\Phi)$) k skupni relativni napaki $\Delta\Gamma_{ul\nu}(\Delta\Phi)$, za tri izbrana kinematična območja $\Delta\Phi$.

Za izračun velikosti matričnega elementa $|V_{ub}|$ uporabimo $R(\Delta\Phi)$, teoretično izračunano [3] delno razpadno širino mezona B v semileptonsko končno stanje brez kvarka c , deljeno z $|V_{ub}|^2$. Ta neposredno poveže izmerjeno delno razpadno širino $\Delta\Gamma_{ul\nu}(\Delta\Phi)$ z $|V_{ub}|$:

$$|V_{ub}| = \sqrt{\frac{\Delta\Gamma_{ul\nu}(\Delta\Phi)}{R(\Delta\Phi)}}. \quad (9.16)$$

Natančnost teoretičnega izračuna $R(\Delta\Phi)$ je močno odvisna od tega, kako natančno znamo določiti parametra oblikovne funkcije $m_b(SF)$ in $\mu_\pi^2(SF)$. Da bi čim bolj natančno določili velikost $|V_{ub}|$, smo opravili prilagajanje porazdelitve energije fotona v inkluzivnem razpadu tipa $B \rightarrow X_s\gamma$ [34] s simuliranimi porazdelitvami, pri katerih smo spreminjali parametra $m_b(SF)$ in $\mu_\pi^2(SF)$. Z metodo najmanjših kvadratov smo določili vrednosti obeh parametrov ter ocenili napako njihove določitve: $m_b(SF) = (4.52 \pm 0.07) \text{ GeV}/c^2$ in $\mu_\pi^2(SF) = (0.27 \pm 0.13) \text{ GeV}^2/c^2$.

Pred kratkim pa je bil objavljen rezultat podobnega prilagajanja [69], v katerem so upoštevali vse objavljene meritve momentov porazdelitev ftonske energije pri razpadih tipa $B \rightarrow X_s\gamma$ ter hadronske invariantne mase in leptonske gibalne količine pro semileptonskih razpadih tipa $B \rightarrow X_c\ell\nu$. Tako so dosegli veliko boljše natančnost določanja parametrov oblikovne funkcije: $m_b(SF) = (4.60 \pm 0.04) \text{ GeV}/c^2$ in $\mu_\pi^2(SF) = (0.20 \pm 0.04) \text{ GeV}^2/c^2$, objavljeni rezultat pa sem uporabil za izračun $R(\Delta\Phi)$:

$\Delta\Phi$	$R(\Delta\Phi)$	oblikovna f.	teo.
M_X/q^2	23.7 ps	8.5	$+10.4$ -9.5
M_X	46.1 ps	9.0	$+7.6$ -6.9
P_+	39.4 ps	11.5	$+7.0$ -6.8

Tabela 9-7. Vrednosti teoretičnega izračuna $R(\Delta\Phi)$ za tri izbrana kinematična območja, z relativnima napakama (v %): napako zaradi določitve oblikovne funkcije ter teoretično napako.

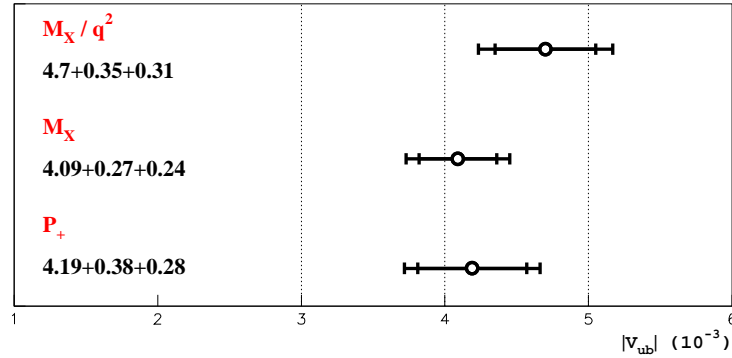
Upoštevajete rezultate iz tabel 9-7, 9-5 in 9-6 določimo velikost matričnega elementa $|V_{ub}|$ ter njegovo napako:

$\Delta\Phi$	$ V_{ub} \times 10^3$	stat.	sist.	$b \rightarrow u$	$b \rightarrow c$	oblikovna f.	teo.
M_X/q^2	4.70	5.0	4.4	3.1	2.7	4.2	$+4.8$ -5.2
M_X	4.09	4.6	3.5	3.1	1.1	4.5	$+3.5$ -3.8
P_+	4.19	4.7	4.6	3.2	4.4	5.8	$+3.4$ -3.5

Tabela 9-8. Izračunane vrednosti $|V_{ub}|$ z relativnimi napakami (v %) za tri izbrana kinematična območja. Vrednosti so izračunane s parametroma oblikovne funkcije $m_b(SF) = (4.60 \pm 0.04) \text{ GeV}/c^2$ in $\mu_\pi^2(SF) = (0.20 \pm 0.04) \text{ GeV}^2/c^2$.

9.7 Interpretacija rezultatov

Meritev, opravljena v okviru tega dela, nam omogoča primerjavo rezultatov za izbrana tri kinematična območja, saj je tako izbira delcev in dogodkov skupna, kinematična območja pa se močno prekrivajo, tako da je tudi doberšen del vzorca skupen. Dobljeni trije rezultati za $|V_{ub}|$ so grafično predstavljeni na sliki 9-6. Ker so napake meritev močno korelirane, smo rezultate primerjali po upoštevanju korelacij. Največje odstopanje med izmerjenimi vrednostmi $|V_{ub}|$



Slika 9-6. Comparison of the $|V_{ub}|$ results from the three signal regions.

smo opazili med meritvama v območju M_X in M_X/q^2 . Po upoštevanju korelacij je razlika: $\Delta|V_{ub}| = (0.61 \pm 0.22(\text{stat.}) \pm 0.06(\text{teo.}) \times 10^{-3}$; odstopanje predstavlja 2.8-kratno statistično napako, oziroma 2.7-kratno skupno napako. Opazili smo tudi rahlo linearno odvisnost rezultata $|V_{ub}|$ od izbrane dodatne selekcije q^2 , ki jo lahko parametriziramo kot:

$$|V_{ub}| = 4.22 \cdot 10^{-3} + 4.72 \cdot 10^{-5} \times \frac{q^2}{1 \text{ GeV}^2/c^2} . \quad (9.17)$$

Iz primerjave natančnosti meritev za posamezna kinematična področja smo zaključili naslednje:

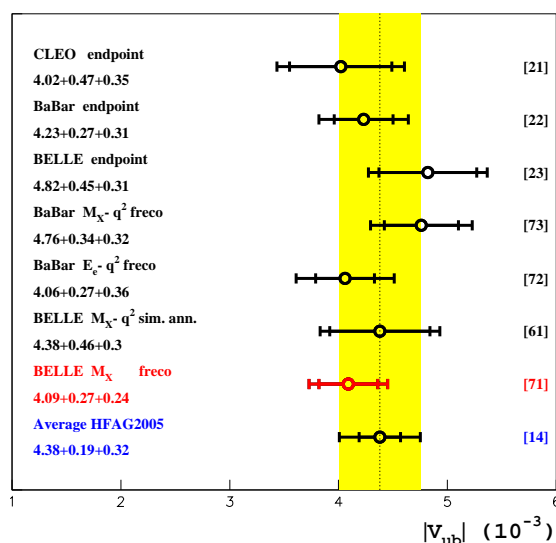
- Dodatna selekcija $q^2 > 8 \text{ GeV}^2/c^2$ kinematičnemu območju M_X ni prinesla nobene opazne eksperimentalne ali teoretične prednosti.
- Meritev $|V_{ub}|$ v kinematičnem območju količine P_+ je najbolj občutljiva na natančnost modeliranja razpadov $b \rightarrow c$ in določanja parametrov oblikovne funkcije in bo zares primerljiva z ostalima metodama šele, ko bo teoretična napaka izračuna $R(\Delta\Phi)$ prevladovala nad drugimi napakami.

Zato izberemo meritev v kinematičnem območju M_X za končni rezultat meritve $|V_{ub}|$, saj je narejen na najbolj inkluzivnem območju in je tudi najmanj občutljiv na prispevke k splošni napaki:

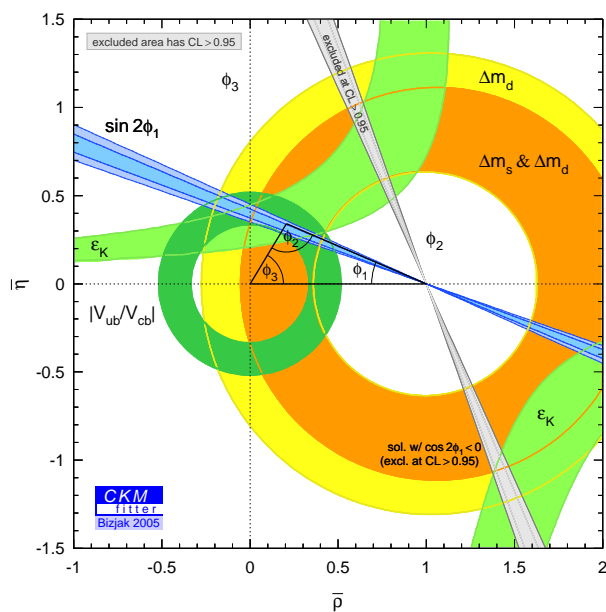
$$|V_{ub}| = (4.09 \pm 0.19 \pm 0.20 \pm_{-0.15}^{+0.14} \pm 0.18) \times 10^{-3} , \quad (9.18)$$

s statistično napako, sistematično napako skupaj z napako modeliranja MC, teoretično napako ter napako zaradi določitve parametrov oblikovne funkcije. Rezultat ima skupno relativno napako 9%, kar pomeni, da je trenutno najbolj natančna meritev $|V_{ub}|$. Primerjava z že obstoječimi meritvami je predstavljena na sliki 9-7.

Meritev $|V_{ub}|$ določa stranico unitarnostnega trikotnika, ki leži nasproti kota ϕ_1 . Interval 95% zaupanja te meritve (enačba 9.18), skupaj z nekaterimi ostalimi meritvami, ki določajo unitarnostni trikotnik, je predstavljen na sliki 9-8.



Slika 9-7. Primerjava obstoječih meritev $|V_{ub}|$: rezultati te analize (rdeče), ostalih novejših inkluzivnih meritev $|V_{ub}|$ (črno), in svetovno povprečje (modro), ki vključuje vse naštetе rezultate [14]. Meritve so opisane v referencah, naštetih desno od meritve.



Slika 9-8. Primer konstrukcije unitarnostnega trikotnika, kjer je spodnja stranica normirana, meritve pa določajo položaj zgornjega oglišča. Posamezne meritve predstavljajo intervali 95% stopnje zaupanja, da leži zgornje oglišče znotraj dela ravnine $\bar{\rho} - \bar{\eta}$: področje, ki ga omejuje rezultat te analize, je označeno s temno zeleno; ostala področja so določena iz svetovnih povprečij meritev parametrov Standardnega modela. Parameter ϵ_K določimo z meritvijo kršitve simetrije CP pri mezonih K , Δm_d in Δm_s določimo iz oscilacij mezonov $B\bar{B}$ in $B_s\bar{B}_s$, $\sin(2\phi_1)$ pa iz meritev razpadov mezonov B , ki kršijo simetrijo CP , kot naprimer $B \rightarrow J/\psi K_S$. Intervali določeni s pomočjo programa iz Ref. [15].

Bibliography

- [1] C. W. Bauer, Z. Ligeti and M. E. Luke, "Precision determination of $|V_{ub}|$ from inclusive decays," Phys. Rev. D **64**, 113004 (2001) [arXiv:hep-ph/0107074].
- [2] S. W. Bosch, B. O. Lange, M. Neubert and G. Paz, "Proposal for a precision measurement of $|V_{ub}|$," Phys. Rev. Lett. **93**, 221801 (2004) [arXiv:hep-ph/0403223].
- [3] B. O. Lange, M. Neubert and G. Paz, "Theory of charmless inclusive B decays and the extraction of $|V_{ub}|$," arXiv:hep-ph/0504071.
- [4] N. Cabibbo, "Unitary Symmetry And Leptonic Decays," Phys. Rev. Lett. **10**, 531 (1963).
- [5] M. Kobayashi and T. Maskawa, "CP Violation In The Renormalizable Theory Of Weak Interaction," Prog. Theor. Phys. **49**, 652 (1973).
- [6] A. B. Carter and A. I. Sanda, "CP Violation In B Meson Decays," Phys. Rev. D **23**, 1567 (1981).
- [7] Q. H. Kim, X. Y. Pham, "Elementary Particles and Their Interactions: Concepts and Phenomena", Springer Verlag Berlin Heidelberg (1998).
- [8] L. L. Chau and W. Y. Keung, "Comments On The Parametrization Of The Kobayashi-Maskawa Matrix," Phys. Rev. Lett. **53**, 1802 (1984).
- [9] L. Wolfenstein, "Parametrization Of The Kobayashi-Maskawa Matrix," Phys. Rev. Lett. **51**, 1945 (1983).
- [10] S. Eidelman *et al.* [Particle Data Group], "Review of particle physics," Phys. Lett. B **592**, 1 (2004).
- [11] M. Battaglia *et al.*, "The CKM matrix and the unitarity triangle," arXiv:hep-ph/0304132.
- [12] A. Abashian *et al.* [BELLE Collaboration], "Measurement of the CP violation parameter $\sin(2\phi_1)$ in B_d^0 meson decays," Phys. Rev. Lett. **86**, 2509 (2001) [arXiv:hep-ex/0102018].
- [13] B. Aubert *et al.* [BABAR Collaboration], "Measurement of CP violating asymmetries in B^0 decays to CP eigenstates," Phys. Rev. Lett. **86**, 2515 (2001) [arXiv:hep-ex/0102030].
- [14] Heavy Flavor Averaging Group (HFAG), "Averages of b-hadron Properties as of Winter 2005", hep-ex/0505100.
- [15] CKMfitter Group (J. Charles *et al.*), Eur. Phys. J. C41, 1-131 (2005) [hep-ph/0406184], updated results and plots available at: <http://ckmfitter.in2p3.fr>.
- [16] N. Isgur and M. B. Wise, "Weak Decays Of Heavy Mesons In The Static Quark Approximation," Phys. Lett. B **232**, 113 (1989).
- [17] N. Isgur and M. B. Wise, "Weak Transition Form-Factors Between Heavy Mesons," Phys. Lett. B **237**, 527 (1990).
- [18] J. Shigemitsu *et al.*, "Semileptonic B decays with $N(f) = 2+1$ dynamical quarks," arXiv:hep-lat/0408019.
- [19] M. Okamoto *et al.*, "Semileptonic $D \rightarrow \pi / K$ and $B \rightarrow \pi / D$ decays in 2+1 flavor lattice QCD," Nucl. Phys. Proc. Suppl. **140**, 461 (2005) [arXiv:hep-lat/0409116].
- [20] P. Ball and R. Zwicky, "New results on $B \rightarrow \pi, K, \eta$ decay formfactors from light-cone sum rules," Phys. Rev. D **71**, 014015 (2005) [arXiv:hep-ph/0406232].
- [21] A. Bornheim *et al.* [CLEO Collaboration], "Improved measurement of $|V(ub)|$ with inclusive semileptonic B decays," Phys. Rev. Lett. **88**, 231803 (2002) [arXiv:hep-ex/0202019].

- [22] B. Aubert *et al.* [BaBar Collaboration], “Measurement of the inclusive electron spectrum in charmless semileptonic B decays near the kinematic endpoint and determination of $|V(ub)|$,” arXiv:hep-ex/0408075.
- [23] A. Limosani *et al.* [Belle Collaboration], “Measurement of inclusive charmless semileptonic B-meson decays at the endpoint of the electron momentum spectrum,” Phys. Lett. B **621**, 28 (2005) [arXiv:hep-ex/0504046].
- [24] A.V. Manohar, M.B. Wise, *Heavy Quark Physics*, Cambridge Monogr. Part. Phys. Nucl. Phys. Cosmol. **10** (2000).
- [25] P. F. Harrison and H. R. Quinn [BABAR Collaboration], “The BaBar physics book: Physics at an asymmetric B factory,” SLAC-R-0504. *Papers from Workshop on Physics at an Asymmetric B Factory (BaBar Collaboration Meeting), Rome, Italy, 11-14 Nov 1996, Princeton, NJ, 17-20 Mar 1997, Orsay, France, 16-19 Jun 1997 and Pasadena, CA, 22-24 Sep 1997.*
- [26] V. Aquila, “Decadimenti semileptonici del mesone B,” Diploma thesis, Universita degli Studi di Genova, 2004.
- [27] K. G. Wilson, “Nonlagrangian Models Of Current Algebra,” Phys. Rev. **179** (1969) 1499.
- [28] T. van Ritbergen, “The second order QCD contribution to the semileptonic $b \rightarrow u$ decay rate,” Phys. Lett. B **454**, 353 (1999) [arXiv:hep-ph/9903226].
- [29] M. Neubert, Phys. Rev. D **49**, 3392 (1994); M. Neubert, Phys. Rev. D **49**, 4623 (1994); I. Bigi, M. A. Shifman, N. G. Uraltsev, and A. I. Vainshtein, Int. J. Mod. Phys. A **9**, 2467 (1994). T. Mannel and M. Neubert, Phys. Rev. D **50**, 2037 (1994).
- [30] S. Hashimoto *et al.*, “Letter of intent for KEK Super B Factory,” KEK-REPORT-2004-4
- [31] F. De Fazio and M. Neubert, “ $B \rightarrow X/u l \text{ anti-}\nu/l$ decay distributions to order $\alpha(s)$,” JHEP **9906**, 017 (1999) [arXiv:hep-ph/9905351].
- [32] S. W. Bosch, B. O. Lange, M. Neubert and G. Paz, “Factorization and shape-function effects in inclusive B-meson decays,” Nucl. Phys. B **699**, 335 (2004) [arXiv:hep-ph/0402094].
- [33] S. W. Bosch, M. Neubert and G. Paz, “Subleading shape functions in inclusive B decays,” JHEP **0411**, 073 (2004) [arXiv:hep-ph/0409115].
- [34] P. Koppenburg *et al.* [Belle Collaboration], “An inclusive measurement of the photon energy spectrum in $b \rightarrow s$ gamma decays,” Phys. Rev. Lett. **93**, 061803 (2004) [arXiv:hep-ex/0403004].
- [35] M. Neubert, “Two-loop relations for heavy-quark parameters in the shape-function scheme,” Phys. Lett. B **612**, 13 (2005) [arXiv:hep-ph/0412241].
- [36] S.W. Bosch, B.O. Lange, M. Neubert and G. Paz, Nucl. Phys. Nucl. Phys. B **699**, 335 (2004); M. Neubert, Eur. Phys. J. C (in print) [arXiv:hep-ph/0408179]; S.W. Bosch, M. Neubert and G. Paz, JHEP **0411**, 073 (2004); M. Neubert, arXiv:hep-ph/0411027; M. Neubert, arXiv:hep-ph/0412241.
- [37] P. Ball, “Weak decay form factors from QCD sum rules on the light-cone,” eConf **C0304052**, WG101 (2003) [arXiv:hep-ph/0306251].
- [38] D. Scora and N. Isgur, “Semileptonic meson decays in the quark model: An update,” Phys. Rev. D **52**, 2783 (1995) [arXiv:hep-ph/9503486].
- [39] A. Limosani and T. Nozaki [Heavy Flavor Averaging Group], “Extraction of the b-quark shape function parameters using the Belle $B \rightarrow X/s$ gamma photon energy spectrum,” arXiv:hep-ex/0407052.
- [40] A. Abashian *et al.* [BELLE Collaboration], “The Belle detector,” Nucl. Instrum. Meth. A **479**, 117 (2002).
- [41] H. Aihara, “The Belle silicon vertex detector,” Nucl. Instrum. Meth. A **466**, 268 (2001) [arXiv:hep-ex/0011028].

- [42] H. Hirano *et al.*, “A high resolution cylindrical drift chamber for the KEK B-factory,” Nucl. Instrum. Meth. A **455**, 294 (2000).
- [43] T. Sumiyoshi *et al.*, “Silica aerogel Cherenkov counter for the KEK B-factory experiment,” Nucl. Instrum. Meth. A **433**, 385 (1999).
- [44] T. Iijima *et al.*, “Aerogel Cherenkov counter for the BELLE detector,” Nucl. Instrum. Meth. A **453**, 321 (2000).
- [45] H. Kichimi *et al.*, “The BELLE TOF system,” Nucl. Instrum. Meth. A **453**, 315 (2000).
- [46] A. Abashian *et al.* [BELLE Collaboration], “The K(L) / mu detector subsystem for the BELLE experiment at the KEKB factory,” Nucl. Instrum. Meth. A **449**, 112 (2000).
- [47] The CLEO QQ generator, see <http://www.ins.cornell.edu/public/CLEO/soft/qq/>.
- [48] D. J. Lange, “The EvtGen particle decay simulation package,” Nucl. Instrum. Meth. A **462**, 152 (2001).
- [49] T. Sjostrand, “PYTHIA 5.7 and JETSET 7.4: Physics and manual,” arXiv:hep-ph/9508391.
- [50] T. Sjöstrand, P. Edén, C. Friberg, L. Lönnblad, G. Miu, S. Mrenna and E. Norrbin, Computer Physics Commun. **135** (2001) 238.
- [51] B. Andersson, G. Gustafson, G. Ingelman and T. Sjostrand, “Parton Fragmentation And String Dynamics,” Phys. Rept. **97**, 31 (1983).
- [52] R. Brun, R. Hagelberg, M. Hansroul and J. C. Lassalle, “Geant: Simulation Program For Particle Physics Experiments. User Guide And Reference Manual,” CERN-DD-78-2-REV ; R. Brun *et al.*, GEANT 3.21, CERN Report DD/EE/84-1, 1984.
- [53] Tracking Group [Belle Collaboration], “Charged Particle Tracking in Belle,” Belle Note 327, 2000.
- [54] A. Abashian *et al.*, “Muon identification in the Belle experiment at KEKB,” Nucl. Instrum. Meth. A **491**, 69 (2002).
- [55] K. Hanagaki, H. Kakuno, H. Ikeda, T. Iijima and T. Tsukamoto, “Electron identification in Belle,” Nucl. Instrum. Meth. A **485**, 490 (2002) [arXiv:hep-ex/0108044].
- [56] F. Fang, “Study of $K_s \rightarrow \pi^+ \pi^-$ Selection,” Belle Note 323, 2003.
- [57] T. Matsumoto, “Studies on $B \rightarrow \pi l \nu$ decays using full reconstruction B tagging,” Belle Note 760, 2004.
- [58] G. C. Fox and S. Wolfram, Phys. Rev. Lett. **41**, 1581 (1978).
- [59] H. Albrecht *et al.* (ARGUS Collaboration), Z. Phys. C **48**, 543 (1990).
- [60] J. E. Gaiser *et al.*, Phys. Rev. D **34**, 711 (1986).
- [61] H. Kakuno *et al.* [BELLE Collaboration], “Measurement of $|V_{ub}|$ using inclusive $B \rightarrow X u l \nu$ decays with a novel X/u reconstruction method,” Phys. Rev. Lett. **92**, 101801 (2004) [arXiv:hep-ex/0311048].
- [62] M. Neubert, Phys. Rept. **245**, 259 (1994).
- [63] J.E.Duboscq *et al.*, Phys. Rev. Lett. **76**, 003898 (1996);
- [64] K. Hagiwara *et al.*, Phys. Rev. **D66**, 010001 (2002).
- [65] A. Limosani, “An investigation of the inclusive charmless semileptonic B meson decays with the Belle detector”. PhD thesis, University of Melbourne, 2004.
- [66] S. Anderson, Ph.D. thesis, University of Minnesota, 2002.

-
- [67] We thank B. Lange for noticing us this fact.
- [68] We thank R. Faccini for suggesting such a function.
- [69] O. Buchmueller and H. Flaecher (Heavy Flavor Averaging Group), hep-ph/0507253.
- [70] P. Abreu *et al.* [DELPHI Collaboration], “Determination of $|V(ub)|/|V(cb)|$ with DELPHI at LEP,” Phys. Lett. B **478**, 14 (2000) [arXiv:hep-ex/0105054].
- [71] I. Bizjak *et al.* [Belle Collaboration], “Measurement of the inclusive charmless semileptonic partial branching fraction of B mesons and determination of $|V(ub)|$ using the full reconstruction tag,” arXiv:hep-ex/0505088.
- [72] B. Aubert *et al.* [BABAR Collaboration], “Determination of $|V(ub)|$ from measurements of the electron and neutrino momenta in inclusive semileptonic B decays,” Phys. Rev. Lett. **95**, 111801 (2005) [arXiv:hep-ex/0506036].
- [73] B. Aubert *et al.* [BABAR Collaboration], “Measurement of the partial branching fraction for inclusive charmless semileptonic B decays and extraction of $|V(ub)|$,” arXiv:hep-ex/0507017.

Izjavljam, da je disertacija rezultat mojega samostojnega raziskovalnega dela.

Ilija Bizjak

Ljubljana, oktober 2005

